UNIVERSITY OF BIRMINGHAM

Development of Hypereutectic Al-Si based P/M Alloys

By

Shei Sia Su

A thesis submitted to the University of Birmingham
for the degree of

Doctor of Philosophy

School of Metallurgy & Materials
College of Engineering and Physical Sciences
The University of Birmingham
Birmingham B15 2TT
England
April 2012

Synopsis

The compaction, sintering and heat treatment processing conditions for the commercial powder, Ecka Alumix 231 with the nominal composition of Al-15Si-2.5Cu-0.5Mg(wt%) have been optimized in this study. It has been found that densification of Ecka Alumix 231 depended largely on the sintering atmosphere and the amount of liquid phase presented. Sintering in nitrogen atmosphere was found to be beneficial due to the formation of AIN which later induced pore filling effect. Presence of hydrogen in the sintering atmosphere, however, was not desirable. Decomposition of MgH_2 at higher temperature was suggested to increase the pore pressure and caused detrimental effect on compact densification.

The effects of alloy additions (i.e. Cu and/or Ni) on sintering and heat treatment response were also investigated in this study. Addition of copper was found to enhance the sintering response by a significant increase in the sintered density, reduced the peak ageing temperatures and time. Nickel addition, however, was detrimental to both sintering and heat treatment response since it reduced the amount of copper content dissolved in the α-aluminum due to the formation of $Al_3(Ni,Cu)_2$ phase. The precipitation sequence for Al-Si-Cu-Mg-(Ni) was suggested to be: Supersaturated solid solution (SSS)→GP zones → θ” → θ’ → θ.

Preface

The work described in this thesis was carried out by the author in the School of Metallurgy and Materials, The University of Birmingham from September 2008 to February 2012, under the supervision of Dr. I T H Chang

To the best of my knowledge, the material presented in this thesis is original, except otherwise noted within the text. None of this research has been submitted for any degree at this or any other university.

Part of the present work was presented in international conference and published as follows:

[1] Su.S.S. and I.T.H. Chang, " Effect of Processing Conditions on Hypereutectic Aluminum-Silicon P/M Alloys", *World PM2010 Proceedings*, Vol. 4, pp 49-57 (2010)

[2] Su.S.S. and I.T.H. Chang, " Development of Hypereutectic Al-Si based alloys", *World PM2010 Proceedings*, Vol.4, pp 58-62 (2010)

Acknowledgements

This dissertation would not have been completed without the support of many wonderful individuals. In particular, I would like to acknowledge the enthusiasm and dedication of my supervisor, Dr I T H Chang. I am deeply grateful for his valuable guidance, support and constant encouragement throughout my PhD. His patience, wisdom and excellent supervision have made this PhD a very rewarding journey.

My sincere gratitude also goes to Dr Winson Kuo from Oxford Instruments who has always offered insightful suggestions and gave significant contribution to boost my knowledge in electron microscopy and enhance my analyzing skills. I would also like to thank Mr. Hang Wang in offering lots of valuable inputs on thermodynamics and is always willing to lend an attentive ear and a critical eye.

I would also like to express my sincere gratitude to many other friends and colleagues who have contributed in countless ways to my dissertation. My sincere thanks go to Dr Martin Strangwood for offering training in optical microscope and Thermocalc software, Dr Yulung Chiu and Dr Rengen Ding for providing valuable advices on TEM sample preparations, Dr Ming Chu for offering training in TEMs, Mr. Paul Stanley for offering training in SEMs/EDS, Mr. David Price for assistance in tensile test, Mr. Frank Biddelstone for assistance in DSC, Mr. Jeff Sutton for assistance in XRD and to Mr. Jas Singh for assistance in the grinding and polishing. I am also grateful to all technical staff of Met & Mat; particularly Tony Burbery, Geoff Dolman, Mick Cunningham, Avril Rogers, Paul Osborne and Anne Cabezas, for their support and help.

Special thanks also go to my group mates: Nick Harrison, Andy Poole, Andy Ward and for providing a pleasant working environment, to Yina Guo, Jiayun Jiang, Chao Yang and all my bible study members for their friendship and unfaltering encouragement over the years of my academic pursuit. I would like to take this opportunity to also thank Overseas Research Scholarship Fund and Professor Paul Bowen, School of Metallurgy and Materials for providing financial support.

Last but not least, I would like to express my gratitude to all of my family. Their support, patience and encouragement have significantly contributed to the completion of my PhD.

Content

Chapter 1

Introduction

With the growing demand to lower carbon emission, the developments of lightweight materials have continued to gain much attention in both automotive and aerospace industries. Wrought and ingot metallurgy metal forming techniques have been used extensively in the manufacturing industries to produce the metallic components. Despite its flexibility in engineering designs, the limited range of alloy chemistry that can be employed and inadequate dimensional tolerances posses a major threat to the industries due to its high secondary machining costs.

Power metallurgy (P/M) approach has received considerable attention as an alternative to wrought and ingot technologies. P/M technology allows fabrication of near net shape products at high production volume and low manufacturing costs. Apart from cost-effective processes, the process variables in P/M can be adjusted to produce parts which are analogous to conventional cast and wrought materials. Other advantages of aluminum P/M are listed below:

- Cost effective manufacturing for complex or unique shapes application
- Minimal waste during machining
- Energy savings since it requires lower sintering temperature and use of cheaper sintering gas, i.e. nitrogen gas
- Good workability

- Excellent corrosion resistance
- Reasonable homogeneity of the microstructure in the final parts

Though P/M Al-Si alloys seem to be promising candidate to replace the cast aluminum-silicon in application, very little studies are focused on this alloy in both alloy design and development processes. Thus, there is a strong need to understand the fundamental of P/M Al-Si alloys and explore the likehood of this alloy with different combination of composition and fabrication methods in the commercial applications.

This PhD project studied several P/M processing parameters of concern and outlines the influences of these parameters on the properties of aluminum-silicon based P/M alloys. Sintering is the key process responsible to produce materials with enhanced properties. However, the dense and stable oxide layer presented at the surface of the aluminum powders often acts as a barrier to sintering process. In order to disrupt the oxide layer, compaction and successive liquid phase sintering are essential to facilitate metal to metal contact and promote particles interdiffusion. Yet, high liquid content can lead to undesirable shape distortion and dimensional changes. Therefore, substantial improvement in the sintering process is required to produce more commercially feasible alloys which can meet the requirements of many load bearing applications.

Control of the sintering parameters which included sintering atmosphere, sintering temperature and sintering time is crucial to produce sufficient amount of liquid to

wet the particles leading to the increased densification rate with less dimensional changes on the parts. Other principal areas of focus include studies on the effects of alloy additions (i.e. Cu, Ni), on the microstructures and mechanical properties of the P/M parts. Control of the alloy additions is necessary to prevent formation of large, brittle intermetallic phases which will lead to detrimental effect in the mechanical properties.

Apart from sintering variables, controlled heat treatment of hypereutectic Al-Si alloys can significantly influence microstructures and mechanical properties. The heat treatment procedures included solution heat treatment and ageing. Solution heat treatment prior to ageing has significant influence on the precipitation process. Solution temperature must be controlled within a narrow range depending on the alloy composition. Moreover, controls of the aging time and temperature are important to obtain uniform distribution of the precipitates within the matrix since the size and distribution of precipitates will determine the strength of the alloy.

The following chapter presents a review of literature related to the topic of interest (Chapter 2). The processing technique and characterization methods applied in this work are explicitly described in Chapter 3. Chapter 4 and 5 presents the details of the results for this work, followed by the discussion of the results. The conclusion drawn from the findings and recommendation for further works to be carried out are summarized in Chapter 6.

Chapter 2

Literature Review

2.1 Introduction

The unique characteristic of powder metallurgy is production of P/M parts without undergoing complete molten state. The use of powder metallurgy can be traced back to ancient civilization when the techniques of melting pure iron or other high melting point metals were very much limited. Egyptian iron implements, Delhi column, just to name a few, were the examples of the application of powder metallurgy in the ancient days. Sponge of metals can be readily produced by reduction of their ores at low temperatures and followed by hammering at either ambient or elevated temperatures into the desired shape [1, 2].

Production of platinum ingots using press-and-sinter route by Wollaston from England had marked the start of modern development in powder metallurgy. This production method was further developed by Coolidge and others in early 1900's to produce tungsten ingots for the use of making filaments for incandescent light bulbs[2].

Another significant development of powder metallurgy was the production of self-lubricating bearing. Bearings produced by PM route allowed a considerable amount of interconnected pores, and weresubsequently degassed to extract the

gas within the pores and immersed the parts in the lubricating oil. The lubricating oil was retained within the pores and it took up 20-25% of the total volume. Other PM products include, carbide-metal cutting tool materials, copper-graphite brushes and various parts for engines[1].

After Word War II, cost savings and productions of parts with close dimensional control were the main drive for the development of powder metallurgy. A number of novel compaction and sintering methods were developed since then. The capacities of presses had increased significantly from a few tonnes to thousands of tons nowadays. Nevertheless, better sintering furnace and precise control of sintering atmospheres have led to significant advancement in the powder metallurgy technique[2].

Nowadays, PM parts are widely used in the automotive industry. Pistons, belt pulley, pump gears and connecting rods are some common parts made by PM process. The improvement to the PM parts either through development of novel powders with superior properties or developing better compacting press, sintering furnace and atmosphere and post-sintering treatment is still an area of intense interest. PM products offers properties comparable to the materials produced by conventional means, for instance casting and forging. LaDelphaet. al had reported that the high performance wrought alloy AA4032-T651 can be simulated using the P/M technology which yielded comparable tensile properties, hardness and aging response [3].

Powder metallurgy (P/M) is considered as one of the most versatile processing route to satisfy these two requirements: ability to modify the alloy chemistry and to produce near-net shape product [4]. Generally, P/M route comprised of three basic processes, whereby metal powders in their elemental or master alloy form are blended with/without lubricants, compacted and sintered at optimum temperature to produce materials with desired properties.These processes, particularly compaction and sintering are to be discussed in details in the following sections. After sintering, the parts can either be ready for use or secondary operations might be required to achieve specific properties. A simple schematic diagram which briefly illustrates the basic P/M processes is shown in Figure 2.1.

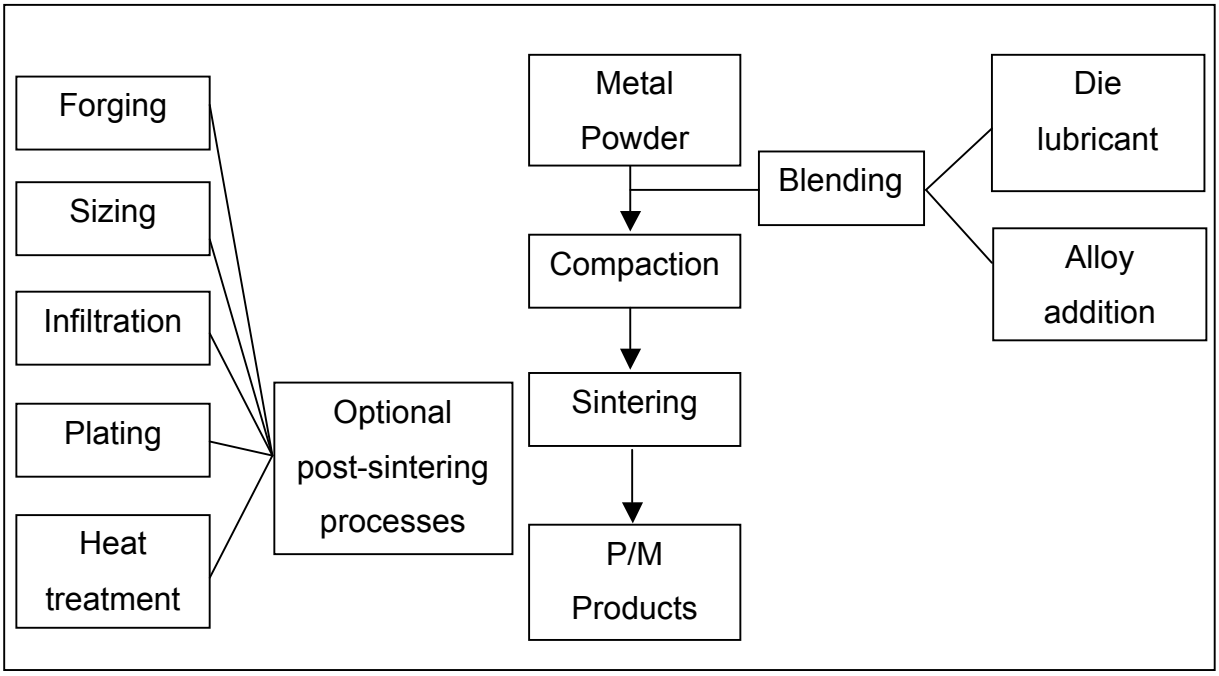

Figure 2.1 Basic Processes involve in Powder Metallurgy Manufacturing

2.2 Powder Production Methods

A considerable range of different powder production methods has been widely used in industries to fabricate metal powders. It is of prime importance to determine the exact powder production technique to be used since it has significant influence on the powder characteristic. Particle size distribution, particle shape and size, thickness of surface oxide are among a few factors largely dependent on powder production technique and can ultimately influence the properties of the finished products. The following sections provided a brief description on the common techniques applied commercially for mass production of powders.

2.2.1 Gas Atomization

Gas atomization refers to the process which involves the use of high velocity jet of air, nitrogen, argon or helium to disintegrate the molten metal stream into fine particles. Gas atomization is widely used for the mass production of commercial powders, including copper and its alloys, aluminum and its alloys, titanium-based alloys, nickel-based alloys, lead, tin, refractory metals, etc [5]. Figure 2.2 displays a schematic design of a vertical gas atomizer. A stream of molten metal is forced through an orifice and injected into a stream of gas that has been confined in nozzle. The atomization pressure generally used is in the range of 0.5 to 4MPa and the gas velocities in the nozzles range from Mach 1 to 3[6]. A rapid gas expansion breaks up the liquid stream into thin sheet which later form ligaments.To minimize the surface energies, the ligaments are further broken down into ellipsoids and

spheres. The small droplets then solidify and separate from gas by cyclone separator[7].

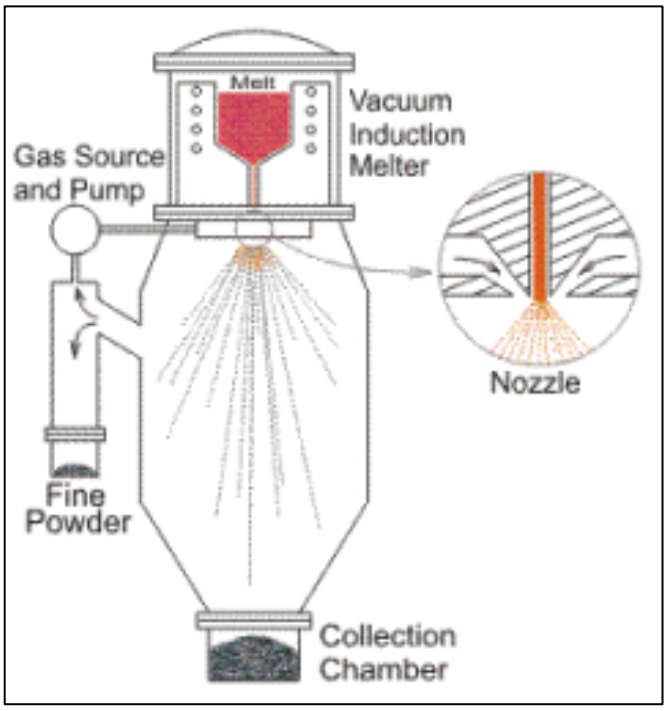

Figure 2.2. Vertical Gas Atomizer [7]

The powders produced in this manner generally have broad size distribution. The particles size distribution depends on the nozzle configuration, gas pressure, gas temperature, gas velocity and temperature of the molten aluminum. One of main parameters controlling the particle size is specific gas consumption and can be expressed in the equation as below:

$$\delta_m = KF^{-1/2} \qquad (2.1)$$

where δ_m is the median atomized particle diameter, K is a function of nozzle design and alloy properties and F is the specific gas consumption expressed in ratio of gas volume to metal mass (m^3/kg). It can be noted that median diameter of

aluminum alloys decreases from ~250μm to below 50μm with the increase of mass flow ratio of gas to metal from 0.3 to 2.0 respectively [5].

In terms of the particle shape, inert gas atomized powders generally exhibit spherical shape. Meanwhile, air atomized powders exhibit a more ligamental shape and oxide formation is noted due to the oxygen pick-up during the exposure of molten metal to air[8]. Nevertheless, Anderson et al. found that the resulting oxide on aluminum alloys was similar to those produced by inert gas atomization[9].

2.2.2 Water Atomization

Water atomization is another widely used atomization process for the production of P/M powders, including iron, copper, copper alloys, nickel, nickel alloys, stainless steels and soft magnetic powders. Water atomized powders are generally used in thermal spray coating, brazing, sintered electrical contacts and in dental amalgams. Figure 2.3 illustrated the basic process of water atomization whereby a stream of molten metal emerges vertically from the tundish. The impinging high pressure water jet cools the molten metal and breaks it into small droplets. The angle of the jets to the vertical, water volume and pressure, thickness of metal stream and temperature of the melts have significant influence on the powder produced using this method [1].

Water atomization differs from gas atomization in many aspects. Water atomization is dominated by the pressure of water in controlling the particle size. Meanwhile, gas to metal ratio is the main factor in controlling the gas-atomized particle size. Commercial water atomization typically used the water pressure in the range of 5 to 20MPa, producing particles with the median sizes of 30 to 150μm. The median particle size can be reduced down to 5 to 20μm when higher water pressures of 50 to 150 MPa are used. Although water atomization is relatively cheaper than gas atomization, powder purity and particle shape remains the primary limitations of this method. The resulting powders are mainly irregular in shape. Besides, oxygen contamination and formation of hydrated layers of the powders also occur with the use of water. Thus, powders separated from water further undergo degassing and drying procedures [8].

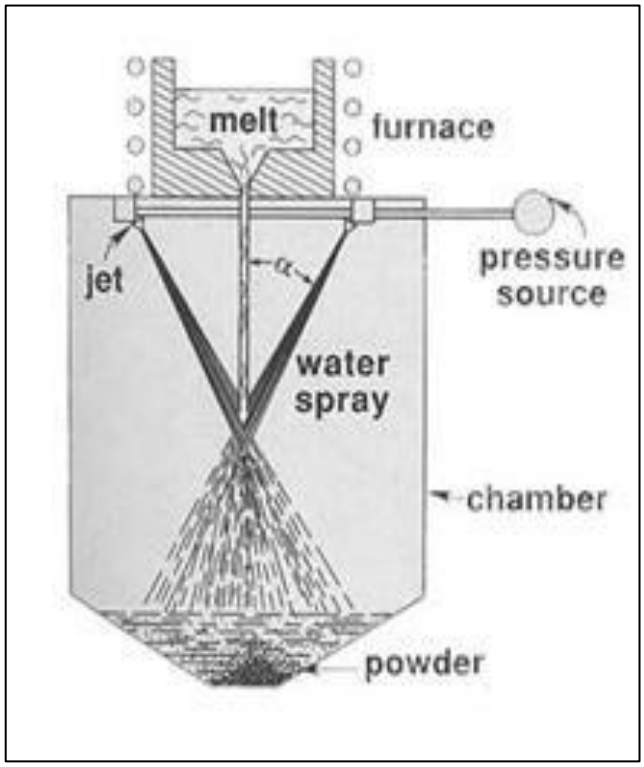

Figure 2.3 Water Atomization Process [7].

2.2.3 Centrifugal Atomization

Though gas and water atomization are largely used for manufacturing of P/M powder, the appearance of non-metallic inclusions in the final powders is unavoidable which later can lead to detrimental effects on the properties of the final products. Centrifugal atomization, on the other hand, can eliminate the aforementioned problem and ensure minimum level porosity within the particles [1]. Titanium, zirconium, molybdenum and vanadium alloysare a few examples of the alloys rountinely atomized using the centrifugal atomization. One of the common centrifugal atomization is rotating electrode process as illustrated in Figure 2.4. As the name applies, the energy source for this type of atomization is centrifugal forces.

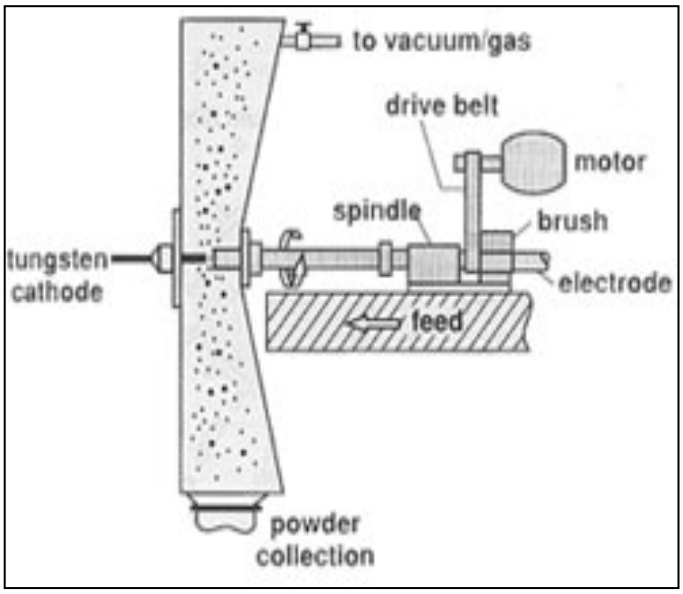

Figure 2.4 Centrifugal Atomization[7]

The consumable electrode which acts as anode is made from metal to be powdered. It is introduced into a chamber through a rapidly rotating spindle. The

end of the electrode is melted by electric arc generated by the tungsten cathode while it rotates around the longitudinal axis. The molten metal is later thrown off by the rapid rod rotation and solidifies before hitting the chamber. Melting of the anode is performed under inert atmosphere; preferably helium gas since it can enhances both the arc stability and heat transfer coefficient during cooling of the atomized droplets[5, 10, 11].

The powder produced using centrifugal atomization is generally spherical with smooth surface but the mean particle size is relatively large ranging from 50 to 150μm due to the mechanical limitation on rotational speed.Other drawbacks include high cost of production, low productivity and high energy consumption as compared to other powder production methods[5].

2.2.4 Mechanical Milling

Mechanical milling refers to mechanical disintegration of the solid metals into smaller particles. This is a common process used for the production of hard metals and oxide powder. Examples of metals produced using mechanical milling includeelectrolytic iron, beryllium and metal hydrides and sensitized stainless steel[6]. Grinding processes are carried out by rotating the jar filled with hard balls and metals to be milled at high speed. Collision between the balls and the metals later crushed it into powders with finer size. Apart from causing fractures, milling operation also deforms and cold welds the impacted particles. Milling can be

performed in either wet or dry conditions. To reduce oxidation on the freshly created particle surfaces, mechanical milling is preferably conducted in protective atmosphere. Surface-active grinding liquid can be used during milling to reduce surface energy of the particle. It enables shorter grinding time and decrease the particle size[12]. The drawback is this fluid might be absorbed and contaminated the final product.

2.2.5 Electrolysis

A number of metallic powders can be produced using electrolysis method. Among these examples are copper, nickel, zinc, beryllium and iron powders. Electrolysis process involves the use of two electrodes connected to the direct current. The anode which is made up of metal whose ions contained in electrolyte undergoes dissolution and deposited at the cathode as the current flows. Electrolysis method generally yields powder of high purity with dendritic morphology. However, it is not possible to produce alloy powder using this method[1, 12]. Additionally, powders obtained from electrolysis need to be washed to remove all the electrolytes, dried, annealed and ground to desired particle size distribution. Due to the relatively low production rate coupled with high electrical energy costs, electrolysis is significantly more costly than other processing technique.

2.2.6 Thermal decomposition

Thermal decomposition generally involves the production of fine and high purity powders from metal compounds after undergoing a series of events. Carbonyl process is one of the common examples for production of iron and nickel powders by decomposition of the respective carbonyls. The process starts by passing the carbon monoxide gas to react with crude metal (e.g. ore, sponge iron, nickel granules, fine scrap iron) at specific temperature and pressure to form carbonyls, $Fe(CO)_5$ and $Ni(CO)_4$. The gaseous products later condense and store under pressure. Decomposition is carried out by reheating the metal carbonyls.Metal and carbon monoxide form following the equation below:

$$Fe(CO)_5 \leftrightarrow Fe + 5CO$$

$$Ni(CO)_4 \leftrightarrow Ni + 4CO$$

Carbon monoxide is extracted and recycled, while the metal powder forms as a result of condensation. The particle size and shape depend on the concentration of carbonyl metals and thermal gradient within the decomposition chamber. Generally, the powder produced by this means has spherical shape with the size range from 2 to 15μm[12].

2.3 Compaction

Compaction is a crucial step in P/M to consolidate the loose powder into compact that has sufficient strength for subsequent handling[2]. In order to reduce the operational costs associated with the secondary machining, compaction plays a significant role in producing parts close to the required shape and dimensions.

Prior to compaction, lubricants are either mixed with powder, lubricating the die wall or both. Lubrication is necessary to minimize die wear, ease the ejection of the compact from the die and improve homogeneity of compact by reducing the green density gradient during compaction. The most common lubricants used are stearic acid, metal stearates and synthetic waxes, such as accrawax[13]. Lubricating of the die wall is carried out by spraying the lubricant which is mixed with volatile solvent, i.e. methanol or acetone. Meanwhile, the amount of admixed lubricant used in powder lubrication varies from 0.5 to 1.5wt%[14]. Most of the commercial aluminum alloy powders are admixed powder with 1.5wt% lubricant.

Most of the powder compactions are carried out by using the mechanical presses and rigid tools which will determine the basic dimensions of the parts. Though uniformity of the density within the compact is preferable, more often, density variation is observed due to friction between powder itself and between powder and the die wall which give rises to the non-uniform distribution of pressure within the compacts. The density variation will imparts some effects on properties variation as well as dimensional changes which take place during sintering. Figure 2.5 illustrates the density variation using different types of compaction.

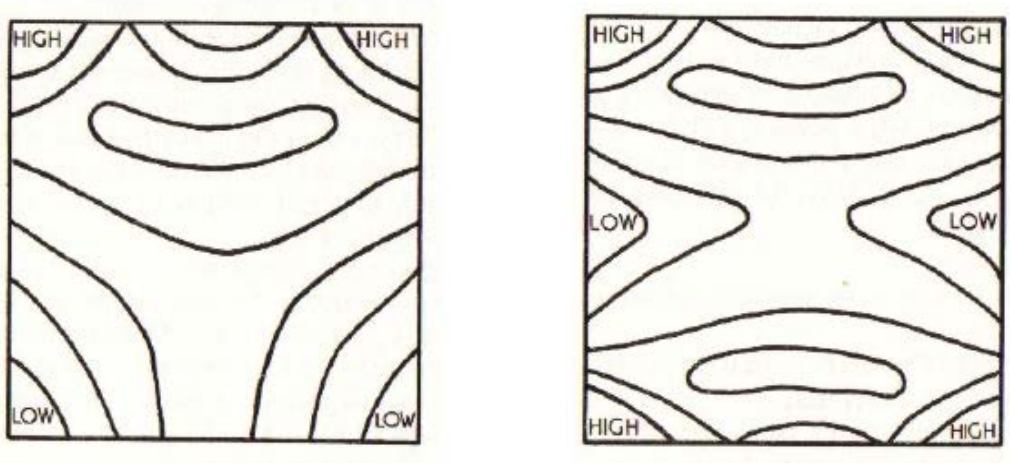

(a) (b)

Figure 2.5. Density distribution during die wall compaction (a) single action pressing (b) double action pressing [15]

There are two main categories of compacting techniques, namely pressure techniques and pressureless techniques. In this context, focus will be put on pressure technique. A few common pressure-based compactions are introduced in Table 2.1. A more detailed uniaxial powder compaction will be discussed in the following section.

Table 2.1. Common types of Compaction Techniques[2]

Compaction Techniques	Characteristic
Die	Conventional technique which allows pressure to be applied in axial direction to one or both ends of powder mass
Isostatic	Flexible container is used for compaction. Pressures are exerted in all direction by a liquid medium
Extrusion	Powders are continuously extruded through the die to form high density body with fixed cross-sectional profile
Forging	Powders are compacted into preform, heated in furnace with controlled atmosphere and subsequently forged to final dimension.

2.3.1 Uniaxial Compaction

Uniaxial die compaction is commonly used in the industry due to its low costs and simplicity. The powders are compacted inside a die by applying pressure along one axis of a die assembly. Product size and shape is thus restricted to the available press capacity. Control of the height to diameter ratio is necessary to reduce density variation and to reduce the friction effect. Compaction can be carried out by using single punch (single action compaction) or by using both punches (double action compaction). Either mechanical or hydraulic presses can be used for the compaction [2].

Figure 2.6 illustrated the sequence of powder filling, pressing and ejection for die compaction. The predetermined powder in the external feed shoe is first filled into the die. The lower punch then positioned itself to allow pressing occurs in the centre of the die, while the upper punch starts to enter into the die. Powder is compacted from both directions at the designated pressure. It is subsequently followed by ejection whereby upper punch is again removed from the die and force applied on the lower punch to eject the green compact [16, 17]. Aluminum alloys powders are normally compacted at relatively low pressure ranging from 138 to 414MPa due to their low yield strength[18, 19].

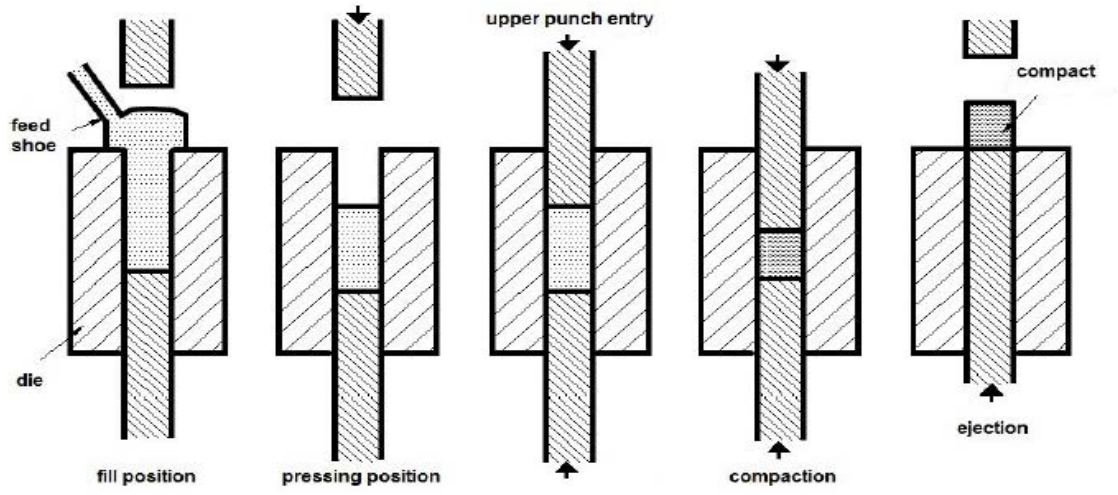

Figure 2.6. Sequence of powder filling, pressing and ejection[16]

Increase of compaction pressure generally shows a logarithmic relationship with the increase of the green density. An example of compressibility characteristic for gas atomized aluminium and electrolytic copper powder is displayed in Figure 2.7 [5]. At low compaction pressure, bulk movement and particles rearrangement occur, resulting in more efficient powder packing. Yet, it is restricted by the frictional forces between neighboring particles and with the tools[2]. Thus, lubrication, either

by mixing the organic lubricant with the powder or coating the die wall with lubricant is necessary. Ease of particles rearrangement is inversely proportional to the apparent density of the powder. Although powder with low apparent density has poor powder flow, it allows more free space for small particles to move within the powder mass which reduces the amount of porosity in the compact[1, 17, 20].

When the compaction pressure is increased, particle deformation appears to be the most important densification mechanism during compaction. Stress transfer between particles allows closing off of porosity to form isolated pores[1, 17, 20]. Shear stress developed during compaction will result in disruption of tenacious oxide layer on the particle. At higher compaction pressure, further densification is limited due to strain hardening.

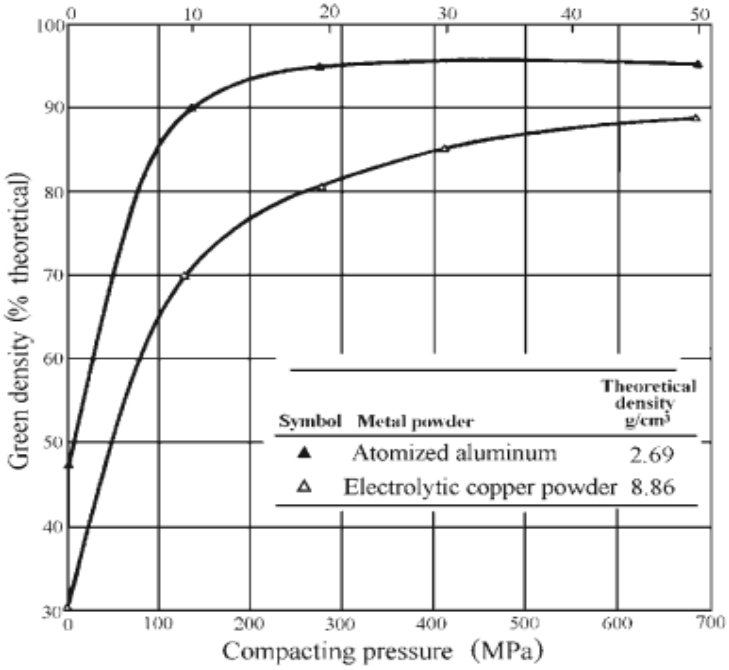

Figure 2.7. Compressibility curves for gas atomized aluminum powder and electrolytic copper powder [5].

2.4 Sintering

Sintering, in the P/M process is responsible to produce density-controlled materials with desired properties when subjected to thermal energy. In the current aluminum alloys P/M industries, there have only been sporadic studies on this processing technique. Therefore, substantial improvement in the sintering process is required to produce more commercially feasible alloys which can meet the requirements of many load bearing applications[21]. Moreover, it will also allow conventional P/M method to appear as a viable alternative to those of casting and wrought operations [22].

Sintering involves applying thermal treatment at the temperature below the melting point of the main constituent to form the metallurgical bonding between particles in powder mass or within the compact[1]. The main driving force for sintering is the reduction of the free energy of the system associated with the decrease in the internal surface free energy. During sintering, neck growth and pore closure occur which leads to the densification or shrinkage of the compacts.

There are two main types of sintering processes: solid state sintering and liquid phase sintering. Solid state sintering involves mass transport within the solid powder particles through surface diffusion, volume diffusion and particle boundary diffusion without the occurrence of liquid phase. Liquid phase sintering, on the other hand, provides better mass transport by having a second phase which acts as high diffusivity path.

Similar to compaction process, variation in the sintering techniques and processing variables can lead to variation in the sintered microstructure as well as the sintered properties of the parts [23]. The variables which can influence the sinterability and microstructures of the powder compact can be summarized in Table 2.2. In general, sintering aims to produce reproducible parts with desired microstructures through careful control of the processing variables[24].

Table 2.2. Major sintering variables affecting the sinterability and microstructure of the powder compact [24].

Variables	Details
Material Variables	Chemical composition, powder shape, powder size, powder size distribution, degree of powder agglomeration
Process Variables	Temperature, time, atmosphere, heating and cooling rate

2.4.1 Driving Force for Sintering

It has been well-recognized that surface energies are the major factor influencing the compact behavior during sintering. Sintering of powder compact is often accompanied by shrinkage event or densification. Decrease in the free surface energy or reduction of total pore/solid interface is the principal driving force for sintering. The total interfacial energy, $\Delta\gamma$ of powder compact can be expressed in the Equation 2.1:

$$\Delta(\gamma A) = \Delta\gamma A + \gamma\Delta A \quad (2.1)$$

where γ is the specific surface or interface energy and A is the total surface area of the compact [24]. Figure 2.8 illustrated that changes in the interfacial energy, $\Delta\gamma$ is due to the densification. Meanwhile, change in the surface area is due to the particle coarsening.

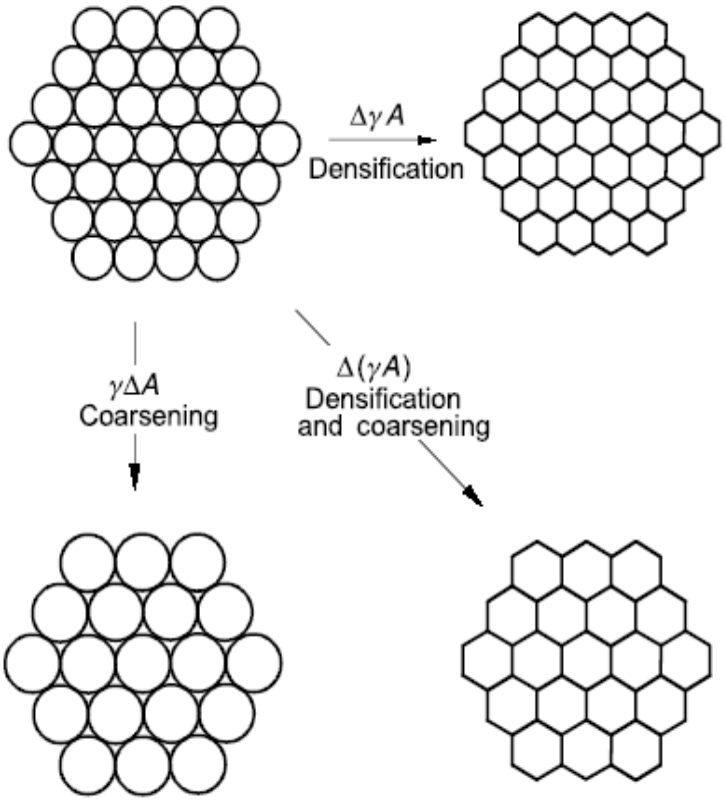

Figure 2.8. Basic Phenomena occurred during sintering [24].

Consider the reduction of total interfacial energy of the system, the microstructure of the compact will drive towards minimum energy configuration. The LaPlace (Young) equation (Equation 2.2a) is commonly applied to explain the context of microstructural variation during sintering.

$$P^{\propto} - P^{\beta} = \gamma \left(\frac{1}{r_1} + \frac{1}{r_2}\right) \quad (2.2a)$$

Similarly,

$$\Delta P = \gamma \left(\frac{1}{r_1} + \frac{1}{r_2}\right) \quad (2.2b)$$

whereΔP is the pressure difference between the α and β phase which is separated by the curved interface, $r_1$and r_2 are referred to the radii of curvatures, and γ is the surface energy.

Figure 2.9 gives a schematic illustration of distribution of vacancy near the curved interface. The concave regions are the sinks for material, whereby convex regions of particle surface or solid-pore interface are the material sources. Decrease in surface energy can be achieved by filling in the concave regions in order to attain a flat surface[25]. The pressure difference given by Equation (2.2b) induces material transport. Redistribution of material over the surface by surface and/or volume diffusion occurred during solid state sintering. In case of liquid phase sintering, liquid flowcan occur due to the capillary action leading to massive flow of material. [25, 26].

Apart from densification, particle coalescence which occurs during sintering as illustrated in Figure 2.8 can also be explained using Equation (2.2b). Two coalescing particles of different size give rise to pressure difference across the particle boundaries. Largerparticles normally have lower pressure than the smaller particles. Thus, large particle grows while smaller particle shrinks due to the

particle boundary migration and solution reprecipitation. The particle growth rate will increase with the increase of solid-liquid surface energy [26].

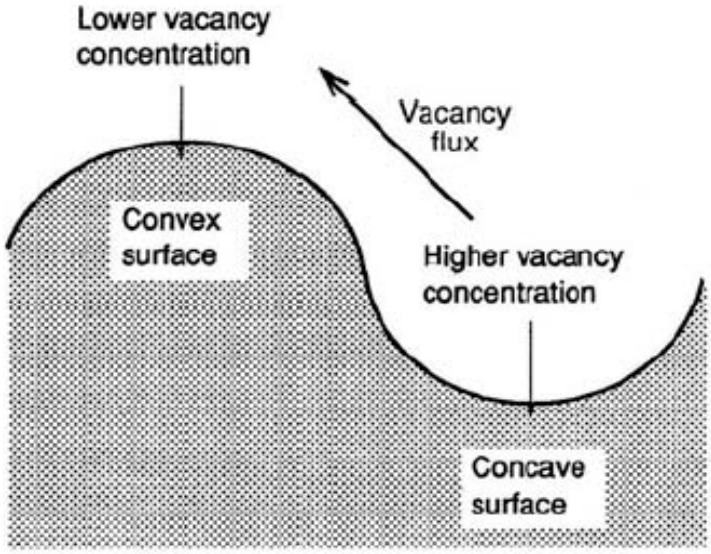

Figure 2.9. Schematic showing the distribution of vacancies near a curved interface

Though the term sintering for one component system can be synomym to shrinkage, it is not the case for multicomponent mixture powder compacts. Sintering of the powder compact consisting of multicomponent mixture, involves two main processes: volume shrinkage and alloy formation. Reduction of free energy for the whole system is thus, contributed by the reduction in surface area due to effect of capillary forces and by the reduction in free energy due to alloy formation. Unlike sintering of one-component compact, kinetics of sintering for two or more component mixtures are more complicated and always accompanied by diffusion homogenization. The homogenization process can result in both compact

shrinkage and compact growth, as a result of contraction and expansion of crystal structure of solid solution[27, 28].

The specific influence of alloy formation on compact densification during sintering is still not clearly understood. Savitskii (2005) has pointed out that basic driving force for sintering mixtures is largely due to reduction of free energy in the system due to alloy formation. The reduction of its surface free energy, on the other hand, will be the additional driving force which will dominate when system attained chemical equilibrium. Contribution of mass transfer due to alloy formation on volume changes during sintering of multi-component powder compact is, thus taken into consideration in this new approach [28].

2.4.2 Wetting Characteristic

Wetting isgenerally associated with equilibrium existed between solid, liquid and vapor phases during sintering. Degree of wetting can be characterized using contact angle which depends on the interfacial energies balance between solid-vapor, liquid-solid, liquid-vapor interfaces. Figure 2.10 displays the relationship between contact angle, θ with three different interfacial energies. It can further be expressed using Equation 2.3.

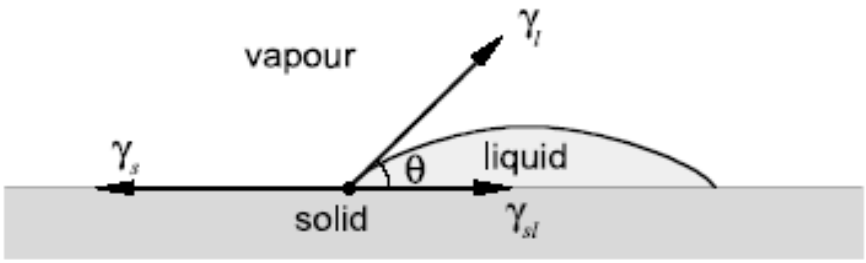

Figure 2.10. Interfacial energies and wetting angle

$$\gamma_{SV} = \gamma_{SL} + \gamma_{LV} \cos\theta \qquad (2.3)$$

where the subscripts S,L, V referred to solid, liquid and vapor respectively. In order for the liquid to wet the solid, the total free energy of the system must decrease. Good wetting occurs when the surface energy for solid-liquid interface is lower as compared to the solid-vapor and liquid-vapor surface energy. Figure 2.11 shows the solid-liquid-vapor equilibrium for both good wetting and poor wetting. During liquid phase sintering, the contact angle determines whether the liquid formation will either lead to densification or swelling. A low contact angle supports wetting since it induces liquid spreading over the solid grains. This later provides capillary attraction which densify the system. Meanwhile, high contact angle resists wetting. Liquid retreats from the solid which results in compact swelling and exudation of the liquid from the pores

.

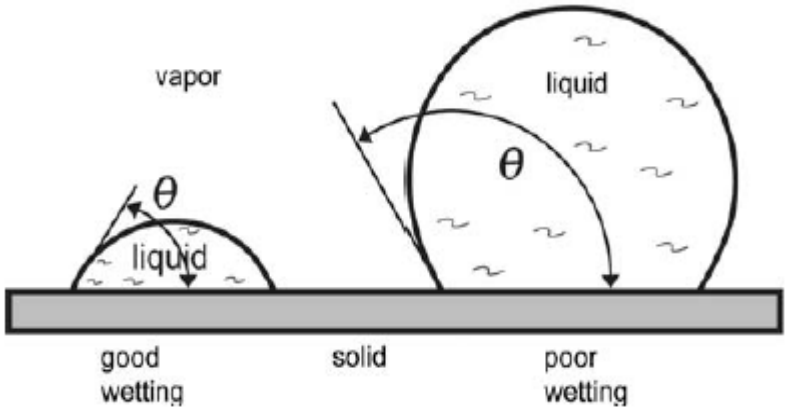

Figure 2.11. A schematic showing different wetting behaviours of a liquid on a horizontal plane.

The contact angle and interfacial energies are influenced by the surface chemistry. Metal surfaces with no impurities are wet by another metal which has high solubility in it [29]. Wetting improves when chemical interaction occurs at the solid-liquid interface [30]. The wettability increases when liquid has increased affinity towards the solid. Very often, commercial powders face the problem on surface impurities. In the case of aluminum alloys, presence of surface oxide on the powder always have detrimental effects on sintering since it inhibits the wetting behavior. Thus, changes of the surface characteristic can alter the wetting behavior [26].

Inert or reducing atmosphere is often used during sintering to keep the oxidizing agents to a minimum. Disruption of the oxide layer can also be carried out by either mechanical or chemical means to attain better wettability during sintering. One example to improve wettability of aluminum alloys is through addition of magnesium. For Al-Sn system, liquid tin is found to wet aluminum only in the

presence of magnesium when the dihedral angle is sharp. Likewise, liquid is exuded during sintering without presence of magnesium as shown in Figure 2.12[21].

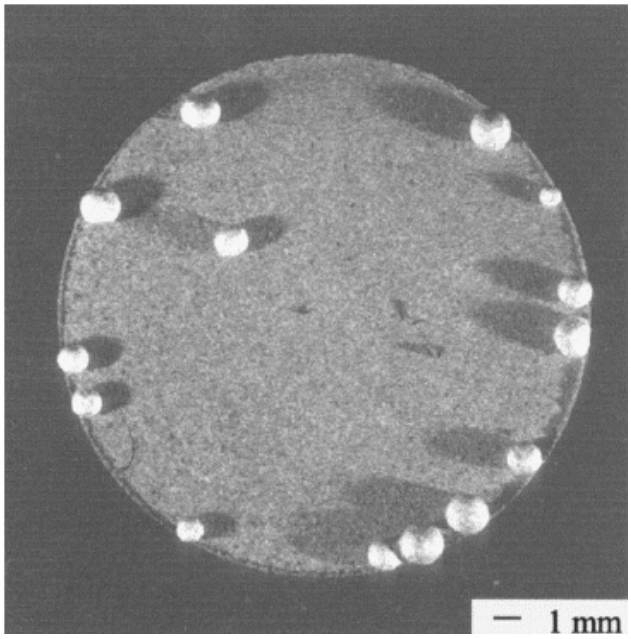

Figure 2.12. Exuded liquid on the surface of an Al-8Sn alloy after sintering at 620°C [21].

2.4.3 Solid State Sintering

In solid state sintering, densification occurs due to the interdiffusion between different metals in solid state[27]. As stated in Section 2.4.1, the main driving force for sintering process is reduction in surface free energy for the particle which later leads to reduction of free energy for the system. From the thermodynamic point of view, the reduction in surface energy can be realized through the formation of low energy solid-solid interfaces (i.e. grain boundaries) to replace the high-energy

solid-vapor interface. This reduction is achieved by a few diffusion mechanisms as displayed in Figure 2.13. The material transport from the solid particles to the particle-particle necks is induced by the difference in bulk pressure, vacancy concentration and vapor pressure[24].

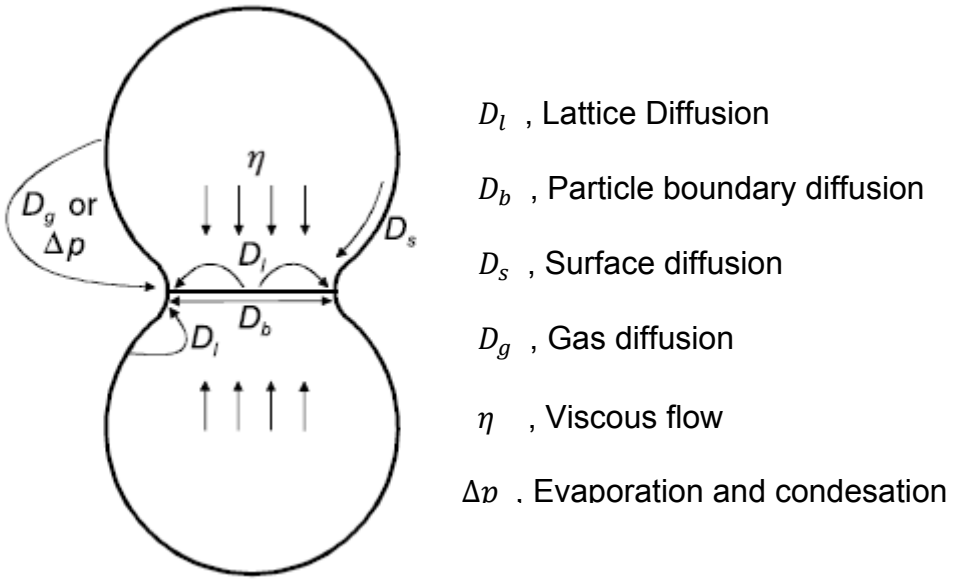

Figure 2.13. Material transport paths[24].

Not all the diffusion mechanisms give rise to compact densification. Lattice diffusion, viscous flow and grain boundary diffusion lead to a decrease in the interparticle distances. In other words, these diffusion mechanisms can contribute to compact shrinkage and densification. Meanwhile, material transport from the particle surface to the necks through surface diffusion or gas diffusion does not lead to a decrease in interparticle distance. Neck growth, on the other hand, occurs due to the redistribution of material[24].

Solid state sintering occurs in three overlapping stages. The initial stage of solid state sintering is characterized by the formation of necks at the contact points between the particles. The neck size continues to increase with the increase of sintering time. At this stage, the pores are interconnected with irregular shape. As sintering proceeds, mass flow occurs due to the curvature gradient near the necks and this leads to considerable densification. Eventually, pores become more spherical and form interconnected channels along 3-particle edges as illustrated in Figure 2.14. During the finals stage of sintering, densification proceeds at very slow rate. Pore channel closure occurs and pores become isolated[24, 31].

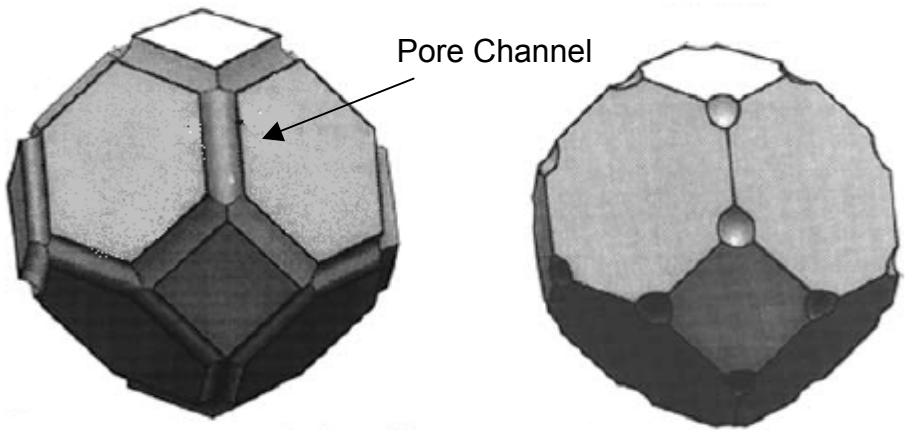

Figure 2.14.Schematic diagram showing (i) intermediate and (ii)final stages of solid stage sintering[24].

2.4.4 Liquid Phase Sintering

Liquid phase sintering (LPS) plays a significant role in the fabrication of ceramic and metallic materials. Liquid phase sintering can be defined as powder consolidation technique in which liquid is used to enhance the atomic diffusion and

rate of inter-particle bonding. The liquid phases can be formed by either melting of the additives components or through an eutectic reaction [26].

Sintering of aluminium-based alloys is often impeded by the presence of oxide layer on the powder particles. It was reported that this oxidelayer can be effectively broken up by addition of ~0.1-1 wt% of Mg to form a spinel phase $MgAlO_4$[23]. More recently, sinterability of aluminium alloys can be significantly improved through liquid phase sintering [21, 32]. The uses of liquid phase can effectively wet the solid particles and allow better diffusion rate through the oxide and the metals. German et al. [26, 33] suggested that an ideal liquid phase sintering should have the following key features:

1. Additive has the melting point below that of the base elements to ease the generation of the liquid
2. Solid solubility of the additive in the base should be lower than that of the base in the additive to prevent additive dissolving in the base which will significantly reduce the amount of liquid phase generated.
3. Base elements should have high diffusivity in the liquid to attain better mass transport and thus, improved sintering.

Liquid phase sintering has significant advantage over the solid-state sintering due to its fast sintering rate. Unlike solid state sintering, liquid flow occurs during liquid phase sintering owing to the capillary action, leading to faster diffusion rate. Consequently, rapid densification of the compacts is expected without the need for

an external pressure. The presence of the liquid phase also aids in particle rearrangement by reducing the inter-particle friction. More efficient packing of the particles is possible as the liquid dissolves the sharp particle edges[26].

Presence of large amount of liquid during sintering results in large amounts of shrinkage by typical liquid phase sintering mechanism [34]. However, high liquid content can lead to shape distortion and dimensional changes [35-37]. Densification and distortion are dependent on the amount of liquid content and pore induced capillarity. Sufficient liquid content can aid the compact to reach its full density even at the particle rearrangement stage, yet with the concomitant distortion. Low liquid content, however, can retain the compact shape but the solid skeleton structure resists densification[33]. Moreover, grain growth occurs simultaneously with the densification. It is not anticipated for high-strength applications. As a result, there is keen interest to optimize the processing condition of liquid phase sintering in order to develop parts with higher density, less distorted shape and fine grain size.

There are a few models developed to explain the densification during liquid phase sintering. It is well accepted that liquid phase sintering occurs in three main stages: particle rearrangement, solution-reprecipitation and solid-state sintering[38, 39]. Figure 2.15 illustrates the schematic diagram of microstructure changes during liquid phase sintering. When the powder compacts containing more than one component is heated at temperature above the solidus of the component, the melt forms and spreads into fine capillaries due to the capillary action. Considerable

densification usually occurs during heating from solid state to liquid phase sintering temperature [40]. Redistribution of solid particles due to liquid flows is termed as particle rearrangement. Sintering proceeds with solution and reprecipitation. Elimination of pores and particle growth occur simultaneously. At the final stage of liquid phase sintering, the sintering occurs at very slow rate similar to solid state sintering. The microstructure of the compacts consists of rigid solid particles with liquid occupying the space between the solid particles[41]. A series of events occurred at different stages of liquid phase sintering is discussed in detail in the following section.

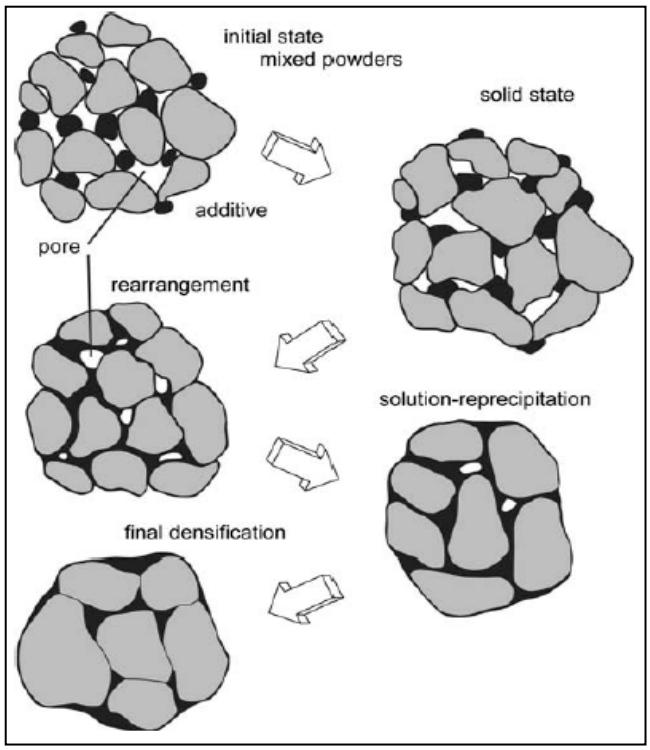

Figure 2.15. Schematic diagram showing microstructural change during liquid phase sintering [41]

2.4.4.1 Particles Rearrangement

The initial stage of liquid phase sintering marks a rapid densification due to the capillary force exerted by the liquid on the solid particles upon melts formation.Dissolution of solid particles into the liquid further allows liquid to spread and fill the pores. This results in higher packing density and rapid shrinkage due to particle rearrangement. Apart from shrinkage event, other events which include expansion due to liquid penetration of grain boundaries, dissolution of surface irregularities and formation of new contacts possibly occur during initial stage of liquid phase sintering [26].

Densification occurs during rearrangement depends on the amount of liquid presented, particle size and solubility of solid in the liquid[23, 26]. Dramatic microstructural changes also occur concurrently upon melt formation including liquid spreading, coalescence, particle sliding, homogenization, particle disintegration and fragmentation [42]. Particle rearrangement largely influences by contact angle, dihedral angle and solid solubility in the liquid. These material characteristics are interrelated with each other.

As stated previously in Section 2.4.2, liquid with good wettability generally exhibits low contact angle. Low contact angle allows appreciable attraction forces between wetted particles which later leads to particle rearrangement and densification due to capillary action. High contact angle, on the other hand, leads to swelling of the compacts due to the large repulsive force between wetted particles.Wetted particles clustered together due to the random packing of powder mixture and

uneven distribution of the liquid. This marks the first stage of particle rearrangement[26].

During the secondary rearrangement, particle disintegration and liquid penetration of grain boundaries occur since the initial melt is undersaturated with solid. In most systems, the liquid is not in equilibrium composition during the initial stage of sintering. As the initial liquid has high curvature, it aids in solubility and penetration of liquid between solid-solid interfaces[41]. Additionally, a low dihedral angle is necessary for a liquid to penetrate and disintegrate the solid particle structure. Particle rearrangement is also aided by the inter-solubility between the solid and liquid [43].Viscous flow occurs when the solid-liquid surface energy is comparatively lower than the solid-vapor surface energy. Subsequent rearrangement allows solid grains pack to a higher coordination.

2.4.4.2 Solution-Reprecipitation

After the liquid formation, continued densification of the compact occurs as a result of solution-reprecipitation. Not all the pores are filled after the rearrangement due to the formation of insufficient liquid. Thus, solid solubility in the liquid is necessary during this intermediate stage of liquid phase sintering.Generally, solution-reprecipitation is characterized by a series of events which occurs simultaneously: particle growth, shape accommodation and densification. There are three main material transport mechanisms during solution-reprecipitation to

densify the structure as illustrated in Figure 2.16. The mechanisms differ from each other in terms of transport path, material source and effect on grain size[26].

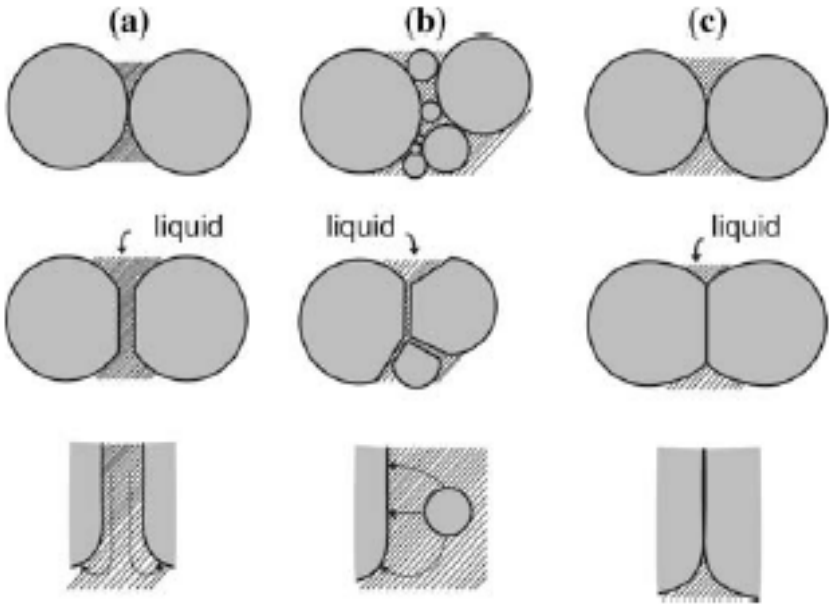

Figure 2.16. Different transport mechanism during solution-reprecipitation: (a) Contact flattening, (b) dissolution of small particles and (c) solid-state bonding [41]

Contact flattening (Figure 2.16a) is one of the important densification mechanisms as described by Kingery[44]. A compressive stress is exerted at the interparticlecontacts due to capillary forces and surface tension of the wetting liquid. Preferential dissolution of the solid occurs at the contact point due to concentration gradient. The dissolved materials then reprecipitate at regions with lower free energy away from the particle contacts (i.e. the surface of the neck regions) [24]. As a result of material transport, the contact area increases and particle shape is accommodated. The center-to-center approach of the neighboring particles result in densification with concurrent pore shrinkage. The densification rate is dependent on the rate of material transport. Densification rate decreases

when the solid dissolution decreases due to the decrease in effective stress at contact area. However, contact flattening does not take into account the effect of particle growth and the decrease in number of particles[45, 46].

Dissolution of small particles and reprecipitation on large particlesis another transport mechanism during solution-reprecipitation[47]. High solubility of solid in the liquid is preferable for active transport mechanism. Small particles generally have higher solubility into liquid since they exhibit larger surface area and higher free energy [48]. Thus, large particles grow at the expense of the small neighboring particles and decrease the net energy of the system. Additionally, large particles also undergo shape accommodation to allow better packing of the solid.

The third transport mechanism involves diffusion through solid diffusion path which leads to the growth of interparticle contact[49, 50]. The neck growth due to the diffusion along the liquid wetted particle boundary results inparticle shape accommodation, accompanied by densification due to center-to-center approach of the particles. Neck growth allows the particle boundary to replace solid-liquid interface area,which is the opposite of the liquid penetration during particle rearrangement. Contact flattening occurringat this stage does not involve particle coarsening but requiresa cooperative redistribution process [51].

2.4.4.3 Pores Filling

Apart from contact flattening as suggested in classical model, Kwon and Yoon found that pore filling plays a significant role in densification during liquid phase sintering[52, 53].Densification by pore filling is induced by particle growth and shape accommodation as illustrated in Figure 2. 17. Difference in the liquid pressure is the driving force for pore filling[54].

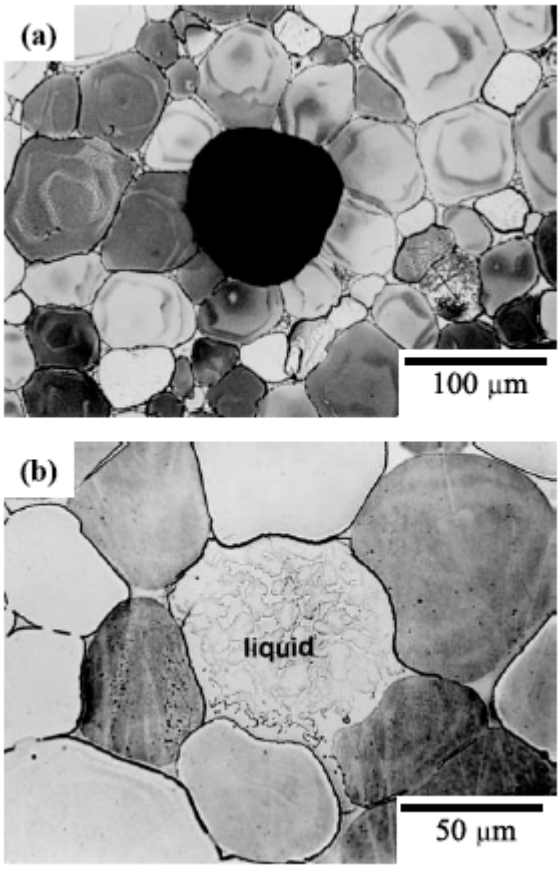

Figure 2.17. Microstructure of 96Mo-4Ni(wt%) (a) before and (b) after pore filling[55]

Liquid preferentially fills the small pores since they have high capillary attraction for wetting liquid. As illustrated in Figure 2.17(a), large pores which are surrounded by smaller particles remain stable since the capillary forces retain the liquid in small channels. During prolonged sintering, particle shape accommodation by particle growth and microstructural homogenization occurs. Elimination of the pores occurs when the particle growth eventually reaches the critical condition which favors the flow of liquid into the pore[56, 57] as illustrated in Figure 2.17(b). The critical condition depends on the pore size, particle size, liquid meniscus radius and angle between the meniscus contact as shown in Figure 2.18 [41].

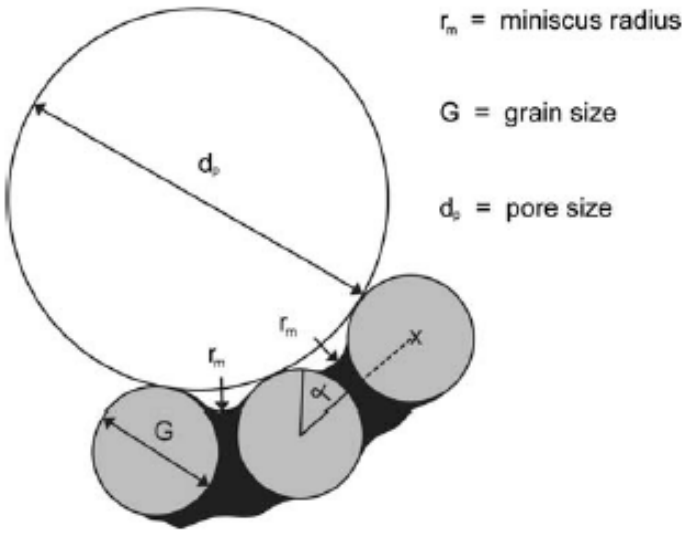

Figure 2.18. Calculated model for pore refilling based on spherical particles surrounding the pore[41].

The liquid meniscus radius at the pore-liquid particle contact,$r_m$can be expressed in the following equation:

$$r_m = \frac{G}{2}\left[\frac{1-cos \propto}{\cos \propto}\right] \qquad (2.4)$$

where $G$is the particle diameter and $\propto$is the angle from the particle center to the solid–liquid–vapor contact point[11, 41]. Particle growth increases the particle radius and the meniscus radius. This in turn reduces the capillary gradient. When the pore size and meniscus radius are equal, liquid flows into the pores is favored since it reduce the liquid pressure[26]. Moreover, pore filling is also favored by low contact angle[54].

2.4.4.4 Particle Coarsening

During the final stage of liquid phase sintering, densification occurrs at relatively slower rate due to the attainment of the rigid solid skeleton. Typically, the microstructure at this stage consists of connected solid particles with liquid occupying the spaces between the particles and approaches a minimum energy solid-liquid configuration. Diffusion continues and contributes to microstructural coarsening.Similar to most of the systems undergoing liquid phase sintering, densification occurs in parallel with coarsening. The densification rate at this stage can be expressed in Equation 2.5[41].

$$\frac{d_\rho}{d_t} = \frac{12 D_S C \Omega}{RTG^2} \beta \cdot \left(\frac{4\gamma_{LV}}{d_p} - P_G \right) \qquad (2.5)$$

where ρ is the fractional density, t is the time, D_s is the diffusion rate of solid into liquid, C is the solubility of solid in the liquid, Ω is the solid atomic volume, R is the gas constant, T is the absolute temperature, G is the particle size, d_p is the pore size, γ_{LV} is the liquid-vapor surface energy, P_G is the gas pressure within the pore

and β is the pore density factor. From Equation 2.5, it can be seen that diffusion and solubility of solid in liquid, pore characteristic and entrapped gas pressure play a significant role on densification.

For low solubility system, for instance W-Cu, densification is mainly dominated by solid state sintering. Meanwhile, an extension of solution-reprecipitation proceeds for systems with considerable solid solubility in the liquid[41].As stated previously, solution-reprecipitation can contribute to particle growth, particle shape accommodation and subsequently leads to final pore removal. Densification rate by solution-reprecipitation decreases as the solid particle contacts flatten.

Several factors can inhibit densification. Presence of gas within the pores is not anticipated since densification can be impeded by pressurization of trapped gas. Complete pore closure can only be achieved over short duration of time if there is no entrapped gas within the pores. Furthermore, pore growth and pore coalescence due to Ostwald Ripening occur duringthe prolonged heating. Large pores grow at the expense of the small pores. The mean pore size increases with the concurrent decrease in pore pressure. As a consequence, swelling of compact occurs rather than densification and decrease the sintered density[26].

2.4.5 Transient Liquid Phase Sintering

Transient liquid phase sintering is widely applied in powder metallurgy for high performance material systems[58]. Generally, it is considered to be a combination between solid state sintering and liquid phase sintering as illustrated in Figure 2.19. The local composition, $X_1$is heated to the sintering temperature, T_2 at which the temperature is slightly above the eutectic temperature but below the solidus line. Small amount of liquid phase formsduring the early stage of sintering, but disappears when the sintering proceeds which isdue to solubility effects or secondary reaction and forms solid solution at equilibrium [59, 60].

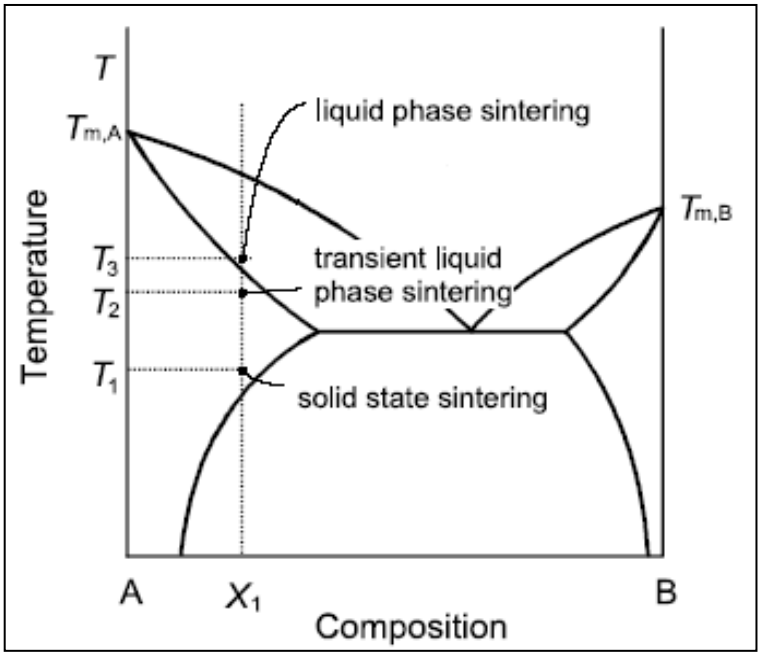

Figure 2.19. Phase diagram indicating occurrence of different types of sintering at varied temperatures.

Transient liquid phase sintering is highly dependent on the processing variables [26, 61]. Similar to liquid phase sintering, the base material used in transient liquid

phase sintering must have high solubility for the additive at the sintering temperature.Sufficient liquid formation and its duration coupled with rapid resolidification kinetics are required to obtain desirable level of densification and to prevent swelling due to homogenization [58]. The transient liquid formed spreads throughout the powder compact due to the capillary action and enhances the mass transfer. This leads to subsequent particle rearrangement and densification [26, 32].Moreover, Corbin and McIsaac has reported that use of proper choice of base metal particle size and heating rate can dramatically increase the liquid formation in these systems. Large base metal particles and fast heating rates are desirable to increase initial liquid formation. However, it can result in slow re-solidification kinetics[62]. Extensive studies are still carried out to understand the important variable controlling transient liquid phase sintering.

Transient liquid phase sintering offers a few advantages over solid state sintering. Due to the formation of transient liquid at relatively lower sintering temperature than temperature required for liquid phase sintering, it can result in rapid densification and possibly form compact with high sintered densities with uniform dimensional change and reduced microstructural coarsening [58]. Moreover, processing through transient liquid phase sintering also allows the use of less expensive mixed elemental powder rather than prealloyed powder to avoid the compaction difficulties.

2.4.6 Supersolidus liquid phase sintering

Production of alloy powders with the size ranging from 20- to 250-μm using powder atomization technologies is of particular interest since the sintered products yield higher mechanical properties and more homogeneous microstructure as compared to the traditional powder metallurgy products. Supersolidus liquid phase sintering (SLPS) involves heating of the prealloyed powders between the solidus and liquidus temperature[63, 64]. SLPS densification takes place by viscous flow driven by capillary force acting on the semisolid structure [63-65]as illustrated in Figure 2.20.

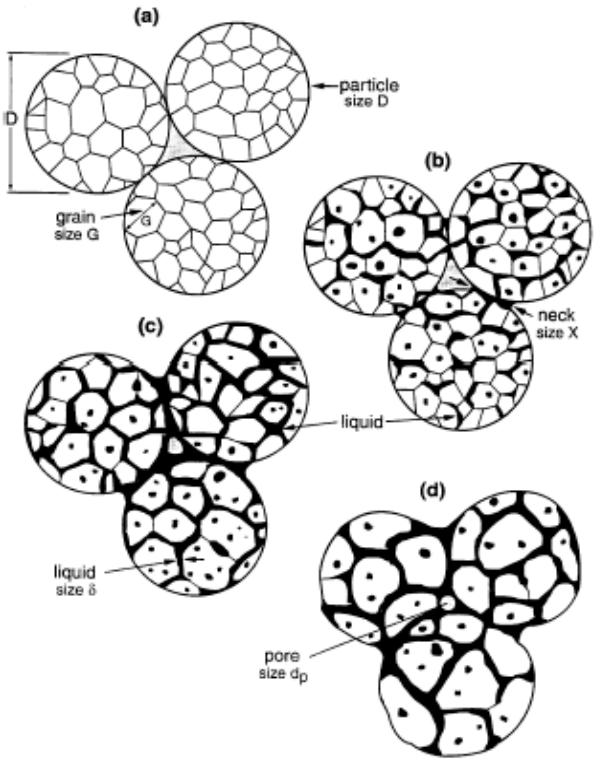

Figure 2.20. Schematic diagram showing SLPS densification by: (a) Initial particle packing, (b) Formation of initial liquid, (c) Viscous flow densification and (d) Final microstructure with closed, spherical pores[63].

As illustrated in Figure 2.20, liquid starts to form at the particle contacts and at particle boundaries within the particles upon reaching the sintering temperature. Densification during SLPS occurs due to the capillary force exerted by the liquid located at the interpaticles necks. Meanwhile, liquid located on grain boundaries have no discernible role on densification but it softens the particles and allows grain sliding during densification[64].Similar to the liquid phase sintering, SLPS densification is highly dependent on the volume of liquid and occurs over a narrow temperature range[63]. High liquid fraction is desirable and enables rapid densification via particle rearrangement, fragmentation, contact flattening, particle shape accommodation and pore removal [66]. However, it reduces the structural rigidity of the compacts and cause shape distortion.

Fabrication of structural components generally requiressufficient volume of liquid to complete densification and homogenization, but it should not lead to undesirable shape distortion [63]. Thus, careful control of the liquid fraction is necessary and can be achieved by optimizing the temperature and powder composition. Altering of either temperature or composition has significant influence on the final density as well as the dimensional stability and strength of the sintered component [67] as the volume fraction of liquid formed influences the final density. Moreover, control of the sintering time is crucial since prolonged holds in the presence of the liquid phase can result in microstructure coarsening with concomitant property decrements.

2.5 Effects of Sintering Variables

Sintering is an economical route widely used for industrial production of aluminum alloys products and advanced components. Extensive studies have been carried out to study various fabrication concerns associated with sintering. It is desirable to obtain sintered products with reproducible properties, close dimensional tolerances and high density without shape distortion. The sinterability, final density, microstructures and mechanical properties of the final products are largely dependent on a variety of variables during sintering process. This section provides an insight into a few important sintering variables: choice and control of operating temperature, particle size and particle shape, use of suitable protective atmosphere, time and temperature profiles during heating, sintering and cooling [12].

2.5.1 Particle Size

Particle size is one of the important parameters controlling the kinetics of sintering. Control of particle size is necessary since it determines the curvatures, contact stress, and capillarity forces during liquid phase sintering[41]. Generally, use of fine powders is more beneficial to sintering than the use of coarse powders.With the decrease in particle size, itprovides greater driving force for sintering to reduce the pore-solid interfacial area and hence a decrease in the free energywithin the system. Figure 2.21 illustrated a typical example of the effect of particle size on densification.

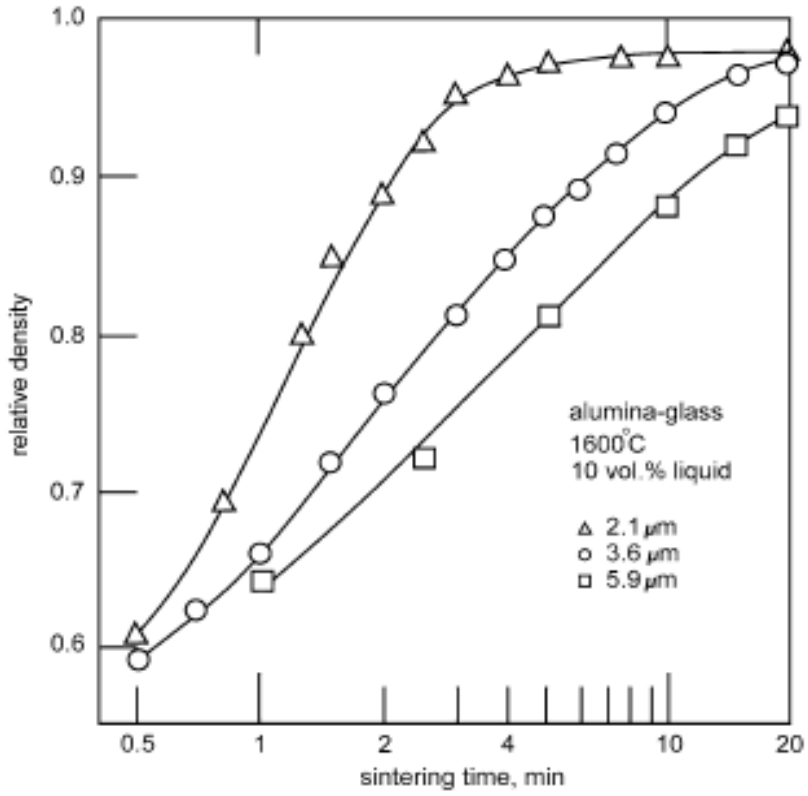

Figure 2.21. Fractional density of alumina-glass with different particle sizes sintered at 1600°C for various time[68].

It can be seen that densification rate improves with the use of smaller particle size. This subsequently leads to higher sintered densities for a fixed sintering process with the decrease in particle size [69]. During liquid phase sintering, the capillary force between particles[26]and solubility of the solid in liquid increase[48] with the decrease of the particle size. This aids in densification, particularly during rearrangement and solution-reprecipication stages.

Smaller particle sizes allow greater particle contact and hence more necking forms between the particles. This provides more efficient material transport through diffusion.Necking between particles also reduces the free energy of the systems

and subsequently leads to densification by coalescence. In addition, small particle size may correspond to smaller internal grain size.Smaller grains have larger contact zone stresses which contribute to contact flattening and thus ease densification [41].

2.5.2 Particle Shape

Sintering characteristic of powder metallurgy product is also influenced by the particle shape. Though there are a variety of different types of particle shapes available, this section mainly focuses on the most common powder obtained by atomization method: spherical- and irregular-shaped particles.

Variation in particle shapes influences the rearrangement due to the interparticle force. Irregular particles generally undergo less rearrangement due to the higher friction force between particles [26]. However, rearrangement of irregular particle can be induced by wetting liquid which generates a rearrangement torque to bring flat surface into contact [70]. The rearrangement torque increases with the increase of the liquid content causing more rearrangement for irregular particles to carry out. Spherical particles, on the other hand, more responsive to capillary force during rearrangement and have greater chance to provide uniform sintered microstructure [71, 72]. The effect of the initial particle shape becomes less significant when solution-reprecipitation start to dominate in the later stage of sintering with the concurrent dissolution and particle shape accommodation.

In the recent investigation on the effect of particle shape on sintering conducted by Liu et al[73], Al-4wt%Sn with irregular shape was reported to havehigher sintered density reaching approximately 90%, whereas spherical particles only achieved a sintered density of nearly 70%. Figure 2.22 illustrated the backscattered images of the microstructure for both irregular and spherical Al-4wt% sintered under the same condition. Spherical 5-μm powders showedvery little evidence of sintering and remained very porous. Meanwhile, the irregular 6- μm ALPOCO powder was well sintered with little porosity remained. It is suggested that the oxide film on irregular shape preferably fractured due to the differential thermal expansion between the aluminum particle and its oxide film[73].

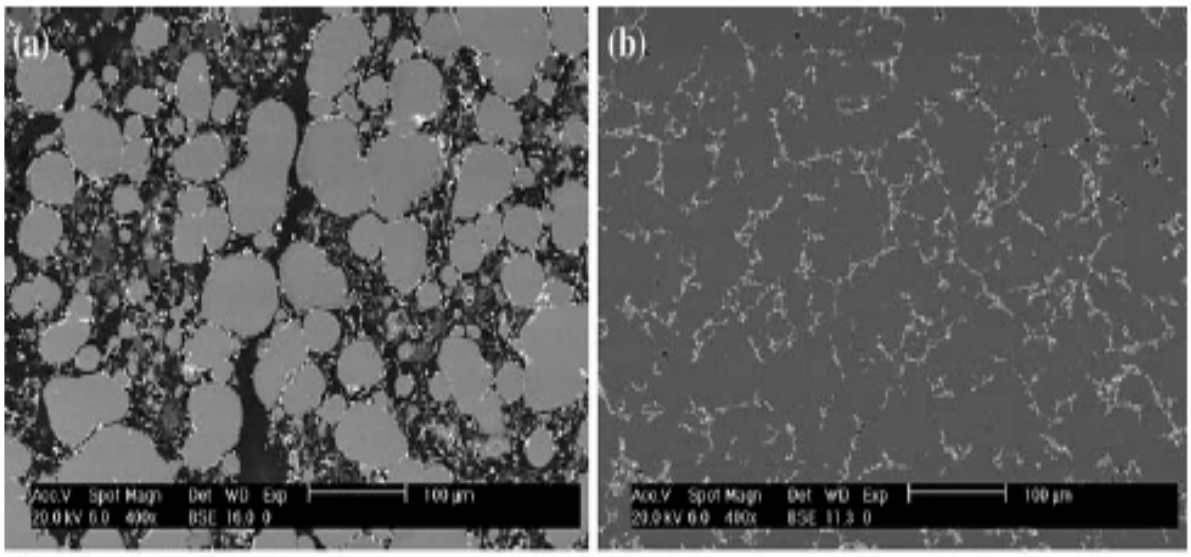

Figure 2.22. Backscattered electron images showing the microstructures of Al-4wt%Sn parts after sintering at 620°C for 2 hrs in argon which are made from (a) ALPOCO 5-μm spherical and(b) ALPOCO 6-μmirregular powders[73].

2.5.3 Sintering Atmosphere

The role of atmosphere during sintering has been studied extensively. Sintering atmosphere plays a crucial role in determining the final properties of the component. Control of the sintering atmosphere is necessary since it might alter material chemistry due to the interaction between the atmosphere and materials being sintered [12, 41]. In several cases, altering the atmosphere condition, for instance partial pressure of oxygen or water can significantly affect the sintered properties. Full densification might be inhibited during sintering in the inert or insoluble gas since the entrapped gas stabilizes the closed pores.

Protective atmosphere generally acts to prevent undesirable reaction during sintering and to facilitate the reduction of surface oxide during powder processing. Therefore, the contact between the particles and hence material transport are not inhibited[12]. Additionally, protective atmosphere also aids in removal of lubricants or binders. This section provides a brief description on the most common sintering atmospheres used in the industry.

2.5.3.1 Pure Gases

Hydrogen gases is widely used as effective reducing atmosphere for high temperature sintering of high-end alloys including stainless steel, tungsten carbide , other tungsten alloys, and ceramic/metallic products. Hydrogen gas can be produced commercially either through electrolysis of distilled water or converting

hydrocarbons mixed with steam using catalyst[12, 13]. It is of common practice to remove all the oxygen and moisture during the production process before hydrogen can be used. Although presence of moisture within the sintering atmosphere is not desirable due to the possibility of oxidation, it has been shown that presence of moisture can increase the potential for densification during sintering of alumina[74].Use of hydrogen atmosphere is often limited due to the cost and handling problems.

Inert gases such as argon and helium are among the most expensive sintering atmospheres and are employed specifically for sintering of extremely reactive metals, for instance superalloys, titanium and zirconium. Apart from their relative high cost, the limited use of inert gas is also due to their lack of reducing ability[12] .

Nitrogen gas, on the other hand, is a cheap and explosion safe inert gas. It is well suited for sintering of metals which do not readily react with the gas to form nitride, for instance iron and copper. However, materials such as titanium and tantalum are not suitable to be sintered in nitrogen atmosphere due to high reactivity towards nitrogen gas. Several studies have suggested that nitrogen atmosphere is efficacious for sintering of aluminum-based compacts to achieve better sintered properties. Formation of aluminum nitride (AIN) is the key factor contributing to the beneficial role of nitrogen [34, 75]. Schaffer et al. [75] have suggested that formation of AIN establishes the pressure gradient between the external and internal atmosphere which later initiates the pores filling mechanism. Pore filling

mechanism is thus one of the important densification mechanisms in sintering of aluminum[75].

Beyond the most commonly used inert sintering atmospheres, nitrogen based mixtures containing predominantly nitrogen along with hydrogen are also employed. The nitrogen-based atmosphere contains low water vapour and small amount of hydrogen which has reducing and carburizing effects. It is suitable for sintering any iron or copper alloy. However, the role of hydrogen in the nitrogen-based atmosphere on sintering of aluminum-based alloys is not clearly understood. Martin and Castroclaimed that hydrogen does not have significant influence on sintering[76]. Yet, there are some investigations which showed that presence of hydrogen is detrimental to sintering[34, 75]. It is suggested that hydrogen can retard pore-filling mechanism, preventing the liquid from filling the pores which leads to minimal shrinkage and densification of the compacts [75].

2.5.3.2 Vacuum

Vacuum sintering is usually used to sinter materials with very high reactivity towards oxygen, moisture and hydrogen. This includes tantalum, titanium, zirconium, vanadium, beryllium, refractory metal carbides, stainless steels and tool steels[31]. Vacuum sintering involves evacuation of the furnace chamber to the desired level of pressure using rotary pump and/or diffusion pumps and maintained it throughout the sintering process. Since there is no gas interaction with the

material to be used, vacuum sintering protects metals from oxidation and allows proper chemistry of the parts to be retained during sintering. Compared with the sintering using inert gases such as argon and helium gases, vacuum sintering is more economical since the operating cost only involves the electrical cost and oil for the vacuum pumps. However, it only allows low production rate and difficult to be applied in a continuous process [77, 78].

2.5.3.3 Dissociated Ammonia

Dissociated ammonia is another common reducing gas containing both hydrogen and nitrogen. It can serve as low cost alternative for the expensive hydrogen gas. Dissociated ammonia is produced by evaporating the liquid ammonia in the vapourizer, followed by dissociated process taking place at temperature between 900 to 1000°C with the use of Ni or Fe catalyst. The dissociated ammonia produced by this means contains 75 vol% hydrogen and 25vol% nitrogen. Moreover, the resulting gas is of high purity, free from CO, CO_2, oxygen or suphur compounds and sufficiently dry to be used directly in the furnace[13, 31]. Dissociated ammonia is commonly used to sinter steels, brass, copper, iron-copper, aluminum and its alloys and stainless steel.

2.5.3.4 Reformed hydrocarbon gases

Reformed hydrocarbon gases are among the most widely used sintering atmosphere owing to their low costs. They are produced through controlled combustion of the hydrocarbons, i.e., methane, propane and butane. There are two types of hydrogen gases: exothermic gas and endothermic gas. Exothermic gas or exogasis produced by burning exothermally the hydrocarbon gas at high air to gas ratio (6:1 to10:1) and subsequently dissociated by the catalyst. The resulting gas has the nitrogen content of 70 to 90 vol% and uses for sintering of copper, tin and silver. However, it can lead to undesirable decarburization effect due to its relative high CO_2 content. Endothermic gas or endogas, on the other hand, contains about 45% hydrogen along with nitrogen, carbon monoxide, carbon dioxide and small amount of water vapour produced by thermal catalytic reaction between hydrocarbon gas and air at low air to gas ratio. Endothermic gas is generally used for sintering of iron-carbon and other alloy steels. Composition of endothermic gas is carefully controlled to maintain the required carbon potential of the steel to be sintered[13, 31].

2.5.4 Sintering Temperature

Optimum sintering temperature isrequired to achieve the desired sintered properties in the final products. Sintering temperature is directly corresponding to the liquid formation causing sufficient amount of liquid to wet the particles leading to the desired densification. Additionally, sintering temperature also influences other

temperature sensitive variables including diffusion rates, wetting and solubility of solid in liquid during liquid phase sintering. At lower sintering temperature, densification rate is relatively slow and mainly dominated by the solubility and diffusivity factors. However, an increase in the sintering temperature marksa drastic increase in sintered density since more liquids formed aiding in particle rearrangement and solution-reprecipitation.It is therefore necessary to control the sintering temperature for optimum densification to be performed and at the same time minimize microstructural coarsening and shape distortion.

2.5.5 Sintering Time

Although sintering time is a relatively weak parameter in comparison with the sintering temperature, satisfactory sintering time is required to bring about necessary improvement in the sintered properties.Most of the major densification is carried out during the first 20 minutes and subsequent extended sintering time is beneficial for continued pore elimination. However, prolonged sintering time is not desirable since it can result in unfavorable pore growth, preferential vaporization and microstructural coarsening leading to degradation in the properties of the final products[26].

2.6 Aluminum Alloys Powder Metallurgy

Aluminum alloys are widely used in the automotive and aerospace industries due to their excellent properties, such as low density, high electric and thermal conductivity and low thermal expansion. The common industrial applications of P/M aluminum alloys can be found as pulleys, rod guides, pistons for shock absorbers, camshaft bearings and brake calipers [18, 79, 80]. Unlike ferrous powder metallurgy, aluminum P/M is still at its infancy stage with limited applications in the industries. Though aluminum alloys has gained substantial importance, particularly in the transportation industry due to their low density, high strength to weight ratio and good resistance to corrosion, it does not exhibit favorable wear resistance and tensile behavior[4].

Aluminum alloys processed through 'press and sinter' route often have lower strength in the finished products [81]. Thus, sintering is the key process to be investigated and optimizedin order to produce materials with enhanced properties.The thermodynamically stable oxide layer on aluminium powder particles which can only be reduced at 600°C with the oxygen partial pressure of $<10^{-50}$atmoften acts as a barrier to sintering process[75].In order to disrupt the oxide layer, compaction and successive liquid phase sintering are essential to facilitate metal to metal contact and promote particles interdiffusion[36, 82]. Moreover, reduction of the surface oxide is also possible with the addition of magnesium [83].

Aluminum based alloys are normally sintered in the protective atmosphereto prevent the occurrence of any undesired chemical reaction which can interfere with the subsequent sintering process.Recent studies have proven that nitrogen atmosphere is beneficial for sintering of aluminum alloys due to the formation of AIN. However, there is still very limited understanding about AIN formation and its contribution towards sintering behaviour.

Aluminum alloys are generally divided into two main categories: (i) cast composition and (ii) wrought composition [84-86] which are further subdivided into heat-treatable and non heat-treatable alloys. For ease of reference, Aluminum Association system employs different nomenclatures for wrought or cast alloys. A wrought alloy is numbered using the four digit system with the first digit indicates the major alloying element of aluminum. The second digit indicates modification from the base element while the third and fourth digit identified specific alloys in the series. The designation of wrought aluminum alloys is shown in Table 2.4. The cast alloy designation system, on the other hand, is based on the three digit number followed by a decimal. Similar to wrought alloy, the first digit in cast alloy identifies the major alloying elements applied. The second and third digit indicates the specific alloy in the series. Meanwhile, the decimal signifies whether the alloy is a casting (.0) or an ingot (.1 or .2). A capital letter prefix (A, B, C etc) indicates modification of the alloys. The designation for cast alloy is given in Table 2.5.

Most of P/M alloys developed nowadays are based on the existing wrought or cast aluminum alloys composition, with little or no changes to optimize them for P/M

processing[8].The most common heat-treatable aluminum P/M alloys exhibit properties comparable to the 2xxx and 6xxx series wrought aluminum alloys [87]. Other advanced aluminum P/M alloys include the use of prealloyed powders with extended solid solubility and incorporation of other reinforcing materials (i.e. metals, ceramic or organic compounds) to form metal matrix composite[8]. Although there are very few commercial press-and-sinter P/M alloys currently available which offer limited range of physical and mechanical properties as well as restricted realm of potential applications [3], aluminum P/M alloys remain a very promising candidate to be developed for commercial application. Consequently, there have been intense interests to obtain better understanding of the alloy development and sintering fundamentals.

Table 2.4 Designation for wrought aluminum alloys[8, 88].

Alloy Series	Description
1xxx	Controlled unalloyed composition with minimum 99.00% Al
2xxx	Heat-treatable alloy with copper as major alloying element
3xxx	Non heat-treatable alloy with manganese as major alloying element
4xxx	Heat-treatable alloy if magnesium is present with silicon as major alloying element
5xxx	Non heat-treatable alloy with magnesium as major alloying element
6xxx	Heat-treatable alloy with magnesium and silicon as major alloying element
7xxx	Heat treatable alloy with zinc as major alloying element
8xxx	Heat-treatable alloys including tins and lithium composition
9xxx	Alloys series reserved for emerging new alloys

Table 2.5. Designation for cast aluminum alloys[8, 88].

Alloy Series	Description
1xx.x	Controlled unalloyed composition with minimum 99.00% Al
2xx.x	Heat-treatable alloy with copper as major alloying element
3xx.x	Alloy with silicon as major alloying element and contains also specified amount o copper and/or magnesium
4xx.x	Non heat-treatable alloy with silicon as major alloying element
5xx.x	Non heat-treatable alloy with magnesium as major alloying element
6xx.x	Unused
7xx.x	Heat treatable alloy with zinc as major alloying element
8xx.x	Heat-treatable alloy in which tin is the major alloying element
9xx.x	Unused

2.6.1 Al-Si P/M alloys

Aluminum-silicon (Al-Si) system forms a rather simple binary phase diagram,as displayed in Figure 2.23with the eutectic composition close to Al-12.6 wt% Si at the eutectic temperature of 577°C. Under the equilibrium condition, aluminum-rich solid solution contains 1.65 wt% silicon at this temperature and solid solubility of silicon in aluminum decreases to 0.1 wt% below 300°C [89].

Al-Si alloys have been used commercially in gears and structural parts where wear resistance play an important role in component structural performances. The hardness and wear resistance increase with the amount of silicon presented. Hypereutectic Al-Si alloys are well known for their outstanding wear resistance, low

weight and low thermal expansion. It is considered as an interesting option to substitute P/M steel. In 2005, German P/M part producer SchwäbischeHüttenwerke (SHW) had successfully produced a P/M aluminum chain sprocket for the BMW cam-phaser system [90]. This promising breakthrough in P/M application has recognized the potential of P/M manufacturing route in structural and mechanical design.

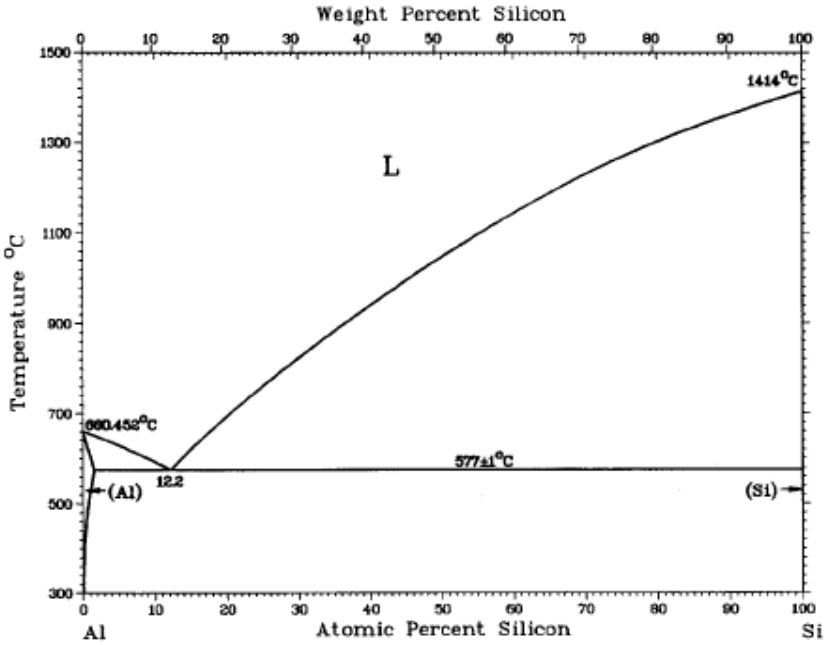

Figure 2.23 Al-Si binary phase diagram[89]

There are two principal techniques which are usually employed in the industries to produce hypereutectic Al-Si alloys, namely casting and powder metallurgy (P/M) [91]. Although hypereutectic Al-Si alloys exhibit good casting characteristics due to their high fluidity, crystallization of large primary silicon particles within the cast matrix always serves as a major threat in the casting industry. Non-uniform

microstructures together with the large and segregated Si particles degrade the mechanical properties and machineability of the alloys [92].

For Al-Si alloys designed for elevated temperature applications, thermal stability is of prime importance. To obtain Al-based alloys with good thermal stability, main strengthening elements with low diffusion coefficient, for instance Ni, Fe, Cr, Mn, Ti, Zrare added [92, 93]. However, using the conventional casting technology will limit the amount of slowly diffusing transition metals to be added, which normally does not exceed approximately 1 wt%. [87]. Higher amount of these elements will reduce plasticity, deformability and strength of the alloys due to the formation of the large, hard and brittle intermetallic phases [93].

Hypereutectic Al-Si P/M alloys, on the other hand, have fine and more uniform microstructure with better controlled size and amount of silicon particles. Alloys processed by P/M techniques generally exhibit better mechanical properties with favourable strength, ductility and low susceptibility to cracks.

2.6.2 Effect of Alloy Additions

Pure aluminum generally exhibits low strength and is not suitable to be used for structural application. In order to increase the strength and to improve the mechanical properties, alloying of aluminum with other metallic elements is necessary. Among the major alloying additions to aluminum includes copper,

manganese, silicon, magnesium and zinc. Other elements, for instance chromium, and zirconiumare added in smaller quantity and useful for grain refinement.

Most of the alloying elements either exist as solid solution with aluminum or form micro-constituents (i.e. element or compound). Copper is one of the major alloying additions commonly used in 2xxx or 2xx.x series aluminum alloys with the concentration range from 1 to 10%. Copper has appreciable solubility in aluminum with the maximum solubility of 2.5 at% achieved at 548°C. Addition of copper can lead to a substantial increase in strength through precipitation hardening.

Magnesium, on the other hand, improves work hardening characteristic of aluminum and increases strength through solid solution strengthening. A more significant increase in strength can result from the combination of magnesium addition with other elements, notably copper and zinc. Addition of zinc as major alloying element in heat-treatable 7xxx and 7xx.x series allow substantial increase through precipitation hardening.

Manganeseis the principal alloying element for non heat-treatable 3xxx series wrought aluminum alloys. It has limited solid solubility in aluminum (1 at%) and increase strength through solid solution strengthening. Addition of silicon also results in moderate increase in strength. Presence of silicon lowers the melting point and increases the fluidity of aluminum. Addition of both magnesium and silicon in appropriate proportions can lead to precipitation strengthening due to the formation of Mg_2Si.

2.6.3 Heat Treatment of Aluminum Alloys

The mechanical properties of aluminum alloys are largely influenced by alloy composition and sintering parameters. To further improve properties such as hardness, strength, residual stress state of a metal product, aluminum alloys are heat-treated at designated temperatures and time to achieve the desirable mechanical properties. There are two types of aluminum alloys available: heat-treatable and non heat-treatable. Heat-treatable aluminum alloys achieve substantial increase in strength through precipitation and deformation. Non heat-treatable alloys, on the other hand, are strengthened through cold deformation or work-hardening process. This section mainly focuses on the heat-treatable aluminum alloys and provides a general overview of the heat treatment procedures applied for these alloys [8]. Table 2.6 provides the basic temper designation for heat-treatable alloys.

Heat treatment of heat-treatable aluminum alloys generally comprises of three major processes: solution heat treatment, quenching and age hardening. Solution heat treatment involves dissolution of soluble phases formed during solidification at relatively high temperature to obtain homogenous concentration of alloying elements in the solid solutions. The metal components are subsequently quenched to obtain supersaturated solid solutions and aged at either room temperature (natural aging) or at elevated temperature (artificial aging). Age hardening allows precipitation of solute atoms from supersaturated solid solution. The details of each procedure are described in the following section.

Table 2.6.T Temper Designation[8].

T Temper	Description
T1	Naturally aged after cooling from an elevated temperature shaping process
T2	Cold worked after cooling from an elevated temperature shaping process and then naturally aged
T3	Solution heat treated, cold worked and naturally aged
T4	Solution heat treated and naturally aged
T5	Artificial aged after cooling from an elevated temperature shaping process
T6	Solution heat-treated and artificially aged
T7	Solution heat-treated and stabilized (over-aged)
T8	Solution heat-treated, cold worked and artificially aged
T9	Solution heat-treated, artificially aged, and cold worked
T10	Cold worked after cooling from an elevated temperature shaping process and then artificially aged

2.6.3.1 Solution Treatment

Solution treatment involves heating of aluminum alloys at relatively high temperature close to eutectic temperature and holdsit for sufficiently long time to produce nearly homogenous solid solution. Solution heat treatment is necessary to obtain maximum concentration of soluble phases in solid solution through dissolution, homogenizes the alloying elements and thus improves the strength of the material after the subsequent aging treatment. The dissolution of soluble phases is influenced by the solution treatment temperature and time.

Solution treatment temperature varies according to alloy composition. It is generally acceptable to have the temperature variation within ±6 °C but some highly alloyed, high strength alloys are restricted to a narrower range of temperatures since the initial eutectic melting temperature is just a few degrees higher than the recommended solution treatment temperature as shown in Table 2.7.It is thus critical to control the solution treatment temperature to avoid overheating and partial melting which can lead to reduction in the mechanical properties.

Table 2.7 Typical solution treating temperature ranges and the initial eutectic temperature for selected 2xxx series aluminum alloys[8].

Alloy	**Solution Heat Treatment Range (°C)**	**Initial Eutectic Melting Temperature (°C)**
2014	496-507	510
2017	496-507	513
2024	488-507	502

Care must also be exercised during solution heat treatment to avoid non-equilibrium melting and underheating. Non-equilibrium condition occursdue to the localized solute concentrations causing lowering of the eutectic temperature and subsequently leads to localized melting. Meanwhile, underheating occurs when the parts are heat-treated below the normal range causing insufficient dissolution of the soluble phase into the solid solution. Thus, less solute is available for the subsequent precipitation hardening. This again results in significant decrease in the final strength.

Apart from critical control of the solution heat treating temperature, solution-treating time plays an equally important role in determining the strength of the final products. It is desirable to have sufficientsolution heat-treating timeto allow good homogeneity within the solid solution. The soak times required for products of various thicknesses varies from less than a minute to 20 hours. Prolonged exposure of the part to high temperature can lead to high temperature oxidation causing surface blistering if high moisture content is presented within the atmosphere. Grain coarsening can also occur due to the excessive solutionizing time.

2.6.3.2 Quenching

Quenching is carried out immediately after the solution treatment to suppress precipitation upon cooling of the materials. High quenching rate is desirable since it rapidly cools the materials and retains sufficiently high amount of solute within the solid solution. Moreover, it also helps to maintain a high number of vacancies at room temperature. Low quenching rate, however, causes appreciable heterogeneous precipitation to occur at the grain boundaries or dislocation. This reduces the amount of supersaturation leading to less amount of solute available for the subsequent hardening and consequently results in lower tensile strength, yield strength, ductility and fracture toughness in the final products. Figure 2.24 displayed the effects on quench rate on yield strength for different Al-Si alloys

subjected to T6 heat treatment. Variation in quenching rate is influenced by the amount of excess Si in the matrix and volume fraction of β-Mg_2Si precipitates.

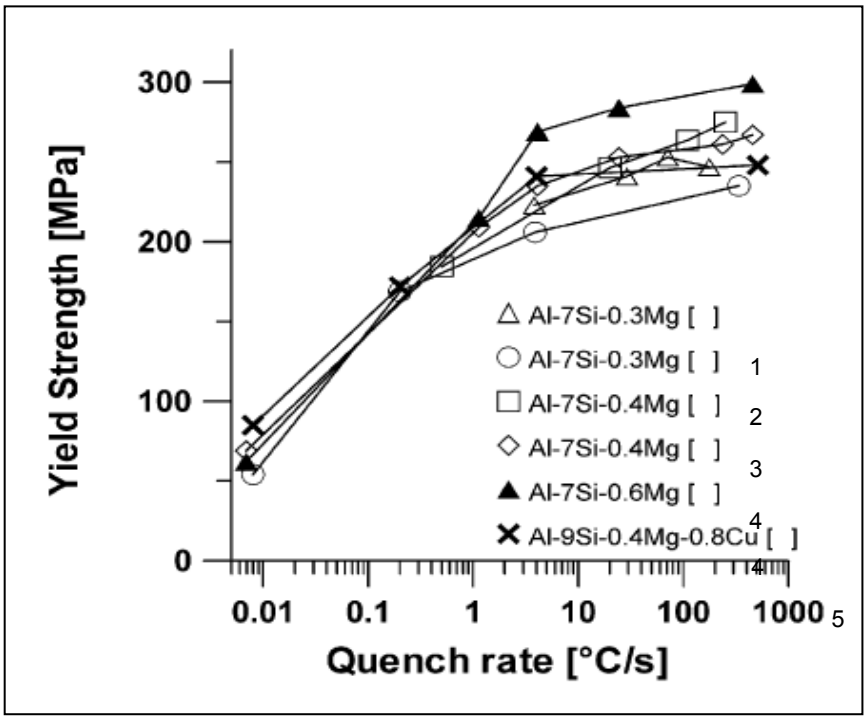

Figure 2.24. Yield strength for T6 heat-treated Al-Si alloys subjected to different quench rates [94-98]

Precipitation kinetics during quenching depends on the degree of supersaturation and diffusion rate. Diffusion rate increases as a function of temperature and a higher rate is achieved at elevated temperature. Inversely, supersaturation is greater at low temperature, providing driving force for precipitation. A critical temperature range for maximum nucleation and growth rate is between 450ºC to 290ºC for most aluminum alloys. Thus, the time spent in this temperature region should be as short as possible to avoid undesirable precipitation [8]. The most frequently used quenching method for commercial heat-treated aluminum alloys

parts are through direct immersion in either water or polyalkylene glycol and by spray quenching [99].

2.6.3.3 Ageing

The final stage in properties development for heat-treatable aluminum alloys is ageing treatment. Some of heat-treatable aluminum alloys, for instance the more highly alloyed 6xxx wrought series, copper containing 7xxx alloys and all of the 2xxx alloys undergo solution heat treatment and quenched prior to ageing treatment[100]. Ageing takes place by decomposition of supersaturated solid solution to form uniform distribution of small precipitates to enhance the strength of the materials. The ageing behavior for different aluminum alloys varies according to the respective alloy compositions which are further discussed in Section 2.6.4. There are two types of ageing treatment whereby natural ageing occurs at room temperature and artificial ageing occurs at elevated temperature.

After the subsequent solution heat treatment and quenching, some of the heat-treatable aluminum alloys are naturally aged at room temperature to T3 or T4 tempers to yield higher tensile strength, yield strength, more resistance to fatigue and higher fracture toughness. Natural ageing increases the material properties by rapid formation of Guiner-Preston (GP) zones due to the high level of supersaturation and high vacancy concentration after quenching. The material properties become stable after approximately 4 to 5 days. Aluminum alloys,

particularly 2xxx series aged at the standard T3- and T4- type tempers require nominal natural aging time of 4 days and the properties improvement hereafter are relatively minor and essentially stable after one week. Other alloys (i.e. Al-Zn-Mg-Cu, Al-Mg-Cu) exhibit less stable properties and are naturally aged over many years.

Artificial ageing, on the other hand,involves precipitation at elevated temperature, normally ranging from 115°C to 190°C with the ageing time varies between 5 to 48 hours[100]. Artificial ageing is time-temperature dependent thermal treatment and requires careful consideration in order to control precipitates size, distribution, morphology which later influences the mechanical behavior of the materials. During artificial ageing, the strength and hardness of the aluminum alloys increases and achieves a maximum value at the optimum ageing temperature and time. The extended ageing times or commonly known as over-ageing leads to progressive decrease in strength due to the growth of the precipitates. The ability of the precipitates to resist dislocation motion during deformation determines the strength of the age-hardened alloys. The nanoscale precipitates which play a crucial role in strengthening of aluminum alloys generally consists of mixtures of intermetallic compounds, for instance Al_2Cu, Al_2CuMg, Mg_2Si, $MgZn_2$[101]. Figure 2.25 displaysthe interaction of precipitates with dislocation. Dislocations can either pass the precipitates by shearing (Friedel effect) or by-passing (Orowan mechanism).

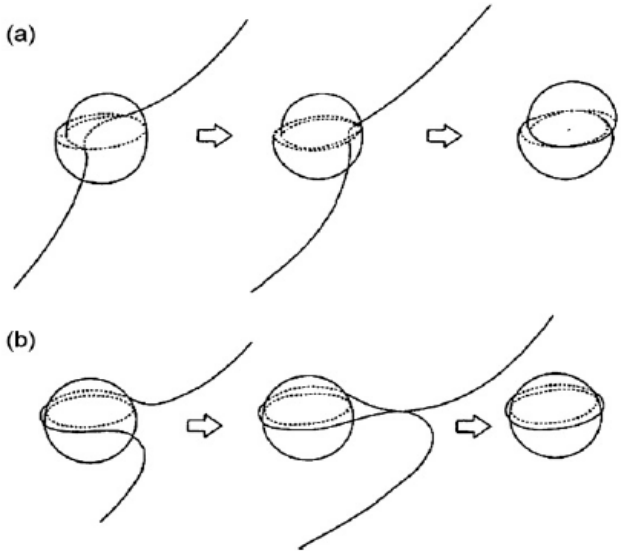

Figure 2.25. Interaction of dislocation with precipitates (a) Friedel effect (b) Orowanmecahanism[102]

2.6.4 Major Precipitation Hardening Alloy Systems

The change in strength during precipitation hardening is determined by the size and distribution of the precipitates coupled with the coherency of the precipitates within the matrix. Decomposition of supersaturated solid solution is very complex and occurs through several precipitation stages as displayed in Figure 2.26.

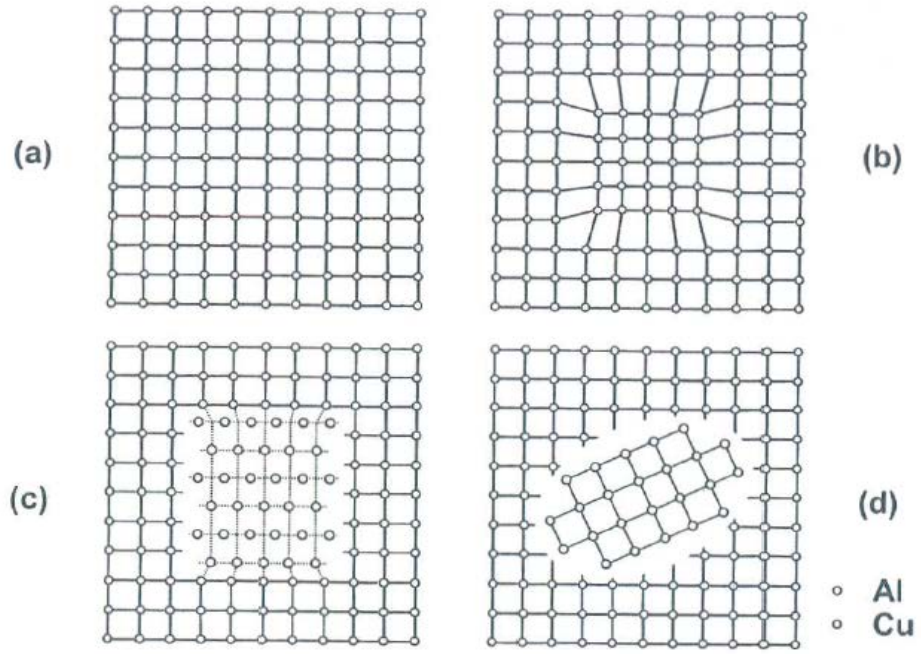

Figure 2.26. Schematic showing different stages during precipitation of aluminum alloys (a) supersaturated solid solution (b) coherent GP zone, (c) semicoherent precipitate, (d) incoherent equilibrium precipitate[8].

A homogeneous supersaturated solid solution forms after solution heat treatment and quenching. The first stages of precipitation marks the formation of local clustering of solute atoms known as Guinier-Preston or GP zones. GP zones are ordered, solute-rich clusters of atoms with approximately one or two atomic layers thick nucleated homogenously and are coherent with the matrix [103]. Difference in the atomic size gives rise to different amount of misfit that occurs when solute atom is placed in the parent lattice. This results in variation in the equilibrium shape of GP zones. For instance, the GP zone for Al-Mg systems is spherical in shape (Figure 2.27a) since the size difference between aluminum and solute is small.

Meanwhile, the GP zones in Al-Cu system exhibits disc shape perpendicular to the <100> direction in aluminum matrix (Figure 2.27b).

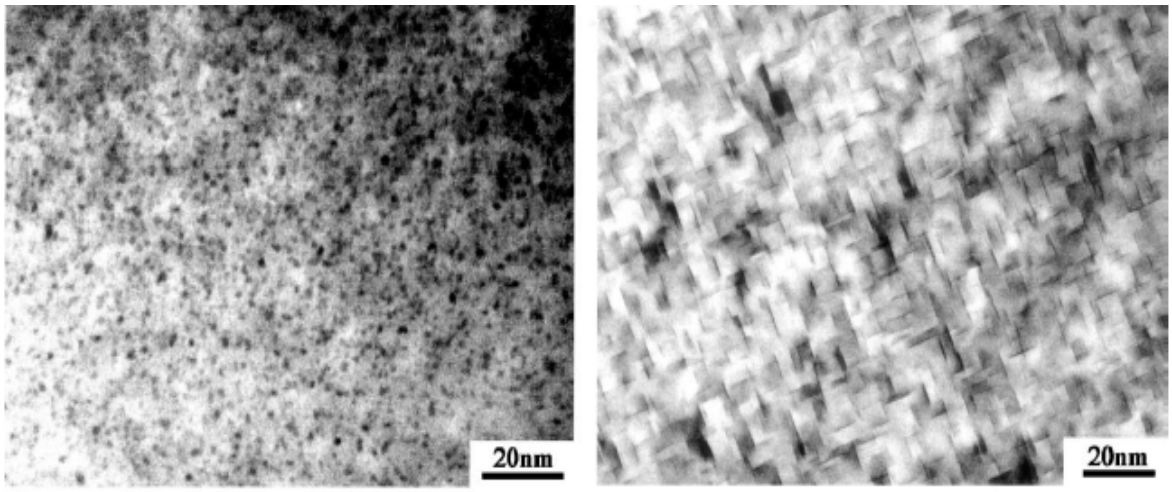

(a) (b)

Figure 2.27. Morphologies of GP zones in different shape: (a) spherical shape (Al-Mg alloys) (b) disc shape (Al-Cu alloy)[103].

Precipitation of metastable phases either coherent or semicoherent with the matrix usually occurred subsequently after the GP zones formation. The semicoherent precipitates generally provides more resistance to the dislocation movement and thus more efficient for hardening than coherent particles. As the size of the semi-coherent precipitates grows, the coherency strain increases until the matrix can no longer support the crystallographic mismatch and thus resulted in formation of stable non-coherent equilibrium precipitates[100].

2.6.4.1 Al-Cu System

Al-Cu system is a common example used in the classic ageing theory and serves as a base for the wrought 2XXX series and casting 2XX.0 series.Among a few examples of wrought Al-Cu alloys which play an important role in the industries include alloys 2025 and 2219. Alloy 2025 (Al-4.5Cu) is used extensively for forgings. Alloy 2219 (Al-6.3Cu), on the other hand, has a wide range of strength, good corrosion resistance, good weldability and excellent elevated temperature properties and has been used for fuel tanks for storing liquefied gases and propellants for missiles and space vehicles [8].

During the ageing of Al-Cu alloys, nonequilibrium precipitates structures are developed sequentially over a few stages at temperatures below the solvus. The precipitation occurrs according to the following sequence[104]:

$$SSS \rightarrow GP\ zones \rightarrow \theta'' \rightarrow \theta' \rightarrow \theta$$

The rapidly cooled supersaturated solid solution (SSS) is first decomposed upon ageing. Cu atoms start to cluster forming two dimensional coherent disc-shaped GP zones with the composition close to the stoichiometry of the Al_2Cu phase [8]. θ" appears as disks or thin plates which lie parallel to the {100} planes in the α-aluminum matrix planes, with the composition similar to that of GP zones. Transformation of θ" into the semicoherent phase θ' depends on the ageing temperature and time. θ' has tetragonal structure with the c_0 decrease from 7.09Å in θ" to 5.08Å[105]. Further precipitation results in θ' phase transformation to equilibrium θ phase. Formation of noncoherent θ phase is not desirable since it is

responsible for softening of the alloys and dislocation by passing the crystal rather than cutting through them.

2.6.4.2 Al-Cu-Mg System

Duralumin, which contains both copper and magnesium, marked the development of first Al-Cu-Mg precipitation hardenable alloy. Nowadays, Al-Cu-Mg alloys are largely used in the aircraft construction. Addition of Mg to Al-Cu alloys improves the hardening effects since Mg increases the binding energy between solute atoms and the vacancies. Al-Cu-Mg alloys allow hardening with the formation of either or both Al_2Cu and Al_2CuMg (S) precipitates depending on the composition of the supersaturated solid solution. At low ageing temperature (below 165°C), Al_2Cu precipitate acts more efficiently contributing to the hardening effects, whereas hardening effect is mainly due to the presence of Al_2CuMg at higher temperatures[8].

The decomposition of Al-Cu-Mg alloys starts with the formation of Guinier-Preston-Bagaryatysky zone (GBP zone) with the clustering of copper and magnesium in $\{100\}_{Al}$and $\{210\}_{Al}$ planes. The transition from S" to S occurs continuously with only slight modification in the lattice parameter for the orthorhombic crystal structure. S" and S precipitates commonly appear in thin elongated laths. The general precipitation sequence for Al-Cu-Mg alloys with Cu:Mg ration close to 2.0 can be summarized as follows[105]:

$$\text{Supersaturated } \alpha \rightarrow \text{ GBP zone } \rightarrow S'' \rightarrow S' \rightarrow S$$

2.6.4.2 Al-Mg-Si System

The 6XXX series alloys containing 0.5-1.5% Si and 0.5-1.5% Mg with various ratios belong to this Al-Mg-Si system. The 6XXX series alloys are widely used as medium strength structural alloys since they exhibit good weldability, corrosion resistance and resistance to stress-corrosion cracking. One of the well-known examples of 6XXX series alloys is Alloy 6061 with the composition of Al-1Mg-0.6Si[103]. The strengthening effects of the Al-Mg-Si alloys are mainly due to the precipitation of Mg_2Si phases. The ageing effect and final properties of the products are largely influenced by variation in the ratio between magnesium and silicon in the supersaturated solid solution. The general sequence of precipitation stages is denoted as below[106, 107]:

$$SSS \rightarrow GP\ zones \rightarrow \beta'' \rightarrow \beta' \rightarrow \beta$$

Precipitation of Al-Si-Mg alloys starts with the formation of spherical GP zones. The GP zones later develop into needle-shape coherent β'' phase with monoclinic crystal structure. At this stage of β'' precipitation, the alloys achieve the peak age condition. As the ageing proceeds, the needles grow and form β' rods and finally reach its equilibrium whereby noncoherentβ phase precipitates as plates or cubes. The crystal structure, on the other hand, undergoes the transition from monoclinic to hexagonal or orthorhombic and finally cubic structure at equilibrium. The transformation of the crystal structure during precipitation still remains unclear[8].

2.6.4.3 Al-Cu-Mg-Si System

Precipitation of Al-Cu-Mg-Si alloys depends on the alloy composition and thermal history or types of artificial heat treatment being applied. The strengthening phase presented during peak-aged condition for this alloy system depends on the Cu:Mg and Mg:Si ratios. A few examples of the precipitates are Mg_2Si (β''), Al_2Cu (θ'), $Al_5Mg_8Si_6Cu_2$ (Q") and Al_2CuMg (S)[108]. Two recent investigations performed by Li et al. [109]and Wang et al. [110]showed that Cu addition with the content varied from 0-4wt% to Al-Si-Mg alloys resulted in a change in precipitation sequence which later influenced the time to peak hardness and age-hardenability. Apart from alloy composition, it has been reported that different precipitates formed when subjected to different annealing condition. Mishra et al. showed that S' phase formed upon T5 annealing, whereas β' phase formed at T6 condition[111].

2.6.4.4 Al-Zn-Mg-Cu System

Commercial wrought (7XXX series) and casting (7XX.X) alloys have the compositions within this Al-Zn-Mg-Cu system. These alloys have very good ageing-hardenability and used extensively in the aircraft application. Precipitation sequence in Al-Zn-Mg-Cu alloys varies depend on the quenching and ageing conditions. The general precipitation sequence is as below[112]:

$$SSS \rightarrow \text{GP zones} \rightarrow \eta' \rightarrow \eta$$

Precipitation of coherent GP zones (MgZn) and semicoherentη' phases are often associated with strengthening of the alloys. The spherical GP zones form from supersaturated solid solution after quenching and aged at approximately 162°C. The GP zones then gradually transform to η' phases, which appear as round or plate-shaped precipitates[8]. The equilibrium η($MgZn_2$) phase can exist in different shapes: plates, rods or laths depending on the orientation relationship[100]. Transition to T phase ($Al_2Mg_3Zn_3$ or $(AlZn)_{49}Mg_{32}$) is also possible depending on the ratio of Mg:Zn. Decomposition of supersaturated solid solution finishes with η formationwith Mg:Zn ratio varies within the range from 2:5 to 1:7. T phase, on the other hand, forms at Mg:Zn = 0.5-6[8].

Ageing of Al-Zn-Mg-Cu alloys often carry out in two steps in order to minimize the ageing time and to improve the corrosion resistance for the alloys. The first stage of ageing consists of heating of the alloys to 100-110°C, 1-24 hour which is aimed to grow GP zones stable at higher temperatures and to provide sites for the subsequent formation of metastable phases. The second step of ageing involves heating up to 150-160°C to develop alloys with desired properties [8].

2.7 References

[1] G. Dowson, *Powder Metallurgy: The Process and its Products*. Hilger, Bristol, 1990.

[2] J. S. Hirschhorn, *Introduction to Powder Metallurgy*: American Powder Metallurgy Institute, Princeton, New Jersey, 1969.

[3] A. D. P. LaDelpha, M. P. Mosher, W. F. Caley, G. J. Kipouros, and D. P. Bishop, "On the Simulation of Wrought AA4032 via P/M Processing," *Materials Science and Engineering: A,* vol. 479, pp. 1-9, 2008.

[4] G. Kipouros, W. Caley, and D. Bishop, "On the Advantages of Using Powder Metallurgy in New Light Metal Alloy Design," *Metallurgical and Materials Transactions A,* vol. 37, pp. 3429-3436, 2006.

[5] O. D. Neikov, S. Naboychenko, V. G. Gopienko, and I. V. Frishberg, *Handbook of Non-Ferrous Metal: Technologies and Applications*. Oxford, UK: Elsevier, 2009.

[6] A. H. Committee, *Powder Metal Technologies and Applications* vol. 7: ASM International 1998.

[7] R. M. German, *Powder Metallurgy Science*, Second ed. Princeton, NJ: Metal Powder Industries Federation, 1994.

[8] G. E. Totten and D. S. Mackenzie, *Handbook of Aluminum: Physical Metallurgy and Processes* vol. 1. New York, NY: Marcel Dekker, INC., 2003.

[9] I. E. Anderson, J. C. Foley, and J. F. Flumerfelt, "Simplified Aluminum Powder Metal Processing Routes for Automotive Applications," presented at the Powder Metallurgy Aluminum and Light Alloys for Automotive Applications Conference, 1998.

[10] A. Lawley, *Atomization: The Production of Metal Powders*. NJ: Metal Powder Industries Federation, 1992.

[11] R. M. German, *Powder Metallurgy Science*. Troy, NJ: Metal Powder Industries Federation, 1984.

[12] W. Schatt and K. P. Wieters, *Powder Metallurgy: Processing and Materials*. Shrewsbury, UK: European Powder Metallurgy Association 1997.

[13] F. V. Lenel, *Powder Metallurgy: Principles and Applications*. New York: Troy, 1980.

[14] W.V.Knopp, *Effect of Type of Lubricant on Green Strength* vol. 2: Metal Powder Industries Federation, 1993.

[15] R.L.Sands and C.R.Shakespear, *Powder Metallurgy*. London: William Clowes and Sons, 1966.

[16] F. Thummler and R. Oberacker, *Introduction to Powder Metallurgy*. London: Institute of Materials, 1993.

[17] G. S. Upadhyaya, *Powder Metallurgy Technology*: International Science Publishing, 1997.

[18] P. Delabre and M. Kherl, "Application of P/M Aluminum Parts-Materials and Processing Schemes," presented at the Proceedings of the Second International P/M and Light Alloys for Automotive Conference, 2000.

[19] *Metals Handbook, Ninth Edition* vol. 7: Powder Metallurgy, American Society for Metals, 1993.

[20] W. D. Jones, *Fundamental Principles of Powder Metallurgy*. London: Institute of Materials, 1960.
[21] G. B. Schaffer, T. B. Sercombe, and R. N. Lumley, "Liquid Phase Sintering of Aluminium Alloys," *Materials Chemistry and Physics,* vol. 67, pp. 85-91, 2001.
[22] N. Showaiter and M. Youseffi, "Compaction, Sintering and Mechanical Properties of Elemental 6061 Al powder With and Without Sintering Aids," *Materials & Design,* vol. 29, pp. 752-762, 2008.
[23] R. M. German, S. Farooq, and C. M. Kipphut, "Kinetics of Liquid Phase Sintering.," *Materials Science and Engineering* vol. A105, pp. 215-224, 1988.
[24] S.-J. L. Kang, *Sintering :Densification,Grain Growth, andMicrostructure*. Burlington, MA: Elsevier Butterworth-Heinemann, 2005.
[25] H. E. Exner and E. Arzt, "Sintering Processes," in *Physical Metallurgy (Fourth Edition)*, W. C. Robert and H. Peter, Eds., ed Oxford: North-Holland, 1996, pp. 2627-2662.
[26] R. M. German, *Liquid Phase Sintering*. Troy, New York: Plenum Press, 1985.
[27] Y. S. Kwon and A. Savitskii, "Solid-State Sintering of Metal Powder Mixtures," *Journal of Materials Synthesis and Processing,* vol. 9, pp. 299-317, 2001.
[28] A. P. Savitskii, "Scientific Approaches to Problems of Mixtures Sintering," *Science of Sintering,* vol. 37, pp. 3-17, 2005.
[29] W.Kurz and D.J.Fisher, *Fundamentals of Solidification*. Rockport, MA: Trans Tech Publications, 1984.
[30] V. D. Frecjette, W. C. Lacourse, and V. L. Burdick, "Surfaces and Interfaces of Glass and Ceramics," in *Phase Distribution in solid-liquid-vapor systems*, H. C. E. a. P. J. A. Aksay I.A. , Ed., ed. New York, NY: Plenum Press, 1974.
[31] P. C. Angelo and R. Subramanian, *Powder Metallurgy: Science, Technology and Application*. New Delhi: PHI Learning Private Limited, 2008.
[32] R. N. Lumley and G. B. Schaffer, "The Effect of Solubility and Particle Size on Liquid Phase Sintering," *Scripta Material,* vol. 35, pp. 589-595, 1996.
[33] M. N. Rahaman, *Ceramic Processing and Sintering. Second Edition*: CRC Press, 2003.
[34] T. Pieczonka, T. Schubert, S. Baunack, and B. Kieback, "Dimensional Behavior of Aluminium Sintered in Different Atmosphere," *Material Science and Engineering A,* vol. 478, pp. 251-256, 2008.
[35] C. Binet, K. L. Lencoski, D. F. Heaney, and R. M. German, "Modeling of Distortion After Densification during Liquid-Phase Sintering," *Metallurgical and Materials Transactions A: Physical Metallurgy and Materials Science,* vol. 35 A, pp. 3833-3841, 2004.
[36] P. Lu, R. M. German, and B. M. Marx, "Liquid Phase Sintering of Tungsten Heavy Alloys," *International Journal of Powder Metallurgy (Princeton, New Jersey),* vol. 37, pp. 45-56, 2001.
[37] R. Raman, R.German, and R. M., "Mathematical Model for Gravity-Induced Distortion During Liquid-Phase Sintering," *Metallurgical and Materials Transactions A: Physical Metallurgy and Materials Science,* vol. 26A, pp. 653-659, 1995.

[38] S.-M. Lee and S.-K. L. Kang, "Evaluation of Densification Mechanisms of Liquid Phase Sintering," *Z. Metallkd.,* vol. 92, pp. 669-674, 2001.
[39] S.-M. Lee, J.-M. Chaiz, C. L. Martin, C. H. Allibert, and S.-K. L. Kang, "Computer Simulation of Particle Rearrangement in the Presence of Liquid," *Metals and Materials,* vol. 5, pp. 197-203, 1999.
[40] J. K. Park, S.-J. Kang, K. Y. Eun, and D. Y. Yoon, "The Microstructural Change During Liquid Phase Sintering," *Metallurgical and Materials Transactions A,* vol. 20A, pp. 837-845, 1989.
[41] R. M. German, P. Suri, and S. J. Park, "Review: Liquid Phase Sintering," *Journal of Materials Science,* vol. 44, pp. 1-39, 2009.
[42] B. E. Magee and J. Lund, "Mechanism of Liquid Phase Sintering in Iron-Copper Powder Compacts," *Metallkde. Z.,* vol. 67, pp. 596-602, 1976.
[43] G. C. Kuczybski, *Sintering and Catalysis*. New York, NY: Plenum Press, 1975.
[44] W. D. Kingery, "Densification during Sintering in the Presence of a Liquid Phase," *Journal of Applied Physics,* vol. 30, pp. 301-306, 1953.
[45] G. C. Kuczybski and C. Gibbon, *Sintering and Related Phenomena*. New York, NY: Gordon and Breach, 1967.
[46] I. Jenkins, Wood, J.V., *Liquid Phase Sintering in Powder Metallurgy - An Overview*: The Institute of Metals, 1991.
[47] D. N. Yoon and W. J. Huppmann, "Grain Growth and Densification During Liquid Phase Sintering of W-Ni," *Acta Materialia,* vol. 27, pp. 693-698, 1979.
[48] T. Courtney, "Densification and Structural Development in Liquid Phase Sintering," *Metallurgical Transactions A,* vol. 15A, pp. 1065-1074, 1984.
[49] G. H. Gessinger and H. F. Fischmeister, "A Modified Model for the Sintering of Tungsten with Nickel Additions," *Journal of the Less Common Metals,* vol. 27, pp. 129-141, 1972.
[50] G. H. Gessinger, H. F. Fischmeister, and H. L. Lukas, "A Model for Second-Stage Liquid-Phase Sintering with a Partially Wetting Liquid," *Acta Metallurgica,* vol. 21, pp. 715-724, 1973.
[51] F. B. Swinkels and M. F. Ashby, "Role of Surface Redistribution in Sintering by Grain Boundary Transport," *Powder Metallurgy,* vol. 2, pp. 1-7, 1980.
[52] O.-J. Kwon and D. N. Yoon, "Closure of isolated pores in liquid phase sintering of W-Ni," *Inter. J. Powder Metall., Powder Tech,* vol. 17, pp. 127-133, 1981.
[53] O. J. Kwon and D. N.Yoon, *The liquid phase sintering of W-Ni*. New York: Plenum Press, 1980.
[54] H.-H. Park, O.-J. Kwon, and D. N. Yoon, "The Critical Grain Size for Liquid Flow into Pores during Liquid Phase Sintering," *Metallurgical and Materials Transactions A,* vol. 17A, pp. 1915-1919, 1986.
[55] S.-J. L. Kang, W. A. Kaysser, G. Petzow, and D. N. Yoon, "Elimination of pores during liquid phase sintering of Mo-Ni," *Powder Metall.,* vol. 27, pp. 97-100, 1984.
[56] S.-J. L. Kang, K.-H. Kim, and D. N. Yoon, "Densification and Shrinkage During Liquid-Phase Sintering," *Journal of the American Ceramic Society,* vol. 74, pp. 425-427, 1991.

[57] J. T. Smith and J. D. Wood, "Elevated Temperature Compressive Creep Behavior of Tungsten Carbide-Cobalt Alloys," *Acta Metallurgica,* vol. 16, pp. 1219-1226, 1968.
[58] R. German and J. Dunlap, "Processing of Iron-Titanium Powder Mixtures by Transient Liquid Phase Sintering," *Metallurgical and Materials Transactions A,* vol. 17, pp. 205-213, 1986.
[59] W. J. Huppmann, "Sintering to High Density," *The International Journal of Powder Metallurgy and Powder Technology,* vol. 21, pp. 184-185, 1985.
[60] S. V. D. Zwaag, *Self Healing Material: An Alternative Approach to 20 Centuries of Materials Science*. Dordrecht, Netherlands: Springer, 2007.
[61] F. J. Puckert, W. A. Kaysser, and G. Petzow, "Transient Liquid Phase Sintering of Ni-Cu," *Zeitschrift Fur Metallkunde,* vol. 74, pp. 737-743, 1983.
[62] S. F. Corbin, "Thermal Analysis and Diffusion Based Modeling of Transient Liquid Phase Sintering," 2001, pp. 377-393.
[63] R. German, "Supersolidus Liquid-Phase Sintering of Prealloyed Powders," *Metallurgical and Materials Transactions A,* vol. 28, pp. 1553-1567, 1997.
[64] A. Lal, R. Iacocca, and R. German, "Densification During the Supersolidus Liquid-Phase Sintering of Nickel-based Prealloyed Powder Mixtures," *Metallurgical and Materials Transactions A,* vol. 30, pp. 2201-2208, 1999.
[65] A. Lal, Lacocca, R. G., German, R. M., "Microstructural Evolution During the Supersolidus Liquid Phase Sintering of Nickel-based Prealloyed Powder Mixtures," *Journal of Materials Science,* vol. 35, pp. 4507-4518, 2000.
[66] R. Tandon and R. M. German, "Supersolidus-Transient Liquid Phase Sintering Using Superalloy Powders," *The International Journal of Powder Metallurgy* vol. 30, pp. 435-443, 1994.
[67] R. M. German, "Advances in High Alloy Sintering Using Supersolidus Liquids, Conference Proceedings," in *PM^{2}TEC97*, Chicago, Illinois, 1997.
[68] O.-H. Kwon and G. L. Messing, "Kinetic Analysis of Solution-Precipitation During Liquid-Phase Sintering of Alumina," *Journal of the American Ceramic Society,* vol. 73, pp. 275-281, 1990.
[69] V. N. Eremenko, Y. V. Naidich, and I. A. Lavrinenko, *Liquid Phase Sintering*. New York, NY: Consultants Bureau, 1970.
[70] J. W. Cahn and R. B. Heady, "Analysis of Capillary Forces in Liquid-Phase Sintering of Jagged Particles," *Journal of the American Ceramic Society,* vol. 53, pp. 406-409, 1970.
[71] J. N. Brecker, "Analysis of Bond Formation in Vitrified Abrasive Wheels," *Journal of American Ceramic Society,* vol. 57, pp. 486-489, 1974.
[72] G. Y. Chin, *Sintering of Ceramics and Metals*. Metals Park, OH: American Society for Metals, 1982.
[73] Z. Y. Liu, T. B. Sercombe, and G. B. Schaffer, "The Effect of Particle Shape on the Sintering of Aluminum," *Metallurgical and Materials Transactions A,* vol. 38, pp. 1351-1357, 2007.
[74] D. Gouvêa and R. H. R. Castro, "Sintering: The Role of Interface Energies," *Applied Surface Science,* vol. 217, pp. 194-201, 2003.
[75] G. B. Schaffer, B. J. Hall, S. J. Bonner, S. H. Huo, and T. B. Sercombe, "The Effect of the Atmosphere and The Role of Pore Filling on the Sintering of Aluminium," *Acta Materialia,* vol. 54, pp. 131-138, 2006.

[76] J. M. Martín and F. Castro, "Liquid Phase Sintering of P/M Aluminium Alloys: Effect of Processing Conditions," *Journal of Materials Processing Technology,* vol. 143-144, pp. 814-821, 2003.
[77] R. Fabian, "Vacuum Technology: Practical Heat Treating and Brazing," ed: ASM International, 1993, p. 179.
[78] K. H. Moyer and W. R. Jones, "Vacuum Sinter Hardening," presented at the Heat Treating Progress, 2002.
[79] T. Schubert, T. Weißgärber, B. Kieback, H. Balzer, H.-C. Neubing, U. Baum, and R. Braun, "Aluminum PM is a Challenge that Industry Can Overcome," *Metal Powder Report,* vol. 60, pp. 32-37, 2005.
[80] D. Apelian and D. Saha, "Aluminium Powder Metallurgy Processed Components- Challenges and Opportunities," in *Proceedings of the Second International P/M and Light Alloys for Automotive Conferences*, 2001, p. 1.
[81] K. S. Dunnett, R. M. Mueller, and D. P. Bishop, "Development of Al-Ni-Mg-(Cu) Aluminum P/M Alloys," *Journal of Materials Processing Technology,* vol. 198, pp. 31-40, 2008.
[82] J. Svoboda, H. Riedel, and R. Gaebel, "Model for liquid phase sintering," *Acta Materialia,* vol. 44, pp. 3215-3226, 1996.
[83] A. Kimura, M. Shibata, K. Kondoh, Y. Takeda, M. Katayama, T. Kanie, and H. Takada, "Reduction Mechanism of Surface Oxide in Aluminum Alloy Powders Containing Magnesium Studied by X-Ray Photoelectron Spectroscopy using Synchrotron Radiation," *Applied Physics Letters,* vol. 70, pp. 3615-3617, 1997.
[84] C. J. Peel, "Aluminum Alloys for Airframes: Limitations and Developmets," presented at the Conference on Metarials at their Limits, The Institute of Metals, Birmingham, U.K. , 1985.
[85] S. G. Esptein, "Technical Report on Aluminum and its Alloys," The Aluminum Association, USA1978.
[86] J. E. Hatch, *Aluminum: Properties and Physical Metallurgy*. Materials Park, Ohio, 1984.
[87] J. R. Davis, *Aluminum and Aluminum Alloys*. Materials Park, Ohio: ASM International, 1993.
[88] T. Srivatsan and S. Vasudevan, "The Science, Technology, and Applications of Aluminum and Aluminum Alloys," in *Advanced Structural Materials*, ed: CRC Press, 2006, pp. 225-274.
[89] F. King, *Aluminum and its alloys*. New York: Ellis Horwood Limited, 1987.
[90] "PM Aluminum Drives Forward in New BMW Breakthrough," *Metal Powder Report,* vol. 61, pp. 13-15, 2006.
[91] C. M. Chen, C. C. Yang, and C. G. Chao, "A Novel Method for Net-Shape Forming of Hypereutectic Al-Si alloys by Thixocasting with Powder Preforms," *Journal of Materials Processing Technology,* vol. 167, pp. 103-109, 2005.
[92] K. Saksl, J. Ďurišin, M. Orolínová, K. Ďurišinová, and P. Lazár, "Structural study on Al-26 mass% Si-8 mass% Ni powder," *Journal of Materials Science,* vol. 40, pp. 1975-1978, 2005.
[93] D. Vojtech, A. Michalcová, J. Pilch, P. Sittner b, P. Serák, and P. Novák, "Structural characteristics and thermal stability of Al-5.7Cr-2.5Fe-1.3Ti alloy

produced by powder metallurgy " *Journal of Alloys and Compounds* vol. 475, pp. 151-156, 2009.
[94] L. V. Emadi, M. S. Whiting, J. H. Sokolowski, P. Burke, and M. Hart, *Optimal Heat Treatment of A356.2 Alloy*. San Diego, CA, United States TMS, 2003.
[95] Seifeddine, G. Timelli, and I. L. Svensson, "Influence of Quench Rate on the Microstructure and Mechanical Properties of Aluminium Alloys A356 and A354," *Int. Foundry Res. ,* vol. 59, pp. 2-10, 2007.
[96] D. L. Zhang, L. H. Zheng, and D. H. StJohn, "Effect of a Short Solution Treatment Time on Microstructure and Mechanical Properties of Modified Al-7wt.%Si-0.3wt.%Mg Alloy," *Journal of Light Metals,* vol. 2, pp. 27-36, 2002.
[97] L. Pedersen and L. Arnberg, "The Effect of Solution Heat Treatment and Quenching Rates on Mechanical Properties and Microstructures in AlSiMg Foundry Alloys," *Metallurgical and Materials Transactions A,* vol. 32, pp. 525-532, 2001.
[98] P. A. Rometsch, L. Arnberg, and D. L. Zhang, "Modelling Dissolution of Mg2Si and Homogenisation in Al–Si–Mg Casting Alloys," *Int. J. Cast Metal. Res. 12* vol. 1999, pp. 1-8, 1999.
[99] "Processing/Microstructure/Property Relationship in 2024 Aluminum Alloy Plates," US Department of Commerce, National Bureau of Standards Technical Report NBSIR 83-2669January 1983.
[100] A. H. Committee, *Heat Treating* vol. 4. United States of America: ASM International, 1991.
[101] I. J. Polmear, *Ligth Alloys, from Traditional Alloys to Nanocrystals*, 4th ed. Oxford, UK: Butterworth-Heinemann, 2006.
[102] V. Gerold, "Precipitation Hardening," in *Dislocations in Solids*, F. R. N. Nabarro, Ed., ed: North-Holland, 1979, p. 222.
[103] N. Kim, "Designing with Aluminum Alloys," in *Handbook of Mechanical Alloy Design*, ed: CRC Press, 2003, pp. 441-486.
[104] R. H. Beton and E. C. Rollason, "Hardness Reversion of Dilute Aluminum-Copper and Aluminum-Copper-Magnesium Alloys," *I. Inst. Metals,* vol. 86, p. 77, 1957.
[105] L. F. Mondolfo, *Aluminum Alloys: Structure and Properties*. London: Butterworth & Co. Ltd, 1979.
[106] I. Dutta and S. M. Allen, "A Calorimetric Study of Precipitation in Commercial Aluminum Alloy 6061," *J. Mater. Sci. Let.,* vol. 10, pp. 323-326, 1991.
[107] G. A. Edwards, K. Stiller, G. L. Dunlop, and M. J. Couper, "The Precipitation Sequence in Al-Mg-Si Alloys," *Acta Materialia,* vol. 46, pp. 3893-3904, 1998.
[108] E. Sjölander and S. Seifeddine, "The Heat Treatment of Al-Si-Cu-Mg Casting Alloys," *Journal of Materials Processing Technology,* vol. 210, pp. 1249-1259, 2010.
[109] Y. J. Li, Brusethaug. S., and A. Olsen, "Influence of Cu on the Mechanical Properties and Precipitation Behaviour of AlSi7Mg0.5 Alloy during Aging Treatment," *Scripta Material,* vol. 54, pp. 99-103, 2006.
[110] G. Wang, Q. Sun, L. Feng, L. Hui, and C. Jing, "Influence of Cu Contetn on Ageing Behaviour of an AlSiCuMg cast alloy.," *Mater. Design* vol. 28, pp. 1001-1005, 2007.

[111] R. K. Mishra, G. W. Smith, W. J. Baxter, A. K. Sachdev, and V. Franetovic, "The Sequence of Precipitation in 339 Aluminum Castings," *J. Mater. Sci. 36,* pp. 461-468, 2001.
[112] R. R. Sawtell and J. T. Staley, "Interactions between Quenching and Aging in Alloy 7075," *Aluminum,* vol. 59, pp. 127-133, 1983.

Chapter 3

Experimental Methods

3.1 Introduction

This chapter presents a detailed description of the material selection, processing routes and characterization method being employed. An overview of the experimental procedures is presented in Figure 3.1. A description of the starting materials' characteristics will be presented in Section 3.2, followed by Section 3.3 which provides an insight of the techniques employed during the processing of metal powders, including powder mixing and blending, compaction, sintering and heat treatment to study the effect of processing conditions and alloy additions on the microstructures and properties of the P/M parts.

Section 3.4 presents a series of characterization techniques employed in this study. The starting materials, sintered and heat treated compacts were characterized to study their microstructures, compositions, sintering response, heat treatment response and mechanical properties. The characterization techniques included a combination of density measurements, differential scanning calorimetry (DSC), dilatometry, X-ray diffraction (XRD), scanning electron microscopy (SEM), energy dispersive X-ray micronanalysis (EDX), transmission electron microscopy (TEM), hardness measurement and tensile testings.

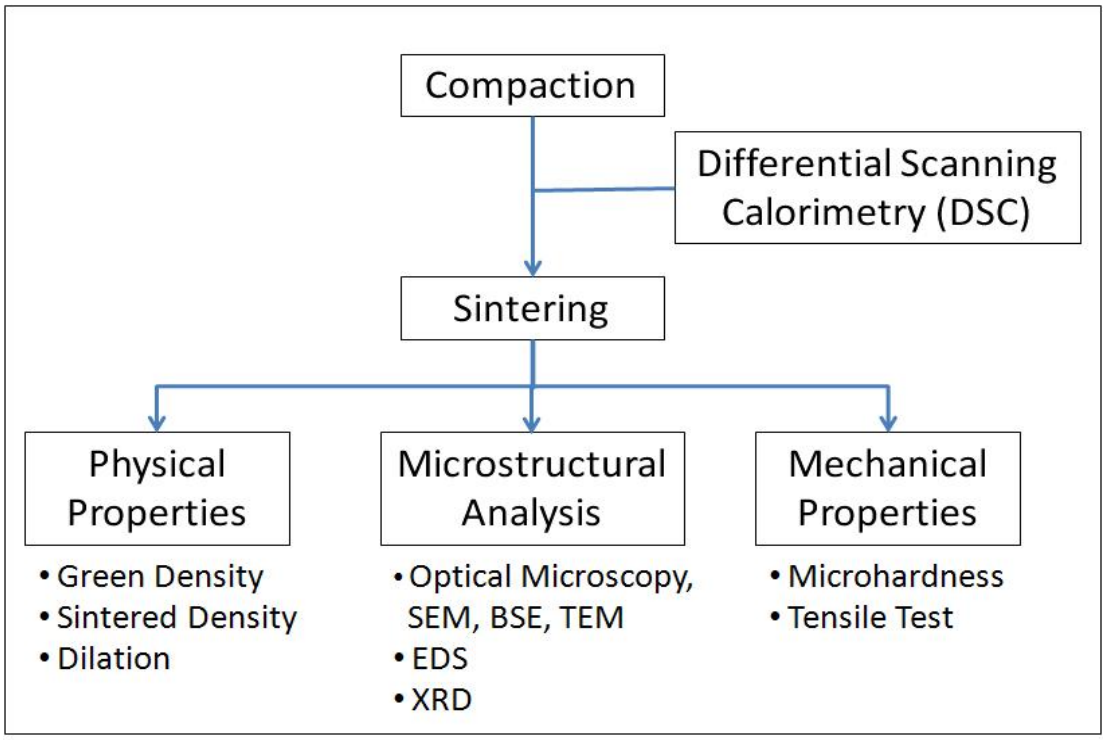

Figure 3.1 Overview of the experimental procedure

3.2 Starting Materials

The raw powder was supplied by Ecka Granules, with the nominal composition of Al-15Si-2.5Cu-0.5Mg (wt%) and contained 1.5 wt% of pre-blended Accrawax lubricant. It was commercially known as Ecka Alumix 231 and acted as benchmark for other Al-Si based alloys used in the subsequent studies. Other metallic powders used included air-atomized aluminum, electrolytic copper and Al-50wt%Mg master alloy powders with the D_{50} of 106 µm, 45 µm and 42 µm respectively. Carbonyl nickel powder with D_{50} of 6 µm and elemental Si powder (99.9 wt%) with D_{50} of 80 µm were utilized in this study as well. Table 3.1 provides further details on the starting materials used in this work.

Table 3.1 Tabulation of the starting materials

Starting Material	Composition	D_{50}(μm)	Supplier
Commercial Alumix 231	Al-15Si-2.5Cu-0.5Mg(wt%)	>45	Ecka Granule
Air atomized aluminum	Al (99.9% purity)	106	AlPoCo Ltd. U.K
Al-Mg master alloy	Al-50wt%Mg	42	AlPoCo Ltd. U.K
Electrolytic copper	Cu	45	Makin Metal Powders Ltd.
Carbony nickel powder	Ni	6	INCO Europe Ltd.
Elemental silicon powder	Si (99.55% purity)	80	Sigma-Aldrich

3.3 Material Processing

3.3.1 Powder Blending

Table 3.2 displays the nominal composition for three different Al-Si based alloys used for this study, with Ecka Alumix 231 (Al-15Si-2.5Cu-0.5Mg) acting as the baseline material. Variations from this baseline were then explored to study the effects of Cu and Ni additions. Blending was carried out using Turbula ^{TM} powder blender with the blending time of 1200s at the amplitude of 50Hz.

Table 3.2. The nominal composition of Al-Si based alloy systems used in the study.

Alloy Systems	Composition (wt%)
Ecka Alumix 231	Al-15Si-2.5Cu-0.5Mg
Alloy A	Al-15Si-4.5Cu-0.5Mg
Alloy B	Al-15Si-2.5Cu-0.9Ni-0.5Mg
Alloy C	Al-15Si-4.5Cu-0.9Ni-0.5Mg

3.3.2 Compaction

The aluminium alloys powder was cold compacted using Denison^{TM} uniaxial hydraulic press. Two different sets of dies were used to produce specimens for thermal analysis and tensile tests.

3.3.2.1 Thermal Analysis Specimen

Compacts for thermal analysis were prepared using a 13mm diameter die set. Prior to compaction, the die wall was lubricated with a solution of Accrawax lubricant suspended in methanol to reduce friction and tool wear. 2.5g of powder was loaded into the pre-lubricated die and pressed at compaction pressure ranging from 200MPa to 600MPa to determine the optimum compaction pressure. The pressure was applied for 60 seconds before it was released and samples being extracted from the die. It was found that 2.5g of powder compacted at the optimum compaction pressure can produce cylinder compact with 13mm diameter and 9mm height. Cylinder compacts with this dimension were used for subsequent sintering, heat treatment and dilatometry tests.

Differential scanning calorimetry (DSC) specimens were prepared by cutting the 9mm thick compact into 2mm thick segments. It was subsequently ground to produce DSC specimens with approximately 40 milligrams mass to ensure accuracy and consistency in DSC measurements.

3.3.2.2 Tensile Specimens

A standardized die with the dimensions according to MPIF Standard No.10 was used to produce tensile specimens. Both the die set and punches were lubricated by spraying a suspension of Accrawax lubricant in the methanol solution. 7g of powder was loaded into the die cavity with care to avoid tapping or vibration. The surface was levelled off using a hard spatula to ensure powder was evenly distributed within the die. The powder was pressed using Denison hydraulic press at the pre-determined optimum compaction pressure for 60 seconds. The die was then turned over and placed on a pair of steel stand while considerable amount of force was applied to extract the tensile specimens.

3.3.3 Sintering

All the compacts were sintered in a Thermal Elite^{TM} horizontal tube furnace using either protective atmospheres or under vacuum condition. Three different sintering atmospheres: (1) nitrogen, (2) vacuum and (3) nitrogen with 3% hydrogen atmospheres were used for the study.

For the study using high purity nitrogen gas and nitrogen with 3% hydrogen, the gas was flowed through the drying column filled with silica gel prior to entering furnace to ensure that the gas reached a dew point below -40°C. Before the sintering cycle started, the furnace was flushed with the above-mentioned gases for 30 minutes. The study on the vacuum atmosphere, on the other hand, was

conducted by having both rotary and diffusion pumps connected to the horizontal tube furnace. The vacuum pressure within the tube furnace was pumped up to 10^{-2} torr using rotary pump before the diffusion pump was subsequently activated to further decrease the pressure down to 10^{-4} torr. The furnace was remained at this pressure for 30 minutes before the sintering cycle started.

The sintering temperatures was determined using high temperature Netzsch 404 Differential Scanning Calorimetry (DSC) to be within the range of 500°C to 566°C based on the amount of liquid phase presented at various temperature. Further details on DSC were given in Section 3.4.3.

The compacts were first de-lubricated at 350°C for 20 min before subjected to desired sintering temperatures at the heating rate of 10K/min. It was subsequently held isothermally for 60 min before furnace cooled down to room temperature. The densities of the compacts sintered under different atmospheres were measured to determine the optimum sintering atmosphere. The sintering atmosphere which produced compacts with highest sintered density was then applied in the subsequent study to sinter compacts with different alloy additions.

3.3.4 Heat Treatment

The conventional T6 heat treatment used in this study involved solution heat treatment, quenching and artificially aging to enhance the mechanical properties of the compacts. After sintering, the compacts were remained in the furnace for the subsequent solution heat treatment to be carried out. Compacts was subjected to various solutionizing temperatures (490°C, 500°C, 510°C, 520°C) over the period of 1 and 10 hours before quenching in cold ethanol. All the solution heat treatment temperature was pre-determined using the differential scanning calorimetry (DSC) traces.

The compacts were later subjected to artificial ageing in a Eurothem conventional air furnace for the time interval between 1 and 48 hours. Different ageing temperatures: 120°C, 160°C, 180°C and 200°C were applied in this study. Table 3.3 summarizes the heat treatment variables used in this study.

Table 3.3. Variables for the T6 heat treatment

Variables	Details
Solutionizing temperatures	490°C, 500°C, 510°C, 520°C
Solutionizing time	1, 10 hours
Ageing Temperature	120°C, 160°C, 180°C and 200°C
Ageing Time	1, 4, 8, 10, 12, 24, 48 hours

3.4 Characaterization Techniques

The techniques and equipment employed to characterize the powders, green compacts, sintered and heat-treated compacts were discussed in details in the following sections.

3.4.1 Apparent Density and Powder Flow Rate Measurement

Apparent density of powder was measured following the Metal Powder Industries Federation Standard No.4. Hall flowmeter funnel together with a cylindrical collecting cup of volume 25 ± 0.05 cm^3 was used. The powder was poured through the Hall flowmeter into the cylindrical container of constant volume until it overflows. The powder was levelled off using spatula without applying any vibration or tapping to the density cup. Apparent density can be calculated by dividing the measured mass of powder with the container volume. The powder flow rate was measured by recording the time needed to empty 50g of powder through a 5mm diameter orifice funnel.

3.4.2 Density Measurement

Both green and sintered densities were determined following MPIF Standard 42, “Determination of the Density of Compacted or Sintered Metal Powder Products”. The mass of the compacts was weighted in the air before being impregnated in the oil at room temperature. The compacts were left oil-impregnated in the vacuum at

10^{-2} torr for at least 4 hours before it was taken out and left in the air for 30 minutes. All the pores within the compacts were presumably preoccupied with the oil at this stage. Excessive oil was gently wiped off. The oil impregnated compacts were weighted in the air before it was immersed in the ethanol. The mass of the oil-impregnated compacts in ethanol was then being measured. Ethanol was used instead of water to prevent any undesired reaction with Al and Mg. The density of the compacts was calculated according to the following equation:

$$\rho = \frac{M_{air}}{M_{oil} - M_{ethanol}} \cdot \rho_{ethanol}$$

where ρ, $\rho_{ethanol}$, M_{air}, M_{oil}, $M_{ethanol}$ were density of compact, density of absolute ethanol, weight of dry compact in the air and weight of oil-impregnated compact in the air, and weight of oil-impregnated compact in the ethanol respectively. The densification coefficient, φ of the compacts was then calculated using the equation below:

$$\varphi = \frac{\rho_s - \rho_g}{\rho_t - \rho_g}$$

where ρ_s , ρ_g , ρ_t were sintered density, green density and theoretical density respectively.

3.4.3 Differential Scanning Calorimetry (DSC)

Phase transformations and their kinetics during heating of the specimens were studied using the heat flux Netzch Jupiter DSC 404. Sample preparation for DSC has previously been stated in Section 3.3.2.1.

The thermal cycle was conducted using the alumina pans. Both the sample and reference pans were positioned on the heat flux plate. The heat flow data for the sample and reference pans were recorded during isothermal and anisothermal cycles.

DSC specimens were subjected to a dynamic heating/cooling rate of 10K/min. Pure argon gas was used as a protective atmosphere. The temperature range used was from 100-700^{0}C. The obtained signal was subtracted from the baseline which was measured by running the same heating schedule with empty alumina pans. Analysis of the DSC traces was performed using Proteus-NETZSCH software. DSC traces obtained were used for the following purposes:

- Determination of sintering temperatures
- Determination of phase transformations during heating of the compacts
- Determination of solutionizing temperatures
- Determination of the precipitation sequences for different Al-Si based alloys

3.4.4 Dilatometry Test

Thermal dilation analyses were carried out using a Netzsch Dil 402C thermal dilatometer. Dilatometer samples were prepared according to the procedure as stated in Section 3.3.2.1. Dilatometer samples were delubricated in a separate furnace to prevent instrument contamination. The samples were subjected to the same heating parameters as applied for sintering of the compacts in the tube furnace. This was to ensure that the expansion/shrinkage event of the compacts were identical to the compacts sintered in the horizontal tube furnace. A nitrogen flow rate of 100ml/min was maintained throughout the tests. An alumina sample was used for background correction. For each alloy, a minimum of two samples were tested to ensure data reproducibility. Analysis of the dilatometry results was performed using the Proteus-NETZSCH software.

3.4.5 Optical and Scanning Electron Microscopy (SEM)

Microstructural assessments were performed using the Zeiss-Axioskop microscope which was equipped with Zeiss KS300^{TM} and a field-emission SEM (JEOL JSM 7000F) which is equipped with an energy dispersive x-ray detector (INCA x-sight model 7559, Oxford Instruments Ltd). Powder samples for SEM studies were prepared by spreading them onto a conductive adhesive carbon disc stuck on top of an aluminium stub. Sintered and heat-treated samples for metallographic examination, on the other hand, were prepared by embedding them into cold mount resin. This was followed by conventional mechanical grinding

using 200, 400, 800, 1200, 4000 grades sand papers before subjected to subsequent polishing using diamond paste down to 1μm for final polishing.

The Zeiss-Axioskop optical microscope was generally used to characterize the microstructure of sintered samples at lower magnification and to measure the porosity within the samples. For each sample, 20 readings of porosity were taken to ensure the accuracy of the measurements.

Both secondary electron imaging and back-scattered imaging mode, on the other hand, were used to characterize the microstructures and morphology of the loose powder, sintered and heat treated compacts. The imaging and microanalysis of the constituent phases were carried out at a fixed working distance of 10mm and accelerating voltage of 20kv. EDX analysis obtained by Oxford INCA x-sight EDX detector was processed using the software package of “The Microanalysis Suite Issue 17a+SP1’. For EDX Quant analysis, silicon was selected as optimization element. EDX analysis was carried out at process time of 5. The acquisition live time and number of acquisition channel fixed at 60s and at 2K respectively. The X-ray count was determined to be at least 1500cts with the dead time between 20-40%

3.4.6 Transmission Electron Microscopy (TEM)

TEM samples were prepared at MSSCORPS CO., LTD, Taiwan using focused ion beam milling in FEI Helious 450S, which consisted of both focused gallium ion

beam and a conventional field-emission scanning electron (FEGSEM) column. The area of interest was firstly coated with 1 μm thick platinum which acted as protective layer against subsequent ion milling process. By using the ion beam, the membrane containing site of interest was extracted from the compacts and transferred via probe tip to custom Omniprobe TEM sample holder or known as 'lift-out grid'. The membrane was attached to the grid by ion beam induced metal deposition, while detached from probe tip using FIB milling. The extracted sample was then thinned to the required thickness for TEM inspection. Gallium ion beam operated at 30 kV with beam current ranging from 65000 down to 9300 pA was used to thin the membrane down to approximately 1μm. The sample was further polished to 150nm using successive currents of 1000pA. The sample was finally cleaned at 41 pA and at 5 kV. TEM investigation was carried out using FEI Tecnai F20 FEG (S)TEM equipped with Oxford EDX at the MSSCORPS CO., LTD, which operated at 200 kV, with an extraction voltage of 3800 V and a gun lens voltage of 0.75 kV. The STEM images, EDX composition line scan and mapping were performed to study the morphology, microstructures and composition of the precipitates after heat treatment.

3.4.7 X-ray Diffraction (XRD)

The XRD samples were ground and polished to get smooth surface in order to produce diffraction peaks with minimum noise. The samples were then mounted on the sample holder and illuminated with X-ray of a fixed wavelength. A Siemens

X-ray diffractometer using a tube with copper Kα radiation (λ = 1.54Å) generated at 40kV and 40mA current and a scan rate of 5^0 min-1 (2θ) was employed in this study to obtain the diffraction pattern. A 2θ ranging from 20° to 120° with a step size of 0.02°/sec was applied. The intensities and angles of the diffracted beams were recorded using a D8 advance (Bruker) equipped with an ultra-fast silicon strip Lynxeye detector. The diffraction pattern obtained was a plot of intensity vs 2θ of the diffracted beam. The intensity of the diffraction peaks is related to the amount of electron density distribution. Phase analysis was performed using XPert Highscore software by comparing the peak position and relative intensities from a set of standard data provided by International Center for Diffraction Data (ICDD).

3.5 Mechanical Testing

3.5.1 Vickers Hardenss

A Mitutoyo MVK-H1 Vickers Hardness testing machine was used to measure the hardness of the polished samples. Samples preparation for hardness measurement was similar to SEM sample preparation to obtain a smooth surface and minimize measurement errors. At least 30 measurements were taken for each sample. Prior to the hardness measurement, the machine was first calibrated using the NAMAS calibration block with the serial number of EP9716400 at 300 gf to obtain the Vickers Hardness Number (VHN) close to 757.3. A fixed load of 100 gf with the load time of 8 sec was set constant throughout the measurements. The spacing between each indentation was at least 3 times larger than the diagonal of

the indentation. In order to obtain the Vickers Hardness Number, the size of the diagonals was accurately measured and calculated using the following formula:

$$VHN = \frac{1.854\,P}{d_{avg}^2}$$

where P is the applied load and d_{avg} is the average of the indentation diagonal in mm.

3.5.2 Tensile Test

Tensile properties of compacts sintered under different sintering atmospheres were determined using a Zwick^{TM} screw tensile testing machine with the cross head speed of 0.2mm min^{-1} at room temperature. Tensile specimen with the standard dimension as outlined under Section 3.3.2.2 were pressed and sintered. At least three tests were performed for each condition. Elongation was measured using an extensometer with the gauge length of 20mm.

3.6 Thermodynamic Calculations

Thermodynamic calculations were performed using the software Thermo-calc version R running on PC/ Windows NT. The database TTAL version 5.0 was used, which was specifically designed for aluminium alloys. All the compositions mentioned in this work are in weight percent (wt%).

Chapter 4

Optimizing The Processing Parameters for Ecka Alumix 231

4.1 Introduction

The newly emerged commercial press-and-sinter hypereutectic Al-Si P/M alloy referred to as Ecka Alumix 231 with the nominal composition of Al-15Si-2.5Cu-0.5Mg (wt%) is deemed to be a promising candidate to replace the cast aluminum-silicon in application. German P/M part producer Schwäbische Hüttenwerke (SHW) reported successful production of P/M aluminum chain sprocket for BMW cam-phaser system using Ecka Alumix 231 [1]. The final properties of aluminum alloys P/M parts are always influenced by its fabrication route. It is therefore necessary to investigate and develop an optimum processing condition for this novel alloy system.

In this chapter, the influence of the processing conditions in terms of compaction pressure, sintering temperature, sintering time and sintering atmospheres are investigated. As mentioned in the literature review, sintering is the key process in P/M fabrication route responsible for the development of strength and other properties for final P/M parts. Formation of liquid phase is crucial to disrupt the oxide layers which later aids in densification. Sintering atmosphere also plays a

vital role on densification. Three different sintering atmospheres were used in this study, namely nitrogen, vacuum and nitrogen with 3% hydrogen atmospheres.

The effects of the processing variables on microstructural developments, densification and mechanical properties of this alloy system are discussed in details in the subsequent sections. Expansion and shrinkages occurred during sintering are also presented. X-ray diffraction and EPMA analysis were carried out to identify different phases presented in both the green and sintered compacts.

4.2 Characterization of Ecka Alumix 231

The characteristics of the raw powder Ecka Alumix 231 were examined in this section. Figure 4.1 shows the broad size distribution of Ecka Alumix 231. The D_{50} of this commercial powder is between the range of 63-75μm and 75-100μm. Other powder properties for Ecka Alumix 231 are summarized in Table 4.1. These properties were similar to the properties as reported by Ecka Granules [2].

Figure 4.2(a) shows the SEM micrograph of the Ecka Alumix 231 (Al-15Si-2.5Cu-0.5Mg). The powder particle for this alloy system was found to have coarse surface and irregular shape. These characteristics are similar to the air-atomized aluminum alloys powder. As illustrated in Figure 4.2(b), Ecka Alumix 231 consisted of two types of powders: elemental Al powder and master alloy Al-Si-Cu-Mg. EDX analysis as displayed in Table 4.1 shows that the dark grey region as indicated by Point 1 denoted the presence of elemental aluminum, whereas the bright grey

area as indicated by region 2 was determined to have the overall composition of Al-28Si-5Cu-1Mg(wt%). This finding agreed quite well with the results as reported by Arribas et. al. [3].

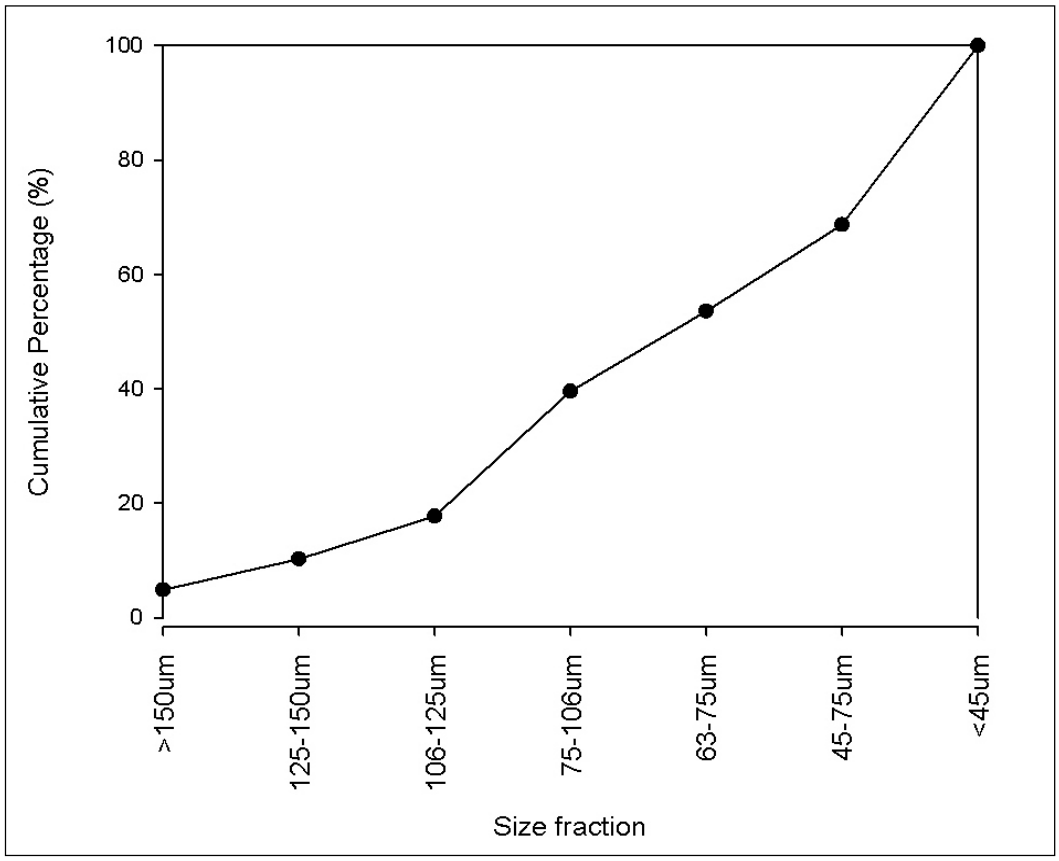

Figure 4.1. Size distribution of Ecka Alumix 231 (Al-14Si-2.5Cu-0.5Mg)

Table 4.1. Typical physical characteristic of Ecka Alumix 231

Apparent Density (g/cm3)	Flowability (s/50g/5.0mm)	Powder Shape
1.05	<30	Irregular

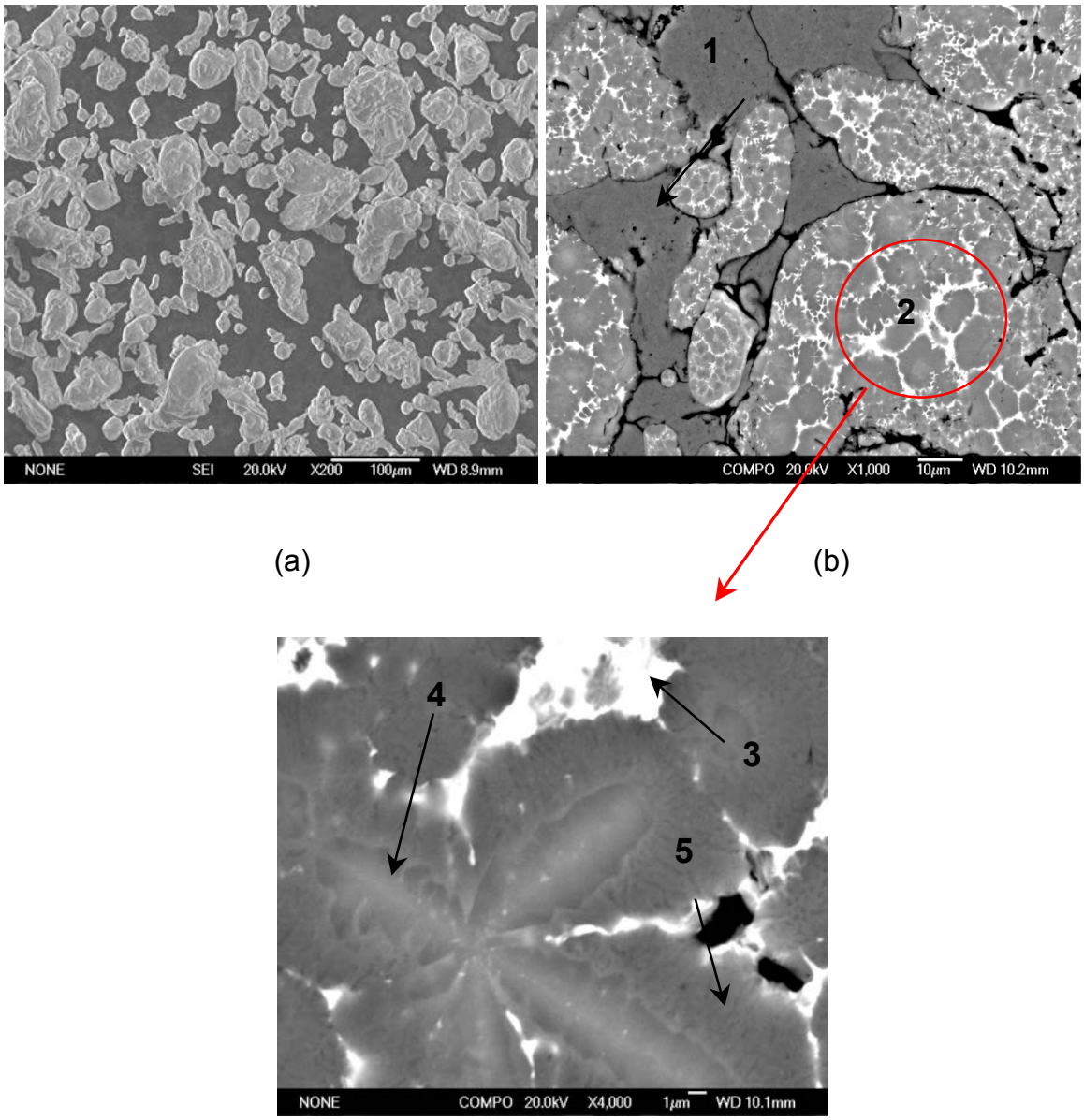

Figure 4.2 (a)Scanning electron micrograph for Ecka Alumix 231 powder at 200X magnification and backscattered electron micrograph for green compact at (b) 1000x magnification and (c) 4000X magnification

Table 4.2

EDX analysis corresponding to the point locations as shown in Figure 4.2(b) and Figure 6.2c (wt%)

Point	Al	Si	Cu	Mg	Fe
1	100.00	0.00	0.00	0.00	0.00
2	65.39 ± 1.29	28.57 ± 1.86	5.15 ± 0.65	0.89 ± 0.12	0.00
3	63.65 ± 1.67	7.08 ± 1.39	26.0.6 ± 2.92	2.61 ± 0.60	0.60 ± 0.08
4	10.83 ± 4.56	89.17 ± 4.56	0.00	0.00	0.00
5	83.53 ± 0.39	13.26 ± 0.71	2.62 ± 0.31	0.89 ± 0.16	0.00

A larger magnification of the master alloy powder (Region 2) was shown in Figure 4.2(c). The master alloy powder in region 2 was comprised of three distinct phases. The chemical compositions for these phases were determined using EDX as shown in Table 4.2. The primary silicon (Point 4) was found to be surrounded by the Al-Si eutectic like structure (Point 5). The bright web-like structure (Point 3), on the other hand, marked the presence of Cu- and Mg-rich intermetallics. The EDX analysis was substantiated by the X-ray diffraction (XRD) result as displayed in Figure 4.3. The presence of α-aluminum, elemental silicon and θ phase ($CuAl_2$) were confirmed. Similar to the findings as reported by Heard et. al [4], the peak at 34.6° 2θ was also observed which was later identified as Q phase ($Cu_2Mg_8Si_6Al_5$) by Arribas et al [3].

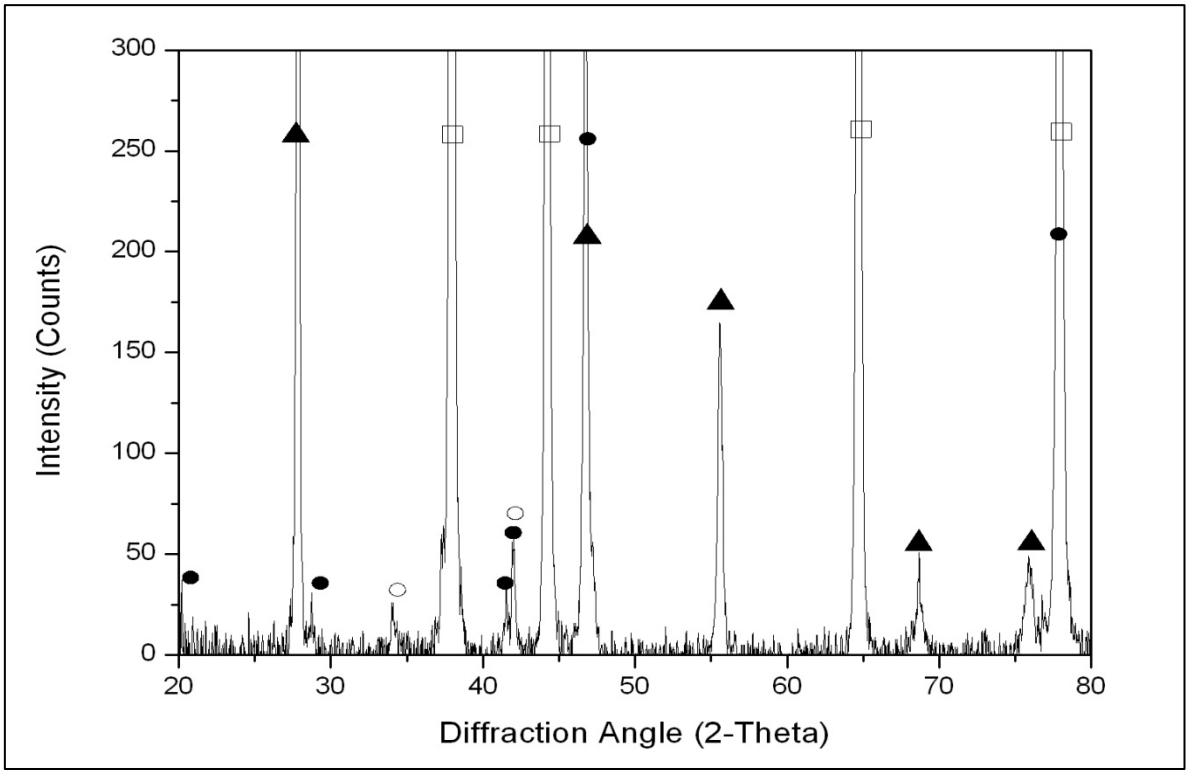

Figure 4.3. XRD pattern corresponding to Ecka Alumix 231 raw powder. Phases positively identified were α - Al (□), Si (▲), θ phase (●) and Q phase (○).

4.3 Optimization of Compaction Pressure

The compressibility curve for Ecka Alumix 231 was developed to determine the suitable compaction pressure used in the subsequent studies. Figure 4.4 displays the green density of the compacts as a function of compaction pressure. It can be noted that the green density of the compacts increased with the increase of the compaction pressure.

At the compaction pressure of 200MPa, the green body achieved the green density of 2.02g/cm^3, which was corresponding to 75.78% of the theoretical value (ρ_t= 2.668g/cm^3). Further increase of the compaction pressure to 400MPa marked a substantial increase of green density to 2.27g/cm^3 or 85.40% of theoretical value. While the green density of the compacts continued to increase with the increase of compaction pressure, the rate of densification decreased at the same time. The compacts pressed at 500MPa and 600MPa did not have very remarkable increase in green density, with only approximately 2% increase in densification. Thus, compaction pressure at 400MPa can be considered as a modest pressing pressure to be used in the subsequent works. High compaction pressure is not generally used in the industry due to the excessive wear of tooling. With this in mind, the upper compaction pressure limit was maintained to be 600MPa.

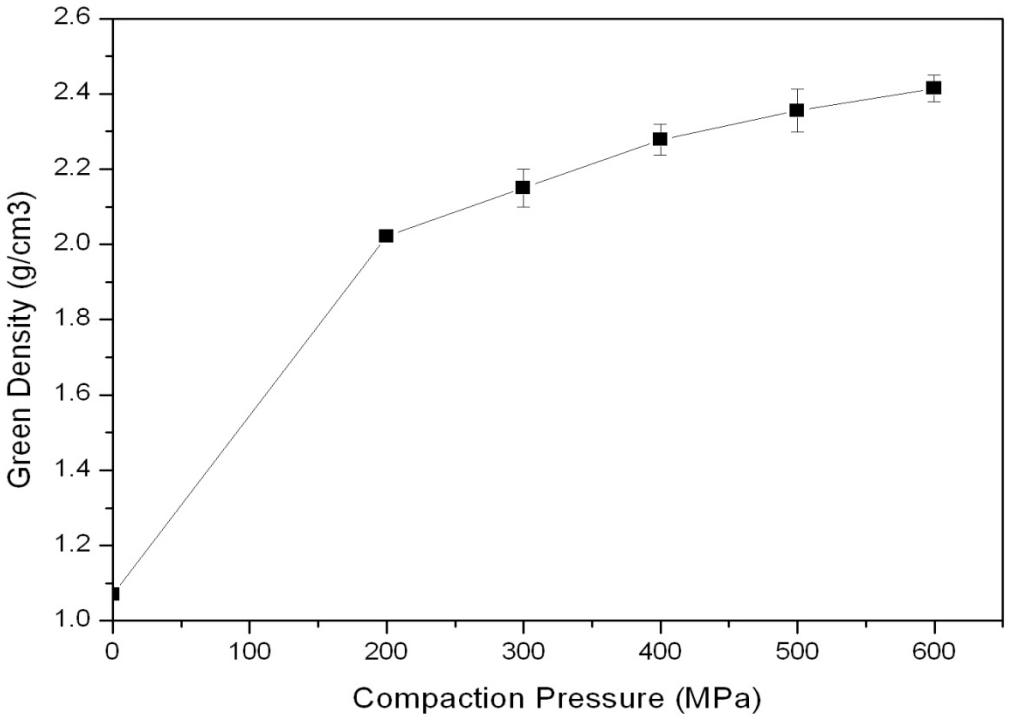

Figure 4.4. Compressibility curve for Ecka Alumix 231

4.4 Optimization of Sintering Temperature

Liquid phase sintering involves the coexistence of the liquid phase with particulate solid at designated sintering temperature. Presence of the liquid phase allows better atomic diffusion, rapid rearrangement of the solid particles than the solid state sintering. This will in term increase the rate of densification. Yet, presence of the excessive liquid content can lead to undesirable compact shape distortion. Thus, it is crucial to determine the amount liquid phase presented at different temperature.

The amount of liquid formed was determined by taking into consideration of the partial area of the endothermic melting peaks obtained from the differential scanning calorimetry (DSC) traces, as shown in Figure 4.5. The results were then tabulated in Table 4.3. The subsequent sintering process was carried out based on the temperature determined through DSC measurement to understand the effects of liquid content on sintering which will be discussed in details in subsequent sections. From the DSC traces of Ecka Alumix 231 as displayed in Figure 4.5, a few major melting events can be noted. It is anticipated that most of the chemical homogenization process occurred within the range of 500 ºC and 580 ºC. The melting events marked a start with two small intensity endothermic peaks being observed at 510 ºC and 525 ºC respectively. These endothermic peaks could be associated with the melting of the ternaries and quaternaries compounds involving Al, Cu, Mg, and Si. The main melting event was indicated by a large

endothermic peak with the maximum intensity at around 575 ºC. Above 635 ºC, Ecka Alumix 231 was fully melted.

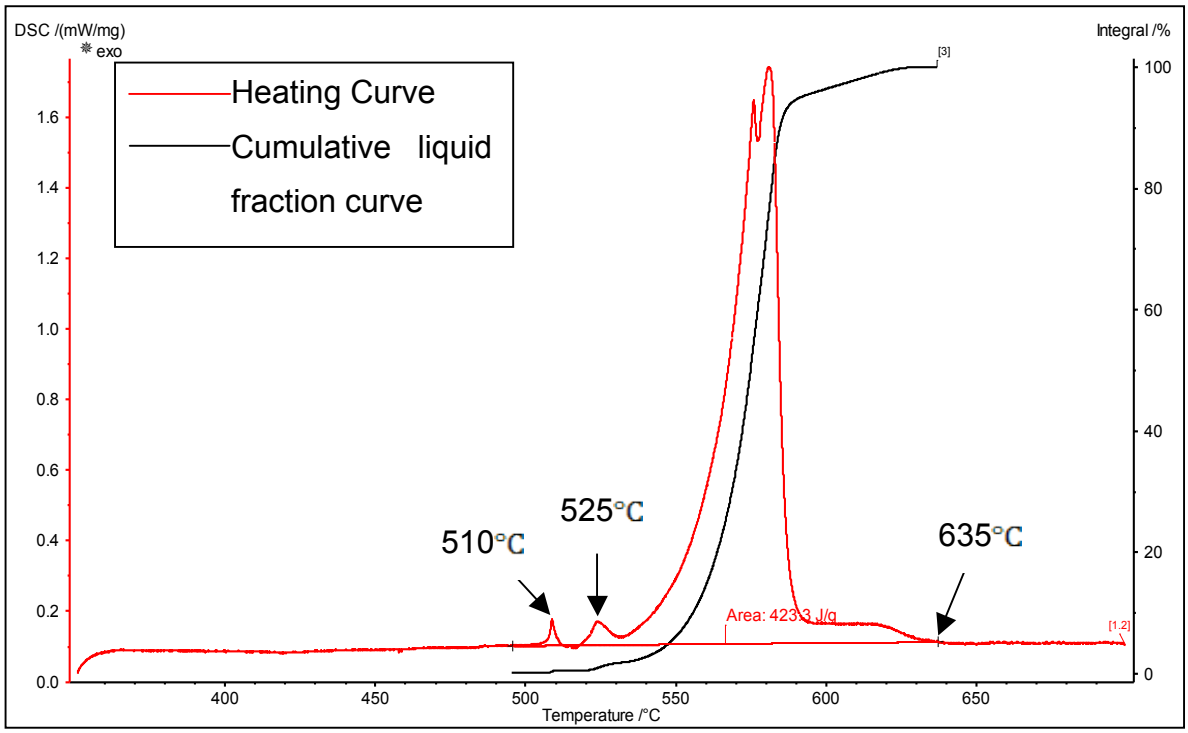

Figure 4.5. Heating curve and cumulative liquid fraction curve for Ecka Alumix 231 obtained from DSC measurement.

Table 4.3. Summary of DSC results showing the amount of liquid presented at different sintering temperature for Ecka Alumix 231

Liquid Content (%)	Sintering Temperature (°C)
0	500
5	547
10	555
15	560
20	563
25	566

4.5 Influence of Processing Conditions on Sintered Density

4.5.1 Effects of Sintering Temperatures on Sintered Density

There are two major parameters which have significant influences on compacts densification: sintering temperature and sintering atmosphere. As tabulated in Table 4.3, with the increase of sintering temperature, larger amount of liquid phase formed. It is therefore necessary to determine the optimum sintering temperature to yield compacts with higher densification. Influences of sintering atmospheres, on the other hand, will be discussed in details in the following section.

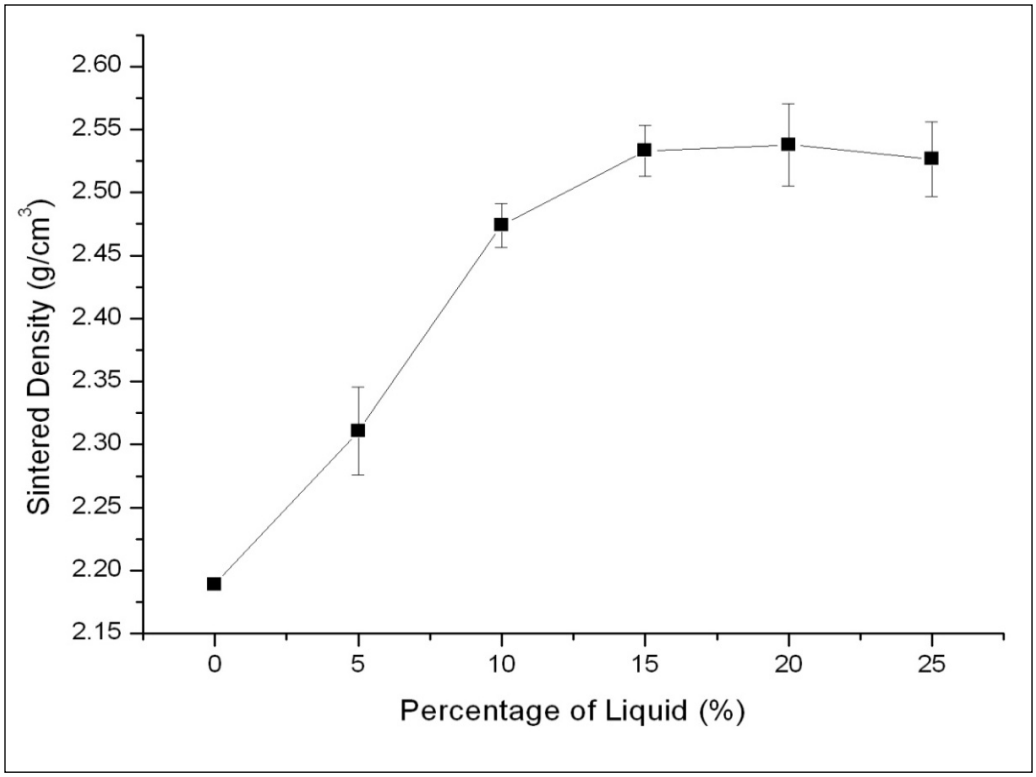

Figure 4.6: Sintered densities for compacts sintered under nitrogen atmosphere at different liquid content.

Figure 4.6 displays the changes in sintered densities at different amount of liquid phase presented for compacts sintered under nitrogen atmosphere. It can be seen that compacts sintered under nitrogen atmosphere achieved the highest density of

2.54g/cm^3 which was corresponding to 95.22% of the theoretical value (ρ_t= 2.668g/cm^3) at liquid content of 15%. This is equivalent to the sintering temperature of 560°C. Sintering of the compacts at higher sintering temperatures did not result in significant compact densification. To obtain a clearer understanding on the relative densification of the compacts, Table 4.4 shows the green density, sintered density and relative densification in both absolute values and percentage of theoretical density.

At the sintering temperature of 500°C, the densification coefficient, φ or relative densification of the compacts (Table 4.4) showed negative value which denoted the occurrence of expansion or swelling events within the compacts. Furthermore, the density of the compacts at this temperature was relatively lower than the green compacts with only 82.07% of the theoretical value being noted, which was 3% lower than the green compacts. As the sintering temperature increased, the relative densification of the compacts started to exhibit positive values which indicated the occurrence of shrinkage or compacts densification. In other words, the densification event started when the liquid phase started to form. However, a decrease in the rate of densification can be observed with the increase of the liquid content. The relative densification only increased from 0.68 to 0.69 when the compacts sintered from 560°C to 566°C. Thus, 560°C is deemed to be the optimum sintering temperature to achieve compacts with higher densification.

Table 4.4:

Tabulation of green and sintered density as well as relative densification for Ecka Alumix 231 sintered in nitrogen atmosphere at different sintering temperatures

Sintering Temperature (°C)	**Green Density ρ_g (g/cm3)**	$\rho_g(\%\rho_t)$	**Sintered Density ρ_s (g/cm3)**	$\rho_s(\%\rho_t)$	**Relative Densification φ**
500	2.27	85.10	2.19	82.07	-0.20
547	2.26	84.72	2.31	86.62	0.12
555	2.27	85.10	2.47	92.74	0.51
560	2.27	85.10	2.54	95.22	0.68
563	2.25	84.35	2.54	95.13	0.68
566	2.25	84.35	2.53	94.72	0.66

* All the densities stated in the table were average value for 4 compacts with error bar less than ±0.01

4.5.2 Effects of Sintering Atmospheres on Sintered Density

Apart from controlling of the amount of liquid phase presented within the compacts, sintering atmosphere also plays an important role in densification. Figure 4.7 depicts the changes in sintered density as function of percentage of liquid phase presented for compacts sintered under three different sintering atmospheres: nitrogen atmosphere, vacuum atmosphere (vacuum pressure of 10^{-4} torr) and nitrogen with 3% hydrogen atmosphere. Tables 4.5 and 4.6 provide further details on green density, sintered density and relative densification for compacts sintered in vacuum and nitrogen with 3% hydrogen atmosphere in both absolute values and percentage of theoretical density. For the nitrogen sintered compacts, the results have been discussed in the previous section, 4.5.1.

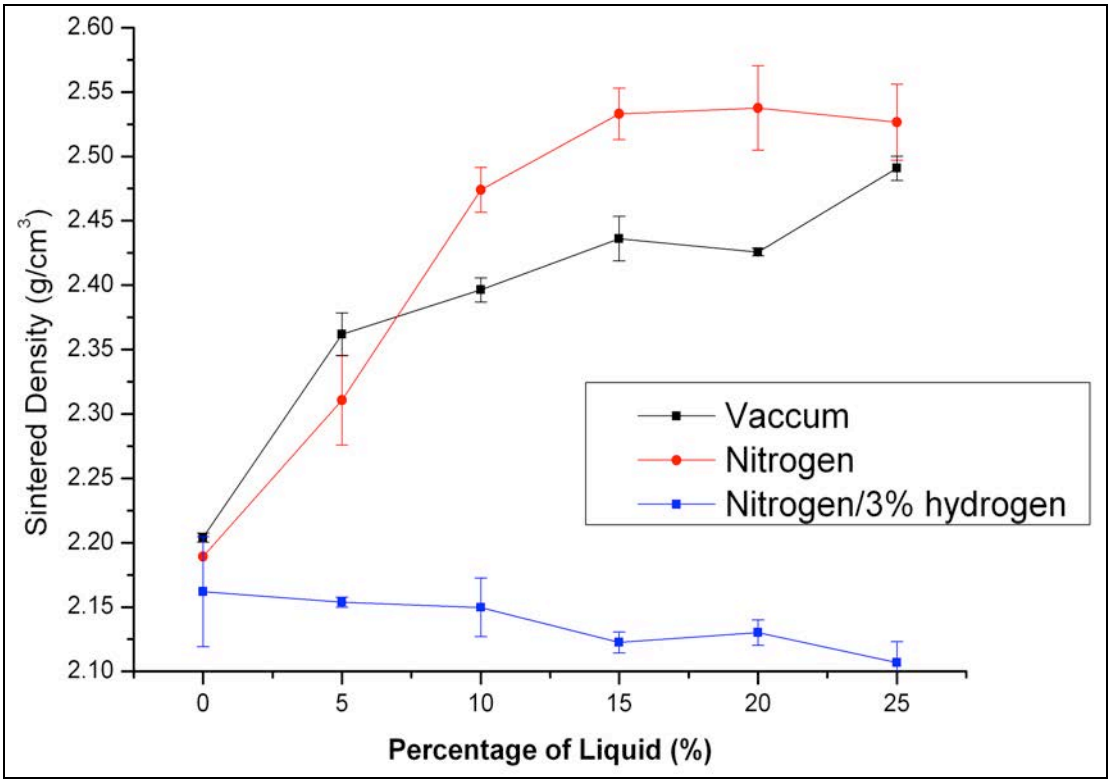

Figure 4.7: Sintered densities for compacts sintered under vacuum, nitrogen/3% hydrogen and nitrogen atmosphere at different liquid content.

From Figure 4.7, it can be noted that nitrogen is the most efficacious sintering atmosphere as compared to compacts sintered under vacuum and nitrogen with 3% hydrogen atmospheres. Compacts sintered under nitrogen atmosphere achieved the highest sintered density when sintered at 560°C, at which 15% of liquid phase presented. Compacts sintered under vacuum atmosphere also showed significant densification with the increase of sintering temperatures. However, the highest sintered density that can be achieved for compacts sintered in vacuum condition (2.49g/cm^3 which was corresponding to 93.37% of the theoretical value) was still lower than the highest sintered density as obtained in the nitrogen atmosphere. Both the compacts sintered in nitrogen and vacuum atmospheres started with swelling with relative densification of -0.20% and -0.14% respectively at 0% liquid phase which was equivalent to 500°C. The relative densification, hereafter increased as the amount of liquid phase presented increased.

Compacts sintered in nitrogen with the 3% hydrogen atmosphere, on the other hand, did not show any significant densification. Table 4.6 shows that with the increase of the amount of liquid phase presented, the densification coefficient continued to give a negative value in which expansion of the compacts occurred continuously. Additional of 3% hydrogen in the nitrogen atmosphere, thus had detrimental effects on densification.

Table 4.5:
Tabulation of green and sintered density as well as relative densification for Ecka Alumix 231 sintered in vacuum atmosphere at different sintering temperatures

Sintering Temperature (°C)	Green Density, ρ_g (g/cm3)	$\rho_g(\%\rho_t)$	Sintered Density, ρ_s (g/cm3)	$\rho_s(\%\rho_t)$	Relative Densification φ
500	2.26	84.72	2.20	82.62	-0.14
547	2.25	82.35	2.36	88.54	0.27
555	2.27	85.10	2.40	89.83	0.32
560	2.27	85.10	2.44	91.32	0.42
563	2.25	84.35	2.43	90.93	0.42
566	2.24	83.97	2.49	93.37	0.59

* All the densities stated in the table were average value for 4 compacts with error bar less than ±0.03

Table 4.6:
Tabulation of green and sintered density as well as relative densification for Ecka Alumix 231 sintered in nitrogen with 3% hydrogen atmosphere at different sintering temperatures

Sintering Temperature (°C)	Green Density, ρ_g (g/cm3)	$\rho_g(\%\rho_t)$	Sintered Density, ρ_s (g/cm3)	$\rho_s(\%\rho_t)$	Relative Densification φ
500	2.25	84.35	2.16	81.04	-0.21
547	2.27	85.10	2.15	80.74	-0.29
555	2.26	84.72	2.15	80.59	-0.27
560	2.25	82.85	2.12	79.56	-0.31
563	2.27	85.10	2.13	79.85	-0.35
566	2.26	84.72	2.11	78.98	-0.38

* All the densities stated in the table were average value for 4 compacts with error bar less than ±0.03

4.5.3 Effects of Sintering Times on Sintered Density

Though sintering time is a relatively weak processing parameter compared to sintering temperature and sintering atmosphere, control of the sintering time is crucial in the economics of sintering process. Sufficient sintering time is required for the diffusion and pore filling to take place and enhance the densification of the compacts. Yet, prolonged sintering time is not recommended since it will reduce rate of production in the industries. Another problem with prolonged sintering is the grain coarsening which can lead to reduction in the mechanical strength.

Figure 4.8 shows the changes in the sintered density for compacts sintered in nitrogen atmospheres at different sintering times. Sintering at 30 minutes was clearly not sufficient for the compacts to attain full densification since it only achieved sintered density of 2.34g/cm3 or 87.57% of the theoretical value. With increase of the sintering time to 45 minutes, a substantial increase in sintered density can be observed. The compacts reached the highest sintered density when sintered at sintering time of 60 minutes. Prolonged sintering time up to 90 minutes did not result in any significant increase in densification. Therefore, sintering time of 60 minutes is desirable to attain better densification in the compacts.

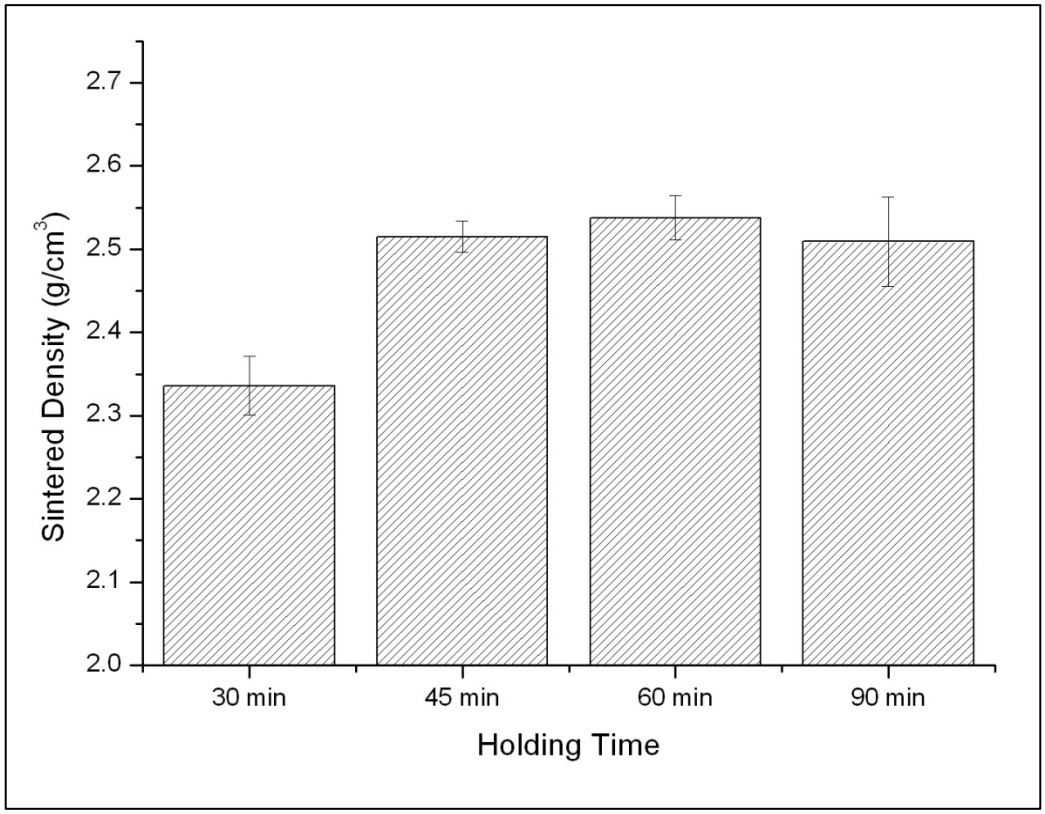

Figure 4.8: Sintered densities for compacts sintered under nitrogen atmosphere at different holding time.

4.6 Thermal Expansion Profile

Control of the dimensional changes in the final parts is one of the crucial requirements in the industry. For this reason, the extent of expansion and shrinkage during sintering needs to be monitored carefully. Several dilatometric experiments have been made, in which Ecka Alumix compacts were heated at a uniform rate to the different sintering temperature and held isothermally at these temperature for 60 minutes.

Figure 4.9 (a)-(c) depicts the dilation curves for Ecka Alumix 231 sintered at 500°C, 547°C and 560°C respectively. As tabulated in Table 4.3, no liquid evolved when the compact was heated up to 500°C. The compact underwent normal thermal expansion up to approximately 480°C (E1) before the contraction set in. The shrinkage (S1) continued for 10 minutes, followed by a plateau. Upon completion of the isothermal sintering, the compact had expanded 0.6% overall. The volume expansion of the compacts at 500°C was thus substantiated the results as reported in Section 4.5.1, whereby a drop in a sintered density was noted during the initial stage of liquid phase sintering.

Meanwhile, two stages of expansion can be observed when the compact was sintered at 547°C. At this sintering temperature, 5% of liquid phase started to form. The compact exhibited a near-uniform expansion with the increase of the temperature (E1) as shown in Figure 4.9(b). The shrinkage event initiated upon reaching 480°C (S1). The second stage of expansion marked a start at 504°C (E2). It was subsequently followed by shrinkage which occurred in two stages.

Rapid shrinkage (S2) occurred over short period of time before near uniform shrinkage started to take place (S3). Though more shrinkage was observed with the increase of sintering temperature, the overall compact still obtain a total expansion of 0.08%.

The dilation curve for compact sintered at 560°C was displayed in Figure 4.9(c). In the earlier studies on compact densification, 560°C was the optimum sintering temperature which required 15% of liquid content to achieve densification. Two similar expansions as observed in compact sintered at 547°C again appeared over here. Shrinkage occurred at a few different stages (S1 to S4) but the rate of shrinkage decreased over time. The compact had shrunk 0.7% overall upon completing the sintering process.

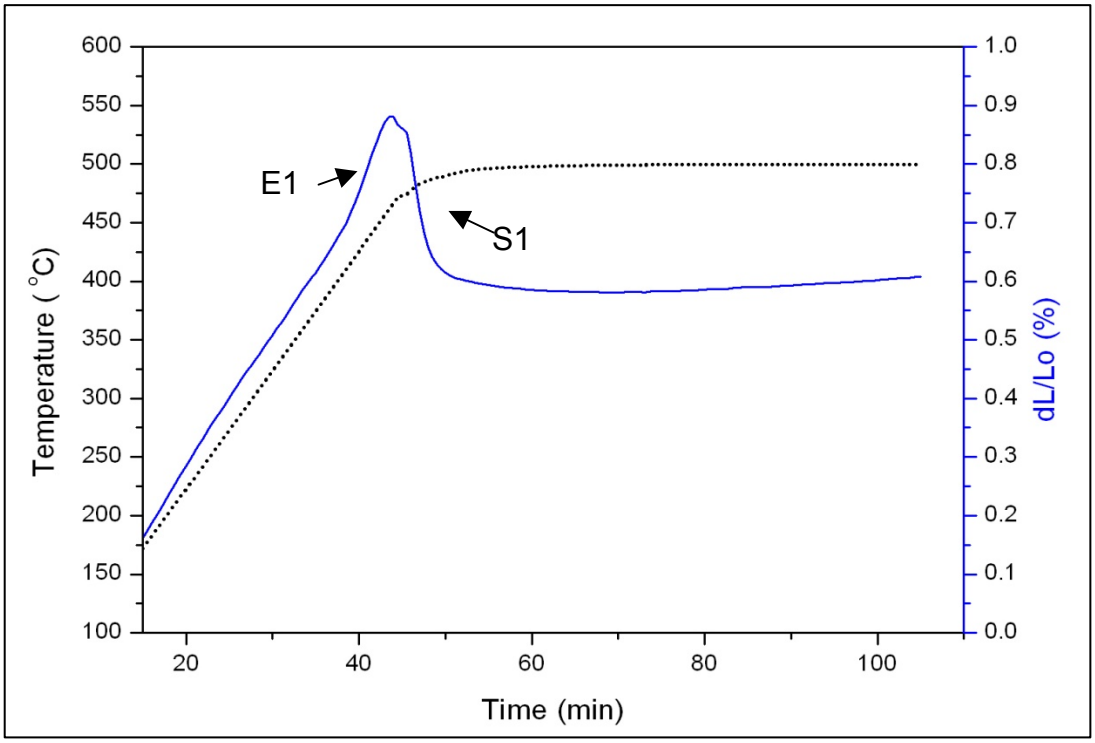

(a)

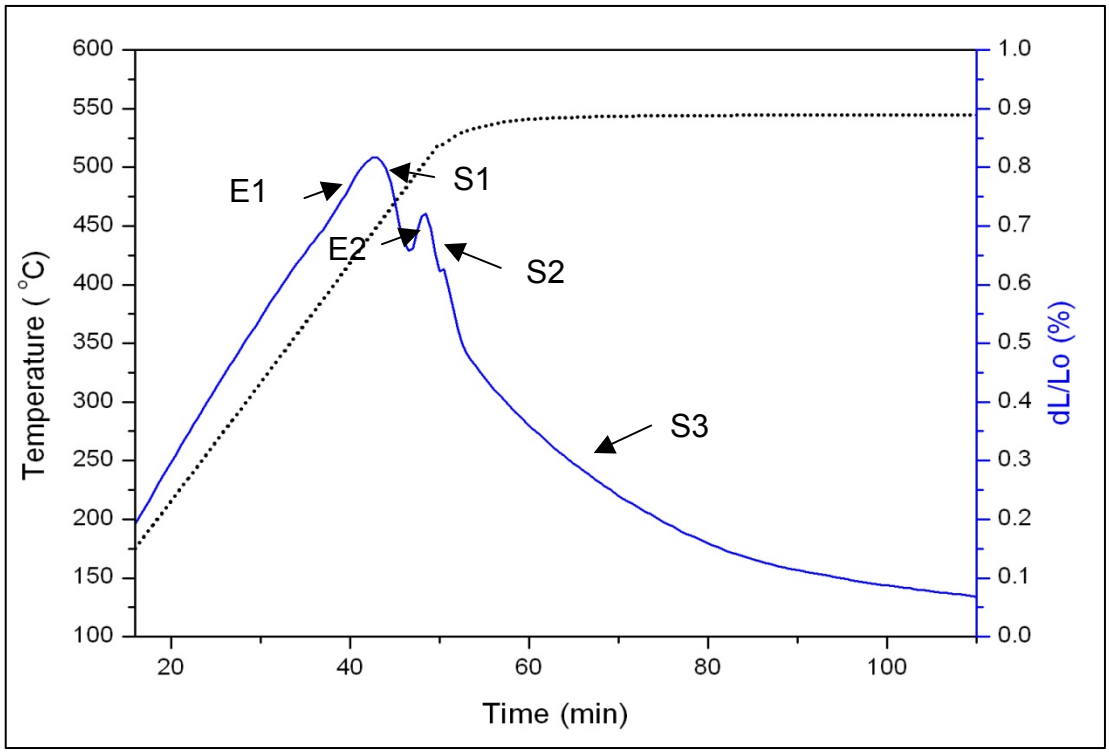

(b)

Figure 4.9: Dilatometer curves for Ecka Alumix 231 sintered at (a)500°C and (b) 547°C.

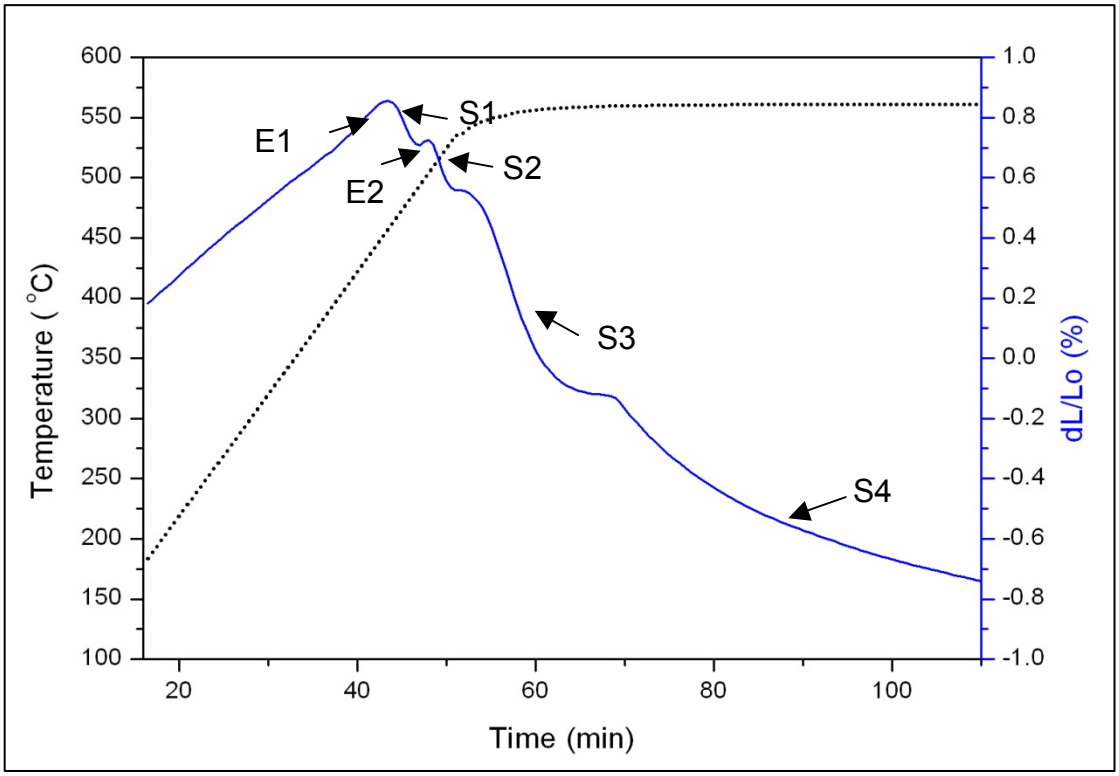

(a)

Figure 4.9 (continued): Time derivatives of dilatometer curves for Ecka Alumix 231 sintered at (c) 560°C.

4.7 Influence of Processing Condition on Microstructures

4.7.1 Microstructural Development of Ecka Alumix 231 at Different Sintering Temperatures

From the DSC traces, two small peaks can be observed at 508ºC and 521ºC respectively. To obtain clearer understanding of the microstructural change during these heating ramps, the compacts were sintered and quenched when they reached the designated temperatures. The microstructures of the compacts at 508ºC and 521ºC were displayed in Figures 4.10 and Figure 4.11.

It can be seen that at 508ºC, the petal-like Si particles embedded in eutectic silicon phase and surrounded by the web-like Cu rich region as observed in the green compact was no longer discernible. The EDX results were summarized in Table 4.7. Small globular Si rich region (dark grey area) started to form. Arribas et al. [3] reported that globulization of eutectic Si phase within the master alloy powder particles marked the first change in microstructures. This comes in good agreement with the microstructure as observed in Figure 4.10(c). Large primary Si particle (Point 4) as shown in Figure 4.10 (c) was found to coexist with the fine dispersion of Si-rich particles (Point 2). The Cu rich region started to break into small Cu-rich droplets. Minor traces of Fe can be detected within the Cu rich region.

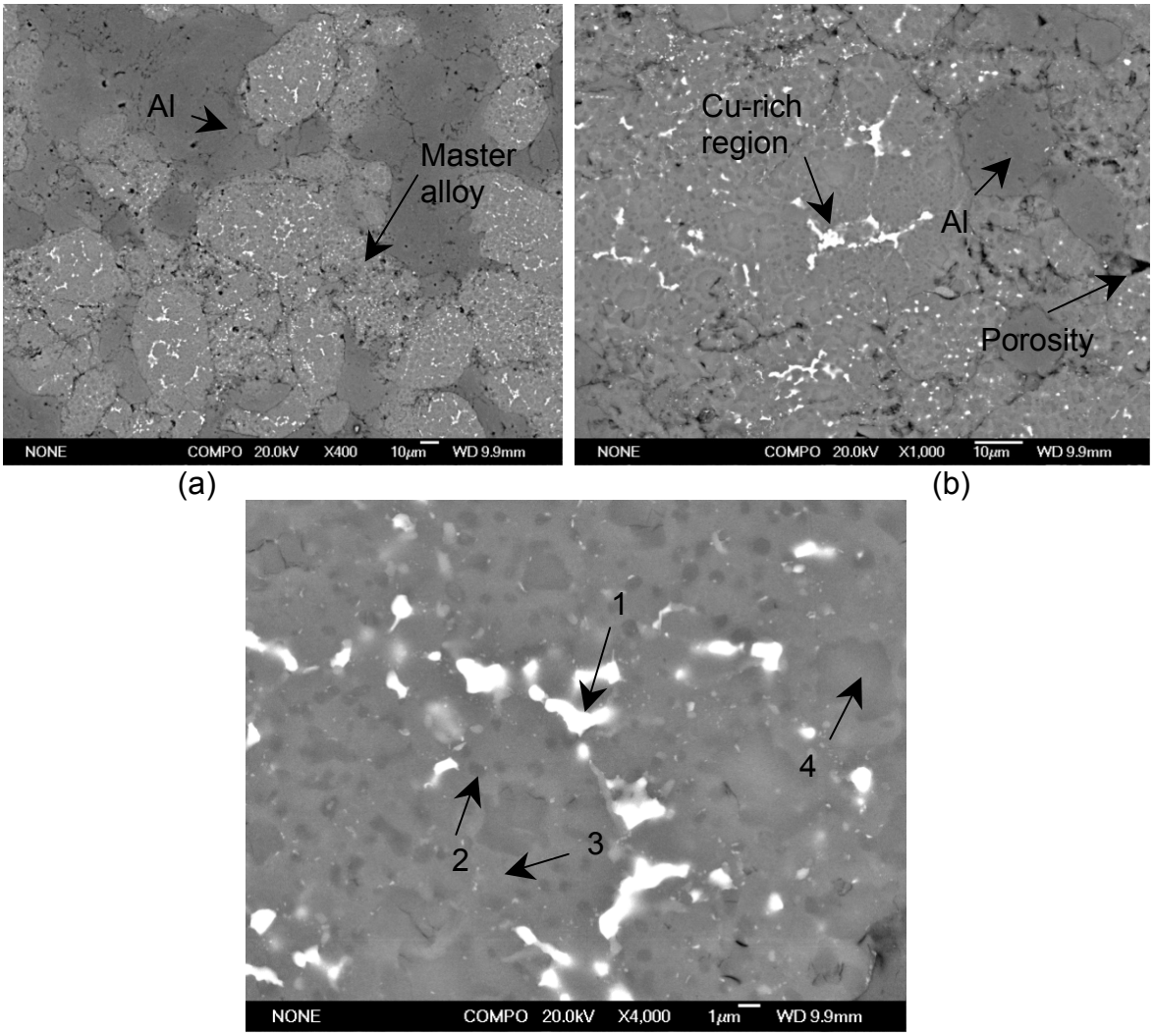

Figure 4.10. Backscattered electron micrograph for compact sintered at 508ºC at different magnifications: (a) 400X (b) 1000x and (c) 4000X .

.

Table 4.7: EDX results corresponding to the point locations shown in Figure (at%)

Point	Al	Si	Cu	Mg	Fe
1	80.38	4.34	12.43	1.98	0.88
2	66.11	32.26	1.17	0.47	0.00
3	83.84	12.80	2.35	1.01	0.00
4	18.11	81.55	0.34	0.00	0.00

When the temperature reached 521^{0}C, most of the microstructural changes still occurred within the master alloy powder particles. At this stage, Cu-rich region (bright area) completely fragmented into small droplets. Some of Cu had diffused either into the liquid phase or into the Al matrix which marked a decrease of copper content within the master alloy as obtained from the EDX results shown in Table 4.8. Clustering of the Si particles started to take place. The fine dispersion of Si particles as observed at 508^{0}C clustered together to form larger Si particles. It is anticipated that the growth of Si particles occurred simultaneously with the increase in the sintering temperature due to the diffusion controlled Ostwald ripening. The amount of Si within the matrix phase in master alloy particles (Point 4) started to decrease as more silicon diffused out and precipitated on the large Si particle. Apart from the growth of the Si particle, the needle-like phase (Point 1) with traces of iron impurities being detected started to appear as shown in Figure 4.11(c). This can be associated with the segregation of Fe due to their low solubility in the Al matrix.

It has been determined previously that densifcation of Ecka Alumix 231 occurred simultaneously with the increase of the sintering temperature. Figure 4.12 illustrated the microstructural changes of Ecka Alumix 231 when subjected to different sintering temperatures: 500ºC, 547ºC, 555ºC, 560ºC, 563ºC and 566ºC. The microstructural development was focused on compacts sintered under nitrogen atmosphere since nitrogen atmosphere was deemed to produce compacts with better densification.

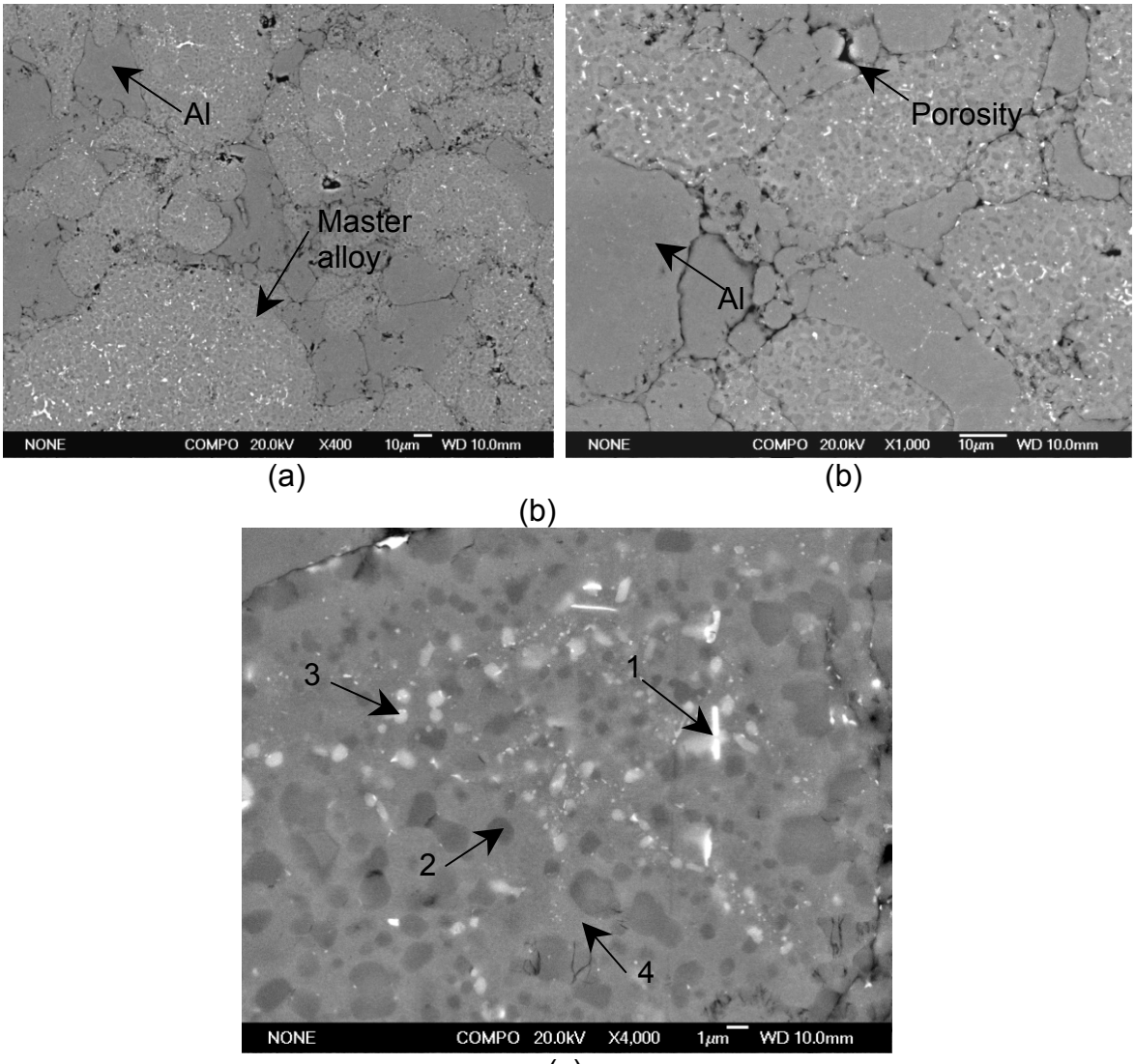

Figure 4.11. Backscattered electron micrograph for compact sintered at 521ºC at different magnifications: (a) 400X and (b) 1000X and (c) 4000X

Table 4.8: EDX results corresponding to the point locations shown in Figure (at%)

Point	Al	Si	Cu	Mg	Fe
1	78.92	8.74	6.44	4.02	1.88
2	58.51	38.66	1.26	1.57	0.00
3	76.00	14.79	3.06	5.95	0.21
4	85.16	10.94	2.11	1.55	0.00

From Figure 4.12 (a), it can be seen that at the sintering temperature of 500ºC, the bright area denoted the Cu-rich region which can be observed within the master alloy powder in green compact started to break from the web-like shape. No remnants of liquid phase can be observed and the Cu rich regions started to diffuse into the grey Al matrix as a result of solid state sintering. The presence of large amount of porosity within the compacts indicated the absence of liquid phase. Thus, liquid phase sintering plays a vital role in densification of the compacts.

As the sintering temperature increased to 547^0C, dramatic microstructural changes can be observed as shown in Figure 4.12 (b). The fine dispersion of Si particles was no longer existed. The necking between the powder particles became more obvious. The liquid phase started to spread between the particles and subsequently eliminated the presence of the small pores. Nevertheless, large pores were still visible as a consequence of particle rearrangement during the liquid phase sintering. At this stage, the needle-like Cu-rich precipitates within Al matrix were observed.

Figure 4.12 (c) illustrated the microstructure of the compact sintered at 555ºC. The formation of a necklace-like structure along the grain boundaries became more apparent. Extensive formation of the liquid phase further aids in the densification and pores elimination with only a small amount of residual porosity being observed. The Cu-rich region which appeared as bright necklace-like structure

decorated along the grain boundaries. The Si-rich regions were found to cluster around the grain boundary.

Degree of densification increases in parallel with the increase in sintering temperature. When the compact was sintered up to 560ºC, a well sintered microstructure can be obtained as shown in Figure 4.12 (d). Grain structure of compacts was fully developed with Cu-rich regions surrounding the grain boundaries. The Si-rich clusters were again observed at the vicinity of the grain boundaries. This can be attributed to the low solubility of Si in the Al matrix. The grain growth became more apparent since an increase in grain size as compared to the previous temperature step was observed. It is anticipated that solution-reprecipitation started to dominate at this stage.

The general microstructure of the compact did not differ much from that of the 560^0C temperature step when compacts sintered at 563ºC. Formation of an abundance of liquid phase with high copper content continued to be observed at the grain boundaries. The primary silicon crystal had relatively grown in size as compared to those observed in previous temperature step. The microstructure of the compacts sintered at 566^0C exhibited similar characteristic to those obtained at 560^0C and 563^0C. Formation of the large liquid coalescence areas was again observed at this temperature step. The only notable difference is mean grain size increased as a result of grain growth due to grain coalescence and grain coarsening. The primary silicon also coalesced to form large aggregates.

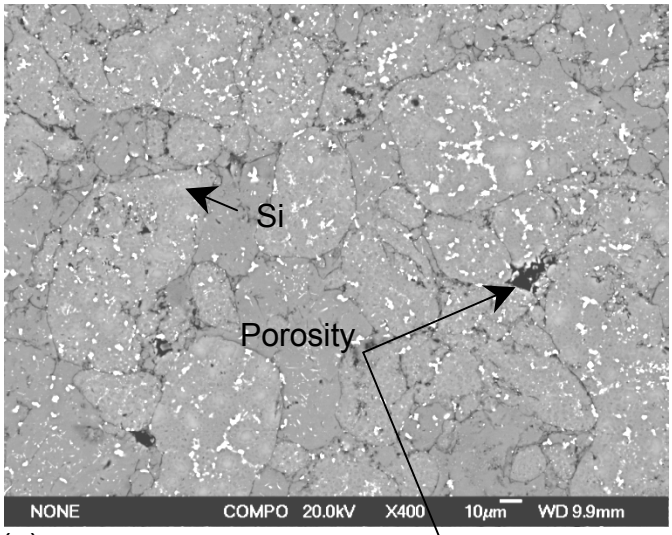

(a)

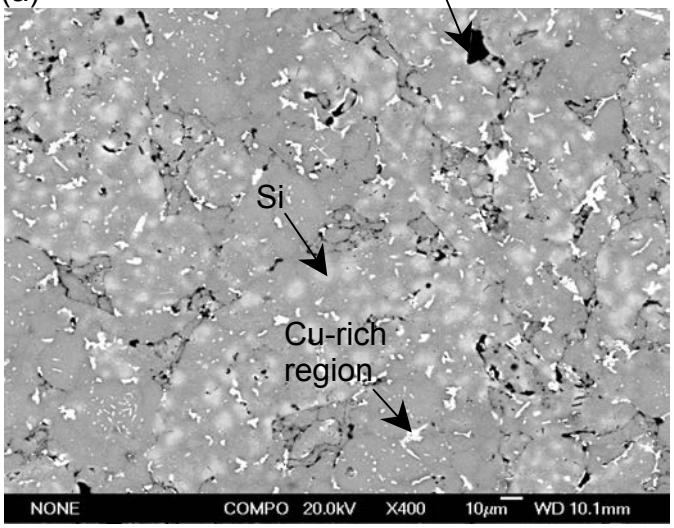

(b)

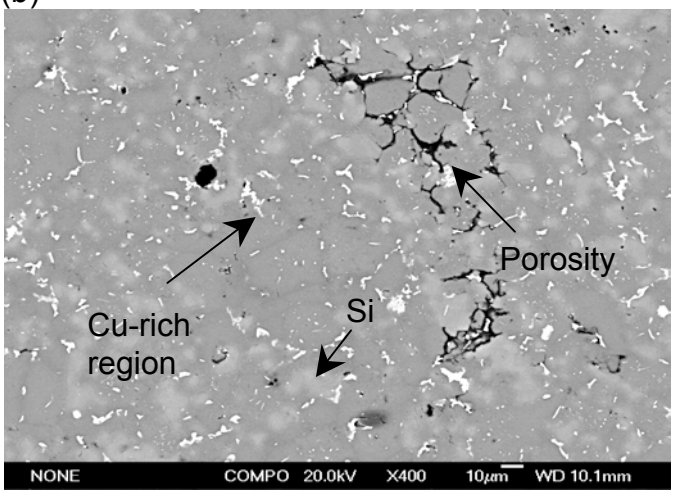

(c)

Figure 4.12 : Microstructures of compacts sintered at different sintering temperatures under nitrogen atmosphere (a) 500 ºC (b) 547 ºC (c) 555 ºC

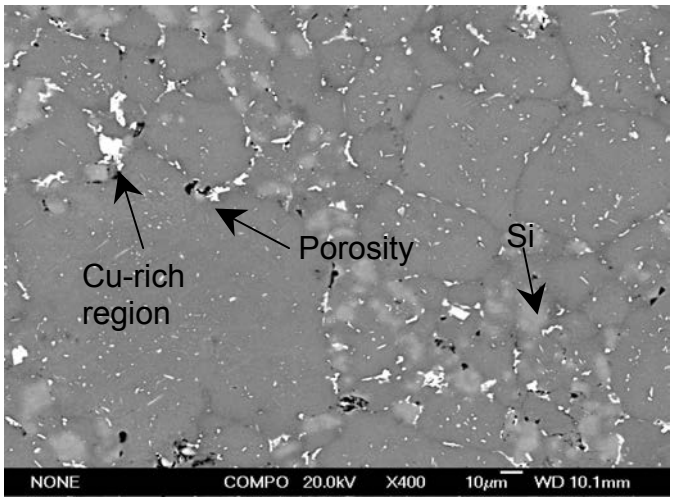

(d)

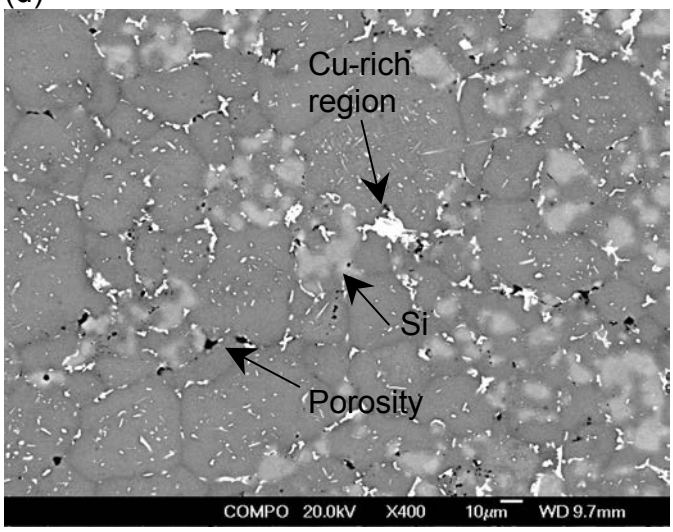

(e)

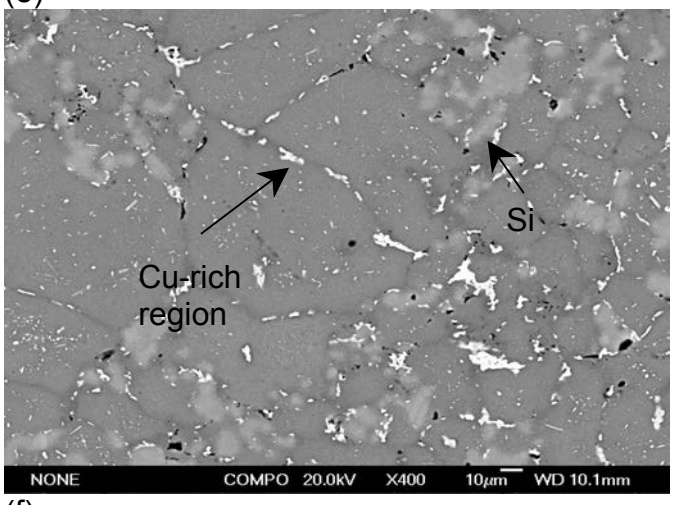

(f)

Figure 4.12 (continued): Microstructures of compacts sintered at different sintering temperature under nitrogen atmosphere (d) 560ºC (e) 563ºC (f) 566ºC

4.7.2 Microstructural Change at Different Sintering Atmospheres

4.7.2.1 Nitrogen Atmosphere

It had been previously disccussed in Section 4.5.2 that nitrogen atmopshere was more efficacious as compared to other sintering atmospheres since it produced compacts with higher densification. Densification of compacts very often can be evidenced from the microstructures features of the sintered compacts. Figure 4.13 displays the backscattered micrographs for compacts sintered under nitrogen atmosphere. It can be observed that the porosity of the nitrogen sintered compacts was largely eradicated within the centre of the compacts as displayed in Figure 4.13 (a). The outer surface of the compact as shown in Figure 4.13 (b), however, was found to have large porosity. This is mainly due to the self-gettering effect occurred at the outer surface of the compact.

The bright area which associated with Cu-rich region was distributed at grain boundaries and some had diffused and precipitated within the Al matrix. The composition of this area (Point 1) was summarized in Table 4.9. Traces of liquid pool can be noted around the grain boundaries (Point 2). This liquid pool had composition close to Q phase ($Cu_2Mg_8Si_6Al_5$). Apart from formation of Q phase, Fe-rich region (Point 4) was found to segregate at the grain boundaries which can be associated with precipitation of $FeSiAl_5$.

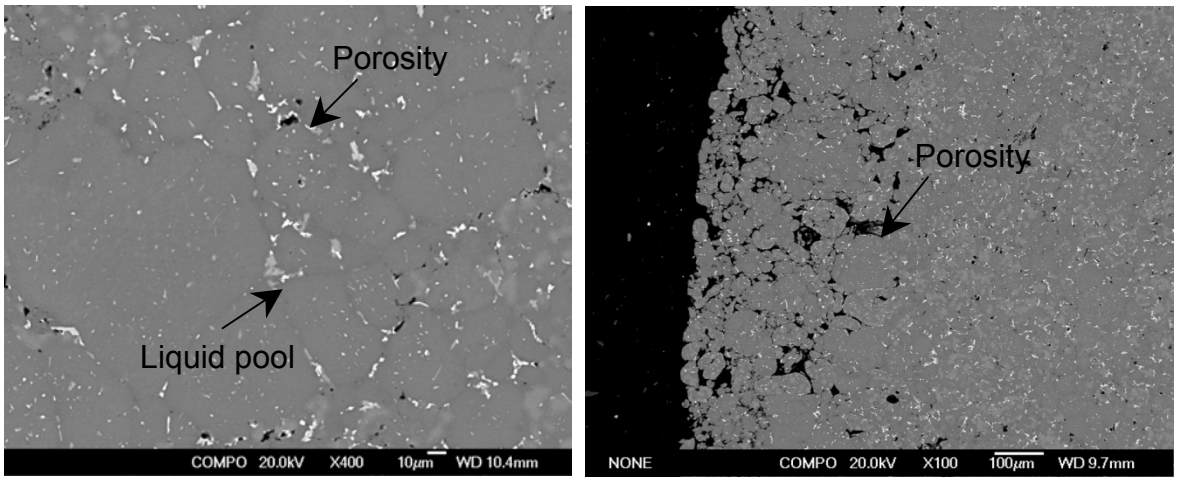

(a) (b)

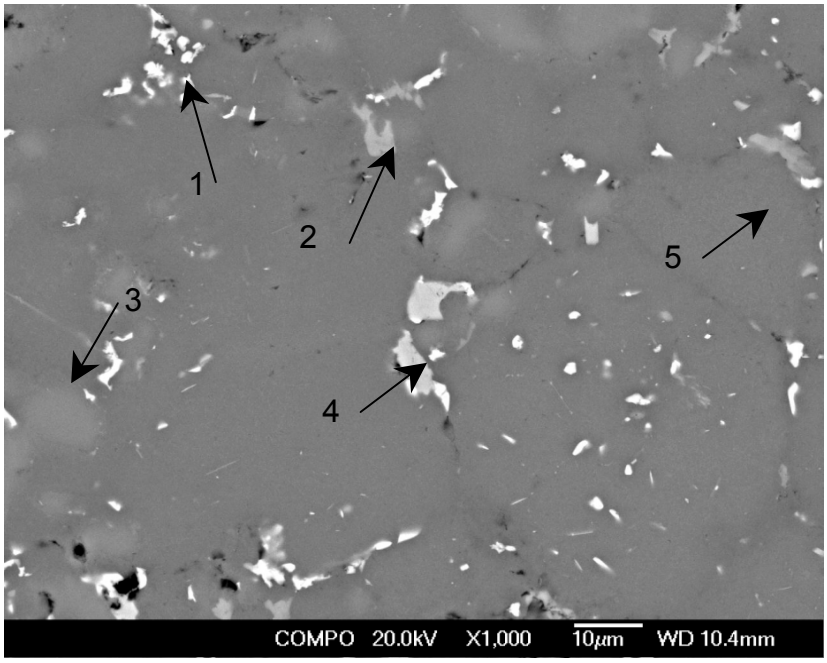

(c)

Figure 4.13. Backscattered electron micrograph of Al-15Si-2.5Cu-0.5Mg sintered at 560°C in nitrogen atmosphere with (a) 400X magnification at the centre and (b) 100X magnification at the outer surface and at (c)1000X magnification at the centre of the compact

Table 4.9: EDX results corresponding to the point locations shown in Figure 4.13 (at%)

Point	Al	Si	Cu	Mg	Fe
1	75.39	5.71	16.69	2.21	0.00
2	30.18	35.27	6.54	28.01	0.00
3	2.13	97.62	0.25	0.00	0.00
4	67.55	18.42	0.57	0.00	13.47
5	98.65	0.67	0.68	0.00	0.00

4.7.2.2 Vacuum Atmosphere

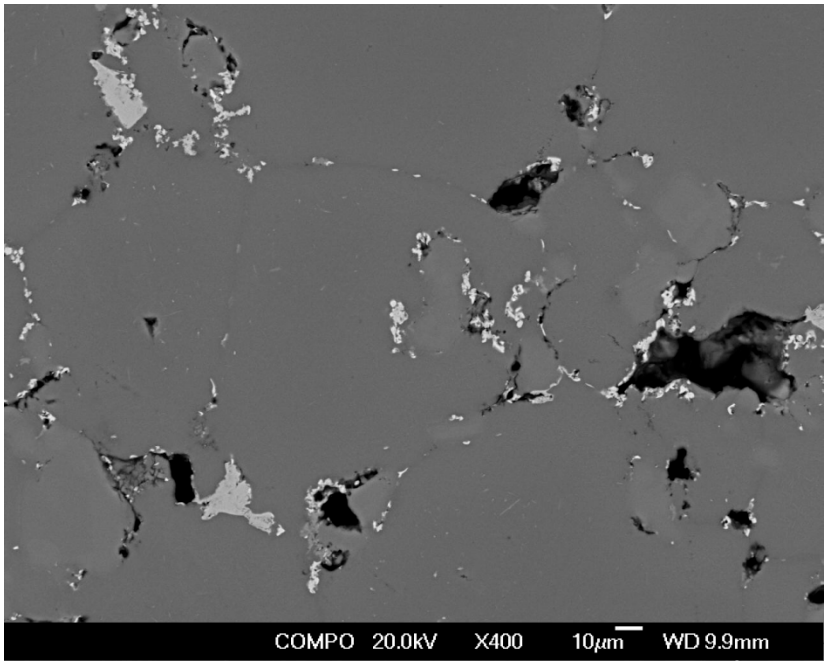

(a)

Figure 4.14. Backscattered electron micrograph of Al-15Si-2.5Cu-0.5Mg sintered at 560°C in vacuum atmosphere at (a) 400Xmagnification

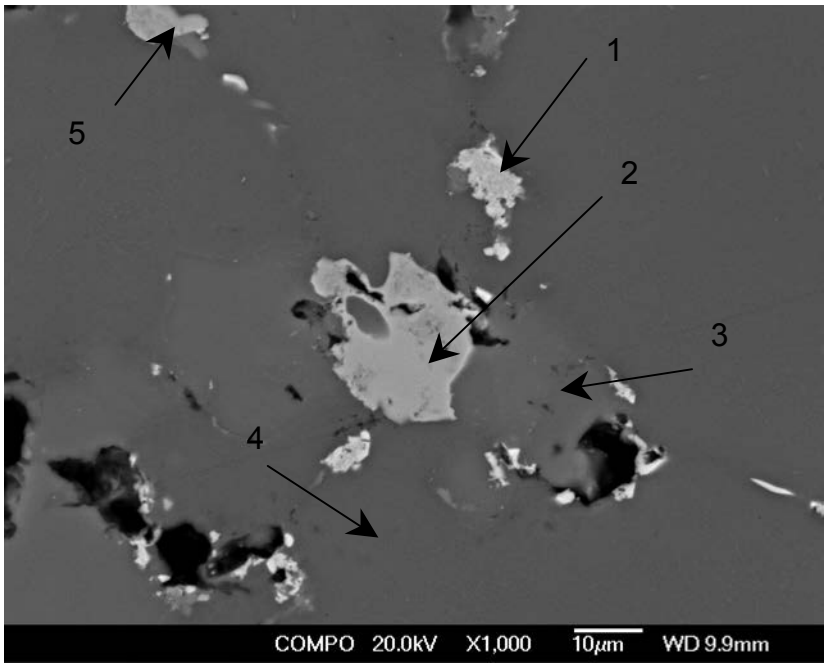

(b)

Figure 4.14 (continued). Backscattered electron micrograph of Al-15Si-2.5Cu-0.5Mg sintered at 560°C in vacuum atmosphere at (b) 1000X magnification

Table 4.10: EDX results corresponding to the point locations shown in Figure 4.14 (at%)

Point	Al	Si	Cu	Mg	Fe
1	75.84	0.96	21.50	1.69	0.00
2	67.95	12.37	3.85	0.00	15.82
3	0.66	99.34	0.00	0.00	0.00
4	97.55	1.20	1.25	0.00	0.00
5	50.09	22.86	5.83	21.22	0.00

Figure 4.14 displays the microstructures of compacts sintered under vacuum condition. Although compacts sintered under vacuum condition obtained significant densification, large visible pores with the sizes ranging from 12-59μm can still be found. Comparatively, the mean pore size for compacts sintered under vaccum condition (31 μm) was found to be larger than compact sintered under nitrogen atmopshere with the mean pore size of 15 μm.

There was very limited spreading of the liquid around the grain boudaries. The necklace-like structure along the grain boundaries as observed in compact sintered in nitrogen atmosphere was not observed in the vacuum sintered compact. Instead, they formed segregation at the grain boundaries indicated by Point 1 and Point 5 as shown in Figure 4.14(b). The composition of these two point were analyzed using the EDX and summarized in Table 4.10. Point 1 and Point 5 can be associated with the formation of Al_2Cu (θ) and Q phase ($Cu_2Mg_8Si_6Al_5$) respectively. The Fe-rich region (Point 2) were again detected in vacuum sintered compact. Silicon (Point 3) was found to segregate mainly at vicinity of the pores. By comparing the size of the silicon, compacts sintered under vaccuum condition obtained larger silicon crystals (approximately 81μm) with the composition near to pure silicon. Grain coarsening can be observed which can be associated with Ostwald ripening.

4.7.2.3 Nitrogen with 3% Hydrogen Atmosphere

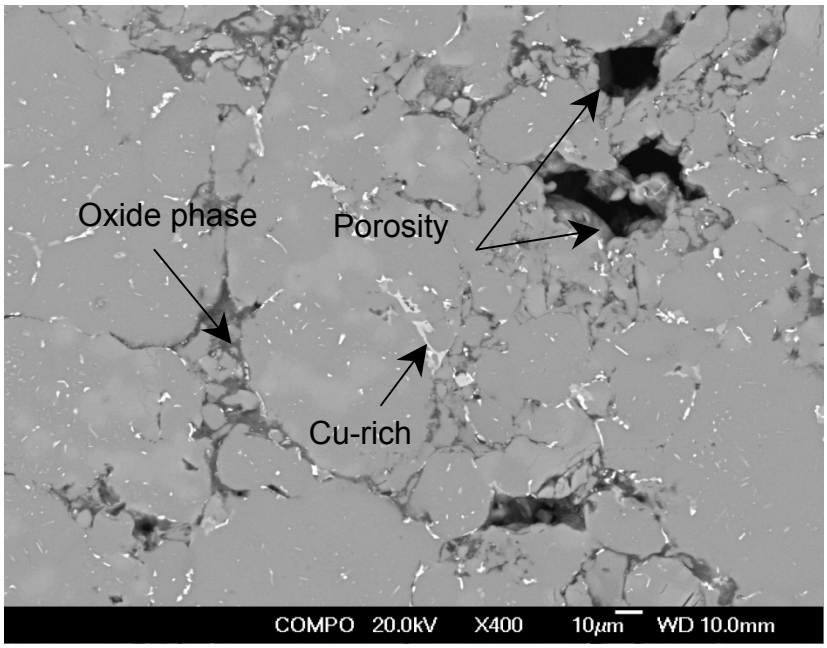

Figure 4.15. Backscattered electron micrograph of Al-15Si-2.5Cu-0.5Mg sintered at 560°C in nitrogen with 3% hydrogen atmosphere at (a) 400Xmagnification

Figure 6.15 depicts the backscattered micrograph of compacts sintered in the nitrogen with 3% hydrogen atmosphere. In the earlier studies on compact densification, compact sintered under nitrogen with the presence of 3% hydrogen did not result in any significant densification. Compact swelling, however, occurred. From the microstructure as displayed in Figure 6.15, it can be seen that solid grains are in poor contact with each other. The particles boundary can still be observed. Coupled with the presence of large porosity, compact exhibited poor sintering behavior. Moreover, limited segregation of liquid pools at the grain boundaries was noted. Cu-rich region had limited diffusion into the immediate vicinity of aluminum matrix. Compacts did not exhibit good wetting characteristic. Presence of the oxide-rich phase can be evidenced from composition mapping as

displayed in Figure 4.16. The oxide layers later hindered the diffusion during liquid phase sintering.

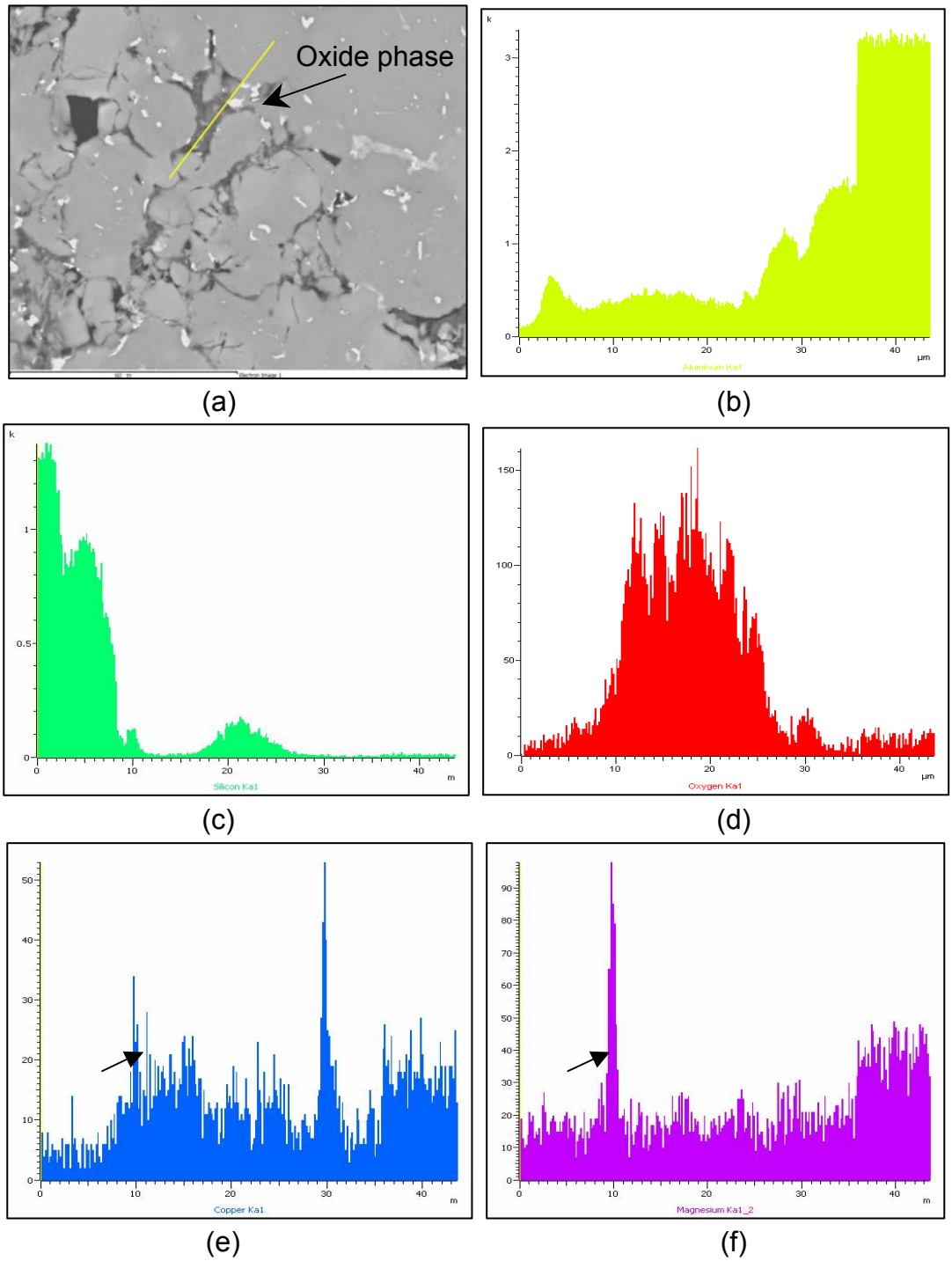

Figure 4.16. (a) Backscattered electron micrograph of compact sintered in nitrogen with 3% hydrogen atmosphere with composition mapping for (b) Aluminum, (c) Silicon, (d) Oxygen (e) Copper, and (f) Magnesium

4.7.3 Microstructural Change at Different Sintering Times

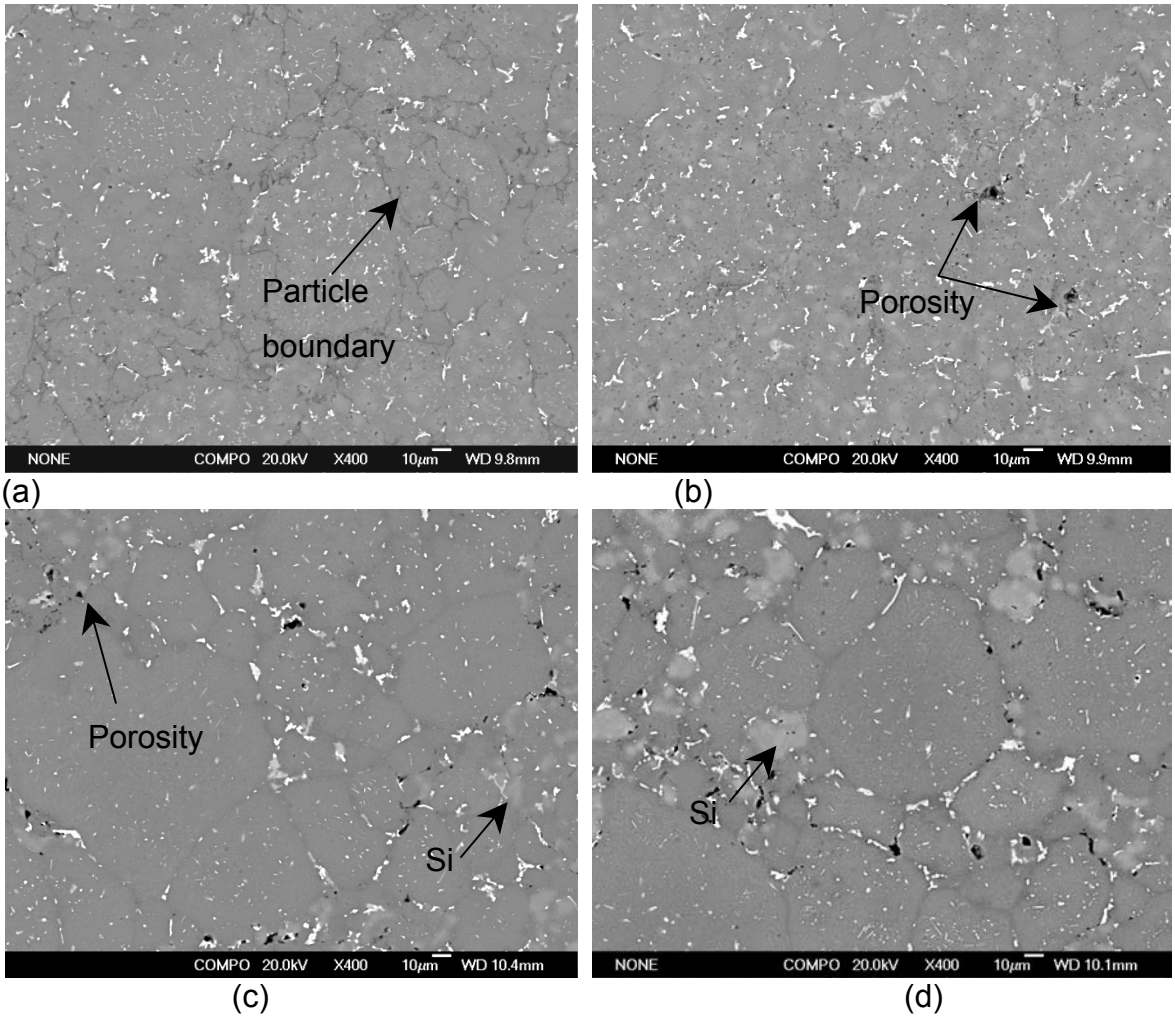

Figure 4.17. Backscattered electron micrograph of Al-15Si-2.5Cu-0.5Mg sintered at 560°C in nitrogen atmosphere for (a) 30 minutes, (b) 45 minutes, (c) 60 minutes and (d) 90 minutes

Control of sintering time is crucial to allow sufficient time for the sintering process to complete in order to attain well-sintered microstructure with better pore closure. Four different sintering times were investigated in this study: 30, 45, 60 and 90 minutes. Figure 4.17(a)-(d) displays the microstructure of the compacts sintered at different sintering times.

It can be seen that sintering time of 30 minutes was not sufficient to allow the liquid phase sintering to complete since particle boundary can still be clearly seen in Figure 4.17 (a). With the increase of the sintering time up to 45 minutes, the microstructure of the compacts exhibited similar characteristic as the compact sintered at 60 minutes, except some small pores can still be noted. Though the microstructures of the compacts sintered at longer sintering time up to 90 minutes did not have remarkable change compared to the compacts sintered at 60 minutes, grain coarsening started to take place. It is therefore determined that 60 minutes of sintering time will be sufficient to attain well-sintered microstructure.

4.8 Influence of Processing Conditions on Mechanical Properties

4.8.1 Effects of Sintering Temperatures on Mechanical Properties

Volume fraction of liquid has influential effects on sintering. To investigate further on the effects of sintering temperature on mechanical properties, the Vickers hardness and porosity of the compacts sintered under nitrogen atmosphere at different liquid content were measured. Figure 4.18 shows that an increase of the liquid content will result in an increase of the hardness value. The increase of the hardness value occurred simultaneously with the increase of the sintered density. It can be seen that compacts underwent substantial increase in both sintered density and hardness value when the liquid content increased to 10%. Though the sintered density started to level off after 15% of the liquid content, the hardness value continued to increase but at a slower rate.

Meanwhile, the changes in porosity for compacts sintered at different amount of liquid phase were displayed in Figure 4.19. It can be noted that the nitrogen sintered compacts achieved the highest sintered density with the lowest percentage of porosity at 15% liquid phase. Thus, it can be summarized that compact sintered at 15% liquid phase which is equivalent to 560°C will be the optimum sintering temperature to obtain compact with highest hardness value and lowest porosity value.

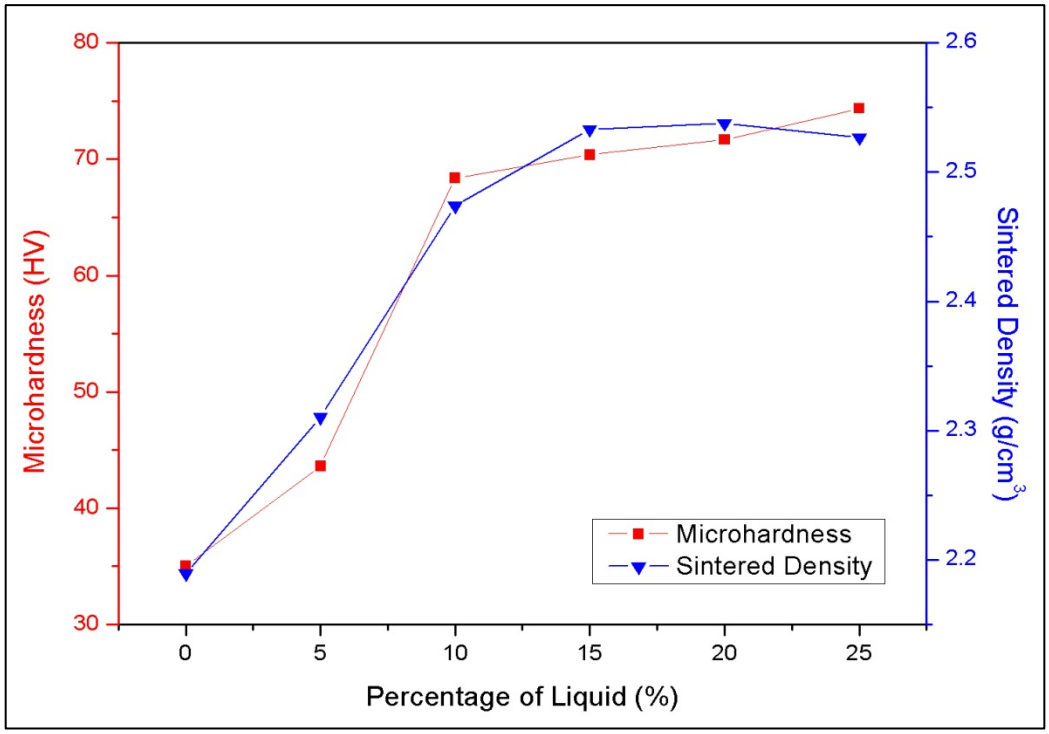

Figure 4.18. Vickers hardness and sintered density for compacts sintered under nitrogen atmosphere at different liquid content

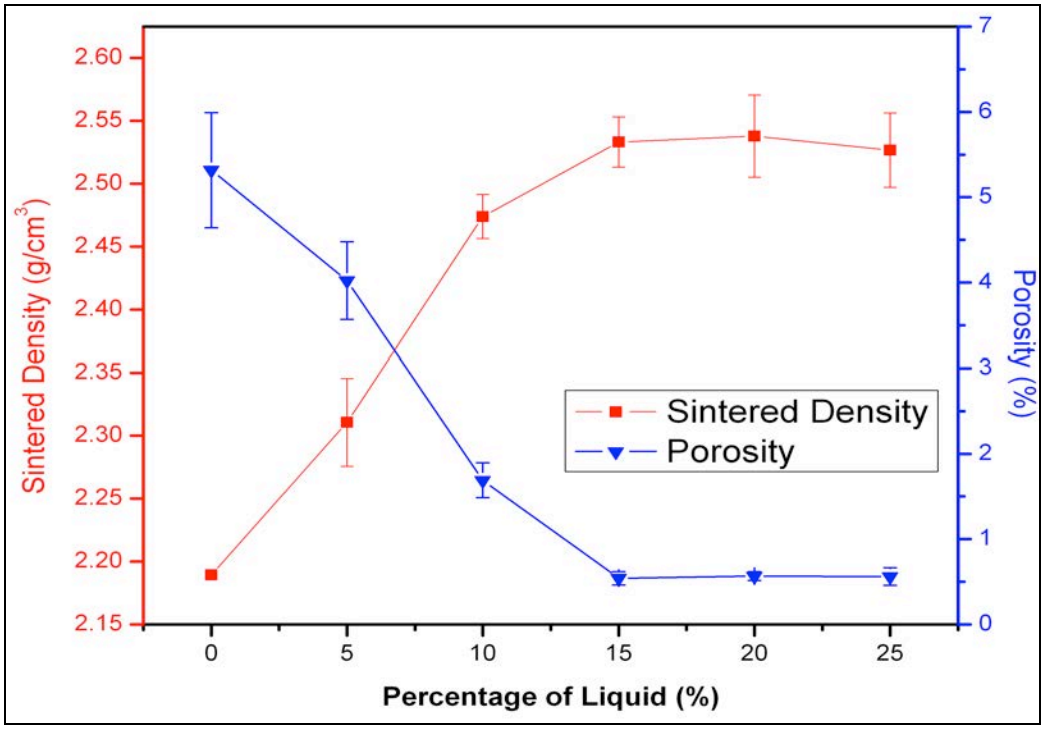

Figure 4.19. Porosity and sintered density for compacts sintered under nitrogen atmosphere at different liquid content

4.8.2 Effects of Sintering Atmospheres on Mechanical Properties

A summary of mechanical properties for compacts sintered in different sintering atmospheres was shown in Table 4.11. Compacts sintered in nitrogen condition had the hardness value (Hv) in close proximity to those sintered in vacuum condition. However, the large differences arised in terms of elastic modulus, tensile strength and ductility of the compacts was believed due to the presence of large porosity as shown in Figure 4.14(a). Compacts sintered in nitrogen with 3% hydrogen atmosphere, however, yielded undesirable mechanical properties. Figure 4.20 depicts the porosity level of compacts sintered at different sintering atmospheres. Pore evolution depends very much on sintering atmospheres. Nitrogen atmosphere is the optimum sintering atmosphere which produces compacts with less than 0.6% porosity, whereas presence of hydrogen in sintering atmosphere leads to swelling of compacts and marked the highest amount of porosity within the compacts.

Table 4.11. Mechanical properties for compacts sintered under different sintering atmosphere

Sintering Atmosphere	E (GPa)	UTS (MPa)	Ductility (%)	Vickers Hardness (Hv)
Nitrogen	55.83 ± 2.94	139.63 ± 1.08	1.68 ± 0.02	70.4 ± 1.14
Vacuum	29.06 ± 1.05	92.48 ± 2.18	0.59 ± 0.07	69.6 ± 1.02
Nitrogen /3% hydrogen	25.59 ±1.11	30.20 ± 1.01	0.16 ± 0.01	38.5 ± 1.07

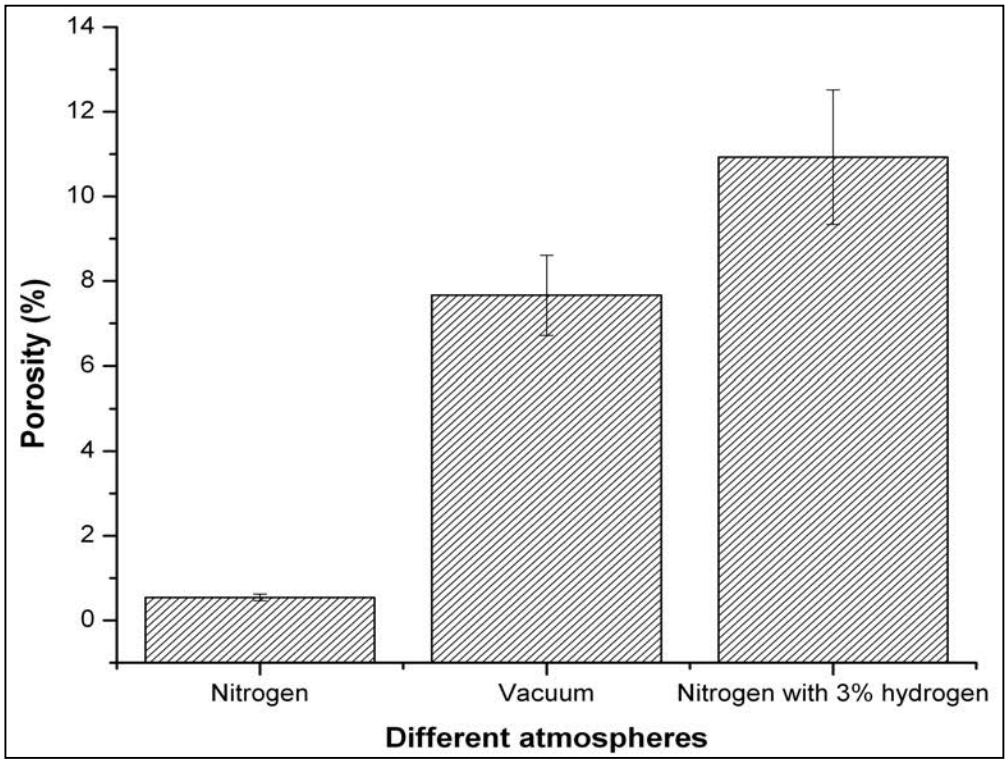

Figure 4.20. Porosity of the compacts sintered under different sintering atmosphere

4.9 X-ray diffraction Analysis

XRD analyses were performed to verify the phases presented within the compacts sintered at different sintering atmospheres. From Figure 4.21(a), it can be summarized that changes in sintering atmospheres will not result in any significant influence in terms of the phase transformation. Compacts sintered under different sintering atmospheres showed identical XRD pattern. A more detailed XRD analysis was conducted for compacts sintered under nitrogen atmosphere as displayed in Figure 4.21(b). The positive phases being detected were α- Al , Si, $CuAl_2$ phase (θ) and Q phase ($Cu_2Mg_8Si_6Al_5$.).

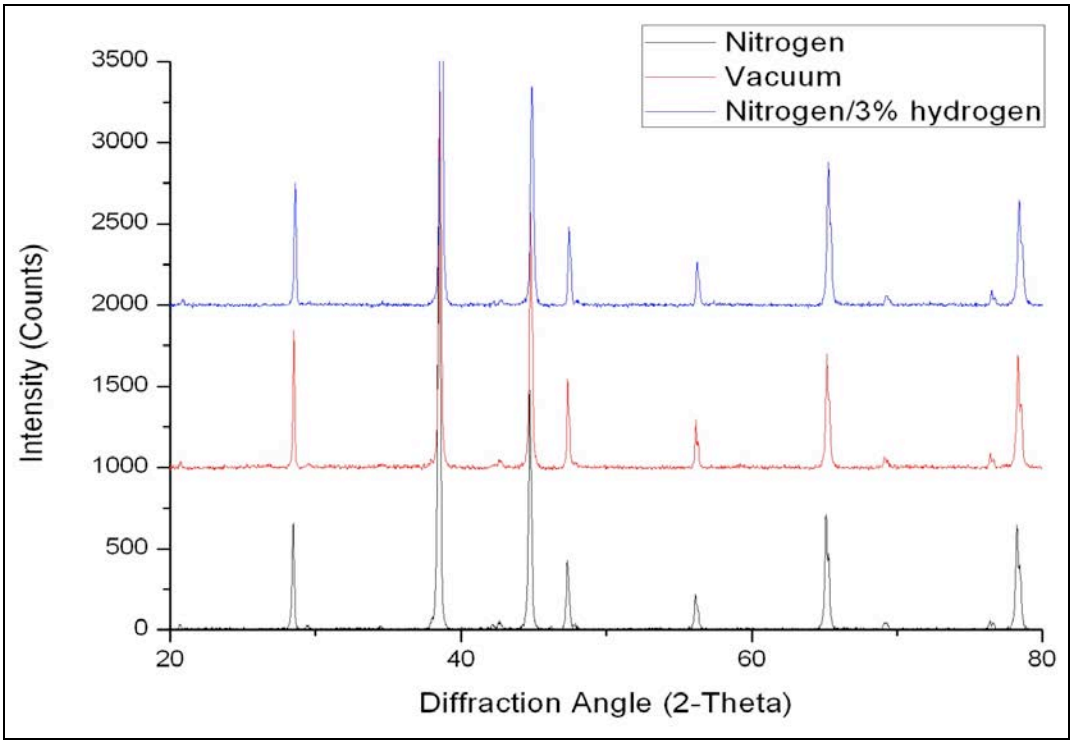

(a)

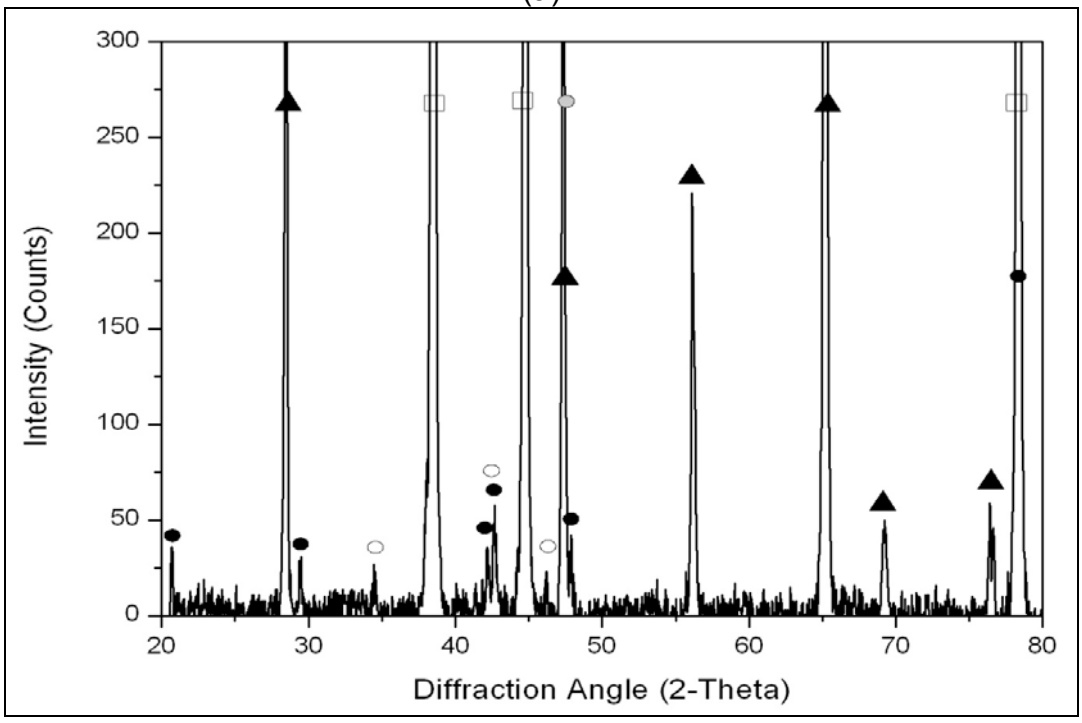

(b)

Figure 4.21. (a) Overall XRD pattern for compacts sintered under different sintering atmospheres and (b) Detailed XRD pattern corresponding to Ecka Alumix 231 sintered in nitrogen atmosphere. Phases positively identified were α- Al (□), Si (▲), θ phase (●) and Q phase (○).

4.10 Thermo-Calc Calculations

As mentioned previously in Section 4.2, Ecka Alumix 231 is comprised of a mixture of elemental powder and master alloy with the composition of Al-28Si-5Cu-1Mg (wt%). With the increase of the sintering temperature, a series of thermal events can be noted from the DSC traces as shown in Figure 4.5. Thermo-Calc software was used to analyze the constituent phases presented at different temperatures. Metallographic observations as displayed previously in Section 4.7.1 showed that the microstructural change occurred mainly within the master alloy during the initial stage of sintering. Thus, the equilibrium diagram of Al-28Si-5Cu-1Mg (wt%) as presented in Figure 4.22(a) was used to gain some understandings of the thermal events during the initial stage of sintering. It had been calculated that the onset of liquid phase formation started at 510°C. This came in close proximity to the onset of the first melting peak of 505°C as observed in DSC traces (Figure 4.5). The melting event taking place at this temperature was suggested to be [3]:

$$FCC + Al_2Cu + Si + Cu_2Mg_8Si_6Al_5 \rightarrow Liquid \qquad (4.1)$$

As the chemical homogenization proceeded with the diffusion and redistribution of Cu, Mg and Si, the composition of the compact approached the overall composition of Al-15Si-2.5Cu-0.5Mg (wt%). As a result, the thermodynamic diagram of Al-15Si-2.5Cu-0.5Mg (wt%) as displayed in Figure 4.22(b) was applied to study the subsequent melting reactions. Liquid formation was calculated to initiate at 526°C. This was corresponding to the second melting peak as observed in Figure 4.5. It was anticipated that the melting reactions involved [3]:

$$FCC + Al_2Cu + Si \rightarrow Liquid \quad (4.2)$$

and /or

$$FCC + Al_2Cu + Si + Fe\ SiAl_5 \rightarrow Liquid \quad (4.3)$$

As the heating temperature increased, Al_2Cu (θ phase) and $Cu_2Mg_8Si_6Al_5$ (Q phase) completely melted. Meanwhile, FCC Aluminum rich solid and Si particles continuously dissolved into the liquid. At approximately 570°C, FCC Al completely dissolved into the liquid while the remaining silicon particles continued to melt until the alloy was fully molten at the temperature of 622°C

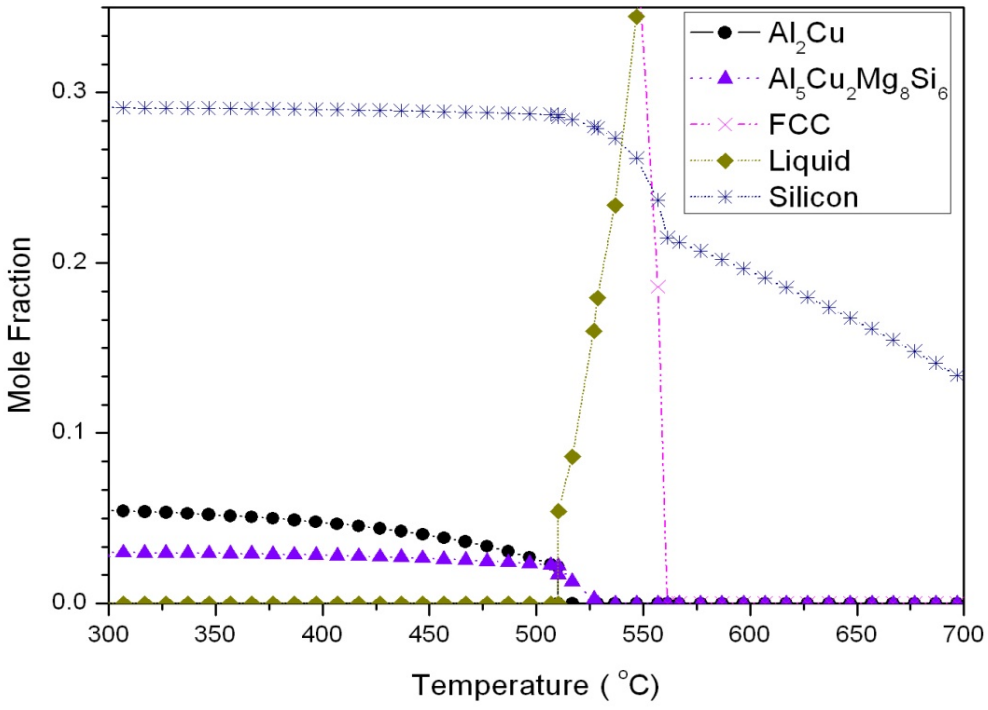

(a)

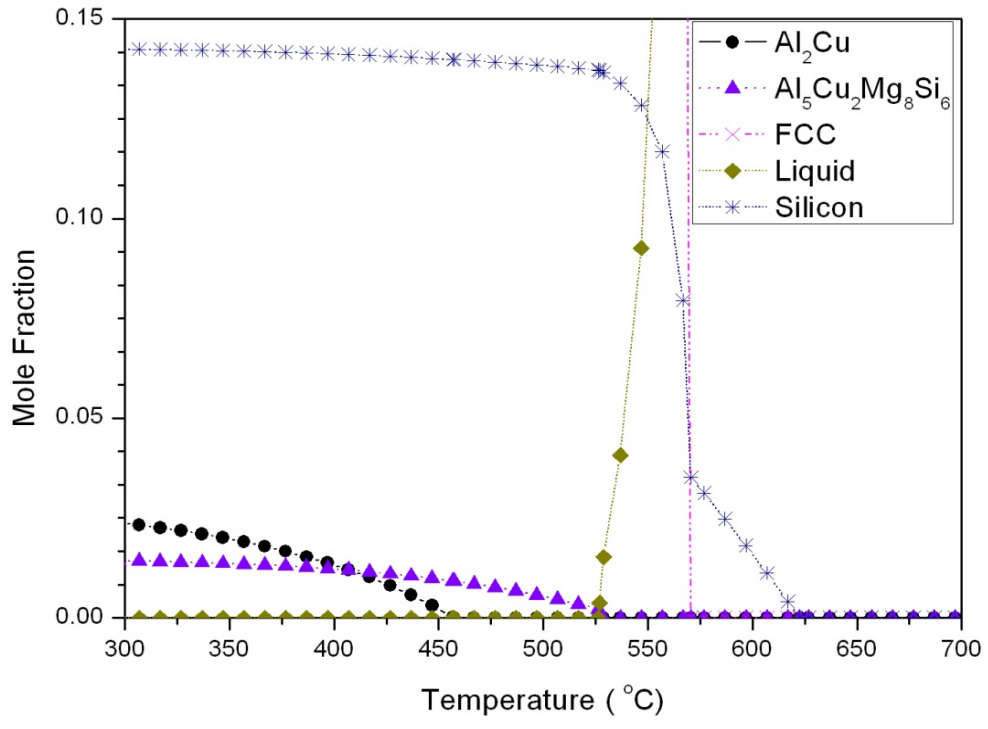

(b)

Figure 4.22. Calculated fraction of phases vs temperature for the composition of (a) Al-28Si-5Cu-1Mg (wt%) and (b) Al-15Si-2.5Cu-0.5Mg(wt%)

4.11 Discussions

4.11.1 Compaction behavior of Ecka Alumix 231

Powder compressibility is usually the first criterion to assess in order to determine the suitable compaction pressure to be applied in the subsequent studies. Compaction will result in increased number of particle-to-particle contacts as the particles flatten and form planar contact interface [5]. The compressibility curve for Ecka Alumix 231 presented graphically in Figure 4.4 showed that green density of the compact increased with the increase of the compaction pressure. Compacts with green density of 2.27g/cm^3 (85.30% of theoretical density) was obtained at the compaction pressure of 400MPa above which there was little densification occurred.

The response of powder during uniaxial compaction occurred in a few stages: rearrangement, deformation and finally bulk compression [6]. The result displayed in Figure 4.4 showed good agreement with the theory outlined by German. It can be noted that when the compaction pressure increased up to 200MPa, densification of the green body achieved 2.02g/cm3 or 75.78% of the theoretical value. This is mainly due to the transitional repacking whereby interparticle sliding took place and particles underwent rearrangement. Localized deformation was expected to occur at the contact points of particles and deformation started to spread through the contact region [6].

The subsequent increase of the compaction pressure from 200MPa to 400MPa marked a substantial increase in green density of the compact from 75.58% to

85.30% of the theoretical density. The densification rate was relatively large at this stage. The increase of the compaction pressure leads to plastic deformation of the particles. Figure 4.2(b) showed that large particle interlocking occurred and frictional welding of the particles at the compaction pressure of 400MPa can be observed. It is anticipated that at this stage, oxide films on particle was broken which will later aid the compaction densification during liquid phase sintering.

With the further increase in compaction pressure, the compaction densification became less profound. Compact densification was relatively slow at this stage since the increase in green density only marked a 2% increase of the theoretical density when the green bodies were compacted up to 600MPa. This stage can be attributed to bulk compression. Further increase in compaction pressure resulted in an increase work hardening of the aluminum particles due to plastic deformation. This subsequently reduced further deformation within the compacts. Thus, only small increment in green density can be noted at higher compaction pressure.

The compressibility of Ecka Alumix 231 was also studied using Heckel relationship following the equation (4.4) below [7]:

$$In\left(\frac{1}{1-D)}\right) = KP + A \qquad (4.4)$$

where K and A are constants, D and P are relative density in fraction and compaction pressure respectively. Figure 4.23 displays the plot of Heckel relationship between In(1/(1-D)) and compaction pressure. The initial curvature

was observed at lower compaction pressure which was due to the particle sliding and rearrangement [7, 8]. This was subsequently followed by linear relationship whereby compaction densification occurred due to plastic deformation. The yield strength of powder slope was determined from the slope of the regression line using the equation (4.5) below [7]:

$$K = \frac{1}{3\sigma} \qquad (4.5)$$

It has been calculated that the yield strength for Ecka Alumix 231 powder was 140.64MPa. In Section 4.2, it had been discussed that Ecka Alumix 231 powder was a mixture of both elemental Al powder and master alloy Al-28Si-5Cu-1Mg. Since Al powder generally exhibited the yield strength within the range of 20 to 105MPa [9], it was anticipated that presence of master alloy contributed to higher yield strength of the compacts.

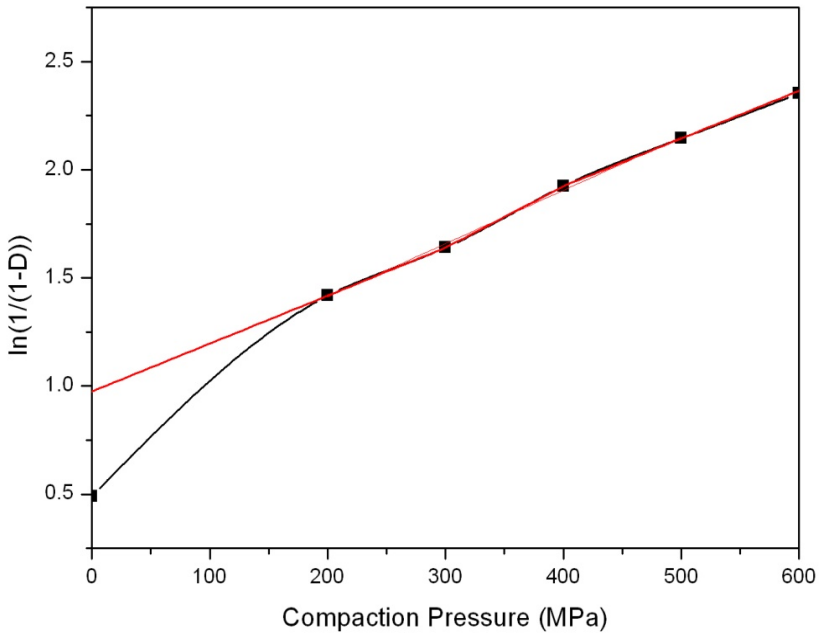

Figure 4.23. Heckel plot of ln(1/(1-D)) vs compaction pressure

4.11.2 The role of sintering atmospheres on Ecka Alumix 231

Presence of surface oxide often poses as a major threat for sintering of aluminum alloys and needs to be disrupted or otherwise removed. Reduction of oxide layer requires a dew point of -140°C or oxygen partial pressure of $<10^{-50}$ atm at 600°C which is not physically attainable [10]. It has been shown that formation of liquid phase can successfully disrupt the oxide layer [11]. Addition of highly reactive magnesium can also enhance the sintering response of aluminum alloys through the formation of spinel $MgAl_2O_4$ which later aids in sintering. The free energy of formation for $MgAl_2O_4$ is more negative than that of the oxides of aluminum. The spinel formation can be shown in the following reaction [12]:

$$3Mg + 4Al_2O_3 \rightarrow 3MgAl_2O_4 + 2Al \qquad (4.6)$$

In this study, both liquid phase sintering and addition of magnesium were incorporated to aid sintering in this alloy. Figure 4.7 displays the sintered densities of Al-15Si-2.5Cu-0.5Mg at different sintering temperatures under three different sintering atmospheres. Compacts sintered in nitrogen condition achieved the highest sintered density at the liquid content of 15%, whereby compacts, sintered in nitrogen with 3% of hydrogen exhibit no significant densification. There is noticeable increase in the relative densification as the liquid phase sintering initiated which is demonstrated by compacts sintered under nitrogen and vacuum condition as tabulated in Tables 4.4 and 4.5 respectively. Similar trend is not observed for compacts sintered under nitrogen with 3% hydrogen atmosphere. The sintered densities, however, decreased slightly with the increase in sintering temperature. Likewise, the relative densification as displayed in Table 4.6 showed

swelling effect with the increase of the liquid formation when compacts sintered in nitrogen with 3% hydrogen atmosphere. Atmosphere indeed plays an active role in sintering of aluminum alloys.

Nitrogen atmosphere seems to be more efficacious as compared to other sintering atmospheres. As discussed previously, addition of magnesium leads to the formation of spinel $MgAl_2O_4$ which later exposed the underlying aluminum metal as shown in reaction (4.6). The beneficial effect of nitrogen might due to the formation of aluminum nitride (AlN) as shown in reaction (4.7) which creates imbalance between the external gas pressure, internal gas pressure within the pores and pressure exerted by liquid meniscus. The pressure difference later induced progressive flow of liquid into the pores [13] as illustrated in Figure 4.23. In other words, pore filling plays a crucial role in the densification of the compacts sintered in nitrogen atmosphere [14].

$$2Al + N_2 \rightarrow 2AlN \qquad (4.7)$$

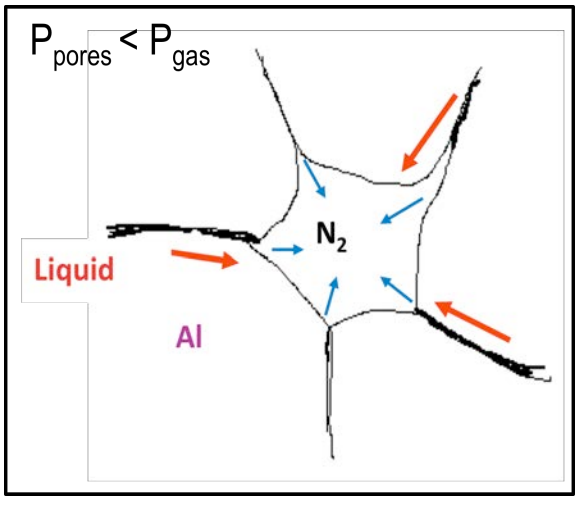

Figure 4.23. Schematic showing pore filling effect when compact sintered in nitrogen atmosphere

Laurent et al. [15] has reported that the contact angle of Al on AlN is found to be 41°, which is half of contact angle of Al on Al_2O_3 when heated to 1273K. Thus, better wettability can be achieved with the formation of AlN. This can be evidenced from the backscattered electron micrograph as shown in Figure 4.13(a), whereby the liquid was well distributed around the grain boundaries. The porosity of the nitrogen sintered compacts was largely eradicated with only approximately 0.6% porosity being noted (Figure 4.20). .

Although compacts sintered under nitrogen attained the highest densification, approximately 450μm thick of outer layer still remained poorly sintered as displayed in Figure 4.13(b). This is mainly due to the self-gettering effect of aluminum alloys. Schaffer and Hall [16] suggested that oxide reduction and aluminum nitride formation also occurred as shown in the reaction (4.8). The poorly sintered outer layer was thus, due to the exposure of compact surface to the oxygen in the fresh gas. The surface layer of the compact served as external getter for the inner layer since the oxygen was consumed faster by the aluminum than it can replenish with the increase of the distance from the compact surface. In other words, the oxygen partial pressure in the gas decreased as it travelled into the pore network and ultimately, becomes low enough for aluminum nitride to form [16].

$$2Al_2O_3 + N_2 \rightarrow 4AlN + 3O_2 \qquad (4.8)$$

Comparatively, the sintered density for compacts sintered in vacuum condition is lower than those sintered in nitrogen atmosphere. Unlike nitrogen atmosphere,

densification of compacts sintered in vacuum condition was not due to formation of AIN which contributed to pore filling effect; instead, particle rearrangement and solution-reprecipitation might play a greater role. The micrographs for both compacts (as shown in Figures 4.13 and 4.14) showed quite a significant difference. Compacts sintered in nitrogen atmosphere has better pore closure with necklace-like liquid pool distributed along the grain boundaries, whereas compacts sintered under vacuum condition had large visible pores and grain coarsening occurred due to Ostwald ripening. Moreover, liquid pool was found to segregate at the grain boundaries. It can be noted that the mean pore sizes for compacts sintered under vacuum condition were relatively larger than those sintered under nitrogen atmosphere.

Showaiter and Youseffi [17] reported similar observation, whereby premixed elemental 6061 Al powder compacts sintered under vacuum condition had lower sintered density and higher porosity than compacts sintered in pure nitrogen conditions. Though significant shrinkage was obtained for Ecka Alumix 231 sintered in vacuum condition as tabulated in Table 4.5, it is suggested that the incomplete elimination of the pores was due to insufficient shrinkage to compensate the swelling due to high solubility of alloying elements (Mg, Si and Cu) during the vacuum sintering process. Coupled with the absence of AIN formation, poor wettability and limited spreading of the liquid phase further lead to higher porosity for compacts sintered under vacuum condition. Since delubrication was carried out at the same time during sintering, the lubricant, Accrawax which was burnt off during the sintering process might not be removed efficiently. The

entrapped gas expanded during sintering with the increase of the temperature and contributed to the formation of large pores [17]. Presence of large pores will lead to degradation of mechanical properties. Although compacts sintered in vacuum condition had the hardness value (HV) in close proximity to those sintered in nitrogen atmosphere, large differences arouse in terms of elastic modulus, tensile strength and ductility of the compacts, which was believed mainly due to the presence of large porosity.

Nitrogen with 3% hydrogen atmosphere, on the other hand, produced compacts with unfavorable sintered densities. Compared with compact sintered under nitrogen atmosphere, presence of hydrogen indeed has deleterious effects on sintering. The question arises as to why the addition of hydrogen to the sintering atmosphere can lead to such a massive difference. The interactions between hydrogen atmosphere and the aluminum alloys, however, remained unclear. Pieczonka et al. (2008) reported that sintering of pure aluminum with the hydrogen volume content of less than 5% critical value in nitrogen/hydrogen mixture did not hinder the densification of the compacts completely [18]. Yet, this does not come in good agreement with the Al-Si-Cu-Mg alloy system used in this study. Figure 4.15 depicts the backscattered micrograph of compacts sintered in the nitrogen with 3% hydrogen atmosphere. The solid grains are in poor contact and this, coupled with the presence of large porosity, denoted the poor sintering behavior of compacts. Schaffer et al. proposed that pore filling mechanism was inhibited in the presence of hydrogen due to the formation of aluminum hydride by either one of the following reactions [14]:

$$2Al + 3H_2 \leftrightarrow 2AlH_3 \quad (4.9)$$

or $$4Al + 6H_2 \leftrightarrow 2Al_2H_6 \quad (4.10)$$

Both reaction (4) and (5) showed that aluminum hydride can decompose easily at temperature above 150°C and thus, created back pressure within the pores which further prevented densification by pore filling. It is noteworthy; however, magnesium has higher affinity than aluminum towards hydrogen. The standard Gibbs free energy ($\Delta G°_f$) for MgH_2 is – 85.42 kJ/mol [19], which suggested a more spontaneous reaction than AlH_3 with $\Delta G°_f$= 48.5 kJ/mol [20]. Thus, MgH_2 is more likely to form than AlH_3 as shown in Equation (4.11) below [13].

$$Mg + H_2 \leftrightarrow MgH_2 \quad (4.11)$$

As discussed previously, oxide layers have detrimental effects on sintering. It can be disrupted either through addition of magnesium or through mechanical mean by compaction. In the case of compacts sintered in nitrogen with 3% hydrogen atmosphere, limited segregation of liquid pools at the grain boundaries was noted. Compacts did not exhibit good wetting characteristic. It is suggested magnesium addition which usually aids in the disruption of oxide layer, formed MgH_2 instead of $MgAl_2O_4$ spinel [13]. Presence of the oxide layers can be evidenced from Figure 4.16. The oxide layers later hindered the diffusion during liquid phase sintering. Since magnesium was used up for the reaction with hydrogen, the inherent oxide layer remained on the aluminum powder, which cannot be disrupted completely by mechanical mean. Thus, it was believed that limited diffusion of Cu (Figure 4.15)

from the Al-Si-Cu-Mg master alloy into the immediate vicinity of aluminum matrix noted poor sintering behavior for compact sintered in nitrogen with 3% hydrogen.

Generally, MgH_2 was considered to be unstable and tends to decompose at higher temperature. The entrapped gas within the pores leads to large porosity as displayed in Figure 4.15. The decomposition reaction will increase the vapor pressure within the pores and cause swelling of the compacts to occur [21]. This can be evidenced by the decrease in relative densification (swelling effect) as displayed in Table 6.6. The pressure of inner pores will affect the surface energy according to the equation (4.12).

$$P_p = \frac{2\gamma}{r} \tag{4.12}$$

where P_p, γ and r denote the gas pressure within the pores, liquid-vapor surface energy and the radius of the pores, respectively. An increase in pore pressure will lead to an increase in surface energy which will give poor wetting behavior on the solid-liquid interface. Thus, densification via liquid phase sintering will be inhibited with the increase in pore pressure [13]. This agreed very well with the results as shown in Figure 4.7 and compacts sintered in nitrogen with 3% hydrogen atmosphere yielded undesirable mechanical properties. The schematic illustration of pore swelling effect due to the presence of hydrogen in the sintering atmosphere is shown in Figure 4.24.

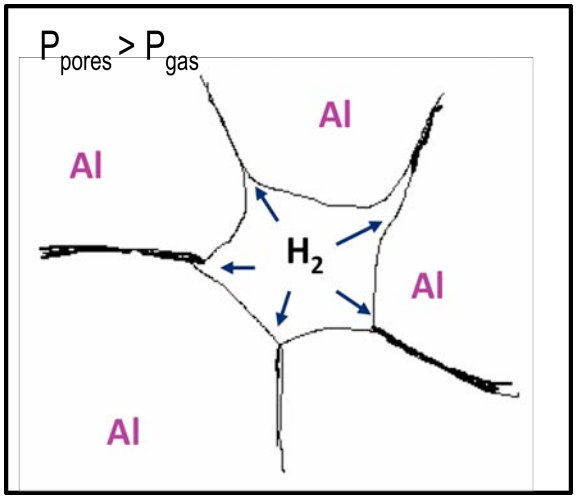

Figure 4.24. Schematic showing pore swelling when compact sintered in nitrogen with 3% hydrogen atmosphere

It has been reported that magnesium can form intermetallic Mg_2Cu with Cu [22]. A sudden increase in both Mg and Cu concentration was noted, as shown by the arrows in Figure 4.16(e) and (f). This can be attributed to the formation of Mg_2Cu from the free magnesium yielded after the decomposition of MgH_2 as shown in reaction (4.11). Mg_2Cu had been reported to further disproportionate into MgH_2 and $MgCu_2$ during hydrogenation following the equation below [23]:

$$2Mg_2Cu + 3H_2 \leftrightarrow 3MgH_2 + MgCu_2 \qquad (4.13)$$

However, high hydrogen pressure was required for the formation of MgH_2 + $MgCu_2$ [24]. In this study, it was not anticipated to form since low gas pressure of 1.5 bar was applied. Furthermore, free magnesium was also suggested to react with oxygen formed from reaction (4.8) to form MgO. However, the XRD peak ($2\theta = 42.8°$) corresponding to MgO [25] was not obvious owing to the high diffraction intensity of Al_2Cu phase.

4.11.3 Influence of the Sintering Temperatures on Ecka Alumix 231

Apart from sintering atmospheres, volume fraction of liquid also has influential effects on sintering. As tabulated in Table 4.3, with the increase in sintering temperature, larger amount of liquid formed. Liquid phase is crucial to provide better mass transport, enhance atomic diffusion and increase rate of inter-particle bonding through the high diffusivity path. This will later improve the overall wetting characteristic and densification of the compacts as the contact angle between the liquid and solid particles is reduced [26]. The backscattered electron micrograph as shown in Figure 4.12 depicted the microstructural changes at different sintering temperatures with the liquid content varied from 0 to 25%.

At 500^{o}C, the formation of liquid phase had not initiated as shown by the DSC traces (Figure 4.5). Solid state sintering, thus dominated at this stage. Figure 4.12(a) showed that particle boundary was still clearly visible at this sintering temperature. This indicated that solid state sintering alone was not sufficient to allow the mass transport between particles, leading to presence of large amount of porosity [13]. Approximately 6% porosity can be noted (Figure 4.19). Most of the microstructural changes occurred within the master alloy. Cu rich region (bright white area) that was originally found in web-like structure encircled the Si rich region in the green compact, started to undergo fragmentation. Solid state interdiffusion occurred at this stage was accompanied by volume change.

This can be evidenced from the dilation curve as shown in Figure 4.9(a), whereby the compact experienced an initial uniform volume expansion (E1), followed by shrinkage after 480°C (S1). With the increase of the temperature, the atoms gained more energy leading to increase of atom vibration. Thus, average distance between the atoms increased and contributed to initial expansion event. Furthermore, silicon was reported to have an increase in linear thermal expansion coefficient from 2.57 x 10^{-6} K^{-1} at 293K to 4.14 x 10^{-6} K^{-1} at 800K [27]. Since Ecka Alumix consisted of 15wt% silicon, it was anticipated that expansion of silicon can also contribute significantly to the initial expansion of the compact with the increase of the temperature. Using the equation (4.14), thermal expansion of Ecka Alumix 231 can be estimated [28]:

$$\frac{\Delta L}{L} = \alpha \Delta T \qquad (4.14)$$

whereby L is the initial length, ΔL is the change of length, α is the thermal expansion coefficient and ΔT is the change in temperature. A390 alloy (Al17.1Si-4.2Cu-0.5Mg-0.08Ti-0.7Fe) with the chemical composition in close proximity to the Ecka Alumix 231 was reported to have thermal expansion coefficient of 19.0x10^{-6}°C^{-1}[29]. Assuming Ecka Alumix 231 was having the same thermal expansion coefficient as A390 alloy up to 480°C, the dilation (ΔL/L in percentage) was estimated to be 0.86% which was in close approximation with the initial expansion of 0.88% as found in this study.

The subsequent shrinkage event (S1) was suggested due to the solid solution formation. Arribas et al [3] reported that globurization of eutectic Si phase occurred

inside the master alloy, Al-30Si-5Cu-1Mg (wt%) before reaching the 450ºC. The microstructure as displayed in Figure 4.12(a) showed that the globurization of Si phase continued at 500ºC. Since less traces of bright Cu-rich region spreading within the master alloy can be observed, it is anticipated that the Cu-rich region underwent both the dissolution and fragmentation. Dissolution of Cu, Si atoms into aluminum matrix was found to decrease the lattice parameter of the Al solid solution. Cu and Si atoms (r_{Cu} = 0.157nm, r_{Si} = 0.146nm) were reported to have atomic radius smaller than Al atoms (r_{Al}= 0.182nm) [30]. Solubility of Cu and Si atoms into Al matrix thus contributed to lattice distortion and decreased the lattice constant of Al. Thus, the occurrence of compact shrinkage at this stage was as a consequence of solid state interdiffusion within the master alloy. The shrinkage counteracted with thermal expansion when the sintering of the compact started. At the sintering temperature of 500ºC, the amount of shrinkage (S1) produced was not sufficient to compensate the initial swelling of the compact. Thus, liquid phase sintering is necessary to attain compact with better densification.

As the sintering temperature increased, the alloying elements (Mg, Cu, Si) started to diffuse out from the master alloy and redistribute evenly in the material. The fine dispersion of Si particles as observed at 500ºC, 508ºC and 525ºC (Figure 4.12(a), 4.10(c), 4.11(c) respectively) had eliminated. This comes in good agreement with the findings as reported by Arribas et al [3]. From Figure 4.12(b), with the formation of 5% liquid content, necking between particles started to form. Though large pores can still be observed, liquid pools started to form at the grain boundaries. Formation of liquid improves the wetting between the particles and

enhances atomic diffusion. Pores shrunk as the interfacial surface energy started to decrease. The porosity of the compact continued to decrease with the increase of the sintering temperature.

Furthermore, the sintered density for compact increased considerably to 2.31g/cm^3 or 86.62% of the theoretical value. The progressive densification/shrinkage due to liquid formation was shown by the dilation curve in Figure 4.9(b). Slight expansion (E2) can be noted upon melting of the compact and subsequently followed by immediate shrinkage during sintering. DSC traces marked the first formation of liquid with the onset of 505^{o}C (Figure 4.5). The swelling (E2) at 504-520^{o}C as observed in both Figure 4.9(b) and (c) was thus, corresponding to the formation of liquid phases. The swelling and shrinkage of the compact during liquid phase sintering was influenced by the liquid formation and behavior of the liquid. Crossin et al suggested that the first liquid formed during liquid phase sintering have poor wettability since it might be in contact with oxide phase. Swelling occurred when the liquid pushed the particles apart [31]. This later leads to volume increase in particles which formed the skeleton of the powder body.

Densification/ shrinkage occurred immediately after the swelling event was due to gradual dissolution of solid phase in liquid which resulted in volume decrease of particles under the action of capillary forces [32]. Moreover, a change in the wetting behavior of the liquid can promote densification during liquid phase sintering [33]. As discussed previously in Section 4.11.2, magnesium will react

with oxide layer to form $MgAl_2O_4$ spinel and expose the underlying Al metal which later reacted with nitrogen to form AIN. Wettability of the liquid increased with the AIN formation. Particles were pulled together under the influence of surface tension and led to compact densification [31, 34].

Compacts exhibited more homogenized distribution of silicon phase and achieved highest sintered density (2.54g/cm^3 or 95.22% of the theoretical value) with the aid of liquid phase at 560°C (Figure 4.6). Meanwhile, the porosity of the compacts was noted to decrease significantly as more liquids flow into the void between the particles which aided densification. As discussed previously in Section 4.11.2, pore filling effect was induced due to the formation of AIN for compacts sintered under nitrogen atmosphere. Thus, 15% of liquid content is optimum to ensure rapid densification and eliminate the pores significantly. The decrease in dimensions as a result of densification can be observed from the dilation curve as displayed in Figure 4.9(c). With more liquid presented, larger degree of shrinkage occurred and the overall compact contracted by approximately 0.6%. Densification occurred at a few stages (S1-S4 as shown in Figure 4.9(c)) with the rate of densification decreased with the increase of the sintering time. The shrinkage (S2) as shown in both Figure 4.9(b) and (c) can be attributed to particle rearrangement, whereby S3 and S4 can be attributed to solution-reprecipitation and pore filling effect. The degree of shrinkage increased with the increase of liquid content.

Further increase of sintering temperature up to 566ºC or 25% of liquid content did not have any significant influence on the sintered density, pores elimination and

hardness value. In terms of microstructural development, grain coarsening and Si growth can be noted due to Ostwald ripening. Figure 4.18 displayed the vickers hardness of the compacts sintered at different sintering temperatures. It can be seen that the Vickers hardness value of the compact increased significantly up to 10% liquid content or sintering temperature of 555^{o}C, above which only small increase in Vickers hardness value was noted (Figure 4.18). However, the sintered density and porosity measurement as displayed in Figure 4.6 and 4.19 respectively showed that better densification and better pore closure were achieved at sintering temperature of 560^{o}C. Hence, we can summarized that compacts sintered at 15% liquid content (560^{o}C) was the optimum sintering temperature to produce compacts with the highest sintered density, mechanical properties and lowest porosity.

Figure 4.25 further elucidated the porosity-property relationship for the compact sintered at different temperatures. It was observed that a linear correlation existed between porosity and Vickers hardness. Vickers hardness decreased rapidly with the increase of the porosity. The strong dependence of Vickers hardness on the volume fraction porosity was consistent with the Minimum Solid Area (MSA) model proposed by Rice [35-37]:

$$H_v = H_0 e^{-bP} \qquad (4.15)$$

where H_v ,H_0 corresponding to measured Vickers Hardness and Vickers hardness for compact at zero porosity respectively, b is a material dependence constant and P is the volume fraction porosity of the compact. The Vickers hardness at zero

porosity, H_0 was obtained through linear regression analysis (Figure 4.5) and was calculated to be 80.40 HV, which comes in good agreement with the Vickers hardness measurement for casted hypereutectic Al-(15-20%) Si alloys [38].

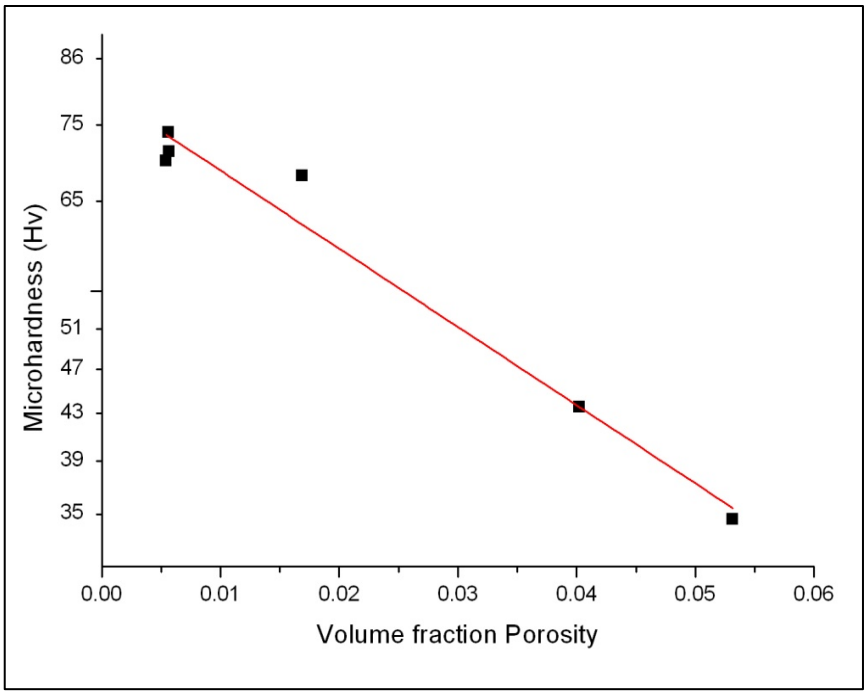

Figure 4.25 Vickers Hardness (HV) as a function of volume fraction porosity

4.11.4 Influence of Sintering Time on Ecka Alumix 231

Densification of the compact is generally dominated by the sintering temperature and sintering atmosphere [39]. Although sintering time is a relatively weak controlling parameter, it is crucial to determine the optimum sintering time to allow sufficient time for densification of compact to occur. Figure 4.8 showed the effect of sintering time on sintered density.

Sintering time of 30 minutes was clearly not sufficient for complete densification to take place. The sintered density of the compact only achieved 2.34g/cm^3 or 87.57% of the theoretical value (Figure 4.8). From the dilation curves as displayed in Figure 4.9(c), it can be seen that the densification/shrinkage event at 30 minutes of sintering time had not reached completion, whereby the last stage (S3), possibly pore filling and solid state sintering stage, had not initiated yet. The microstructure of the compact as shown in Figure 4.17 (a) again proved that sintering of compact at 30 minutes is not sufficient since particle boundary can still be observed possibly due to incomplete diffusion and spreading of the liquid.

Major densification occurred in the first 45 minutes. A significant increase in sintered density can be noted. Longer sintering times, however, did not bring significant increase in the sintered density. In terms of microstructural development, extended time is beneficial for continued pore elimination. By comparing the microstructures of the compacts sintered at 45 and 60 minutes as displayed in Figure 4.17(b) and (c) respectively, compact sintered at 60 minutes showed better pore closure with less large pores being observed. This can be attributed to pore filling effect whereby the liquid flows into voids and eliminates the pores. Prolonged sintering time is not desirable since it will lead to microstructural coarsening. It is, thus, determined that sintering time of 60 minutes is preferable to attain compacts with satisfactory densification and better pore closure.

4.11.5 Phase transformation during sintering of Ecka Alumix 231

Ecka Alumix 231 is a mixture of two types of powder particles with irregular shape as displayed in Figure 4.2(b). The EDX analysis further confirmed that the master alloy (Point 2) has the chemical composition of Al-28Si-5Cu-1Mg (wt%), whereby the other powder particles (Point 1) were pure aluminum. From Figure 4.2(c), the master alloy consisted of three different phases and the chemical composition for each respective phase was displayed in Table 4.2. The web-like structure (Point 3) was suggested to be as a consequence of Cu- and Mg-rich intermetallic precipitation during solidification [3]. It was found to surround Al-Si eutectic-like structure (Point 5) with silicon crystals (Point 4) embedded in it. Traces of Fe can be detected but it is considered as impurity commonly found during the processing of aluminum alloys [40]. The XRD result as displayed in Figure 4.3 again confirmed the presence of α-aluminum, elemental silicon and θ phase ($CuAl_2$) and Q phase ($Cu_2Mg_8Si_6Al_5$). This comes in good agreement with the findings as reported by Arribas et al. [3].

From Figure 4.12 (a), changes of the microstructure as early as 500^{o}C prior to liquid formation can be noted. Most of the microstructural changes occurred within the master alloy particles at this stage. This can be attributed to globulization of Al-Si eutectic. Arribas et al [3] has reported that the globulization event occurred even before reaching 450^{o}C. The calculated thermodynamic diagram as shown in Figure 4.22(a) can provide some insights to explain the microstructural change. It is anticipated that the solid state interdiffusion occurred prior to liquid phase formation. At equilibrium state, the system has θ phase ($CuAl_2$), Q phase

($Cu_2Mg_8Si_6Al_5$), FCC aluminum and primary silicon coexisting with each other. As a result, dissolution of alloying elements, i.e. Mg, Cu, Si into the aluminum matrix is anticipated to occur. This later contributed to the volume change as observed Figure 4.9(a).

DSC traces as displayed in Figure 4.5 showed that the formation of the first liquid occurred at the onset of 505^{o}C and subsequently followed by another melting event which initiated at 515^{o}C. The liquid generated mainly inside the master alloy particles. Formation of these liquids represented a non-equilibrium condition due to the chemical gradient presented within the compact [34]. Although local composition varied from place to place, chemical homogenization process started to take place. A series of reactions occurred involving θ phase ($CuAl_2$), Q phase ($Cu_2Mg_8Si_6Al_5$), FCC aluminum and silicon to form the liquid phase [41]. This comes in good agreement with the Thermo-Calc calculation as presented in Figure 4.22(a). Globulization event as observed at 500^{o}C proceeded when the compact heated to 508^{o}C and 521^{o}C (Figure 4.10 and 4.11). The petal-like structure denoting the Si rich region, previously observed in the green compact was no longer visible. Si transport mechanism was enhanced with the formation of liquid phase [3]. The growth of globular Si-rich region and coarsening of Si particles can be noted when the compact was heated to 525^{o}C as displayed in Figure 4.11(c). The Cu-rich region, on the other hand, fragmented into small droplets. This can be attributed to its higher solubility and diffusivity in liquid than in FCC aluminum matrix. The impurity Fe started to segregate due to its low solubility in the aluminum matrix.

With the increase of sintering temperature to 547^{o}C, more liquid phase evolved. The fine dispersion of Si particles was completely removed. Diffusion of Si, Cu, Mg became more profound with aid of the liquid phase. Necking, particle rearrangement and progressively liquid flows to close the pores increased with the increase of the sintering temperature. Upon reaching 560^{o}C, chemical homogenization nearly came to an end. The compact had the composition near to equilibrium state. From the microstructure as displayed in Figure 4.12(d), most of the θ and Q phase formed the liquid phase and spread along the grain boundaries to form the necklace-like structure. This comes in good agreement with thermodynamic calculation shown in Figure 4.22(b).

Fe-rich region as displayed in Figure 4.13 (c) was found to segregate at the grain boundary and had the composition close to $FeSiAl_5$. The same event was observed in the compact sintered under vacuum condition as shown in Figure 4.14(b). Mondolfo [42] had suggested that aluminum alloy containing Fe <0.7 wt% most likely have the eutectic $FeSiAl_5$ formed within the intermetallic phase. Growth of primary silicon can be noted with the increase of the sintering temperature due to Ostwald ripening. Figure 4.21 (a) showed that compacts sintered under different sintering atmospheres have identical phases presented. Further elaboration of the XRD analysis (Figure 4.21(b)) showed the presence of α- Al, Si, $CuAl_2$ phase (θ) and Q phase ($Cu_2Mg_8Si_6Al_5$.).

4.12 References

[1] "PM Aluminum Drives Forward in New BMW Breakthrough," *Metal Powder Report,* vol. 61, pp. 13-15, 2006.

[2] "Technical Data Sheet Certificate of Analysis," in *Ecka Granule Velder GmbH*, ed, 2008.

[3] I. Arribas, J. M. Martín, and F. Castro, "The Initial Stage of Liquid Phase Sintering for An Al-14Si-2.5Cu-0.5Mg (wt%) P/M Alloy," *Materials Science and Engineering: A,* vol. 527, pp. 3949-3966, 2010.

[4] D. W. Heard, I. W. Donaldson, and D. P. Bishop, "Metallurgical Assessment of a Hypereutectic Aluminum-Silicon P/M Alloy," *Journal of Materials Processing Technology,* vol. 209, pp. 5902-5911, 2009.

[5] J. A. Greenwood and J. H. Tripp, "The Elastic Contact of Rough Spheres," *Journal of Applied Mechanics,* vol. 89, pp. 153-159, 1967.

[6] R. M. German, *Particle Packing Characterisitics*. New Jersey, 1989.

[7] R. W. Heckel, *Trans. Met. Soc. AIME,* vol. 221, p. 671, 1961.

[8] P. J. Denny, "Compaction Equations: A Comparison of The Heckel and Kawakita Equations," *Powder Technology,* vol. 127, pp. 162-172, 2002.

[9] P. Enghag, "Encyclopedia of the Elements, Technical Data History Processing Applications," ed. Weinheim: WILEY-VCH Verlag GmbH@ Co. KGaA, 2004, p. 834.

[10] C. Lall, *International Journal Powder Metallurgy,* vol. 27, p. 315, 1991.

[11] G.B. Schaffer, T.B. Sercombe, and R. N. Lumley, "Liquid Phase Sintering of Aluminium Alloys," *Materials Chemistry and Physics,* vol. 67, pp. 85-91, 2001.

[12] E. P. Y. D.H. Kim, and J.S. Kim, *J. Mater. Sci. Lett,* vol. 15, pp. 1429-31, 1996.

[13] Su.S.S. and I. T. Chang, "Effect of Processing Conditions on Hypereutectic Aluminum-Silicon P/M Alloys," 2010, pp. 49-57.

[14] G. B. Schaffer, B. J. Hall, S. J. Bonner, S. H. Huo, and T. B. Sercombe, "The Effect of the Atmosphere and The Role of Pore Filling on the Sintering of Aluminium," *Acta Materialia,* vol. 54, pp. 131-138, 2006.

[15] Laurent V., Chatain D., C. Chatillon, and N. Eustathopoulos, *Acta Materialia,* vol. 36, p. 1797, 1988.

[16] G. Schaffer and B. Hall, "The Influence of the Atmosphere on the Sintering of Aluminum," *Metallurgical and Materials Transactions A,* vol. 33, pp. 3279-3284, 2002.

[17] N. Showaiter and M. Youseffi, "Compaction, Sintering and Mechanical Properties of Elemental 6061 Al powder With and Without Sintering Aids," *Materials & Design,* vol. 29, pp. 752-762, 2008.

[18] T. Pieczonka, T. Schubert, S. Baunack, and B. Kieback, "Dimensional behaviour of aluminium sintered in different atmospheres," *Materials Science and Engineering: A,* vol. 478, pp. 251-256, 2008.

[19] Y.J. Liang, Y.C. Che, and X. X. Liu, *Thermodynamic data handbook of inorganic substances (1st ed.)* Shenyang, China: Northeastern University Press, 1993.

[20] J. Graetz and J. J. Reilly, "Thermodynamics of the and polymorphs of AlH3," *Journal of Alloys and Compounds,* vol. 424, pp. 262-265, 2006.
[21] R. M. German, "Liquid Phase Sintering," *Plenum Press, New York,* 1985 1985.
[22] P. Villars, *Pearson's Handbook Desk Edition* vol. 2: ASM International, 1997.
[23] J. J. Reilly and R. H. Wiswall, "Reaction of hydrogen with alloys of magnesium and copper," *Inorganic Chemistry,* vol. 6, pp. 2220-2223, 1967/12/01 1967.
[24] A. Andreasen, M. B. Sørensen, R. Burkarl, B. Møller, A. M. Molenbroek, A. S. Pedersen, T. Vegge, and T. R. Jensen, "Dehydrogenation Kinetics of Air-Exposed MgH2/Mg2Cu and MgH2/MgCu2 Studied with In Situ X-ray Powder Diffraction," *Applied Physics A: Materials Science & Processing,* vol. 82, pp. 515-521, 2006.
[25] H. Shao, Y. Wang, H. Xu, and X. Li, "Hydrogen Storage Properties of Magnesium Ultrafine Particles Prepared by Hydrogen Plasma-Metal Reaction," *Materials Science and Engineering: B,* vol. 110, pp. 221-226, 2004.
[26] S. J. L. Kang, "Sintering: Densification, Grain Growth & Microstructure," *Elsevier Butterworth-Heinemnn, Oxford, UK,* 2005.
[27] Hiromichi W., Naofumi Y., and O. Masahira, "Linear Thermal Expansion Coefficient of Silicon from 293 to 1000K," *International Journal of Thermophysics,* vol. 25, pp. 221-236, 2004.
[28] W. Gao and N. M. Sammes, *An Introduction to Electronic and Ionic Materials*. Singapore: World Scientific Publishing Co. Pte. Ltd. , 1999.
[29] D. M. Smith, "High Strength Wear Resistant Aluminum Alloys and Process," United States Patent, 1984.
[30] L. G. Hou, Y. H. Cai, H. Cui, and J. S. Zhang, "Microstructure Evolution and Phase Transformation of Traditional Cast and Spray-Formed Hypereutectic Aluminium-Silicon Alloys Induced by Heat Treatment," *International Journal of Minerals, Metallurgy, and Materials,* vol. 17, pp. 297-306, 2010.
[31] E. Crossin, J. Y. Yao, and G. B. Schaffer, "Swelling During Liquid Phase Sintering of Al-Mg-Si-Cu Alloys," *Powder Metallurgy,* vol. 50, pp. 354-358, 2007.
[32] A. P. Savitskii, "Scientific Approaches to Problems of Mixtures Sintering," *Science of Sintering,* vol. 37, pp. 3-17, 2005.
[33] G. B. Schaffer, J. Y. Yao, S. J. Bonner, E. Crossin, S. J. Pas, and H. A.J., "The Effect of Tin and Nitrogen on Liquid Phase Sintering of Al-Cu-Mg-Si Alloys," *Acta Materialia,* vol. 56, pp. 2615-2624, 2008.
[34] R. M. German, P. Suri, and S. J. Park, "Review: Liquid Phase Sintering," *Journal of Materials Science,* vol. 44, pp. 1-39, 2009.
[35] P. E. Wang and T. K. Chaki, "Sintering Behaviour and Mechanical Properties of Hydroxyapatite and Dicalcium Phosphate," *Journal of Materials Science: Materials in Medicine,* vol. 4, pp. 150-158, 1993.
[36] R. W. Rice, "Evaluation and Extension of Physical Property-Porosity Models Based on Minimum Solid Area," *Journal of Materials Science,* vol. 31, pp. 102-118, 1996.

[37] T. P. Hoepfner and E. D. Case, "The Influence of The Microstructure on The Hardness of Sintered Hydroxyapatite," *Ceramics International,* vol. 29, pp. 699-706, 2003.
[38] H. Torabian, J. P. Pathak, and S. N. Tiwari, "Wear Characteristics of Al-Si Alloys," *Wear,* vol. 172, pp. 49-58, 1994.
[39] R. M. German, *Liquid Phase Sintering*. Troy, New York: Plenum Press, 1985.
[40] "Casting Metallurgy," in *Die Cast Engineering*, ed: CRC Press, 2004, pp. 105-138.
[41] N. A. Belov, D. H. Eskin, and A. A. Aksenov, *Multicomponent Phase Diagrams: Applications for Commercial Aluminum Alloys*: Elsevier, 2005.
[42] L. F. Mondolfo, *Aluminum Alloys: Structure and Properties*. London: Butterworth & Co. Ltd, 1979.

Chapter 5

Alloying Additions and Heat Treatment of Hypereutectic Al-Si based P/M alloys

5.1 Introduction

Alloy development and optimization are subjects of intense interest for PM industry. The development of P/M aluminum-silicon system is put under focus in this study due to its excellent wear resistance and potential replacement to conventional cast and wrought materials. As discussed previously in literature review, P/M approach helps to eliminate the shortcomings of wrought and ingot metallurgy by offering considerable improvement in the dimensional control, exhibiting uniform microstructures and allowing a wider range of alloy chemistry to be employed [1]. Industrial application of aluminum P/M has always been impeded by the limited availability of commercial press-and-sinter P/M alloys. A few examples of commercial aluminum alloy systems widely used in manufacturing of industrial parts are AC2014 (Al-4.4wt%Cu-0.8wt%Si-0.6wt%Mg), A6061 (Al-1Mgwt%-0.6Siwt%-0.25wt%Cu) and Alumix 431 (Al-5.5wt%Zn-2.5wt%Mg-1.5wt%Cu).

Due to limited availability of the commercial P/M alloys, the main goal of the present investigation was to develop novel alloy systems with enhanced properties.

Table 5.1 displays the nominal composition for three different alloys used for this study, with Ecka Alumix 231 (Al-15Si-2.5Cu-0.5Mg) acts as the baseline material. Variations from this baseline were then explored to study the effects of Cu and Ni additions.

Table 5.1. The nominal composition for three different alloys used in the study.

Alloys	Composition (wt%)
Ecka Alumix 231	Al-15Si-2.5Cu-0.5Mg
Alloy A	Al-15Si-4.5Cu-0.5Mg
Alloy B	Al-15Si-2.5Cu-0.9Ni-0.5Mg
Alloy C	Al-15Si-4.5Cu-0.9Ni-0.5Mg

Al-Si based alloys widely used in piston production and other automotive application generally consists of a few major alloying components which include nickel, copper, magnesium etc. Addition of these alloying elements allows formation of several intermetallic phases such as Al_2Cu, Mg_2Si, $Al_5Cu_2Mg_8Si_6$, Al_3Ni, Al_3CuNi, Al_7Cu_4Ni and others depending on the alloy composition [2, 3]. The main alloying elements of interests in this study are copper and nickel. Copper addition has been recognized to aid sintering by formation of liquid phase [4] and improve mechanical properties through heat treatment response via formation of precipitates such as θ ($CuAl_2$) [5]. Nickel, on the other hand, was incorporated as the fifth element into the quaternary Al-Si-Cu-Mg systems. Nickel additions to Al-based alloys have been reported to have beneficial effect on elevated temperatures applications and enhance wear resistance properties due to the formation of intermetallic Ni-phases [6, 7]. In the recent work by Hennessey et al., Al-12.2Si-4.5Cu-0.9Ni-0.5Mg P/M alloy which was similar to that of wrought alloy AA4032 yielded properties comparable to the existing P/M alloys [8]. The copper

content of 4.5wt% and Ni content of 0.9wt% were thus added to the baseline system (Ecka Alumix 231) which aims to increase the overall properties of the baseline system.

Since the optimal processing route for commercial Ecka Alumix 231 has been established in the previous chapter, the alloys as shown in Table 5.1 were subjected to the optimal processing condition. Nitrogen sintering atmosphere and sintering time of 60 minutes were necessary to obtain compacts with desirable densification, microstructures and mechanical properties. Due to the variation in the alloy composition, sintering temperatures for other Al-Si based alloys were determined again using differential scanning calorimetry (DSC). The effects of alloying additions on compressibility, sinterability, microstructures and mechanical properties will be discussed further in the following sections.

Artificial T6 treatment is generally used to enhance the properties of heat-treatable alloys. Although numerous works have been carried out to assess the effect of solution heat treatment and ageing on the microstructure and mechanical behavior of Al-Si-Cu-Mg alloys, more systematic investigation is required due to the wide range of nominal chemical composition available for these alloys leading to variation in heat treatment response. Thus, the optimal solution treatment and ageing parameters for each alloys systems were established and the precipitation behaviors for each alloys were studied in details. X-ray diffraction and EPMA analysis were also carried out to identify different phases presented in the heat treated samples.

5.2 Effect of Compaction Pressure on Green Density

The first property to be assessed was compressibility for different alloys. The compressibility curves for different Al-Si based alloys were determined to develop a suitable compaction pressure used in the subsequent studies. Meanwhile, it was also aimed to study the effect of alloying addition on compressibility. Figure 5.1 displays the green density of the compacts as function of compaction pressure for different Al-Si based alloys. In general, green density of the compacts for different Al-Si based alloys increased with the increase of the compaction pressure. The green density increased in parallel with the compaction pressure due to the increased force to close up the porosity. It was noted that the green density continue to increase upon reaching 600MPa.

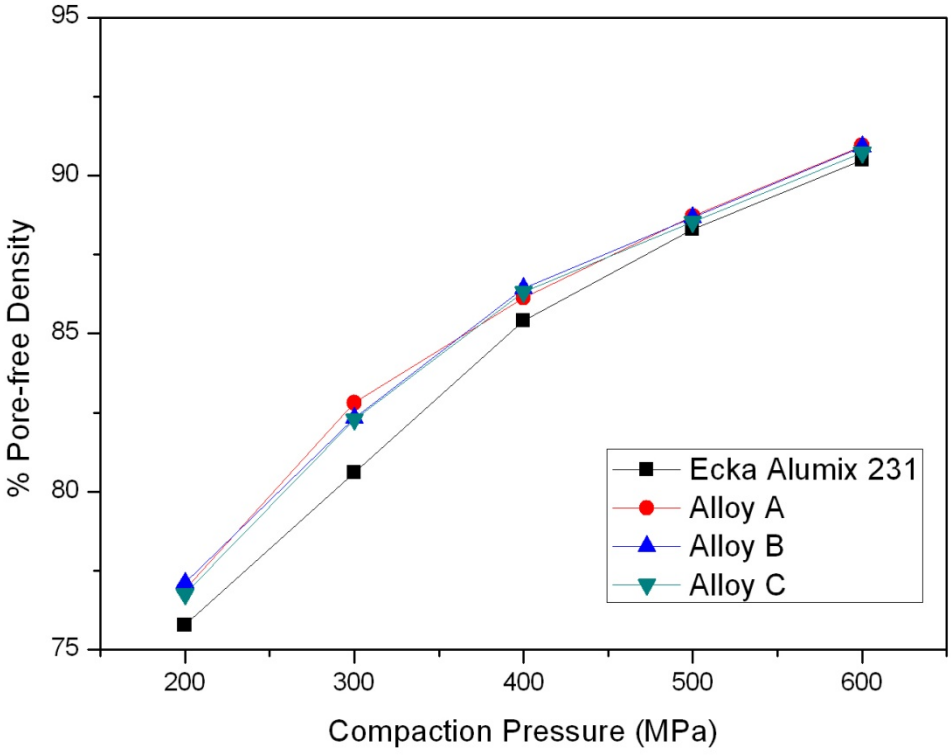

Figure 5.1: Effect of compositional change on compressibility for different alloys

A more precise tabulation of density increase was displayed in Table 5.2. By comparing with the theoretical density, it can be noted that addition of Cu and/or Ni only resulted in a slight increase in relative densification at lower compaction pressure. With the increase of the compaction pressure up to 300MPa, approximately 2% increase in relative densification as compared with Ecka Alumix 231 can be noted. Further increase of the compaction pressure did not result in any significant increase in relative densification. From a practical perspective, a suitable compaction pressure for all alloys was maintained at 400MPa, whereby, further increase in densification became less remarkable. At this compaction pressure, the green compact for Alloy A, B, C achieved 86.13%, 86.43% and 86.32% of the theoretical density respectively.

Table 5.2: Tabulation of green density for Ecka Alumix 231 pressed at different compaction pressure.

Compaction Pressure (MPa)	Ecka Alumix 231		Alloy A		Alloy B		Alloy C	
	Green* Density, ρ_g (g/cm3)	$\rho_g(\%\rho_t)$	Green* Density, ρ_g (g/cm3)	$\rho_g(\%\rho_t)$	Green* Density, ρ_g (g/cm3)	$\rho_g(\%\rho_t)$	Green* Density, ρ_g (g/cm3)	$\rho_g(\%\rho_t)$
200	2.02	75.78	2.08	76.89	2.07	77.12	2.09	76.77
300	2.15	80.60	2.24	82.81	2.21	82.33	2.24	82.28
400	2.27	85.40	2.33	86.13	2.32	86.43	2.35	86.32
500	2.35	88.29	2.40	88.72	2.38	88.67	2.41	88.53
600	2.41	90.49	2.46	90.94	2.44	90.90	2.47	90.73

* All the green densities stated in the table were average value for 4 compacts with error bar less than ±0.008

5.3 Determination of Suitable Sintering Temperature

The amount of liquid generated at a given sintering temperature was determined using differential scanning calorimetry test (DSC), as displayed in Figure 5.2(a)-(c). A few major melting events can be noted. An extensive liquid formation occurred within the range of 500 ºC and 580 ºC. Similar with DSC traces for Ecka Alumix 231 (Figure 4.5), two small intensity endothermic peaks at 507 ºC and 524 ºC respectively marked the start of the melting events which could be associated with the melting of the ternary and quaternary compounds involving Al, Cu, Mg, Fe and Si. The melting events proceeded with a shouldering effect at approximately 540ºC. This shouldering effect was only observed in DSC traces for Alloy A (Al-15Si-4.5Cu-0.5Mg) and Alloy C (Al-15Si-4.5Cu-0.9Ni-0.5Mg) and could possibly due to the liquid formation due to melting of the Al-Al_2Cu (θ). A large endothermic peak with the maximum intensity around 570ºC to 575ºC indicated the major melting event of Al-Si eutectic. Above approximately 640 ºC, Ecka Alumix 231 achieved a fully molten state.

A summary of the amount of liquid phase generated at various sintering temperatures for different alloys was shown in Table 5.3. These sintering temperatures were then used to assess the optimal sintering response for different alloys. As depicted in Table 5.3, an increase in the sintering temperature marked an increase in the amount of liquid phase presented which later aided in liquid phase sintering. Addition of copper generally can enhance liquid phase formation. In other words, Alloy A and Alloy C with more copper content required a lower sintering temperature to generate certain amount of liquid phase within the compacts. Nickel addition, however, did not result in significant lowering of sintering temperature as compared to the other alloys.

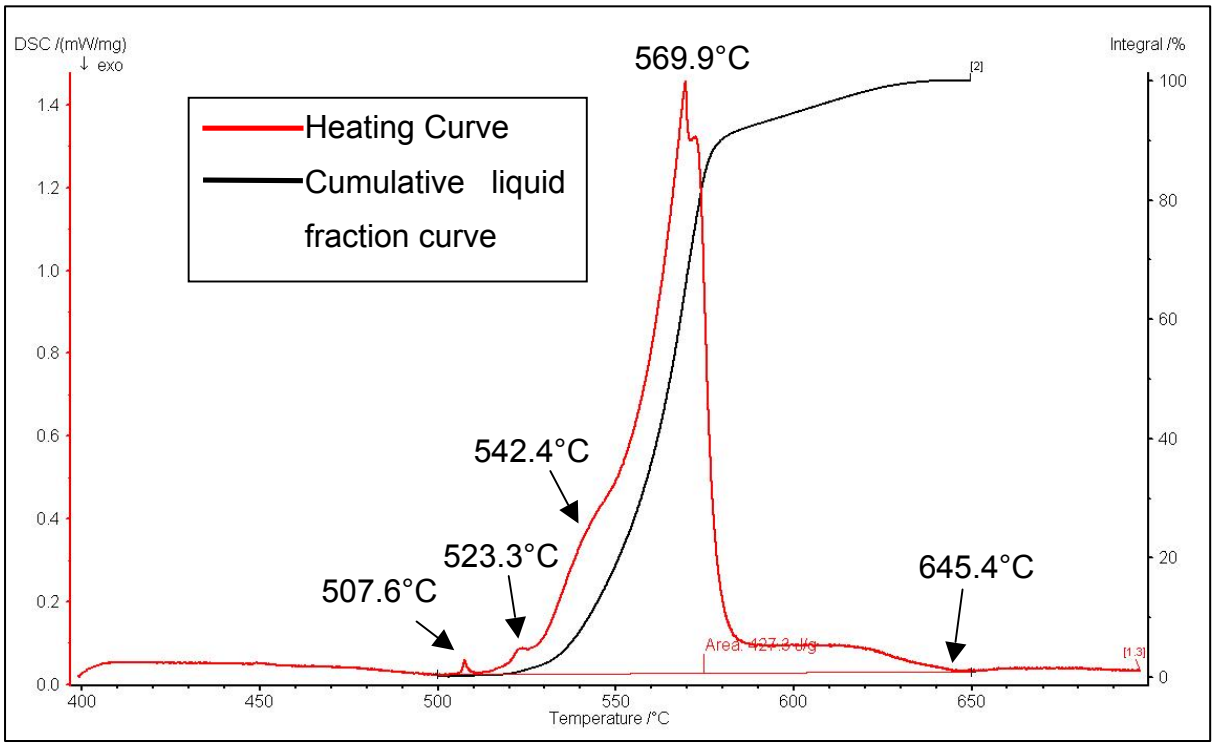

(a)

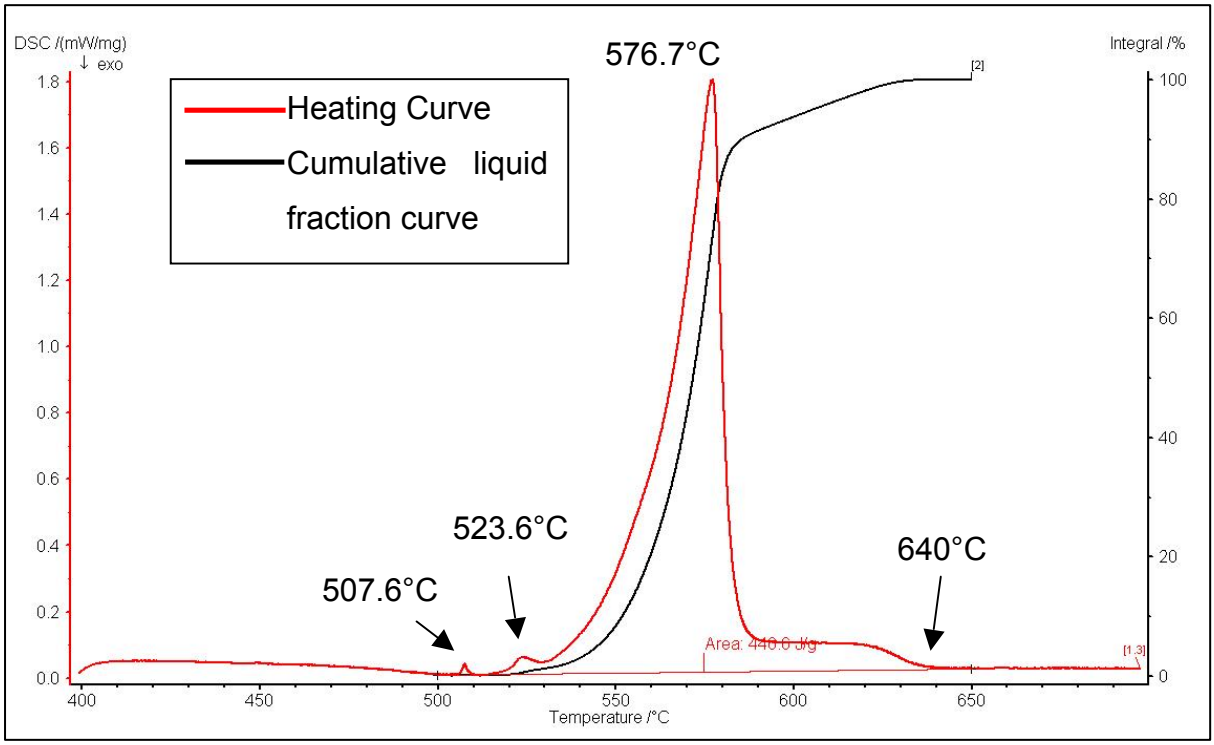

(b)

Figure 5.2. Heating curve and cumulative liquid fraction curve for (a) Alloy A (Al-15Si-4.5Cu-0.5Mg), (b) Alloy B (Al-15Si-2.5Cu-0.9Ni-0.5Mg) obtained from DSC measurement.

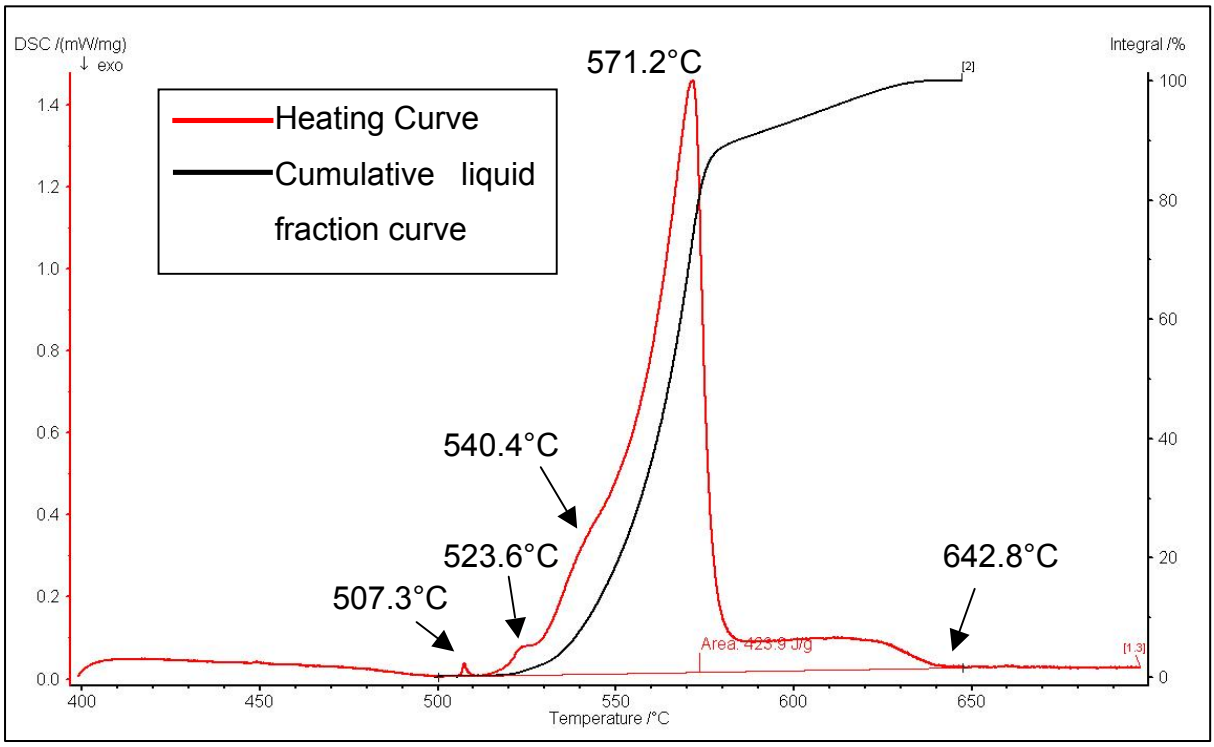

(c)

Figure 5.2 (continued). Heating curve and cumulative liquid fraction curve for (c) Alloy C (Al-15Si-4.5Cu-0.9Ni-0.5Mg) obtained from DSC measurement.

Table 5.3. Summary of DSC results showing the amount of liquid presented at different sintering temperature for different alloys

Liquid Content (%)	Sintering Temperature (°C)			
	Ecka Alumix 231	Alloy A	Alloy B	Alloy C
0	500	500	500	500
5	547	537	545	537
10	555	543	552	543
15	560	547	557	547
20	563	551	560	551
25	566	555	563	555

5.4 Effects of Alloying Additions on Sintered Density

The main purpose of alloying additions was to increase the strength and mechanical properties of the materials. The effects of adding Cu and Ni either individually or in combination, on sintered density were investigated and displayed in Figure 5.3. Increase of the sintering temperature marked with a substantial increase in densification for all different alloys. All the Al-Si based alloys with either Cu and/Ni addition experienced a sharp increase in densification at the lower sintering temperatures. The sintered density increased in parallel with the increase of sintering temperature and eventually reached a plateau at higher sintering temperature. Above 15% of liquid phase, no significant increase in sintered density was noted. A more detailed account of the influence of alloy additions on relative densification of the compacts was tabulated in Table 5.4 to 5.6.

Similar to commercial Ecka Alumix 231 (Al-15Si-2.5Cu-0.5Mg), sintering of all alloys initiated with swelling at 500°C with the relative densification showing negative value. A dramatic increase in densification for Alloy A, B and C can be noted with the presence of 5% liquid phase. Alloy A (Al-15Si-4.5Cu-0.5Mg) achieved the highest sintered density of 2.61g/cm^3 which corresponds to 96.32% of the theoretical value ($\boldsymbol{\rho_t}$= 2.705g/cm^3) at 543°C or equivalent to presence of 10% of the liquid phase. Meanwhile, Alloy B (Al-15Si-2.5Cu-0.9Ni-0.5Mg) and C (Al-15Si-4.5Cu-0.9Ni-0.5Mg) achieved the highest sintered density at 557°C and 547°C which corresponds to 95.14% ($\boldsymbol{\rho_t}$= 2.554 g/cm^3) and 95.35% ($\boldsymbol{\rho_t}$= 2.722 g/cm^3) respectively. Overall, the sintered density was leveled off with increasing amount of liquid in excess of 15% for all Al-Si based alloys.

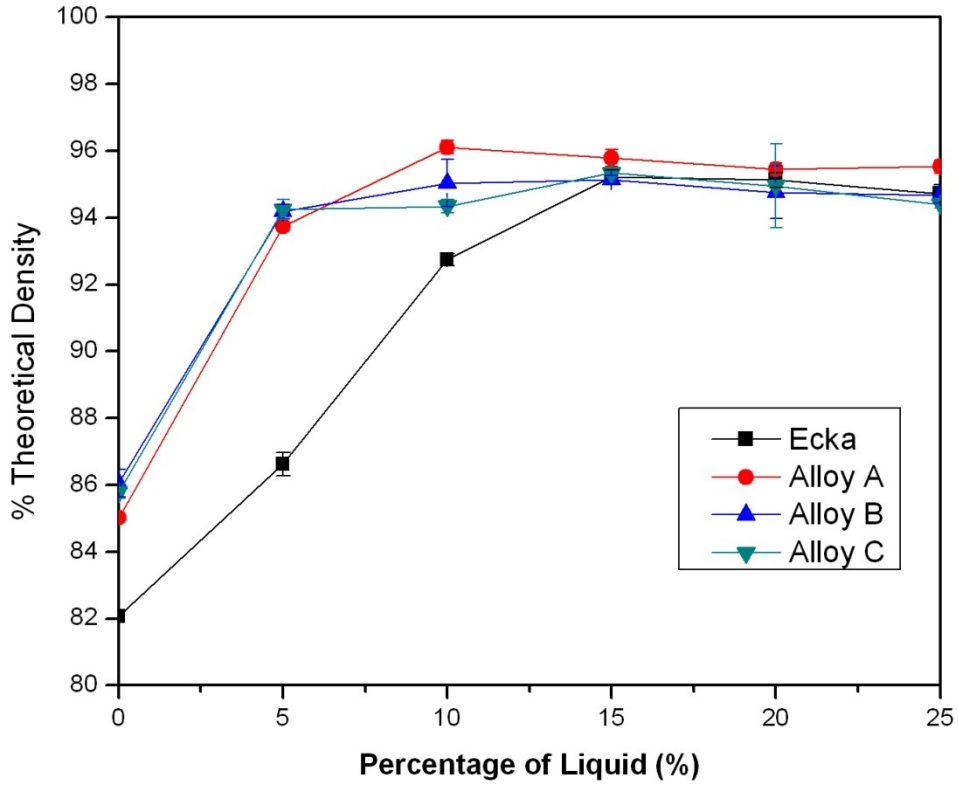

Figure 5.3. Effect of compositional change on sinterability for different alloys

Table 5.4:

Tabulation of green and sintered density as well as relative densification for Alloy A (Al-15Si-4.5Cu-0.5Mg) sintered in nitrogen atmosphere at different sintering temperatures for 1 hour

Sintering temperature (°C)	**Green Density ρ_g(g/cm3)**	**$\rho_g(\%\rho_t)$**	**Sintered Density ρ_s (g/cm3)**	**$\rho_s(\%\rho_t)$**	**Relative Densification φ**
500	2.33	86.13	2.30	85.02	-0.08
537	2.32	85.76	2.54	93.74	0.56
543	2.33	86.13	2.61	96.32	0.73
547	2.33	86.13	2.59	95.78	0.70
551	2.34	86.50	2.58	95.45	0.66
555	2.32	85.76	2.58	95.53	0.69

* All the densities stated in the table were average value for 4 compacts with error bar less than ±0.005

Table 5.5:

Tabulation of green and sintered density as well as relative densification for Alloy B (Al-15Si-2.5Cu-0.9Ni-0.5Mg) sintered in nitrogen atmosphere at different sintering temperatures for 1 hour

Sintering temperature (°C)	**Green Density ρ_g(g/cm3)**	**$\rho_g(\%\rho_t)$**	**Sintered Density ρ_s (g/cm3)**	**$\rho_s(\%\rho_t)$**	**Relative Densification φ**
500	2.33	86.80	2.31	86.06	-0.06
545	2.31	86.06	2.53	94.19	0.58
552	2.32	86.43	2.55	95.04	0.62
557	2.32	86.43	2.55	95.14	0.64
560	2.31	86.06	2.54	94.77	0.60
563	2.32	86.43	2.59	94.67	0.61

* All the densities stated in the table were average value for 4 compacts with error bar less than ±0.008

Table 5.6:

Tabulation of green and sintered density as well as relative densification for Alloy C (Al-15Si-4.5Cu-0.9Ni-0.5Mg) sintered in nitrogen atmosphere at different sintering temperatures for 1 hour

Sintering temperature (°C)	**Green Density ρ_g(g/cm3)**	**$\rho_g(\%\rho_t)$**	**Sintered Density ρ_s (g/cm3)**	**$\rho_s(\%\rho_t)$**	**Relative Densification φ**
500	2.35	86.32	2.34	85.78	-0.04
537	2.34	85.96	2.57	94.25	0.59
543	2.35	86.32	2.57	94.34	0.59
547	2.35	86.32	2.60	95.35	0.66
551	2.36	86.69	2.58	94.95	0.62
555	2.34	85.96	2.57	94.41	0.60

* All the densities stated in the table were average value for 4 compacts with error bar less than ±0.010

5.5 Determination of Optimal Heat Treatment Parameters

It has previously been stated that strengthening of aluminum can be achieved by alloying aluminum with other elements to give rise to solid solution strengthening, precipitation hardening and second phase hardening mechanism. An artificial precipitation-hardening heat treatment (T6) generally consists of three major stages: solution heat treatment, quenching and precipitation hardening or ageing. This section is aimed to determine the optimal heat treatment parameters with the focus on the solution heat treatment temperatures, solutionizing times, ageing temperatures and ageing times.

5.5.1 Determination of Solution Treatment Temperatures

The main purpose of solution heat treatment is to dissolve alloying elements within the aluminum-rich α-matrix at elevated temperature. Variation in the alloying additions, particularly copper content has direct influences on solution treatment temperatures. Ideally, solution heat treatment is to be controlled within a narrow range to avoid localized melting since it can lead to void formation and substantially decreases the mechanical properties of the materials [9]. Hence, the first parameter of concern is to determine the suitable solution treatment temperatures. Differential scanning calorimetry (DSC) was employed to determine the onset of melting for the sintered compacts. It was likely that a different solution heat treatment temperature would be required for different Al-Si based alloys.

Figure 5.4(a)-(d) depicts the DSC traces for different Al-Si based alloys. All the alloys showed similar trend with the presence of a deep endothermic peak at the onset

temperature ranging from 490°C to 520°C, corresponding to melting behaviour. The melting event for commercial powder Ecka Alumix 231 (Figure 5.4a) was found to initiate at the temperature of 505°C. Meanwhile, addition of copper up to 4.5wt% contributed to a drop in onset temperature for endothermic peak to 496°C (Figure 5.4b). This was followed by a second endothermic peak with the onset temperature of 515°C. The onset of endothermic peak for Alloy B with the nickel addition of 0.9wt%, on the other hand, showed a shift to higher temperature with 515°C being recorded (Figure 5.4c). Alloy C with both copper and nickel addition, however, showed similar onset temperature for endothermic peaks as Ecka Alumix 231. It was postulated that the effects of copper and nickel additions had counteracted each other leading to no significant shift in the incipient melting temperature.

Although it is commonly accepted that localized melting or partial melting can deteriorate the properties of materials, there have been discrepancies on whether presence of small amount of liquid phase can promote a measurable increase in the final properties of the materials. Thus, to investigate the possibility of enhancement in material properties, several solution heat treatment temperatures were determined as shown in Table 5.7.

Table 5.7. Designated solution heat treatment temperatures for different alloys

Alloys	**Solution Heat Treatment Temperature (°C)**
Ecka Alumix 231	490, 500, 510, 520
Alloy A	490, 500, 510
Alloy B	500, 510, 520
Alloy C	490, 500, 510

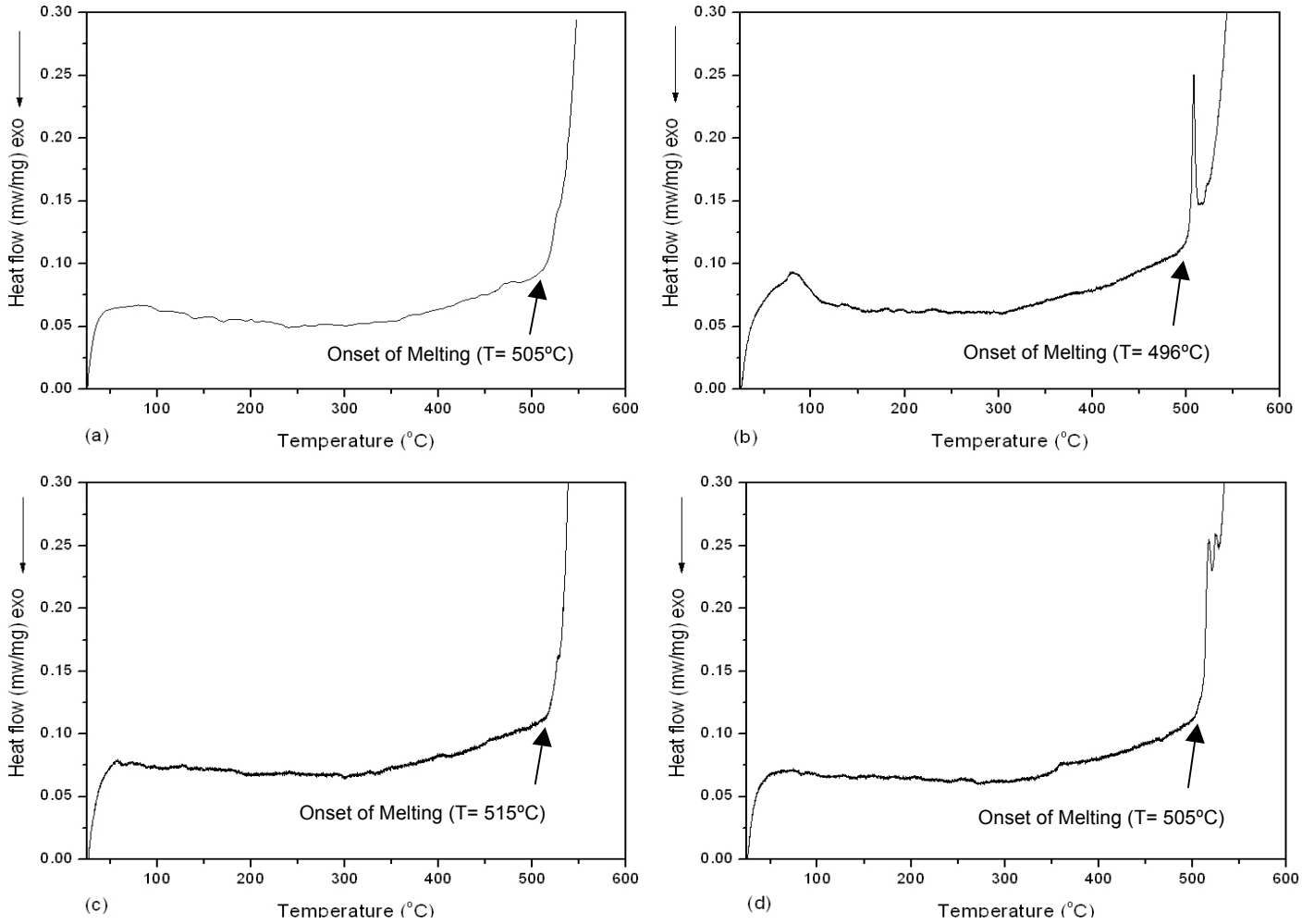
Heat flow (mw/mg) exo
0.30
0.25
0.20
0.15
0.10
0.05
0.00
100
200
300
400
500
600
Temperature (°C)
(a)
Onset of Melting (T= 505ºC)
(b)
Onset of Melting (T= 496ºC)
(c)
Onset of Melting (T= 515ºC)
(d)
Onset of Melting (T= 505ºC)

5.5.2 Effects of Solution Heat Treatment Temperatures on Ageing Response

Solution heat treatment plays an important role on the subsequent precipitation process. Solution heat treatment involves heating of metal to an elevated temperature at which second phases dissolve into the matrix phase to form homogenous solid solution, and subsequently quenched to room temperature to attain metastable, supersaturated solid solution. In general, it is not desirable for partial melting or localized melting to occur during solution heat treatment stage since it can deteriorate the properties of the materials. However, some studies reported that small amount of liquid phase formed during solution heat treatment is proven to be efficacious and has appreciable increase in tensile strength [10]. Thus, it is necessary to determine the optimal solution heat-treating temperatures for Al-Si based alloys.

Compacts were sintered under optimal condition and solutionized at temperatures as shown in Table 5.7, prior to ageing at 120ºC over different ageing times ranging from 1 to 48 hours. The progress of precipitation at a given ageing temperature was shown in Figure 5.5 (a)-(d), where the changes in Vickers hardness were plotted as function of ageing time. The scattering of the hardness results was about ±5%. All the alloys showed similar trend, whereby the hardness value increased until a maximum and subsequently decreased with the prolonged ageing time. From Figure 5.5(a), a remarkable difference in hardness value for Ecka Alumix 231 solutionized at different solution heat treatment temperatures (490ºC, 500ºC, 510ºC and 520ºC) can be noted even after ageing for 60 min. The maximum hardness value of 115.38 HV was achieved by compacts solutionized at 510ºC after ageing for 8 hours at 120ºC. Meanwhile, compacts solutionized at 500ºC required longer ageing time to achieve its

maximum hardness value which was still slightly lower than those solutionized at 510ºC. Subsequent ageing after the time at which the maximum hardness was attained or commonly known as overaging caused a progressive decrease in hardness value. This can be attributed to the growth of the precipitates. Overall, the maximum hardness value attained by Ecka Alumix 231 compacts solutionized at different temperatures prior to ageing at 120ºC followed this sequence: 510 ºC > 500 ºC >520 ºC > 490ºC.

Alloy A attained its maximum hardness value of 131.78HV after solutionized at 510ºC and aged for 12 hours at 120ºC. From Figure 5.5 (b), it can be seen that the maximum hardness values achieved by compacts solutionizined at temperatures of 490ºC and 500ºC were comparatively lower than compacts solutionized at 510ºC. As mentioned earlier in Section 5.5.1, the onset melting of Alloy A was 496ºC. Thus, a small of amount of liquid phase was believed to contribute to a more complete dissolution of alloying elements within the α-aluminum matrix leading to higher strengthening effects during subsequent ageing.

Alloy B, on the other hand, reached the highest hardness value of 110.44HV after solutionizing at 510ºC and subsequently aged at 120ºC (Figure 5.5c). It is believed that solution heat treatment of 500ºC might not be sufficient for complete dissolution of the alloying elements, while solutionizing at 520ºC caused overheating of the compacts. Both of these solution heat treatment temperatures might later contribute to lower maximum hardness values.

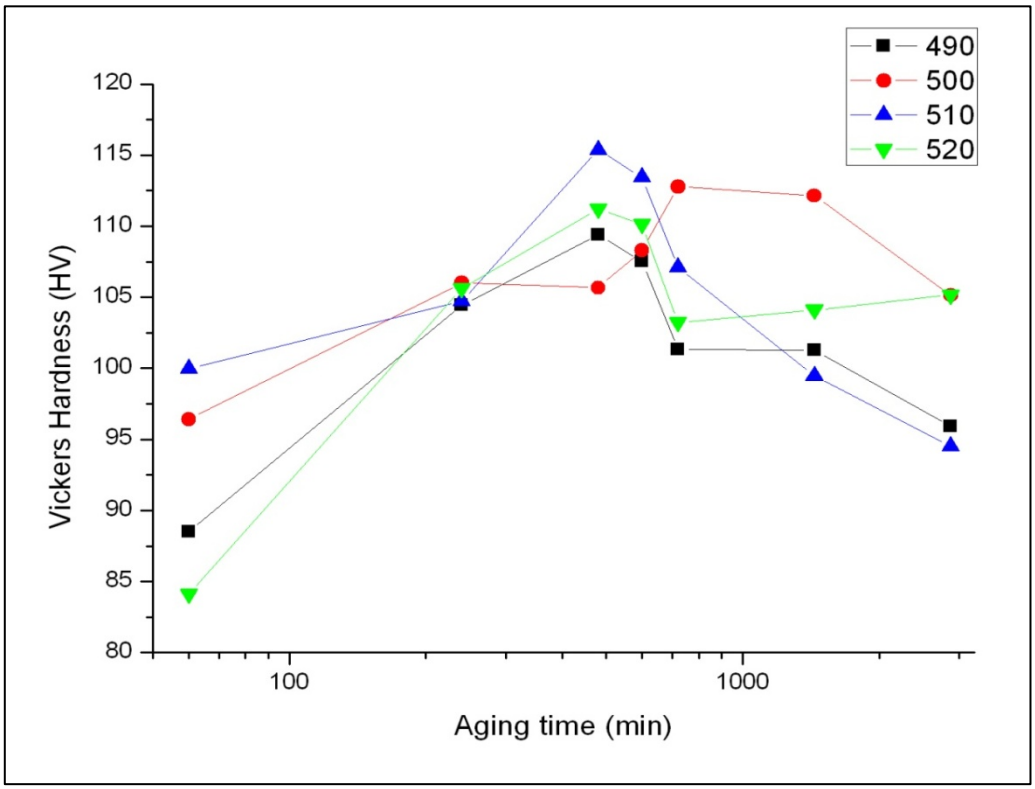

(a)

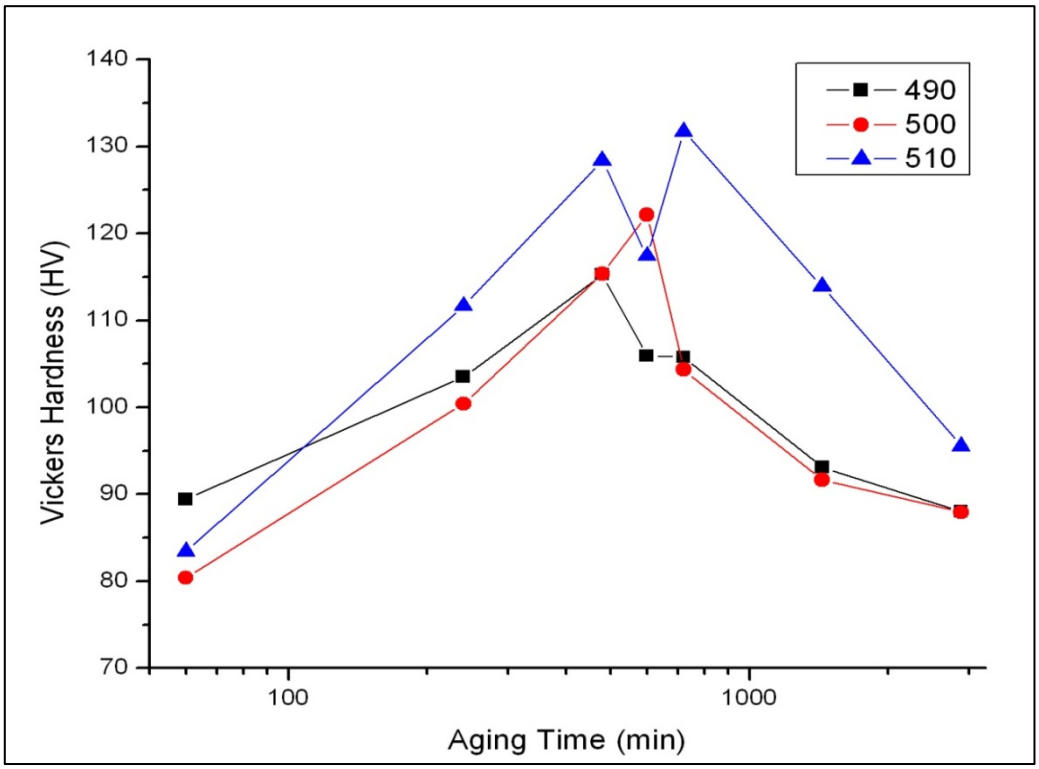

(b)

Figure 5.5. Artificial ageing curves for (a) Ecka Alumix 231 and (b) Alloy A solutionized at different temperatures for 1 hour and aged at 120ºC over a period of 1 to 48 hours.

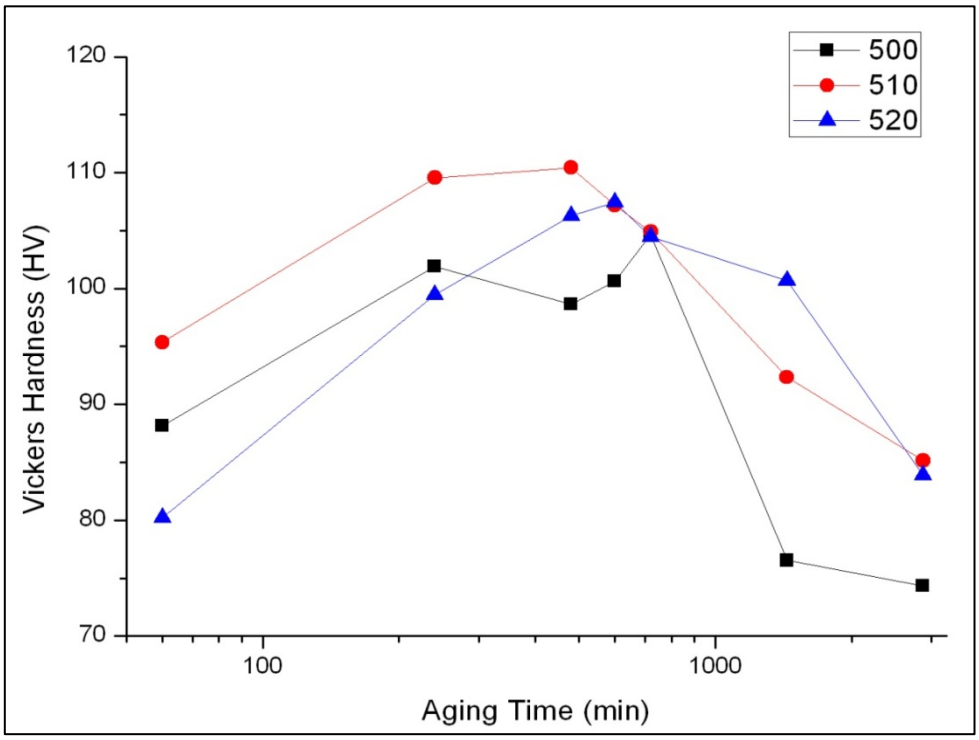

(c)

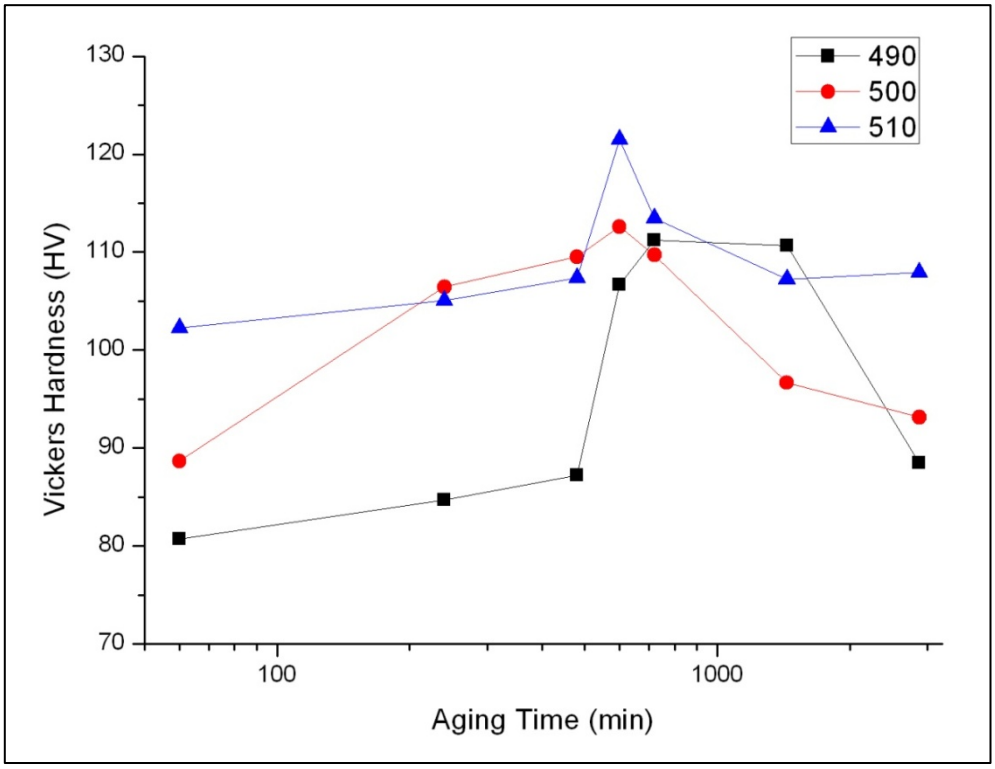

(d)

Figure 5.5 (continued). Artificial aging curves for (c) Alloy B and (d) Alloy C solutionized at different temperatures for 1 hour and aged at 120ºC over a period of 1to 48 hours.

From Figure 5.5 (d), Alloy C with the combined Cu and Ni additions showed that solutionizing temperatures of 510ºC is beneficial. The maximum hardness value of 121.53 HV was reached after ageing for 12 hours at the ageing temperature of 120ºC. A summary of peak hardness for Al-Si based alloys solutionized at optimum temperature and aged at constant temperature of 120ºC over a period of 1 to 48 hours is displayed in Table 5.8. It can be summarized that solution heat treatment of 510ºC was efficacious for all different alloys to allow maximum dissolution of the alloying element into the aluminum matrix. Copper addition was deemed to increase the hardness and possibly the strength of the material. However, nickel addition did not have significant contribution to hardening effects but it showed sign of deterioration. Addition of both copper and nickel addition in Alloy C showed relatively higher hardness value than commercial Ecka Alumix 231 but the hardness value obtained was not greater than Alloy A with individual copper addition.

Table 5.8. Summary of peak hardness for different alloys after being solutionized, quenched and aged at 120ºC at different time intervals.

Alloys	**Peak Hardness (HV)**	**Solutionizing Temperature (ºC)**
Ecka Alumix 231	115.38	510
Alloy A	131.78	510
Alloy B	110.44	510
Alloy C	121.53	510

5.5.3 Effects of Solution Heat-Treatment Times on Ageing Response

Apart from solution heat treatment temperature, solution heat-treatment times also play a crucial role in strengthening of the materials. In general, solution time can vary from less than a minute to 20 hours depending on the thickness of the materials. Sufficient solution heat-treatment time is necessary to allow a satisfactory degree of soluble phase constituent to dissolve within the aluminum matrix in order to achieve a homogenous solid solution. Although the recommended solution time for compacts with the thickness of approximately 9mm to be within the range of 65 to 75 minutes [11], some studies suggested that longer solution time was required for complete dissolution of the soluble phases in Al-Si-Cu-Mg quaternary alloys. In this regards, compacts for different alloys were solutionized at 510ºC and soaked at different time intervals to assess the influence on the resultant hardness value after subsequent ageing at 120ºC.

Figure 5.6 displays a comparison between hardness value for different alloys solutionized over 60 minutes and 600 minutes. Longer solution time did not seem to have significant contribution in hardening effect. Inversely, slight decrease in hardness can be noted. Decrease in hardness value with prolonged solution time was more pronounced with the increasing copper content. The decrease in hardening effects can be attributed to coarsening due to Ostwald ripening.

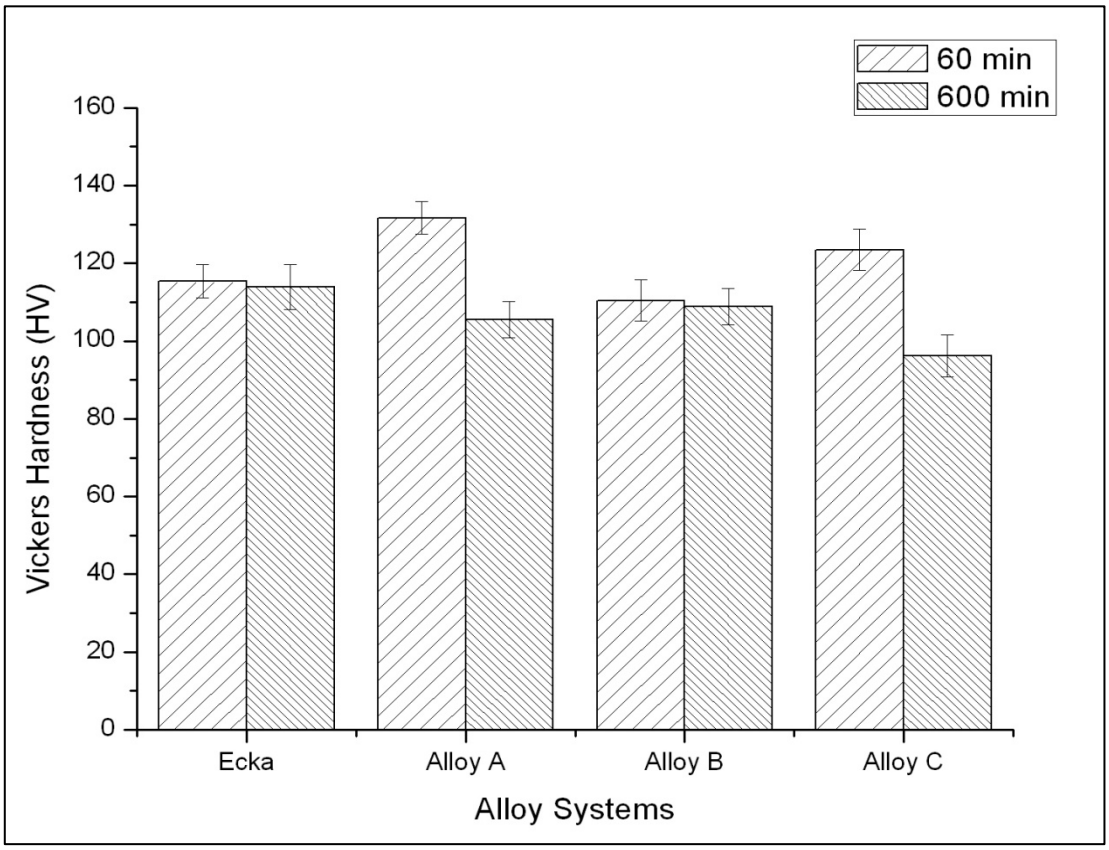

Figure 5.6. Vickers hardness for different alloys solutionized at 510ºC, soaked at different time intervals and subsequently aged at 120ºC.

5.5.4 Age Hardening Characteristic for Al-Si based Alloys

As stated in the literature review, appreciable improvement in mechanical properties of aluminum alloys can be achieved by precipitation caused by decomposition of the supersaturated solid solution during ageing or precipitation-hardening process. The strengthening effects of alloys arise due to hindrance of dislocation motion through the shearing of the coherent or semicoherent particles. Control of experimental ageing conditions is necessary since it can give rise to significant changes in precipitation response for different alloys. Thus, it is necessary to investigate the optimal ageing temperature and time to produce compact with satisfactory strength.

Figure 5.7(a)-(d) shows the changes in microhardness behavior as function of ageing time for different Al-Si based alloys subjected to T6 artificial heat treatment with the ageing temperature varied from 120ºC, 160ºC, 180ºC to 200ºC. It is generally observed that all the alloys experienced an increase in microhardness until a maximum value, after which softening of the compacts started to initiate as evidenced by lowering the microhardness values. The increase of the microhardness value can be attributed to the increase of the size, amount and distribution of the precipitates. Meanwhile, softening in the later stage is mainly due to the growth of the precipitates due to Ostwald ripening and loss of coherency of precipitates within the matrix [11].

The age-hardening characteristic for different alloys is very much dependent on the ageing conditions. It is commonly known that low ageing temperature can lead to longer time for precipitation. From Figure 5.7(a)-(d), it is obvious that peak hardness for the alloys aged at 120ºC was relatively lower than those aged at 160ºC. This can be attributed to low precipitation rate at 120ºC leading to less amount of precipitates

contributing to the hardening effects. However, with the increase of the ageing temperature to 160ºC, all the alloys experienced a more pronounced increase in peak hardness value. It can be noted that the microhardness increase for Alloy A has come top of the list with the peak hardness increased from 131.72HV when aged at 120ºC to 150.30HV when aged at 160ºC. Meanwhile, Ecka Alumix 231, Alloy B and Alloy C experienced a measurable increase in peak hardness from 115.38HV, 110.44 HV and 121.53 HV when aged at 120ºC to 126.23HV, 121.58HV and 132.17HV respectively with the increase of ageing temperature to 160ºC.

With further increase of the ageing temperatures to 180ºC, Alloy A and C experienced a drop in the peak hardness. Meanwhile, Ecka Alumix 231 was among the four alloys which achieved the highest peak hardness of 133.28HV after ageing for 8 hours. A slight increase in microhardness value was also observed for Alloy B, with approximately 123.47HV being achieved when aged at 180ºC. As compared with compacts aged at 160ºC, both Ecka Alumix 231 and Alloy B achieved the peak hardness at relative shorter time with the increase of the ageing temperature to 180ºC as shown in Figure 5.7(a) and (c) respectively.

Continuous increase of ageing temperature to 200ºC was deemed to be detrimental for hardening of alloys since the peak hardness for these alloys were comparatively lower than those aged at 160ºC and/or 180ºC. Despite the undesirable lowering of the peak hardness, a measurable increase in hardening can be noted during the early stage of ageing. This can be evidenced with the noticeable increase in microhardness when aged for 1 hour for all the alloys.

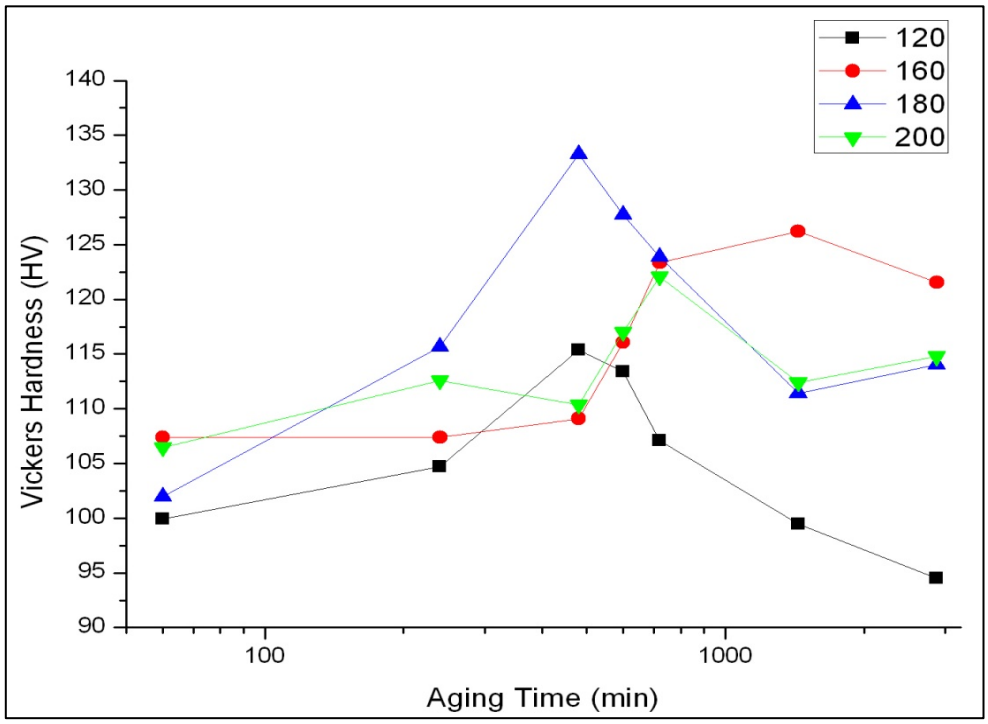

(a)

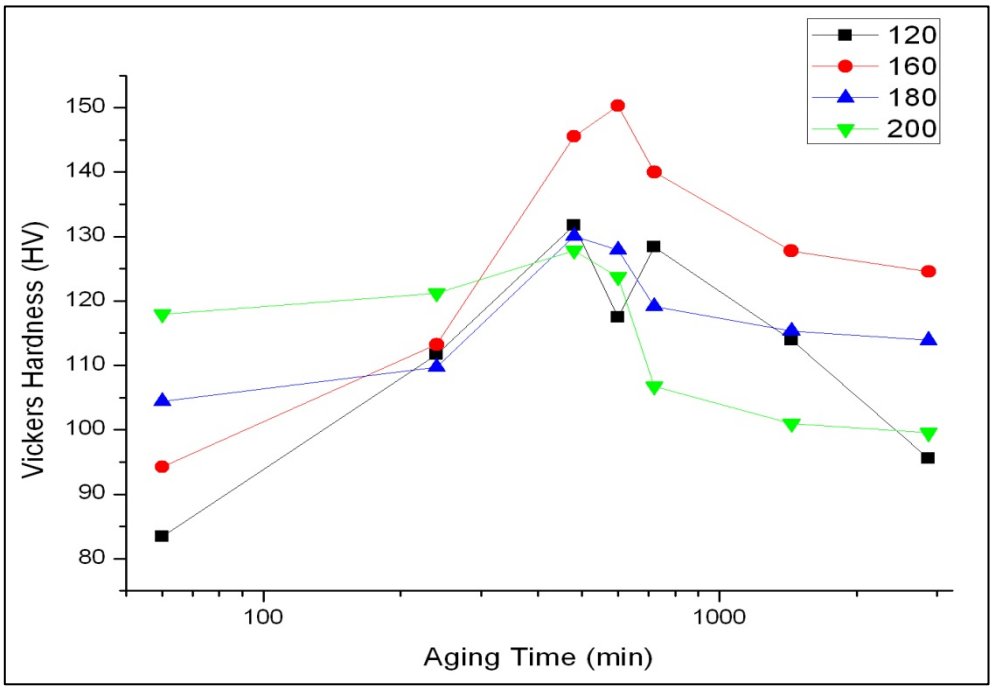

(b)

Figure 5.7. Artificial aging curves for (a) Ecka Alumix 231 (Al-15Si-2.5Cu-0.5Mg) and (b) Alloy A (Al-15Si-4.5Cu-0.5Mg) solutionized at 510ºC and aged at different temperatures.

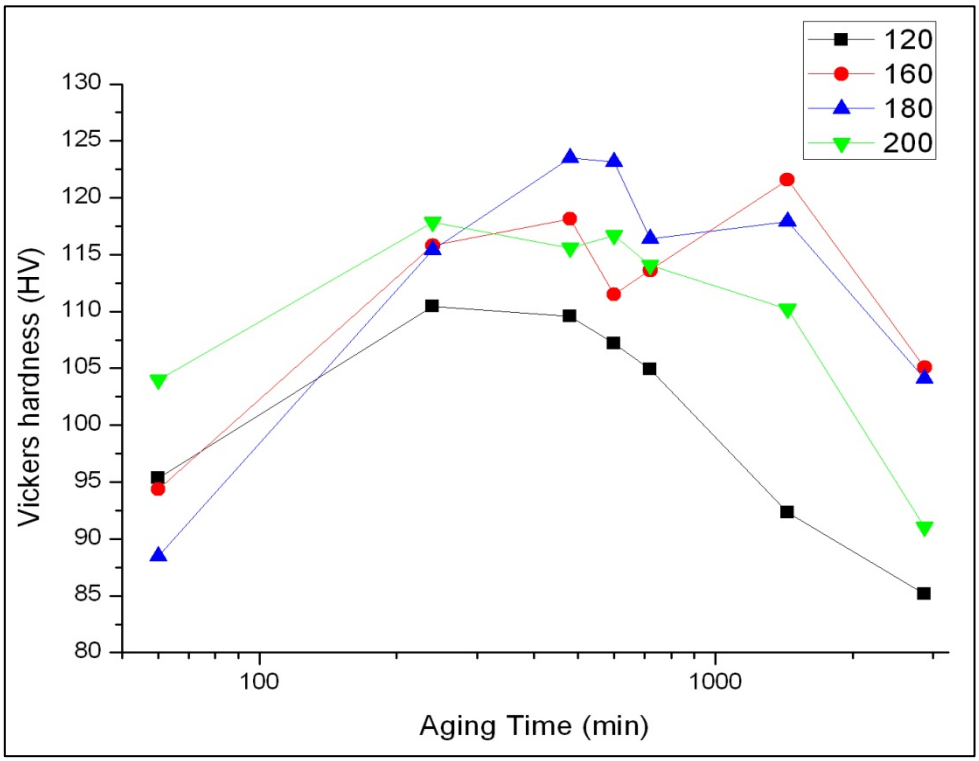

(c)

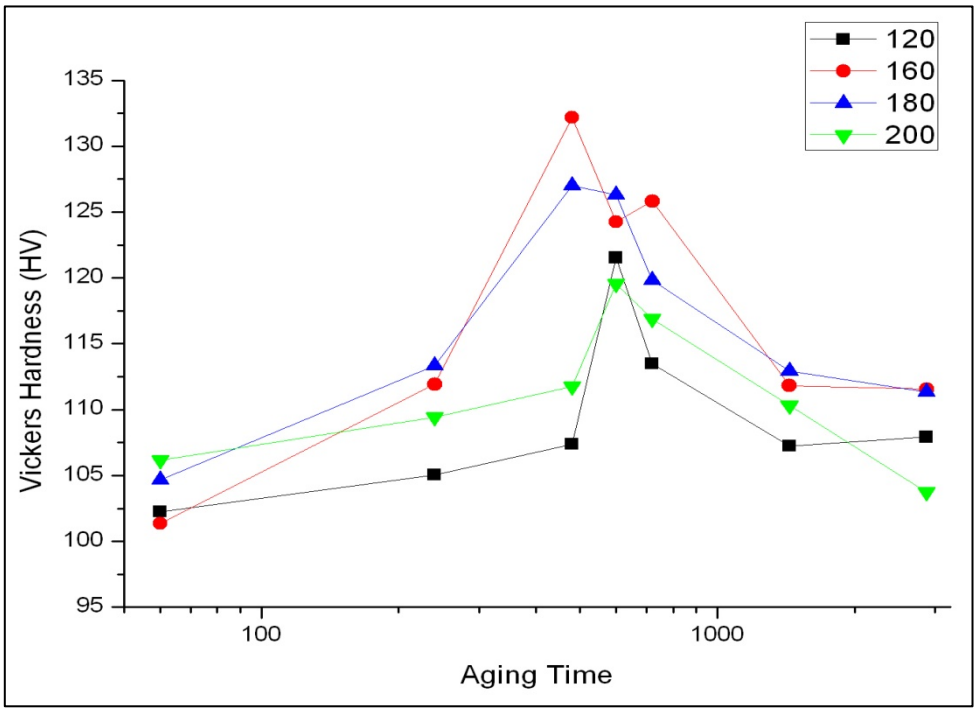

(d)

Figure 5.7 (continued). Artificial aging curves for (c) Alloy B (Al-15Si-2.5Cu-0.9Ni-0.5Mg) and (d) Alloy C (Al-15Si-4.5Cu-0.9Ni-0.5Mg) solutionized at 510ºC and aged at different temperatures.

Apart from ageing temperature and ageing time, composition variation also plays a vital role in influencing the ageing characteristic. Figure 5.8 summarizes the peak hardness for different alloy systems obtained after subjected to different ageing temperatures. It can be clearly seen that Alloy A and C with higher copper content up to 4.5wt%Cu required lower ageing temperature of 160°C to achieve the maximum hardness. Moreover, increase of copper content also enhanced the microhardness of the compacts greatly, with the microhardness of Alloy A caming top of the list after subjected to the artificial ageing. Addition of nickel, on the other hand, manifested a drop in microhardness value as compared to Ecka Alumix 231 over the range of ageing temperatures being applied.

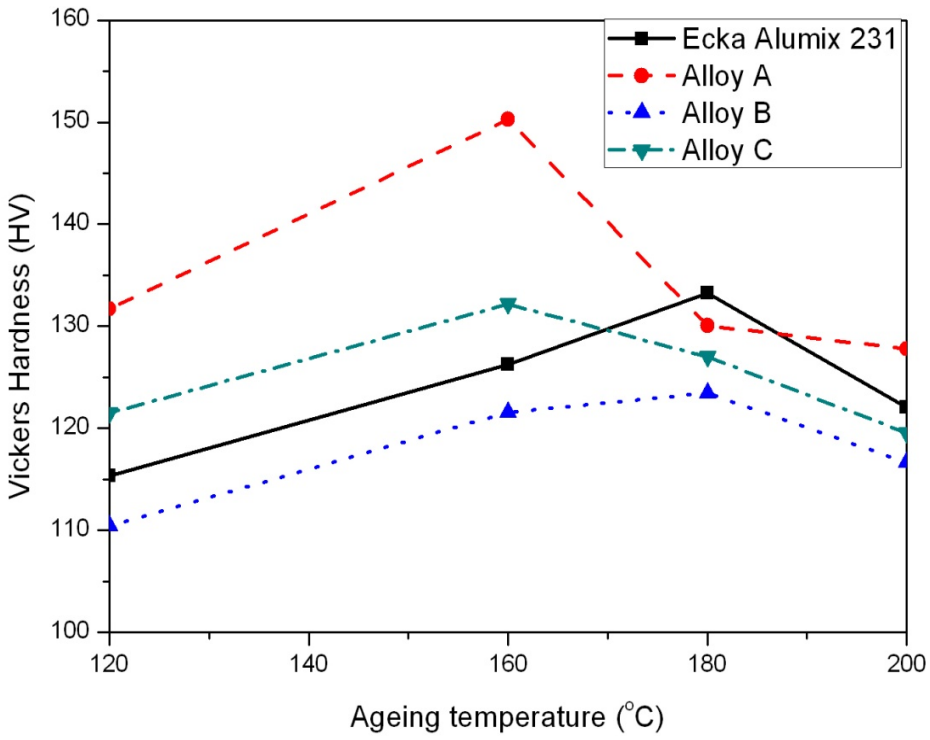

Figure 5.8. Maximum Vickers hardness obtained at different ageing temperatures for Ecka Alumix 231, Alloy A, B and C.

A further comparison of microhardness values for different alloys between the as –sintered state and after T6 artificial age-hardening is displayed in Table 5.10. It can be seen that the effect of composition variation on microhardness is more significant after subjected to optimal heat treatment. Increase of Cu content up to 4.5wt% as found in Alloy A contributed to a significant rise in microhardness value from 70.13HV in as –sintered state to 150.30HV at peak-aged condition which marked a total increase of 80.17HV. The microhardness increase in Alloy A was comparatively higher than Ecka Alumix 231, whereby only an increase of 62.77 HV from as-sintered state to peak aged condition was noted for Ecka Alumix 231. The strong increase in hardness with the increase of copper addition is mainly due to the solid solution strengthening of copper on α-aluminum matrix.

Nickel addition, however was detrimental to both sintering and precipitation hardening. Both Alloy B and Alloy C showed relatively lower microhardness value in the as-sintered state with only 60.73 and 60.94 observed respectively. Although both alloys experienced an increase in microhardness value after heat treatment, Alloy B with addition of 0.9wt% Ni showed approximately the same amount of microhardness increase as compared to Ecka Alumix 231. Alloy C which contained both Cu content of 4.5wt% and Ni content of 0.9wt%, on the other hand, was observed to have significant microhardness increase up to 131.17 HV which was still lower than microhardness value as observed in Alloy A. Thus, it can be summarized that Ni addition is not beneficial in strengthening of the alloys.

Table 5.10. Hardness increase between the sintered and heat-treated compacts for different alloys.

Alloy System	Vickers Hardness (HV)		Hardness Increase
	Sintered Compact	Heat Treated Compact	
Ecka Alumix 231	70.51	133.28	62.77
Alloy A	70.13	150.30	80.17
Alloy B	60.73	123.47	62.74
Alloy C	60.94	132.17	71.23

5.6 Precipitation Behaviors for Al-Si based Alloys

To study the precipitation behavior during ageing, differential scanning calorimetry (DSC) was employed. Figure 5.9 shows the rate of heat evolution for different alloys plotted as function of temperatures. It can be seen that each alloy exhibited two exothermic peaks within the temperature range of 190°C to 350°C. Each exothermic peak denoted the occurrence of specific precipitation events. Formation of GP zones was not detected in all alloys since there was no exothermic peak being observed between 100°C to 200°C. The first exothermic peak appeared within the temperature range of 190°C to 260°C can be attributed to the precipitation of coherent θ", S" and/or Q" phases. Meanwhile, the second exothermic peak which occurred between the ranges of 260 to 250°C can be attributed to the precipitation of semi-coherent θ', S' and/or Q' phases.

Additionally, it has been reported that precipitation dynamics of the different alloys is closely related to the position of the exothermic peak in DSC curves [12]. For Alloy A with increased copper content, there was no shift in the position for peak 1 but peak 2

was shifted to a lower temperatures. This indicated that increase copper content promoted the precipitation of semi-coherent phases. Meanwhile, both Alloy B and C was found to have peak 1 slightly shifted to higher temperature which indicated higher thermodynamical stimulus required for precipitation of coherent phases for alloys with nickel additions. Additionally, Alloy B showed less significant peak 2 which can be attributed to no and/or less precipitation of semi-coherent phases for Alloy B. This might contribute to lowering of hardness value. Further understandings on the precipitates formed during ageing were investigated using transmission electron microscopy (TEM).

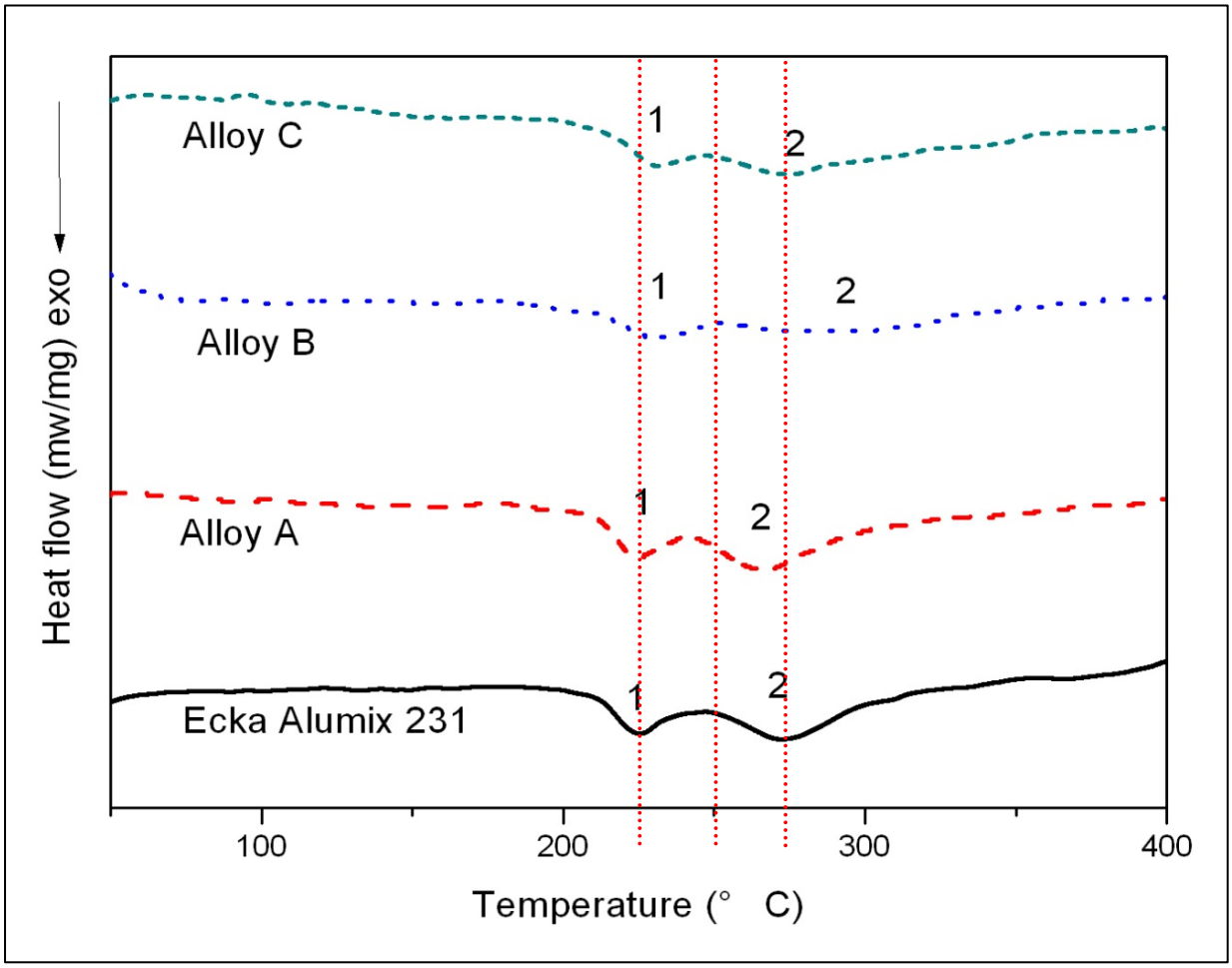

Figure 5.9. DSC traces at a heating rate of 10°C/min for the as-quenched alloys after solution treatment

A summary of the reaction enthalpy is shown in Table 5.11. Reaction enthalpy refers to the area under the exothermic peaks which provides information regarding molar heat of reaction and volume fraction of phases presented [13]. Addition of copper was deemed to increase the reaction enthalpy which might possibly relate to increase in the amount of precipitates during ageing, whilst nickel addition showed a decrease in the reaction enthalpy. This indicates that nickel addition impeded the formation of useful precipitates which can strengthen the alloys. This is consistent with the lower hardness value in Alloy B and C resulted from nickel addition as observed in Section 5.5.4.

Table 5.11. Reaction Enthalpy (ΔQ), J/g for different alloy system

Alloy System	**Reaction Enthalpy(ΔQ), J/g**
Ecka Alumix 231	-26.11
Alloy A	-28.09
Alloy B	-21.14
Alloy C	-23.35

5.7 Microstructural Development

5.7.1 Microstructural Characterization of the Sintered Compacts

It has previously been discussed in Section 5.4 that addition of Cu and Ni can improve the sintering response. Energy dispersive X-rays was performed on compacts sintered under nitrogen atmosphere as a means to assess the microstructural changes for different alloys. The EDX identification of the phases presented in all different alloys was substantiated by the XRD results as shown in Figure 5.11 and Figure 5.14.

Figure 5.10 depicts the well-sintered microstructures of Alloy A (Al-15Si-4.5Cu-0.5Mg), with the chemical analysis for different locations (Point 1-5) given in Table 5.12. Similar to the microstructure of Ecka Alumix 231, the necklace-like bright area which can be associated with the formation of $CuAl_2$ (θ) was found to distribute along the grain boundaries (Point 1). However, Alloy A with higher copper content (4.5wt%) was found to have substantial increase in the amount of $CuAl_2$ (θ) phase along the grain boundaries. This comes in good agreement with the XRD analysis as displayed in Figure 5.11, whereby higher intensity of θ phase was noted. Furthermore, more copper was also found to diffuse into the aluminum matrix. This can be evidenced from EDX results, whereby the copper content within the aluminium matrix increased from 0.68 at% (Point 5, Table 4.9) in Ecka Alumix 231 to 0.89 at% (Point 5, Table 5.12) as found in Alloy A. Presence of Q phase ($Cu_2Mg_8Si_6Al_5$) and Fe-rich region with the composition close to $FeSiAl_5$ can also be traced within Alloy A as indicated by Point 2 and 3 respectively.

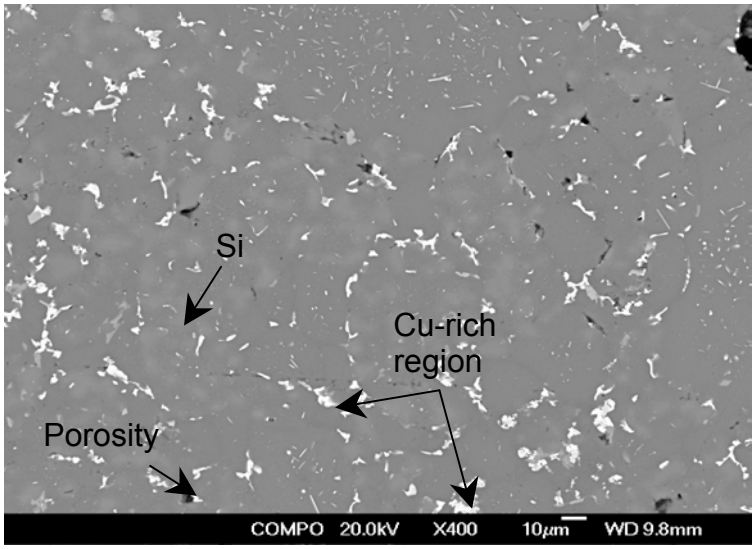

(a)

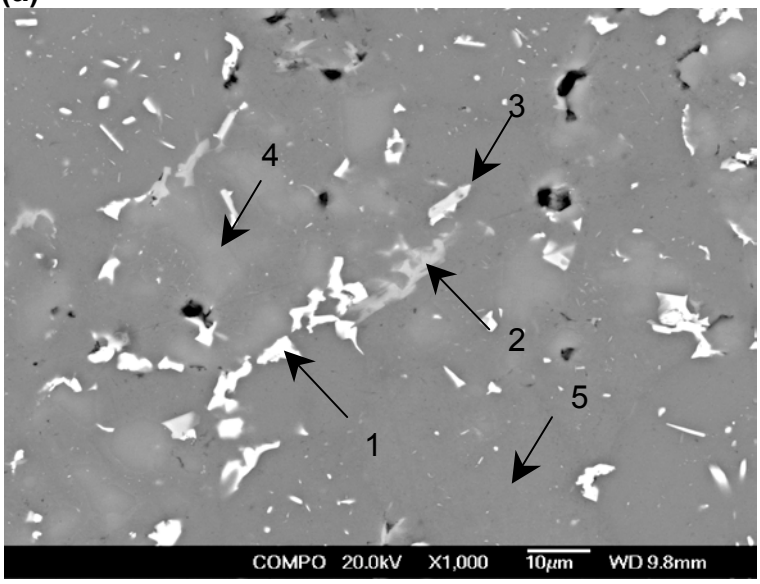

(b)

Figure 5.10. Backscattered electron micrograph of the sintered Alloy A (Al-15Si-4.5Cu-0.5Mg) at (a) 400X magnification and (b) 1000X magnification

Table 5.12. EDX results corresponding to the point locations shown in Figure 5.10 (at%)

Point	Al	Si	Cu	Mg	Fe
1	73.78	1.07	25.15	0.00	0.00
2	35.08	31.56	6.40	26.96	0.00
3	66.01	19.65	0.46	0.00	13.88
4	17.98	82.02	0.00	0.00	0.00
5	98.68	0.43	0.89	0.00	0.00

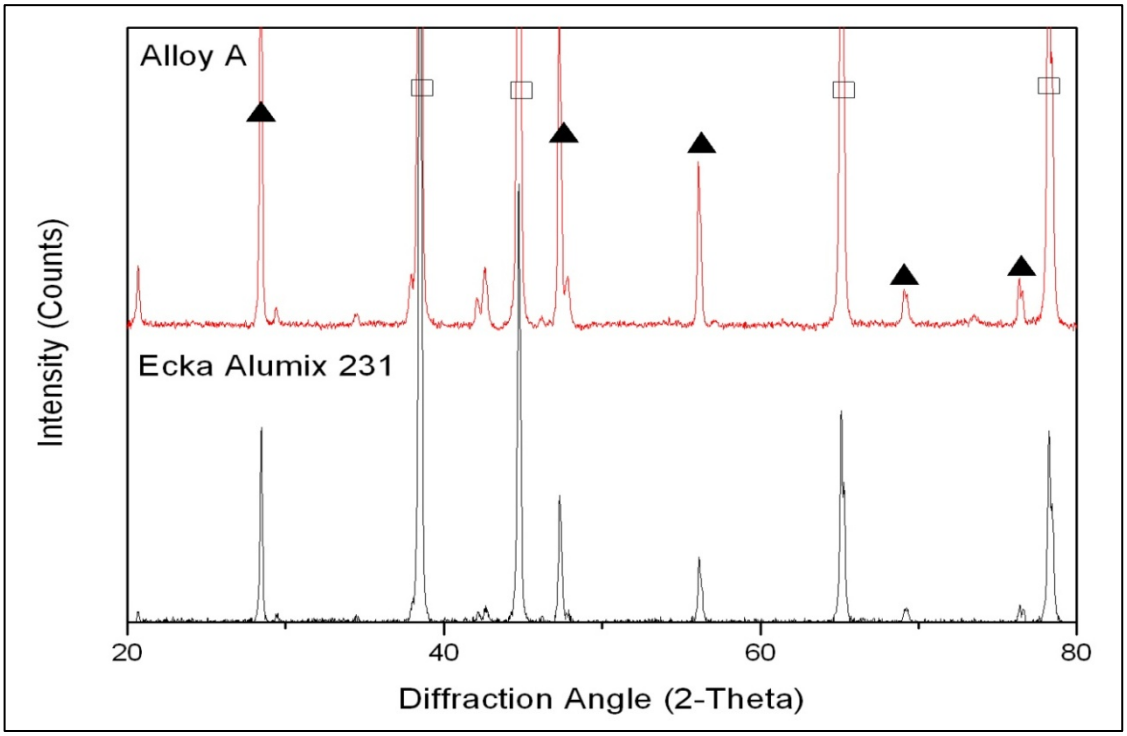

(a)

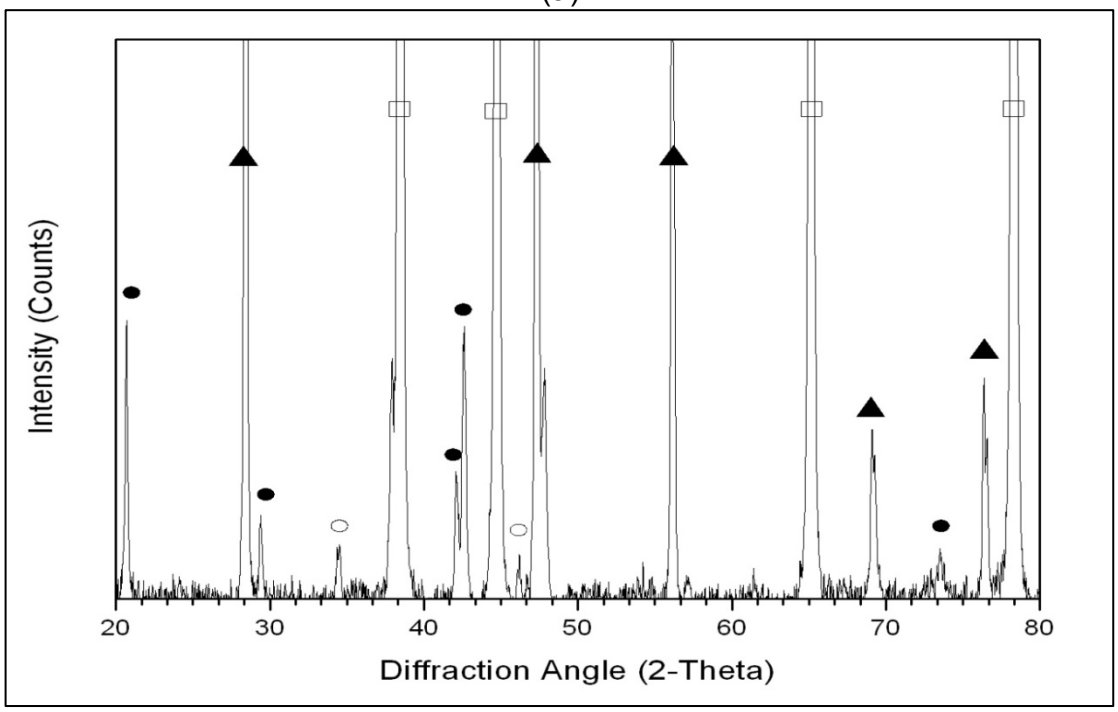

(b)

Figure 5.11. XRD pattern corresponding to sintered (a) Ecka Alumix 231 and Alloy A (Al-15Si-4.5Cu-0.5Mg). (b) Detailed XRD pattern corresponding to Alloy A sintered in nitrogen atmosphere. Phases positively identified were α- Al (□), Si (▲), θ phase (●), and Q phase (○).

With the addition of 0.9wt% Ni, both Alloy B (Al-15Si-2.5Cu-0.5Ni-0.5Mg) and C (Al-15Si-4.5Cu-0.9Ni-0.5Mg) started to exhibit the ribbon like features as displayed in Figures 5.12 and 5.13. The spreading of the ribbon-like features was more obvious in Alloy C with higher copper content up to 4.5wt%. The EDX point analyses were again carried out over a series of location within the microstructure for each alloy to determine their chemical constituents. The bright ribbon-like features were found to be Al-Ni based intermetallic phase in which appreciable copper had dissolved. XRD traces as shown in Figure 5.14 again confirmed that this intermetallic phase can be attributed to the formation of $Al_3(Ni,Cu)_2$ phase. Other phases detected included α-aluminum with minor concentration of copper and silicon, primary silicon, $CuAl_2$ (θ) phase and Q phase ($Cu_2Mg_8Si_6Al_5$). Since copper had appreciable solubility in nickel, it was observed that the copper content within aluminum matrix decreased greatly with only 0.36 at% being traced in Alloy B. Although Alloy C had similar copper content as Alloy A (4.5wt%), the amount of copper content diffused into aluminum matrix was comparatively lower, with only 0.67at% being detected due to the formation of $Al_3(Ni,Cu)_2$ phase. The presence of Al-Ni-Si-Cu-Fe intermetallic was also being detected in both Alloy B and C but appeared at greatly reduced frequency. The complex intermetallic was observed to be entrapped within the ribbon-like phases and exhibited blocky shaped structures as indicated by Point 3 in Figure 5.12 and Figure 5.13 respectively. Presence of Fe was deemed to reduce the concentration of copper and nickel. Its atomic ratios suggested that this phase was possibly a variant of Al_9FeNi. However, no plausible identification can be confirmed due to its chemical complexity and small size.

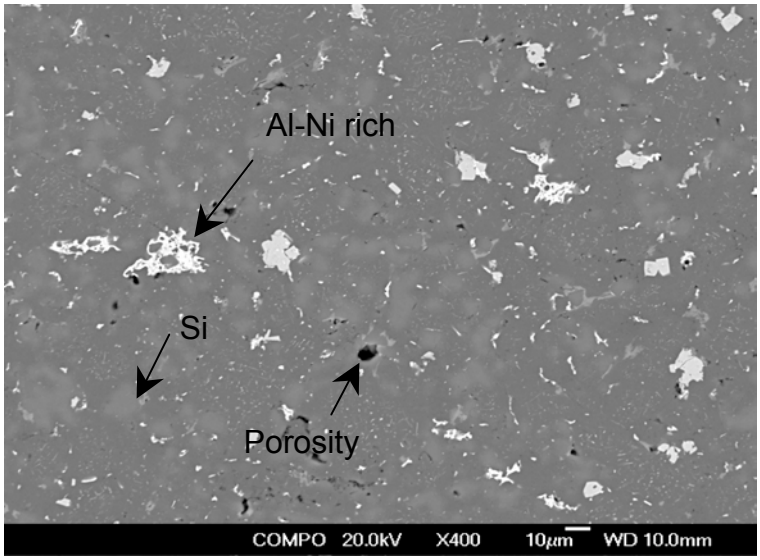

(a)

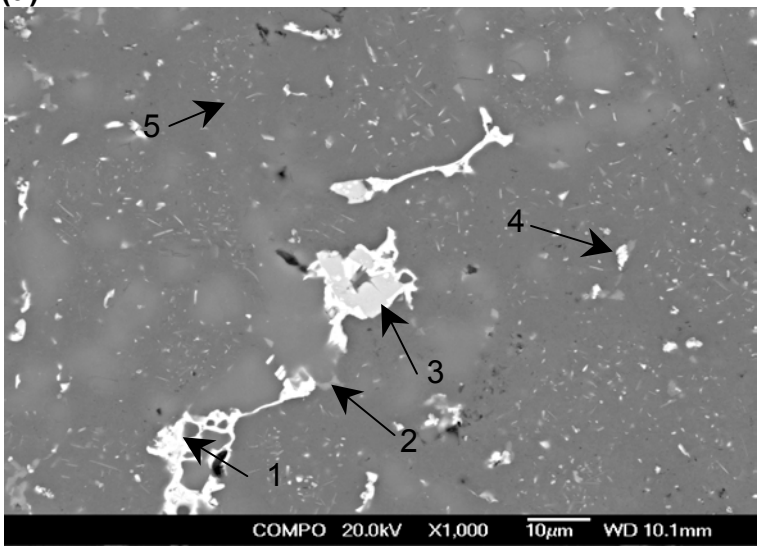

(b)

Figure 5.12. Backscattered electron micrograph of the sintered Alloy B with the nominal composition of Al-15Si-2.5Cu-0.9Ni-0.5Mg (wt%).

Table 5.13: EDX results corresponding to the point locations shown in Figure 5.11 (at%)

Point	Al	Si	Cu	Ni	Mg	Fe
1	60.84	3.53	15.55	20.08	0.00	0.00
2	49.04	21.14	6.14	0.69	23.00	0.00
3	70.24	6.86	5.02	12.96	0.00	4.92
4	75.48	1.03	21.29	0.72	1.48	0.00
5	95.90	3.49	0.36	0.00	0.25	0.00

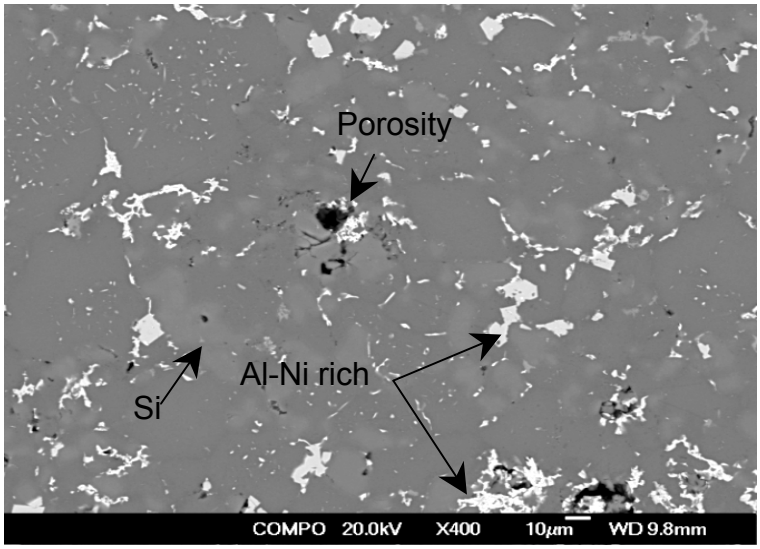

(a)

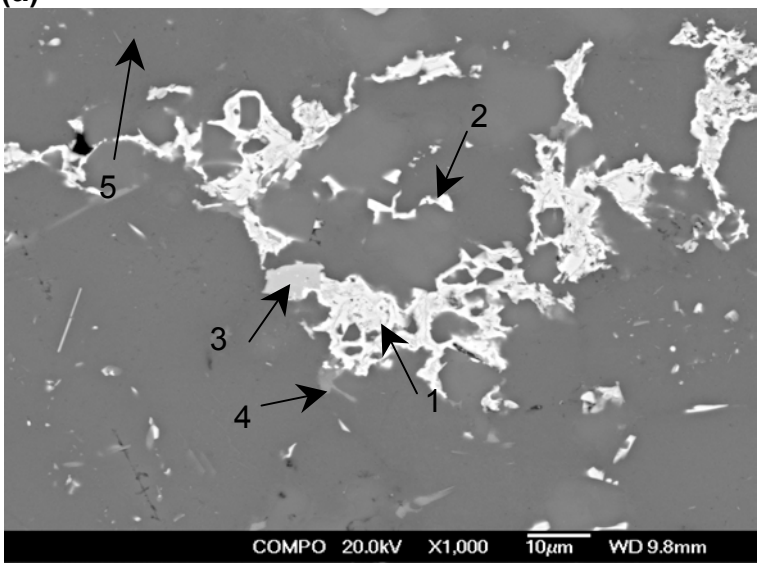

(b)

Figure 5.13. Backscattered electron micrograph of the sintered Alloy C with the nominal composition of Al-15Si-4.5Cu-0.9Ni-0.5Mg (wt%).

Table 5.14: EDX results corresponding to the point locations shown in Figure 5.12 (at%)

Point	Al	Si	Cu	Ni	Mg	Fe
1	64.33	0.00	22.11	13.56	0.00	0.00
2	69.85	9.92	20.23	0.00	0.00	0.00
3	69.78	6.01	5.11	14.00	0.00	5.10
4	43.30	28.19	6.62	0.40	21.48	0.00
5	98.49	0.85	0.67	0.00	0.00	0.00

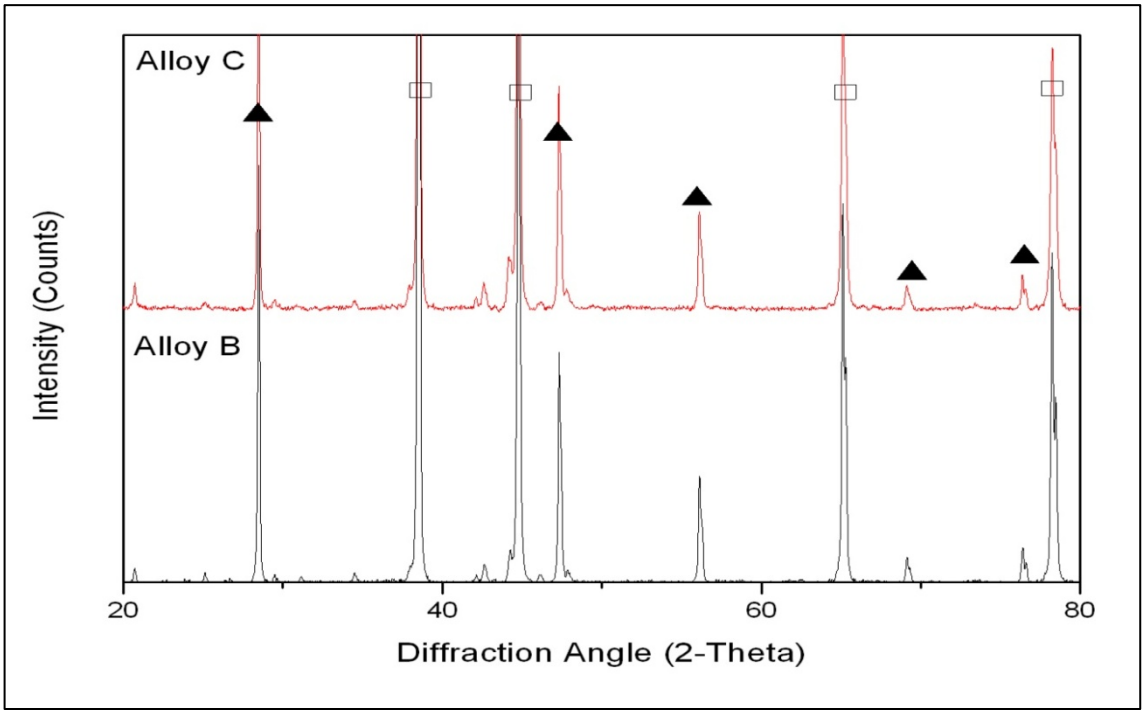

(a)

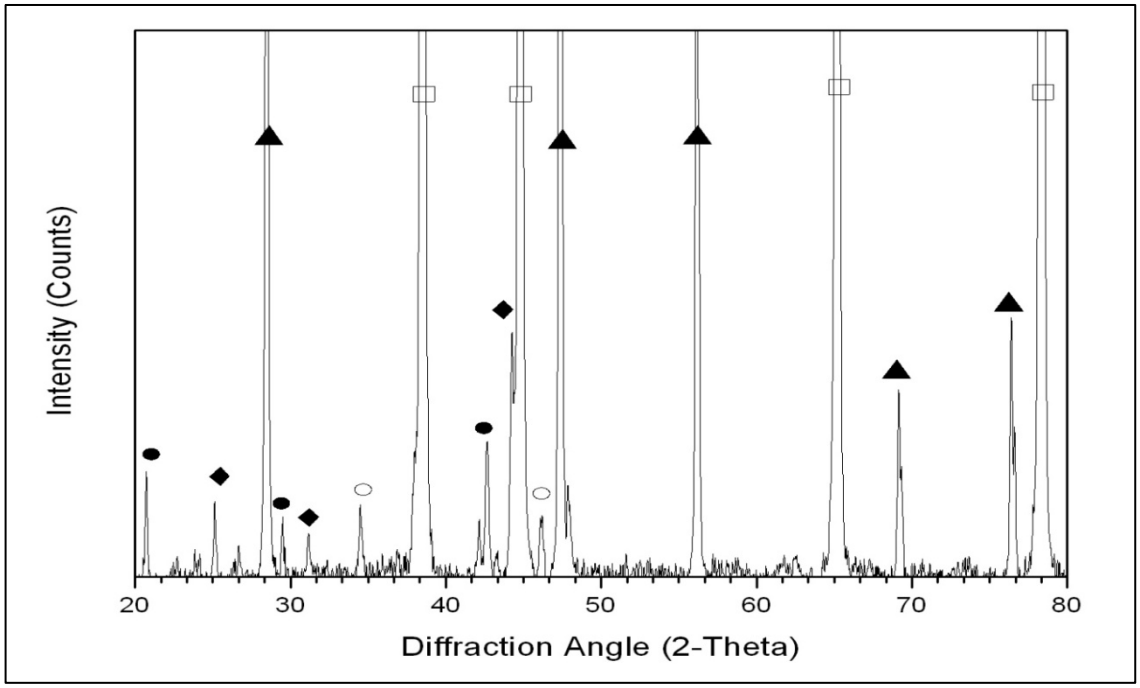

(b)

Figure 5.14. XRD pattern corresponding to (a) sintered Alloy B and C. (b) Detailed XRD pattern corresponding to Alloy C sintered in nitrogen atmosphere. Phases positively identified were α- Al (□), Si (▲), θ phase (●), Q phase (○), and Al_3Ni_2 phase (♦).

5.7.2 Microstructural Characterization of the Sintered and Solution heat-treated Compacts

Solution heat treatment plays a significant role in influencing the precipitation hardening. It has previously been determined in Sections 5.5.2 and 5.5.3 that all the alloys were subjected to the same optimal solution heat treatment condition, whereby solution temperature of 510ºC and solutionizing time of 1 hour were required. This allowed sufficient dissolution of alloying elements into the aluminum matrix. Figure 5.15(a)-(d) displays the back-scattered electron images for Ecka Alumix 231, Alloy A, B and C quenched directly after subjected to optimal solution heat treatment.

The back-scattered image for Ecka Alumix 231 as displayed in Figure 5.15(a) was relatively featureless with α-aluminum grains and porosity being discernible. Trace of Fe-rich region which can be associated with $FeSiAl_5$ remained intact. As compared with the microstructures of the as-sintered compacts, the bright copper rich region around the grain boundaries which has been determined to be $CuAl_2$ (θ) phase was no longer being observed after the solution heat treatment. This result was again substantiated by the XRD result as shown in Figure 5.16 with the absence of the peaks for θ phase.

Unlike Ecka Alumix 231, although similar solution heat treatment condition was applied, microstructure of Alloy A was found to have bright area denoting the presence of copper-rich regions distributed around the grain boundaries. The amount of bright θ phase as observed in microstructure attained after solution heat treatment and quenching, however, was very much reduced as compared to that of the

as-sintered stage. This can be attributed to the dissolution of some copper-rich phases into the α-aluminum matrix during the solution heat treatment. XRD results again confirmed the presence of θ phase within the compacts but no discernible traces of Q phase were being observed. From Figure 15.15(c) and (d), it can be seen that the bright ribbon-like structure as observed in the sintered Alloy B and C (Figure 5.12 and 5.13) persisted even after solution heat treatment. The chemical composition of this ribbon-like structure was similar to that previously determined in 5.7.1, whereby it denoted the presence of Al_3Ni_2 into which appreciable copper had dissolved. Similar to Alloy A, no discernible traces of Q phase are observed from the XRD result of Alloy B and C after undergoing solution heat treatment and quenching. Moreover, the XRD traces for Alloy C also suggested that not all the Al_2Cu or θ phase had dissolved into the solid solution since minor amount of θ phase can still be detected.

Apart from identifying the phases presented, it is also important to investigate the copper and magnesium concentration within the α-aluminum matrix. Figure 5.17 shows that the copper content (at%) for all alloys increased significantly after solution heat treatment. Table 5.15 further provides a summary that detailed the average atomic percentage of copper and magnesium in the solid solution for different alloys. It can be seen that the amount of copper concentration in the solid solution decreased with the addition of Ni. Meanwhile, addition of copper up to 4.5wt% can contribute to a significant increase in the copper concentration in the solid solution due to the dissolution of more copper-rich phase into the solid solution during solution heat treatment. Furthermore, increase of the copper content also contributed to an increase in the Cu:Mg ratio with the highest Cu:Mg ratio of 7.07 being noted for Alloy

A. Variation in the Cu:Mg ratio can influence the precipitation which will be discussed in details in Section 5.9.4.

As mentioned previously in Section 5.5.3, solution heat-treating time of 1 hour is sufficient to allow the dissolution of soluble constituent into the solid solution. It has previously been determined that increase of the solution heat-treating time up to 10 hours did not seem to enhance the hardening effect of the compact. In fact, slight decrease in the hardness was noted with the prolonged solution heat-treating time. Figure 5.18 displays the typical microstructural changes experienced for all alloys solution heat treated at different durations. Microstructures of Alloy A solution heat treated at 510^{o}C for 1 and 10 hours were used as examples. It can be seen that most of silicon-rich phase appeared in irregular blocky shape although some experienced fragmentation and spheroidization by breaking into small spherical or round shape. With the prolonged solution heat-treating time up to 10 hours, it can be seen that fragmentation and spheroidization occurred extensively. More silicon-rich phases were broken into small particles. Coarsening of the silicon-rich phases became more obvious with the extended time for solution heat treatment. The large blocky silicon-rich phases solution heat-treated at 10 hours were comparatively larger than those solution heat-treated at 1 hour which was suggested to be due to Ostwald ripening. Although it has been reported elsewhere that longer solution treating time was required for dissolution of blocky Al_2Cu as found in alloys with high copper content (e.g. Alloy A and C) [14], presence of Al_2Cu can still be detected even after solution heat treating for 10 hours in Figure 5.18(b).

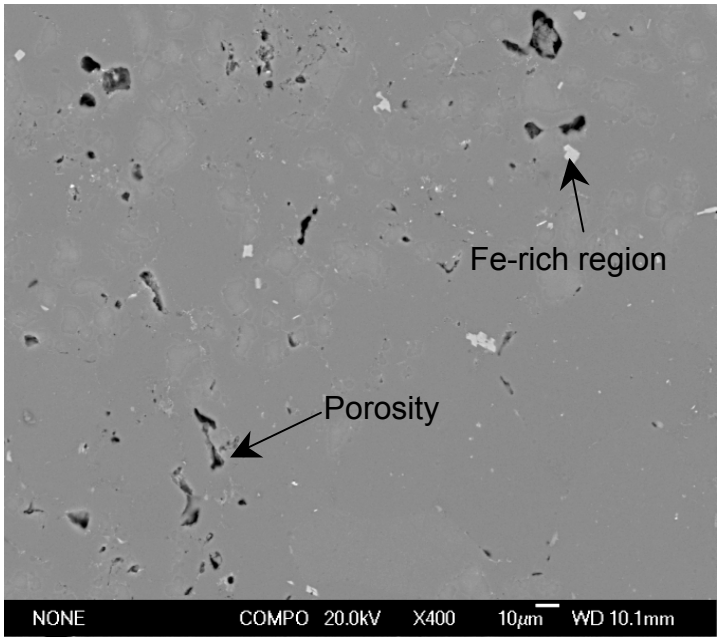

(a)

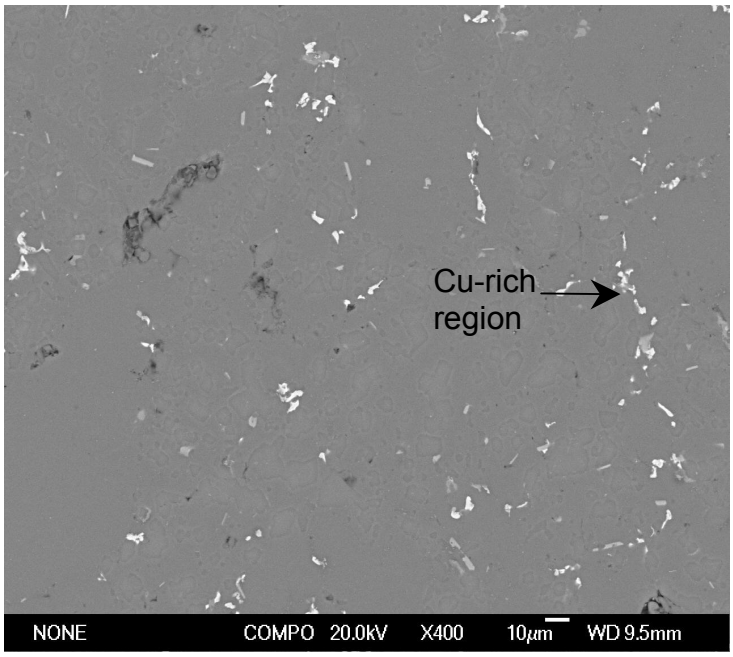

(b)

Figure 5.15. Backscattered electron micrograph of the as quenched compacts after solution heat treatment : (a) Ecka Alumix 231(Al-15Si-2.5Cu-0.5Mg) and (b) Alloy A (Al-15Si-4.5Cu-0.5Mg)

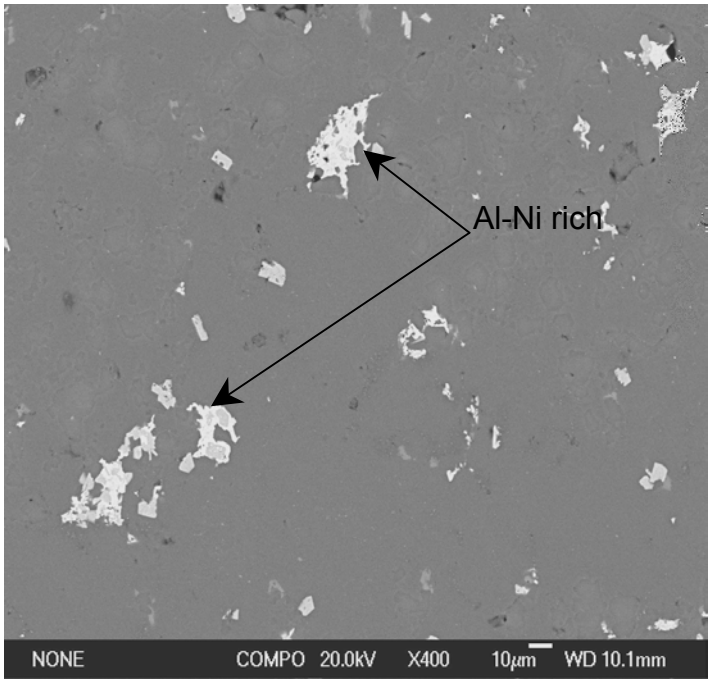

(c)

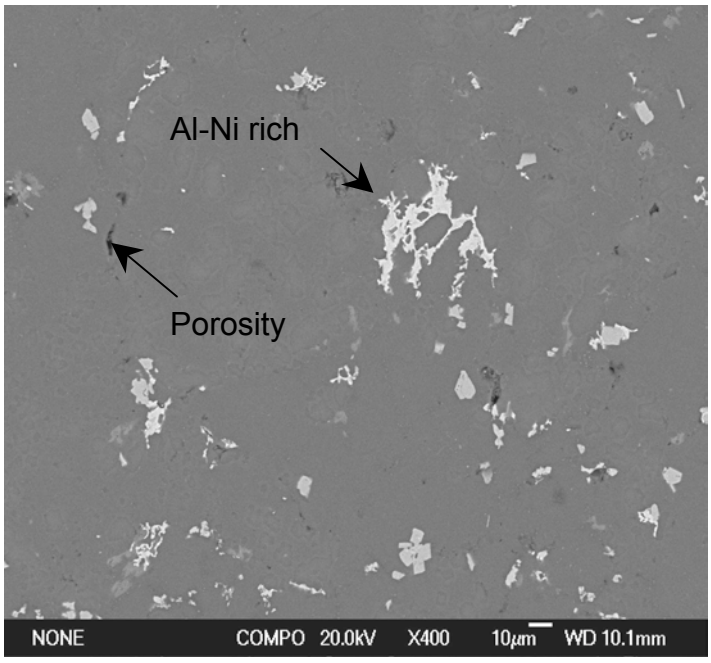

(d)

Figure 5.15 (continued). Backscattered electron micrograph of the as quenched compacts after solution heat treatment: (c) Alloy B (Al-15Si-2.5Cu-0.9Ni-0.5Mg) and (d) Alloy C (Al-15Si-4.5Cu-0.9Ni-0.5Mg).

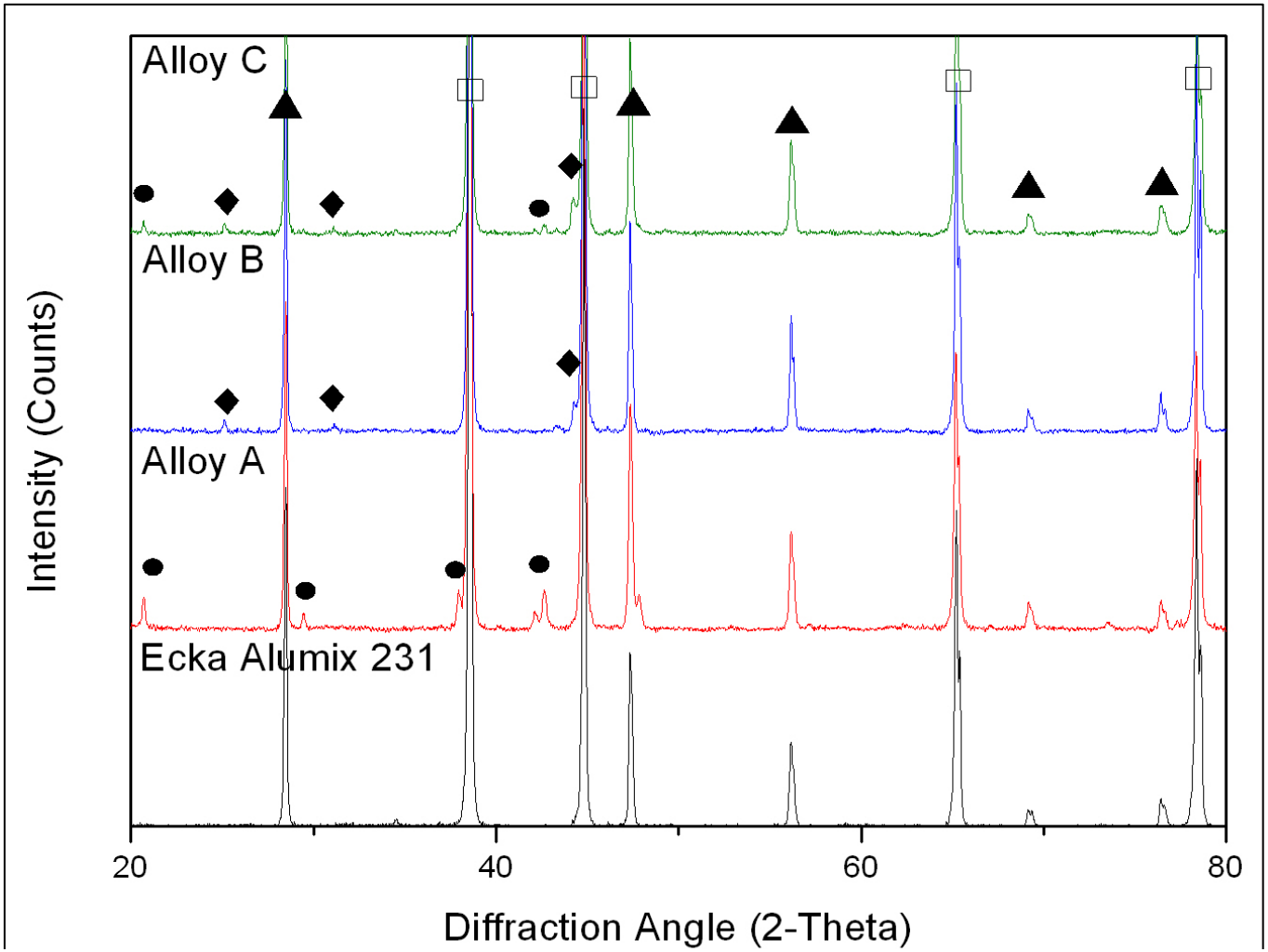
Alloy C
Alloy B
Alloy A
Ecka Alumix 231
Intensity (Counts)
20
40
60
80
Diffraction Angle (2-Theta)

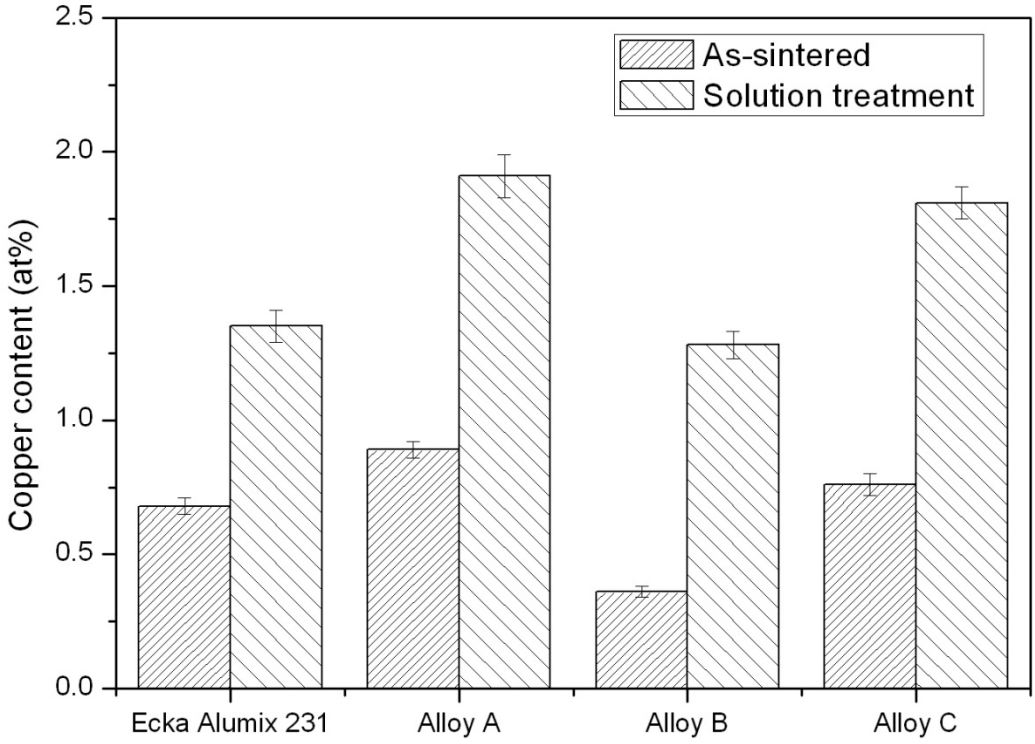

Figure 5.17. Comparison of the atomic percent of copper in α-aluminum matrix between as-sintered state and after solution heat treatment/quenching

Table 5.15: Average atomic percent of copper and magnesium in solid solution for different alloys

Alloys	**Cu (at%)**	**Mg(at%)**	**Cu:Mg ratio**
Ecka Alumix 231	1.35 ± 0.06	0.32 ± 0.06	4.22
Alloy A	1.91 ± 0.08	0.27 ± 0.03	7.07
Alloy B	1.28 ± 0.05	0.31± 0.04	4.13
Alloy C	1.81 ± 0.06	0.28 ± 0.06	6.46

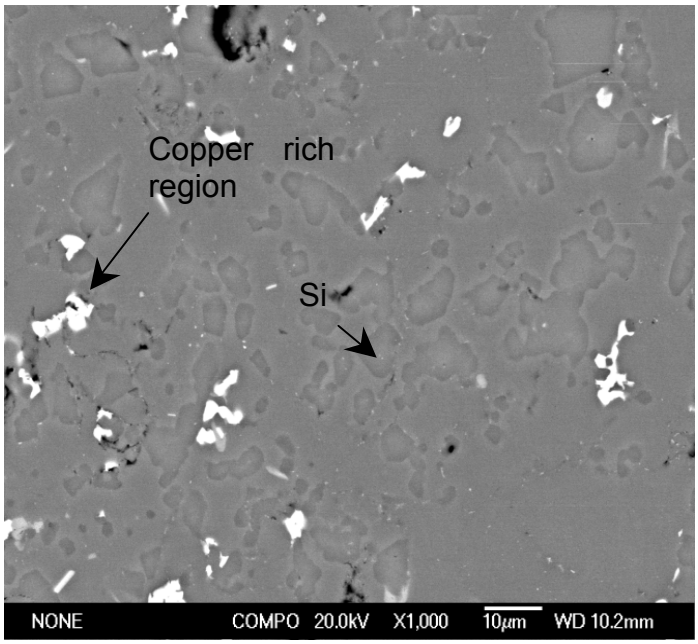

(a)

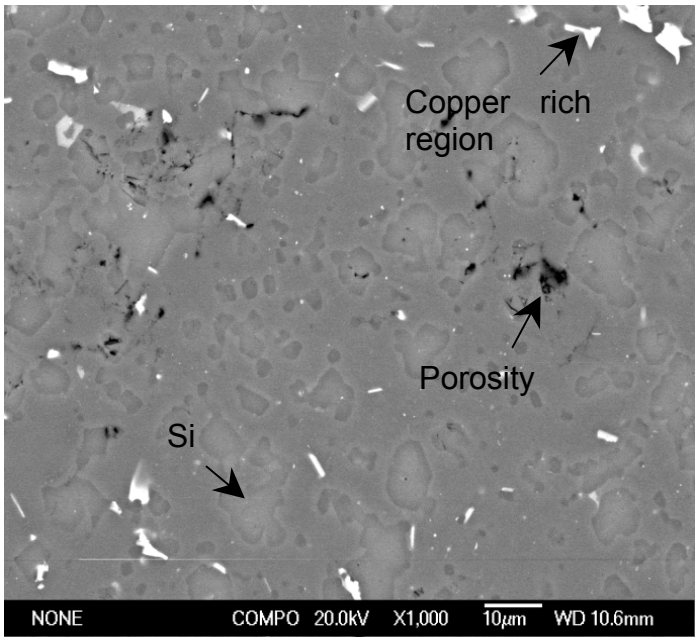

(b)

Figure 5.18. Backscattered electron micrograph showing typical microstructural change after subjected to solution heat treating temperature of 510ºC for (a) 1 hour and (b) 10 hours

5.7.3 Microstructural Characterization of the Sintered and Age-hardened Compacts

As mentioned previously in literature review, age-hardening behavior of aluminum alloys is largely dependent on the alloy composition. Besides, the age hardening response is also influenced by the volume fraction, shape and structure of the precipitates. Thus, it is crucial to investigate the microstructural changes for the aged-hardened alloys used in this study. Generally, precipitation hardening for multi-component systems is rather complicated since several phases in metastable situation may exist which contribute to subsequent age hardening effect. Transmission electron microscopy (TEM) and energy dispersive spectrum (EDX) analysis were therefore used to identify the precipitates. The phases identified using EDX analysis were later substantiated by the XRD results as displayed in Figure 5.23(a)-(d).

Figure 5.19 displays the microstructures of Ecka Alumix 231 obtained at its peak aged condition after being subjected to the optimal artificial heat treatment. It can be seen that the plate-like precipitates with the thickness varied from approximately 5nm to 45nm distributed evenly within the α-aluminum matrix. The EDX line scan of the plate-like precipitate has confirmed that the main strengthening precipitates had the composition close to the Al_2Cu or equilibrium θ phase. It is suggested that the strengthening phases at the peak aged condition as appeared in Figure 5.19(a) and (b) are predominated by metastable θ’ phase which is responsible for the hardening properties. The phases presented after artificial treatment was substantiated by the XRD result as shown in Figure 5.23(a). It was again confirmed the presence of Al_2Cu

phase. Other phases detected included α-aluminum, silicon and slight amount of Q phase ($Cu_2Mg_8Si_6Al_5$).

With the increase of copper content to 4.5wt%, there are two interesting features being observed for Alloy A as shown in Figure 5.20(a). The light contrast region as indicated by Point 1 was found to have precipitates with the similar characteristic as observed in Ecka Alumix 231. However, the plate-like precipitates in Alloy A were comparatively smaller in size and have higher distribution density than Ecka Alumix 231. This is suggested to be the main reason contributing to the higher hardening effect in Alloy A as reported in Section 5.5.4. Another feature being observed was indicated by Point 2. Figure 5.20(c) displayed the X-ray mapping of the selective area within the region with dark contrast. X-ray mapping result showed the presence of Mg, Si and Cu-rich phase within the α-aluminum matrix. It is suggested that the dark contrast region was attributed to the formation of Q' phase. The emergence of peaks associated with the presence of Q' phase was again confirmed from the XRD traces as shown in Figure 5.23(b). It is worth mentioning that the peaks associated with $Cu_2Mg_8Si_6Al_5$ phase was not observed after the solution heat treatment but reappeared after the ageing process.

Alloy B with the addition of 0.9wt% Ni, on the other hand, did not exhibit the same microstructural characteristic as shown in both Ecka Alumix 231 and Alloy A. There was no discernible trace of plate-like precipitates. Instead, the STEM images for Alloy B showed more like local variation in contrast than occurrence of a separate phase. The difference in contrast as observed in the STEM image was suggested mainly due to the stress field occurred around the precipitates due to local expansion or

shrinkage of the matrix crystal lattice. This can be attributed to the formation of coherent θ" phase or sometimes referred as GP_2 within the α-aluminum matrix. Table 5.16 displays the point analyses at different locations of Alloy B. The θ" phase were found to have the copper content varying from 10 to 40 at% which comes in good agreement with the finding of Hono et al. [15]. The EDX identification of the θ" phase was substantiated by XRD result as shown in Figure 5.23(c). It again demonstrated the presence of Al_2Cu phase.

From Figure 5.22(a), presence of both large near-spherical shaped phase and small plate-like precipitates can be noted for Alloy C consisting of both 4.5wt% copper and 0.9wt% nickel. The X-ray mapping of the large-spherical shape phase demonstrated the presence of Cu-, Ni- and Fe-rich phases which are suggested to be due to the presence of $Al_3(Ni,Cu)_2$ and $AlFeSi_5$. It has previously been reported that presence of nickel lowered the hardening of the alloys. From Figure 5.22(a), it can be seen that the area in close proximity to the $Al_3(Ni,Cu)_2$ was found to be depleted of plate-like precipitates. It is suggested that presence of copper absorbing features reduced the dissolution of the copper into α-aluminum matrix which later led to reduction in ageing response. The plate-like precipitates found in Alloy C (Figure 5.22(b)) had similar size as found in Alloy A but with much lower distribution density. There were some traces of disc-shaped phase being observed as well. The EDX spectra of this disc-shaped phase is displayed in Figure 5.22(c), whereby similar composition to θ' phase was noted. The differences in shape for θ' phases can be attributed to the presence of different θ' planes. The XRD result as displayed in Figure 5.23(d) again demonstrated the presence of Al_2Cu, $Cu_2Mg_8Si_6Al_5$ and $Al_3(Ni, Cu)_2$ phase. No other kind of

precipitates was observed for all the alloys, suggesting that Al_2Cu precipitates are the main strengthening phase responsible for the hardening properties.

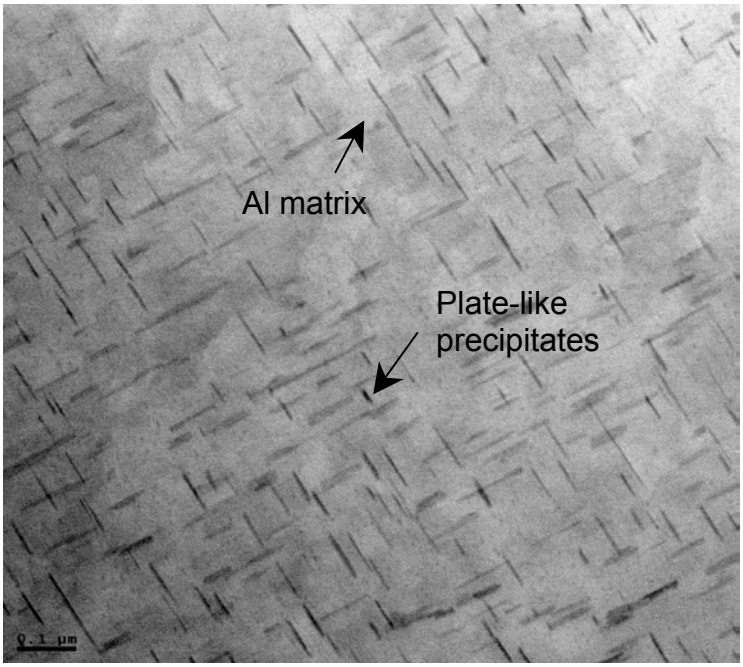

(a)

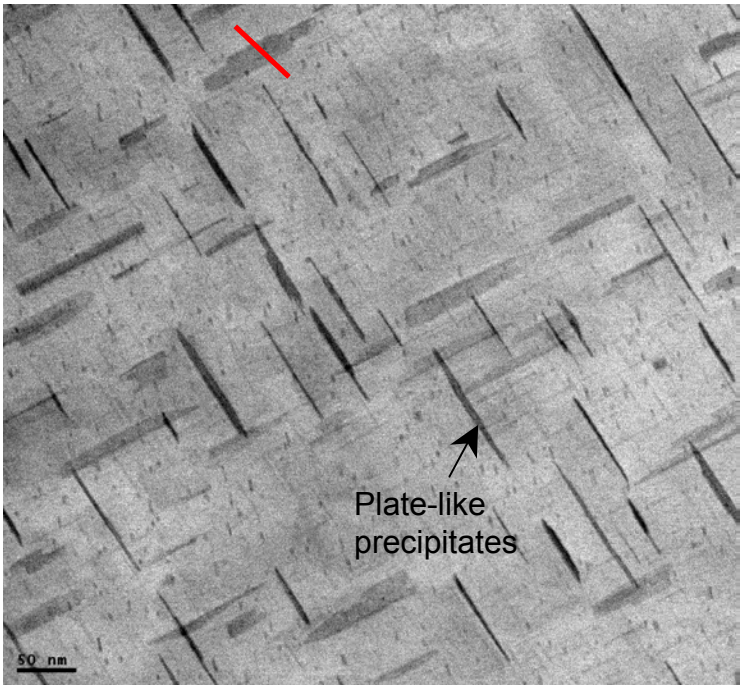

(b)

Figure 5.19. STEM images observed in heat treated Ecka Alumix 231 (Al-15Si-2.5Cu-0.5Mg) at (a) low magnification and (b) high magnification

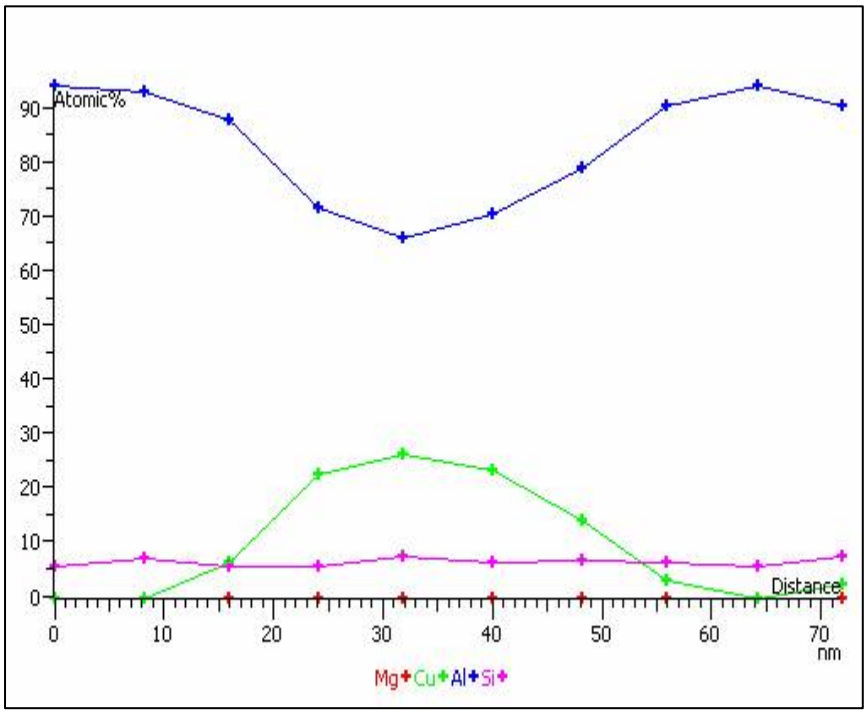

(c)

Figure 5.19 (continued). (c) Line scan corresponding to the selected area in (b)

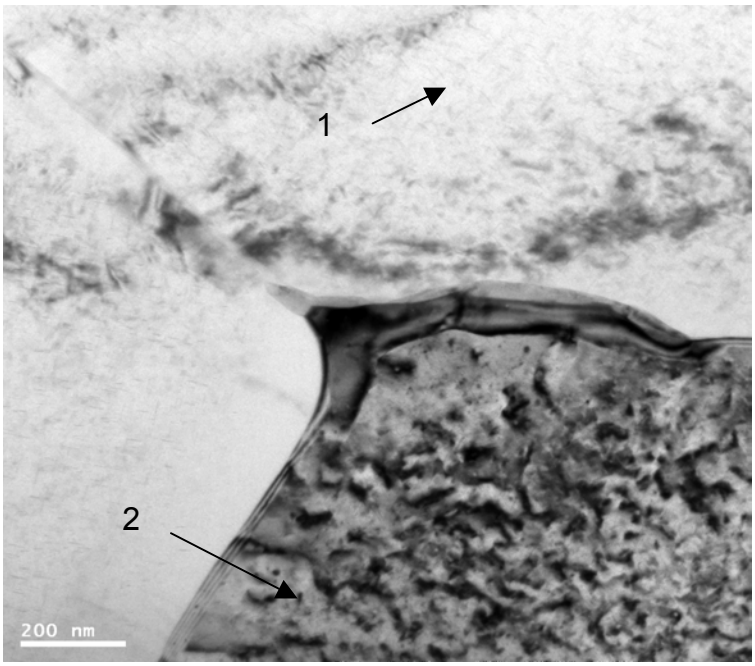

(a)

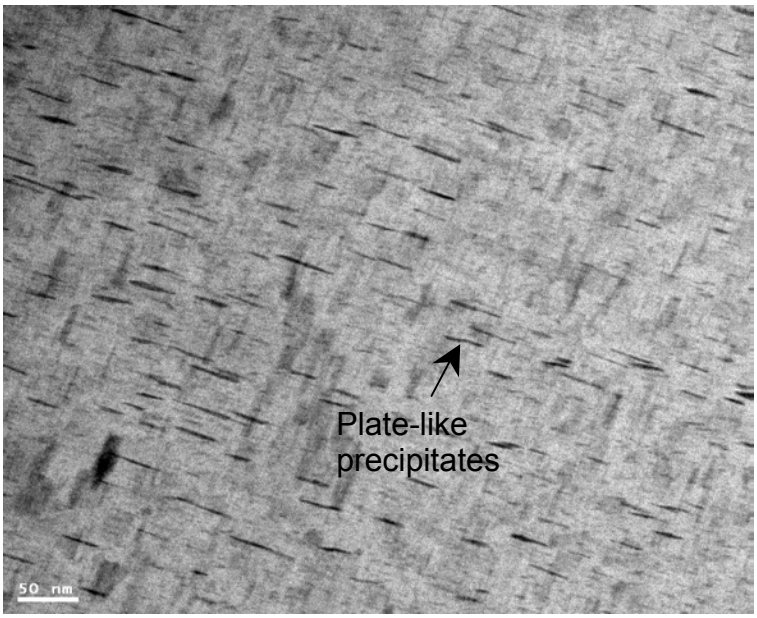

(b)

Figure 5.20. STEM images observed in heat treated Alloy A (Al-15Si-4.5Cu-0.5Mg): (a) low magnification and (b) high magnification corresponding to the location 1 shown in (a)

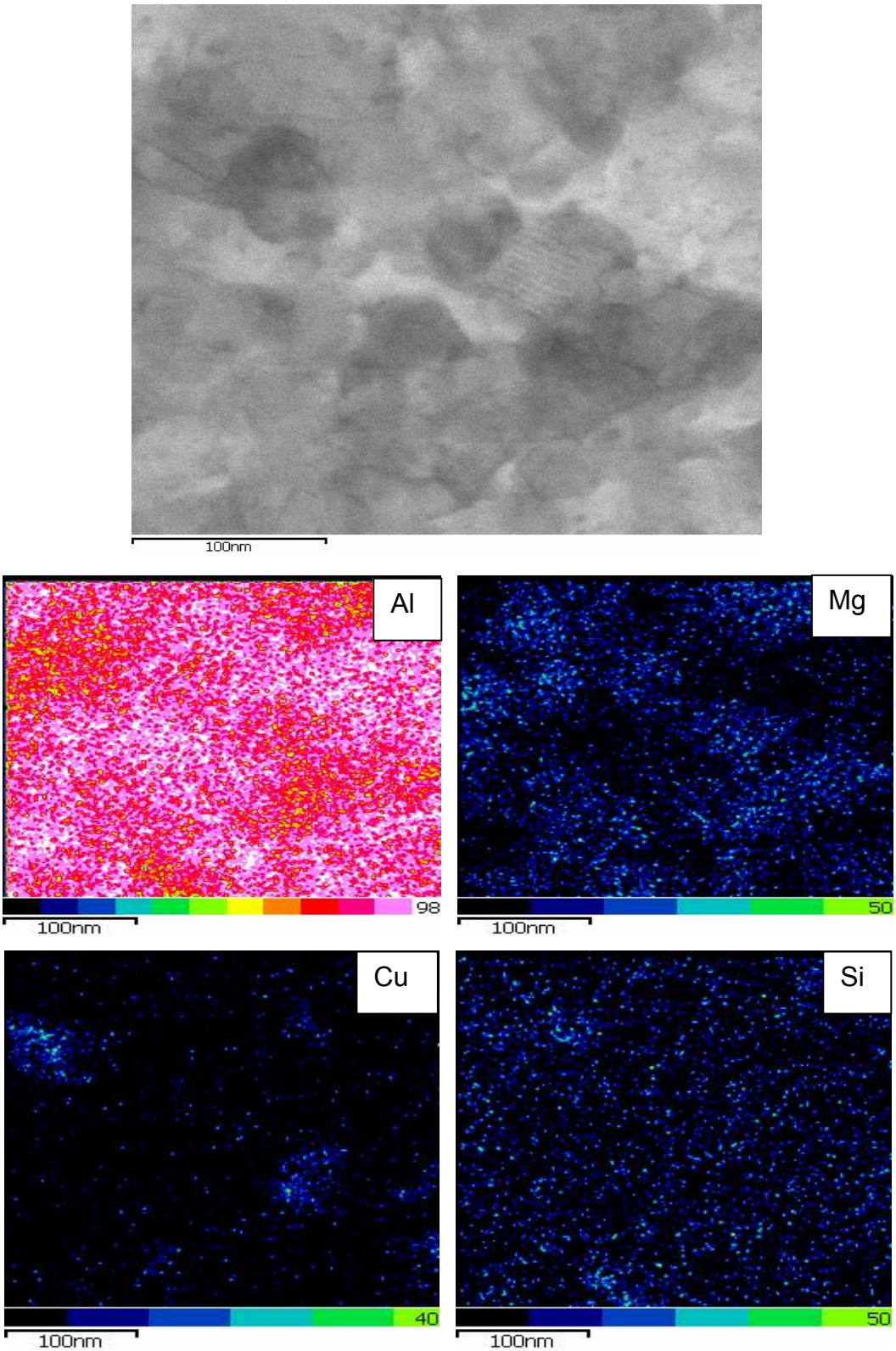

Figure 5.20 (continued). (c) STEM image of heat-treated Alloy A (Al-15Si-4.5Cu-0.5Mg) corresponding to the location 2 shown in (a) and Quant maps of interested region.

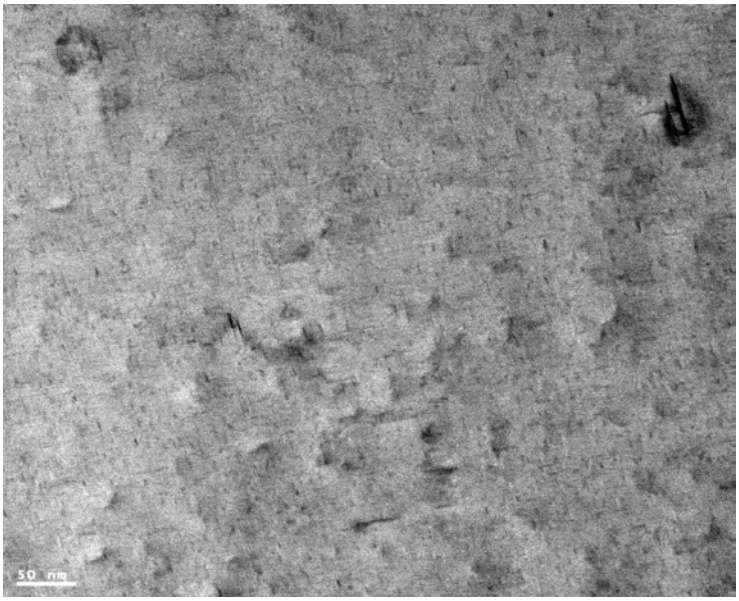

(a)

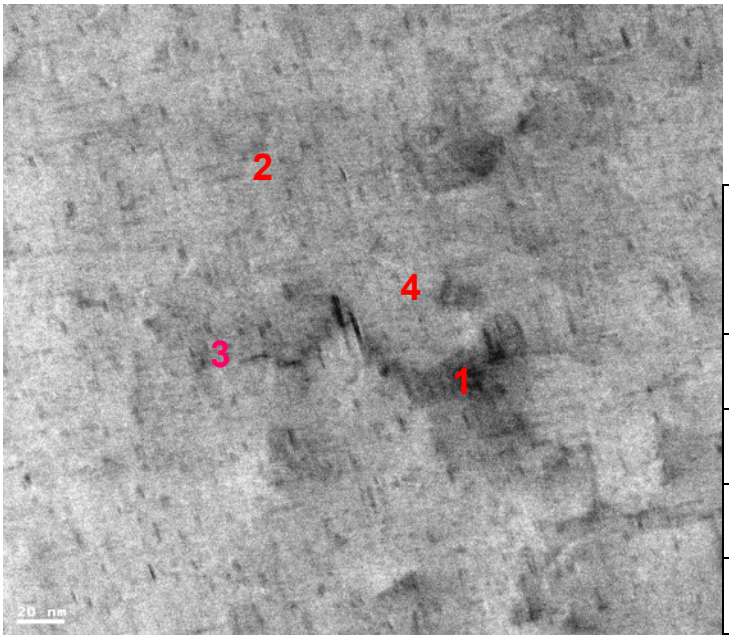

(b)

Table 5.16 EDX Point Analysis for different locations as shown in Figure 5.20(b) (at%)

Point Location	Al	Cu	Si
1	33.23	37.89	28.88
2	50.16	11.62	38.22
3	39.09	23.78	37.13
4	41.22	20.70	38.08

Figure 5.21. STEM images observed in heat-treated Alloy B (Al-15Si-2.5Cu-0.9Ni-0.5Mg) at (a) low magnification and (b) high magnification coupled with the EDX analysis for different

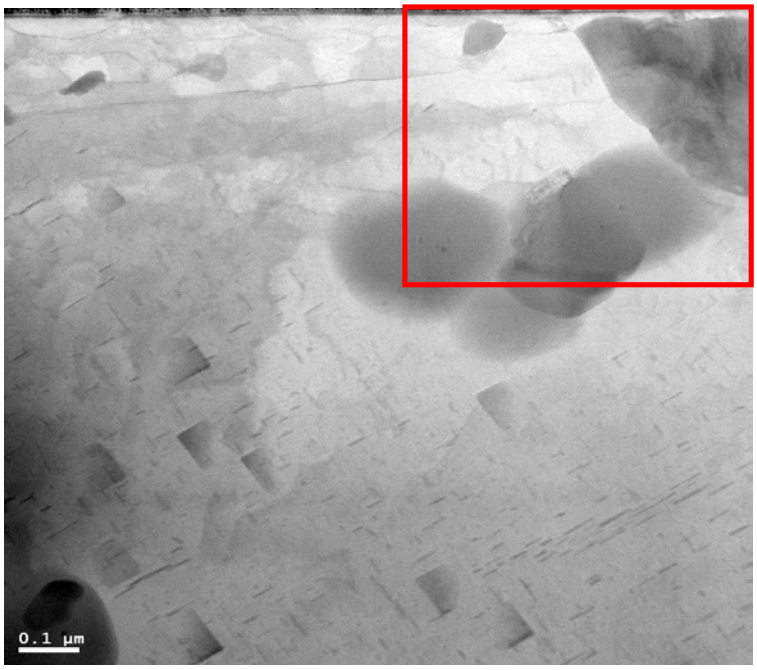

(a)

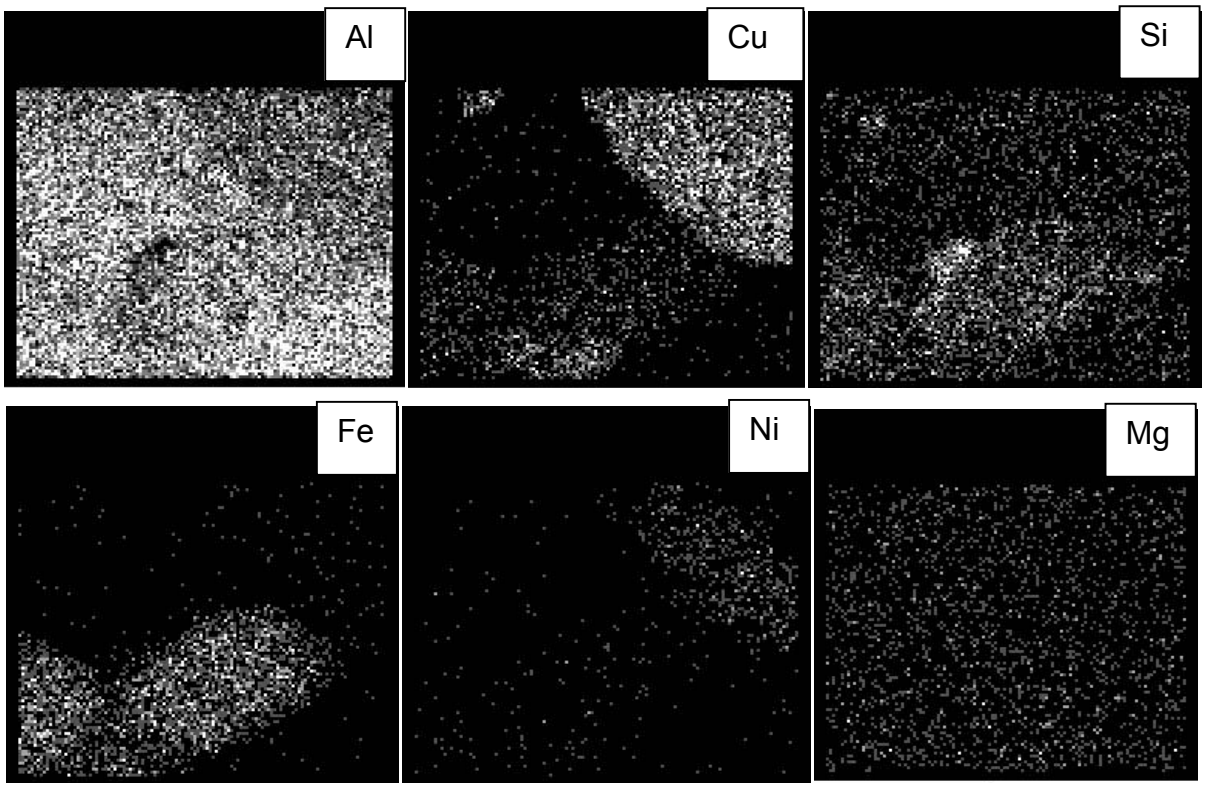

(b)

Figure 5.22. (a) STEM images observed in heat-treated Alloy C (Al-15Si-4.5Cu-0.9Ni-0.5Mg) and (b) the corresponding mapping of the selected area in (a).

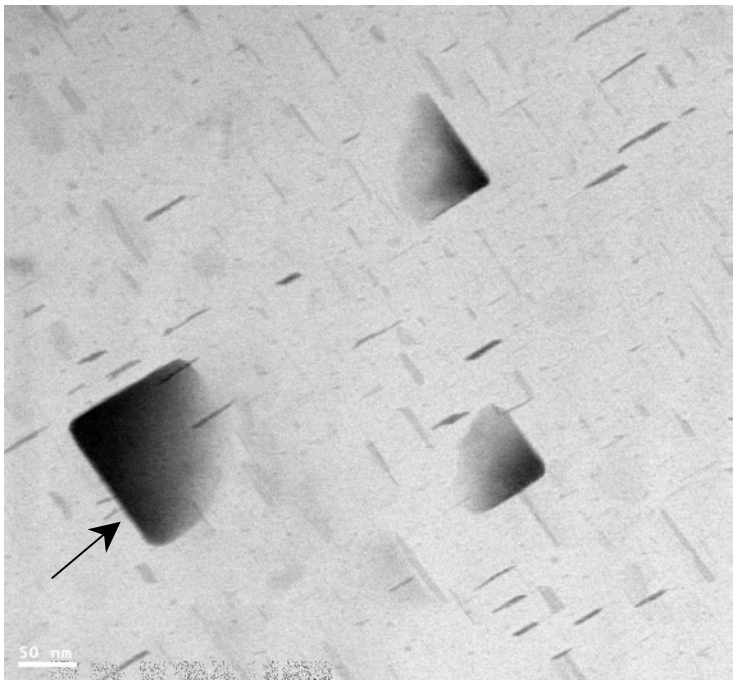

(a)

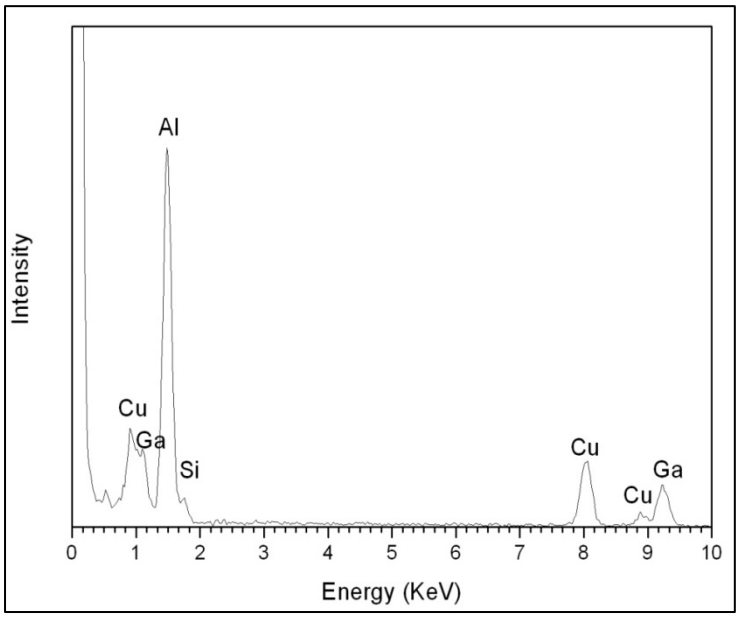

(b)

Figure 5.22 (continued). (a) STEM images observed in heat-treated Alloy C (Al-15Si-4.5Cu-0.9Ni-0.5Mg) and (b) EDX spectra of the Al_2Cu precipitates as shown in (a).

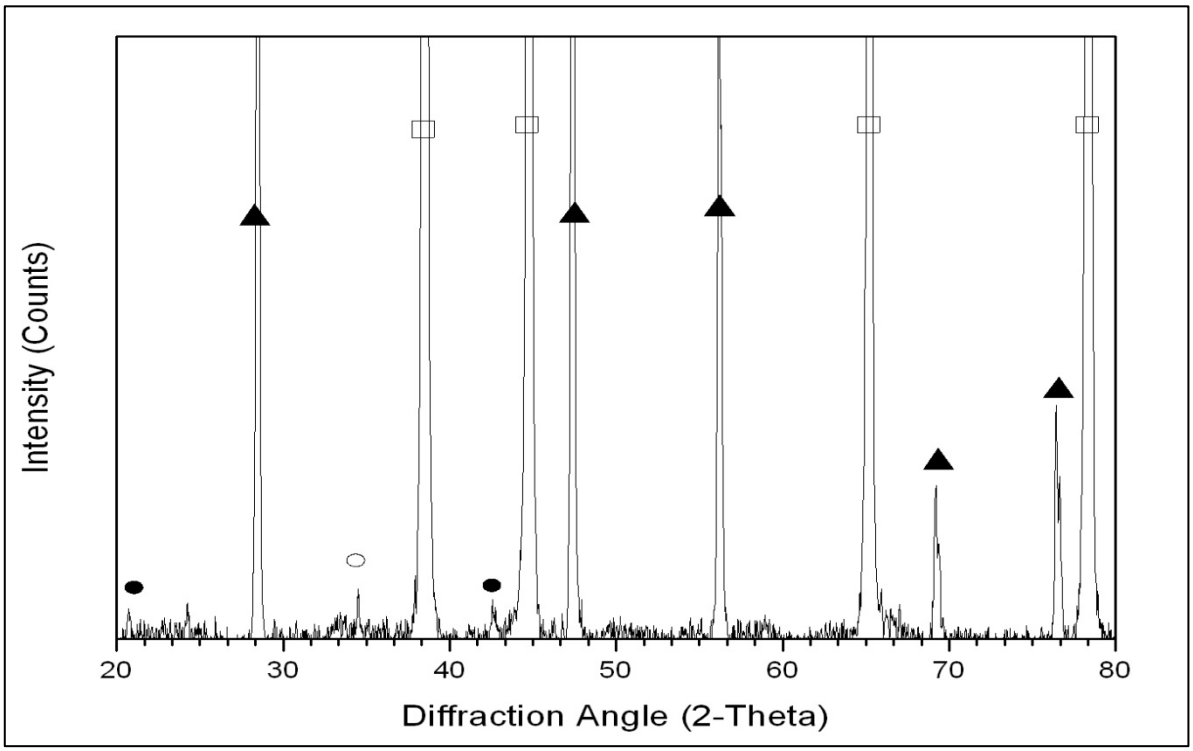

(a)

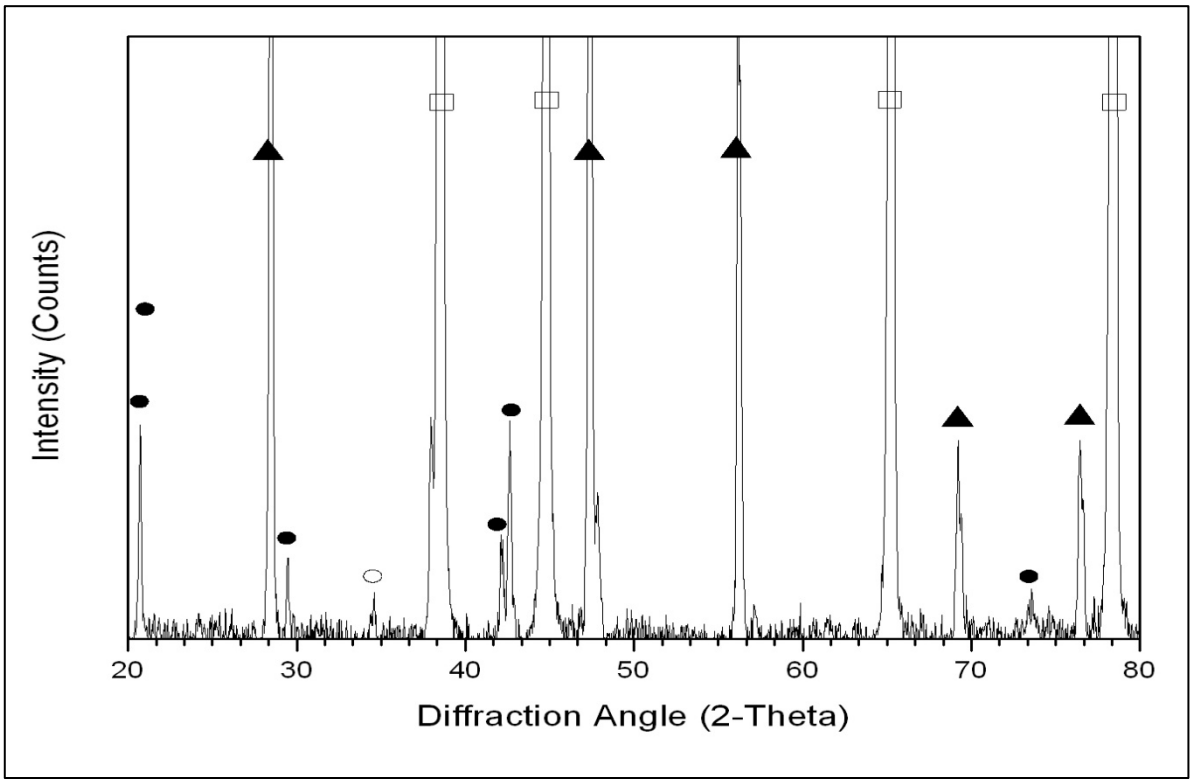

(b)

Figure 5.23. XRD results corresponding to aged (a) Ecka Alumix 231 and (b) Alloy A. Phases positively identified were α- Al (□), Si (▲), θ phase (●), and Q phase (⬭).

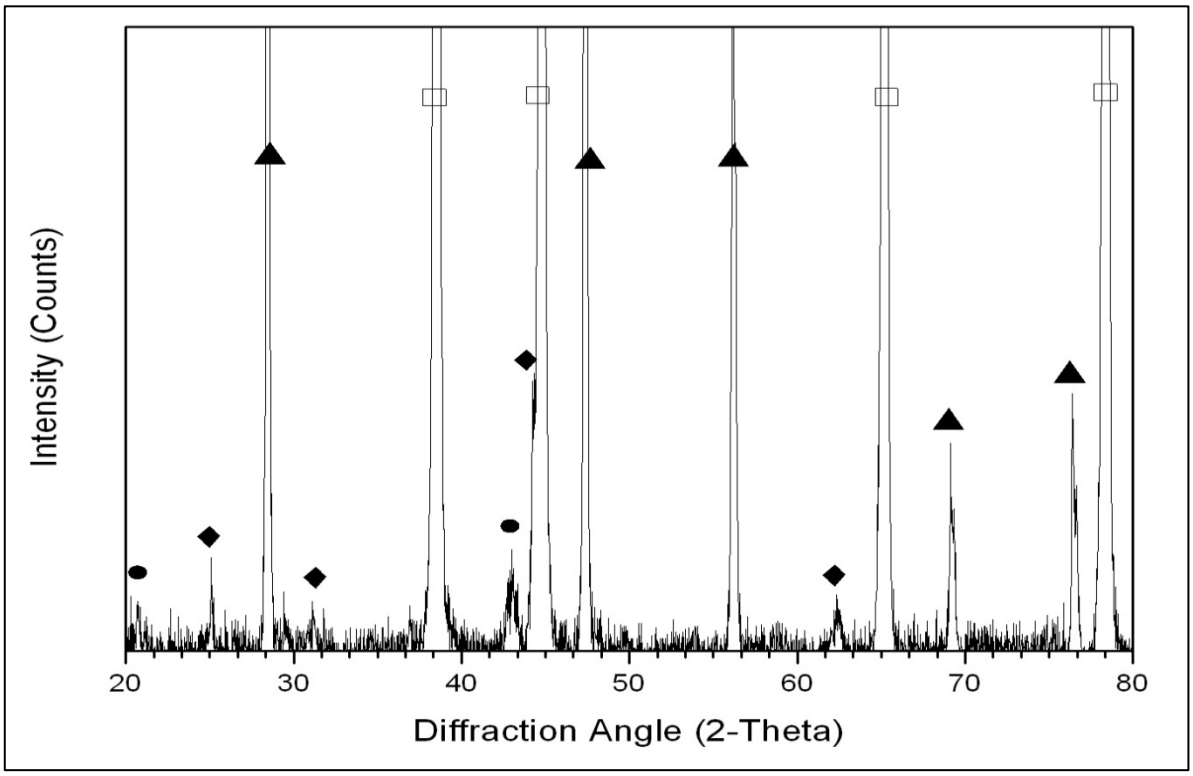

(c)

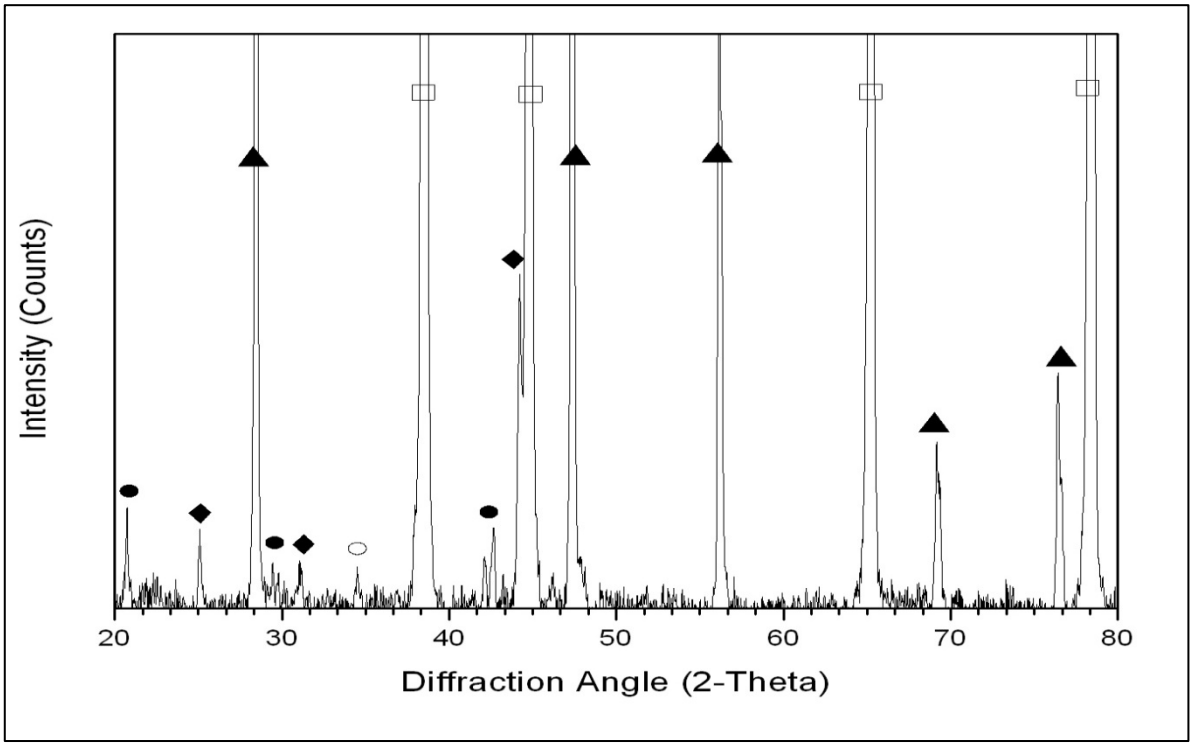

(d)

Figure 5.23 (continued). XRD results corresponding to aged (c) Alloy B and (d) Alloy C. Phases positively identified were α- Al (□), Si (▲), θ phase (●), Q phase (⬭), and Al_3Ni_2 phase (◆).

5.8 Thermo-Calc Calculations

The constituent phases presented in different Al-Si based alloys and the temperatures range at which liquid phases started to form were calculated using the Thermo-Calc software and the results are displayed in Figure 5.24(a)-(c). DSC traces for the green compact as displayed in Figure 5.2(a)-(c) showed that the onset of melting temperatures for all Al-Si based alloys was approximately 505°C, similar to that of Ecka Alumix 231. The experimental liquid formation temperature was relatively lower than the calculated temperatures, which was mainly due to the inhomogeneous behavior of the alloys prepared from both elemental and master powder.

The compact was suggested to reach equilibrium state after subsequent sintering and furnace cooled down. However, the DSC traces for the sintered compacts as shown in Figure 5.4 showed that the onset of melting temperatures for Ecka Alumix 231, Alloy A, B and C were 505°C, 496°C, 515°C, 505°C respectively. The calculated liquid formation temperatures, on the other hand, were found to be 526°C, 510°C, 529°C and 517°C for Ecka Alumix 231, Alloy A, B and C respectively. The deviation from the experimental result within the range of 14-21°C was noted. Thus, the calculated thermodynamic diagram as shown in Figure 5.24(a)-(c) can only serve as a reference to study the evolution of different phases.

Alloy A with the nominal composition of Al-15Si-4.5Cu-0.5Mg (wt%) was calculated to exhibit similar phases as Ecka Alumix 231 (Al-15Si-2.5Cu-0.5Mg). Formation of Al_2Cu, $Al_5Cu_2Mg_8Si_6$, FCC Al and silicon was predicted. However, with the increase of the

copper content to 4.5wt%, the melting temperature of $Cu_2Mg_8Si_6Al_5$ shifted to a lower temperature of 515°C.

With the addition of nickel, both Alloy B (Al-15Si-2.5Cu-0.9Ni-0.5Mg) and Alloy C (Al-15Si-4.5Cu-0.9Ni-0.5Mg) were predicted to form $Al_3(Ni, Cu)_2$ phase which was confirmed by EDX and XRD results. Although it has been reported elsewhere that Al_3Ni also presented as copper absorbing feature, there were no traces of Al_3Ni being detected or predicted since possibility of Al_3Ni formation decreased with the increase of Cu:Ni ratio [2]. Apart from $Al_3(Ni, Cu)_2$, $Al_5Cu_2Mg_8Si_6$, FCC Al and silicon, Alloy B with the nominal composition of (wt%) was predicted to form Al_7Cu_4Ni phase. In accordance to the quinary prediction of Alloy B, no traces of Al_2Cu should be noted. However, both EDX and XRD results confirmed the presence of Al_2Cu phase instead of Al_7Cu_4Ni phase. Al_2Cu phase was predicted to form when the copper content increased to 4.5wt% as observed in Alloy C (Al-15Si-4.5Cu-0.9Ni-0.5Mg). Thus, it was postulated that the composition change during sintering process led to the increase of copper concentration up to the critical concentration for Al_2Cu formation. Thus, instead of forming Al_7Cu_4Ni phase, Al_2Cu was detected. Furthermore, since Al_7Cu_4Ni phase formed at relatively low temperature, the low kinetic mobility of the Cu and Ni atoms may hinder the formation of Al_7Cu_4Ni phase.

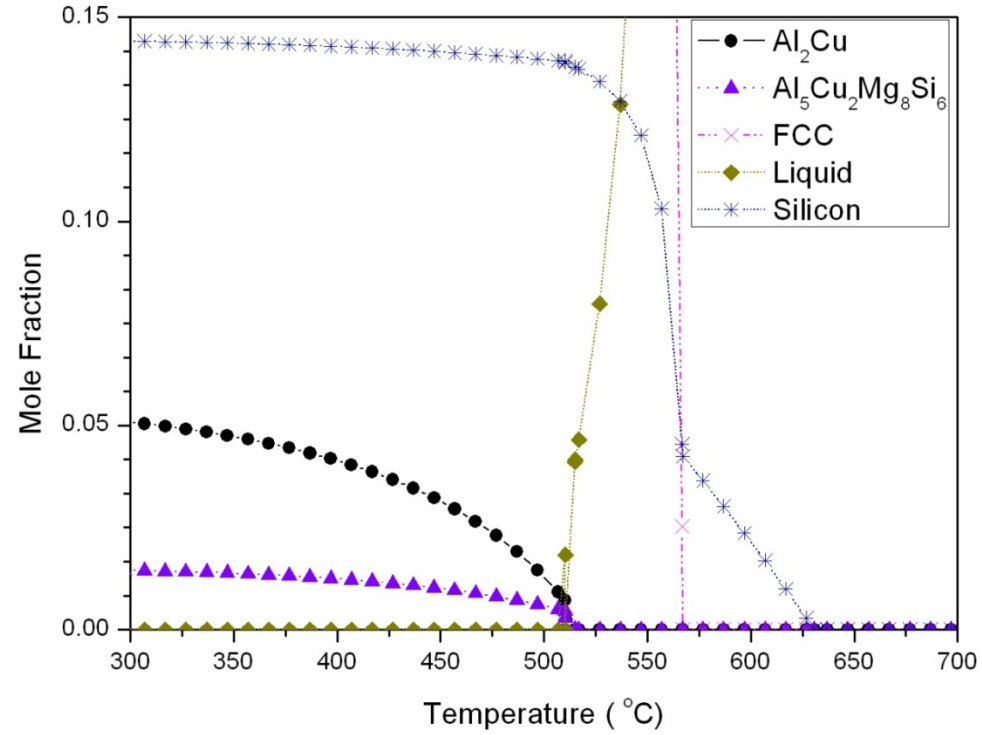

(a)

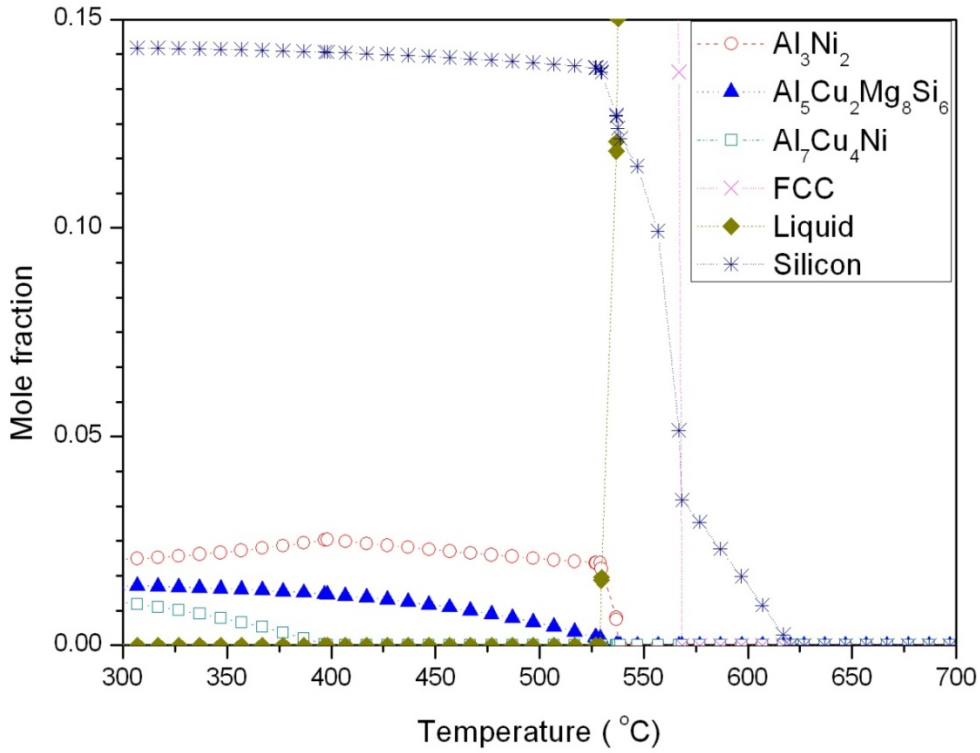

(b)

Figure 5.24. Calculated fraction of phases vs temperature for (a) Alloy A (Al-15Si-4.5Cu-0.5Mg) and (b) Alloy B (Al-15Si-2.5Cu-0.9Ni-0.5Mg).

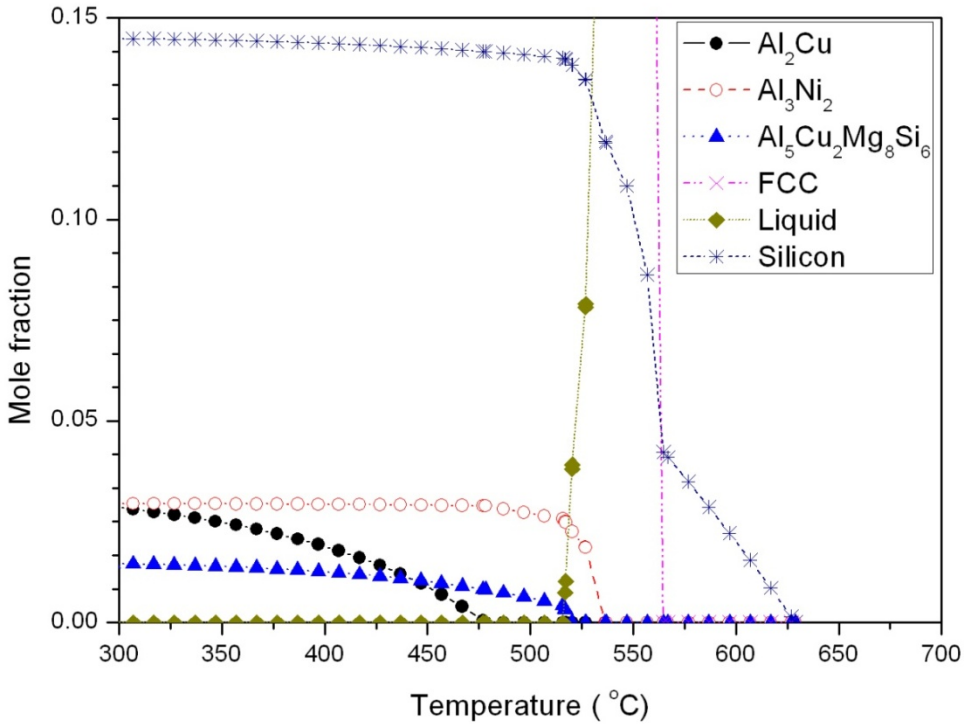

(c)

Figure 5.24 (continued). Calculated fraction of phases vs temperature for the composition of (c) Alloy C (Al-15Si-4.5Cu-0.9Ni-0.5Mg).

5.9 Discussion

5.9.1 Influence of Alloy Additions on Compressibility

The compressibility curve for all the Al-Si based alloys used in this study was presented graphically in Figure 5.1. It can be seen that the green density of the compact increased with the increase of the compaction pressure. In comparison with the compressibility curve of Ecka Alumix 231, addition of small amount of alloying elements, i.e. copper and nickel did not result in significant improvement in overall relative densification. However, substantial increase in green density of the compact

can be noted during the initial stage of compaction. Approximately 9 to 10% of densification was noted with the increase of the compaction pressure from 200 to 400MPa. Since the alloying elements used in the study were comparatively smaller in size with D_{50} for elemental copper and nickel to be 45μm and 6μm respectively, particles with smaller size can fill the inter-particle voids more effectively. Particle rearrangement occurred and the powder particles moved against each other contributing to better packing density. As the compaction pressure increased, plastic deformation started to take place. Furthermore, the number of particle-to-particle contacts also increased with the increase of the compaction pressure [16].

With the increase of the compaction pressure above 400MPa, the densification behavior for Alloy A, B and C exhibited similar characteristics as Ecka Alumix 231, which had previously been discussed in Chapter 4. Densification of the compacts started to proceed at slower rate with around 2-3% increase in densification. Further increase of the compaction pressure did not result in any significant densification. Due to the increase in work hardening of the particles, further deformation was hindered within the compacts. Thus, the rate of densification decreased and densification of the compacts became less significant.

By applying the Heckel equation as shown in Equation 4.4, all the Al-Si based alloys were found to follow a linear relationship with compaction pressure as displayed in Figure 5.25. Compaction densification occurred mainly due to plastic deformation. The yield strength of the powder was again determined from the slope of the regression line using the Equation 4.5 and the results were shown in Table 5.17. It

can be seen that yield strength of the Alloy A, B, C with Cu and/or Ni additions was comparatively higher than Ecka Alumix 231. Johanson had reported that bulk strength can be influenced by the number of particle contacts per adjacent particle [17]. Since the alloying elements used in this study had relatively smaller size, they can fill the voids between the particles more effectively. Thus, they contributed to higher number of particle contacts and consequently increased the yield strength of Alloy A, B, and C.

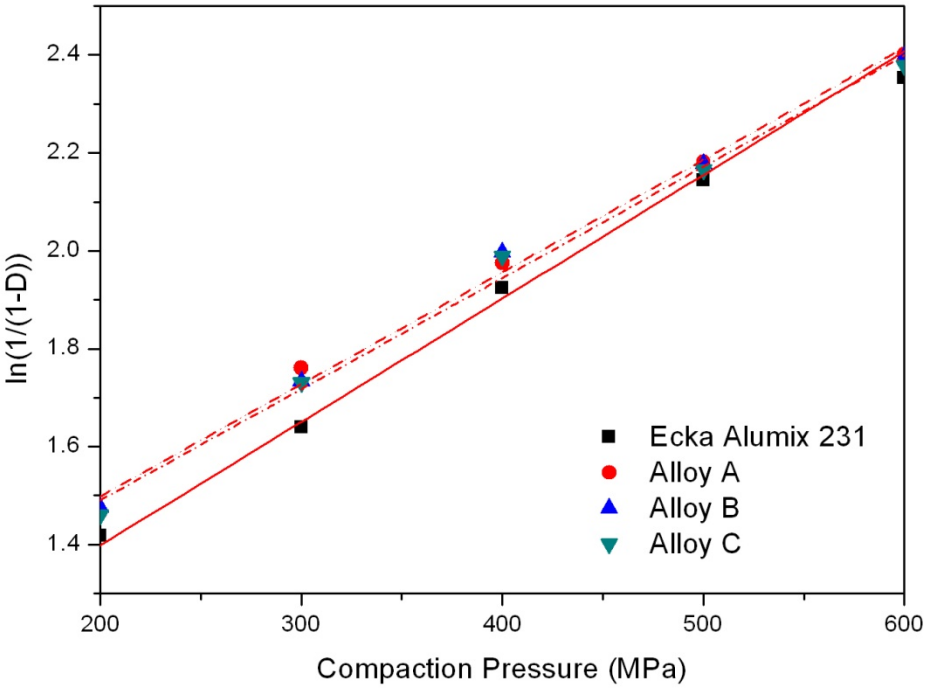

Figure 5.25. Heckel plot of ln(1/(1-D)) vs compaction pressure for different Al-Si based alloys

Table 5.17. Yield Strength for different Al-Si based alloys

Alloy System	Yield Strength (MPa)
Ecka Alumix 231 (Al-15Si-2.5Cu-0.5Mg)	140.64
Alloy A (Al-15Si-4.5Cu-0.5Mg)	145.56
Alloy B (Al-15Si-2.5Cu-0.9Ni-0.5Mg)	145.56
Alloy C (Al-15Si-4.5Cu-0.9Ni-0.5Mg)	146.84

5.9.2 Influence of Alloy Additions on Sinterability

Due to the variation in the alloy composition as shown in Table 5.1, appropriate P/M processing scheme for these alloys needed to be established. Nitrogen atmosphere which has previously been proven in Chapter 4 to be beneficial for sintering was also applied throughout the present study. Sintering temperature was thus the main processing parameter of concern. In general, volume fraction of liquid phase increased with the increase of the sintering temperature. Liquid formation is crucial to improve the overall wetting characteristic, enhance mass transport and contribute to densification of the compacts [18].

It is worth to note that densification for Alloy A (Al-15Si-4.5Cu-0.5Mg), B (Al-15Si-2.5Cu-0.9Ni-0.5Mg) and C (Al-15Si-4.5Cu-0.9Ni-0.5Mg) with copper and/or nickel additions started at lower sintering temperatures as compared to the Ecka Alumix 231 with the nominal composition of Al-15Si-2.5Cu-0.5Mg (wt%), as shown in Figure 5.3. As tabulated in Table 5.4-5.6, approximately 7-9% increase in densification was noted with the presence of 5% liquid phase. The rate of densification, however, decreased with the increase of sintering temperature. The significant increase in densification at low sintering temperature was suggested due to the higher green density noted for the aforementioned alloys. Alloys A, B and C with the respective green density of 86.13%, 86.43% and 86.32% of the theoretical density were found to have slightly higher densification than Ecka Alumix 231(85.40% of theoretical density). Higher green density thus resulted in a higher sintered density [19]. The effects of green density on sintered density became less profound with the

increase of liquid formation. It is anticipated that densification was dominated by the amount of liquid phase formed above 15% liquid phase.

Copper additions to the Ecka Alumix 231 baseline system had pronounced effect on both liquid formation and densification during sintering. As tabulated in Table 5.3, it can be seen that Alloy A (Al-15Si-4.5Cu-0.5Mg) and Alloy C (Al-15Si-4.5Cu-0.9Ni-0.5Mg) which consisted of copper content of 4.5wt% required comparatively lower sintering temperature than Ecka Alumix 231 (Al-15Si-2.5Cu-0.5Mg) to generate equivalent amount of liquid phase. In other words, addition of copper was deemed to enhance liquid phase formation. This can be attributed to the formation of several low melting eutectics which later aided in liquid phase sintering [20]. The liquid formation can be traced from DSC results as displayed in Figure 5.2(a) and (c) whereby two small endothermic peaks were observed at 507°C and 523°C which corresponded to melting of α-Al + $CuAl_2$ + Si + $Cu_2Mg_8Si_6Al_5$ and α-Al +$CuAl_2$ + Si respectively [21]. Both DSC traces for Alloy A and C also showed additional shouldering effects at approximately 540°C which can be attributed to the melting of α-Al + $CuAl_2$ eutectic [22]. These events manifested a remarkable increase in liquid formation leading to lower sintering temperatures required for Alloy A and C.

Apart from enhancing liquid formation, copper addition to the Ecka Alumix 231 baseline system also marked a positive shift in the sintering response. Copper is a common alloying element used in the commercial Al-Si based P/M alloys. For instance, Alloy AC2014 contained 4.5wt% copper content to facilitate liquid formation

and for strengthening purpose. Alloy A with a similar copper content to AC2014 marked a noticeable increase in densification throughout the range of sintering temperatures applied, as shown in Figure 5.3. The remarkable improvement in sintered density with the increase of the copper content comes in good agreement with the results reported by Hennessey et al [8]. However, the finding was in contradiction with the results reported by Dunnett et al., Zhou and Duszczyk, whereby a reduction in sintered density was noted with the increase of copper content. The reduction in sintered density was reported due to compact swelling [23, 24]. Since swelling of the compact was mainly found in the compact with high green density [25, 26], a reduction in sintered density due to swelling was not anticipated for Alloy A with relatively low green density (86.13% of theoretical density).

The enhanced sintered quality for Alloy A can further be demonstrated through the microstructures as displayed in Figure 5.10. Alloy A exhibited a well sintered microstructure with only minor amount of porosity was noted. As discussed previously in Chapter 4, sintering in nitrogen atmosphere promoted the formation of AIN which increased the wettability of the liquid, induced pores filling effects and later contributed to subsequent compact densification [27, 28]. With the appreciable addition of copper from 2.5wt% to 4.5wt%, more Al_2Cu intermetallic phase was formed along the grain boundaries. Since most of the Al_2Cu phase was found to distribute at the grain boundaries, it played a less significant role in strengthening of the compacts. Thus, increase in copper content did not have significant effect on increasing the microhardness value as shown in Table 5.10. It is postulated that Al_2Cu played a greater role in hardening after controlled heat treatment. Apart from α-aluminum,

silicon and Al_2Cu, other phases presented within Alloy A were quite similar to that of Ecka Alumix 231. This included Q phase ($Cu_2Mg_8Si_6Al_5$) and minor amount of $FeSiAl_5$ formed from the impurity Fe. The phases presented in Alloy A came in good agreement with the Thermocalc prediction as displayed in Figure 5.24.

Transition element nickel, on the other hand, have been introduced at low concentration (0.9wt%) in both Alloy B (Al-15Si-2.5Cu-0.9Ni-0.5Mg) and C (Al-15Si-4.5Cu-0.9Ni-0.5Mg). Many conventional wrought/cast aluminum alloys had incorporate nickel addition as a means to simultaneously strengthen the alloy through precipitation hardening and dispersoid strengthening. Examples of alloys include 2618, 2218, 8801 which have Ni and/or Fe addition of approximately 1wt%. Apart from the effort to achieve higher mechanical properties, dispersoid addition also allows strengthening without undergoing expensive heat treatment practices [29]. However, in most cases for aluminum P/M alloys, transition element nickel merely exists as trace impurities with less than 0.1wt%. There are very limited studies on the effects of incorporating the nickel addition in the aluminum P/M alloys. Thus, it is of particular interest to investigate the effects of nickel addition by incorporating 0.9wt% nickel which is similar to those applied in wrought alloy into the Ecka Alumix 231 baseline system.

Figure 5.3 depicts the effects of nickel and/or copper additions in regards to the sintering response. Generally, all alloys experienced compact densification with the increase of sintering temperature. In comparison with the Ecka Alumix 231 baseline system, slight decrease in sintered density can be realized with the incorporation of

elemental nickel powder even though Alloy B (Al-15Si-2.5Cu-0.9Ni-0.5Mg) achieved sintered density of 95.14% of the full theoretical value. Meanwhile, Alloy C with combined 4.5wt% copper and 0.9wt% nickel addition (Al-15Si-4.5Cu-0.9Ni-0.5Mg) was found to behave similarly to Alloy B (Al-15Si-2.5Cu-0.9Ni-0.5Mg). Though similar amount of copper content as Alloy A (Al-15Si-4.5Cu--0.5Mg) had been added, no significant improvement in sintered density was realized. In the previous studies by Dunnet et al., the effects of nickel addition on quaternary Al-Cu-Mg-XNi systems had been investigated in details. No significant densification was reported for the alloys with low nickel addition. An abrupt increase in sintered density only observed when the nickel content increased to 15wt% [23].

The degradation in sintered density as observed in Alloy B and C was suggested due to the preferential reaction of copper with nickel leading to reduced amount of liquid phase present at a given sintering temperature. It has been known that $Al_3(Ni, Cu)_2$ phase had the ability to absorb appreciable amount of copper from the α-aluminum grains [23]. Presence of $Al_3(Ni, Cu)_2$ phase can be evidenced from the microstructures of Alloy B and C as shown in Figures 5.12 and 5.13, whereby ribbon-like structure sparsely distributed along the grain boundaries. Minor amount of blocky structure with the chemical composition close to Al_9FeNi can also be detected but appeared at very much reduced frequency. Although only small amount of Al_9FeNi can be noted, it was suggested that Al_9FeNi can also contribute to the lowering of copper content since traces of copper was consistently detected. Furthermore, there were no obvious dispersoid strengthening features being observed in α-aluminum grains. Nickel addition was prompted to form coarse intermetallic $Al_3(Ni, Cu)_2$ phase along the grain

boundaries, which was suggested to have no significant contribution to the dispersoid strengthening of the base alloy.

In terms of the microhardness of compacts, both Alloy B and C experienced an apparent reduction in microhardness, amounting to a loss of nearly 13-14% as compared to Ecka Alumix 231 (Table 5.10). Cooke et al. reported that nickel addition in either elemental or prealloyed form to the base system of Al-2.3Cu-1.6Mg-0.2Sn deteriorated both the sintering response and mechanical properties of the sintered products. It has been reported that maximum reduction in sintered density and acute loss of nearly 10% of hardness were accounted with the addition of highest nickel content up to 2wt% [29]. This comes in good agreement with the results of the study. Addition of elemental nickel, thus, posed an adverse effect on the sintering response of the Ecka Alumix 231 alloy.

5.9.3 Influence of Solution Heat Treatment for Different Al-Si based Alloys

Control of the chemical composition and heat treatment parameters is crucial since it exerts important role in influencing the mechanical properties of the final product. In an attempt to develop suitable heat treatment procedure for different alloys, the first approach is to establish appropriate solution treatment temperature and time. The main purpose of solution heat treatment is to maximize the concentration of age-hardening constituents in the solid solution. The compacts were subsequently

quenched to obtain supersaturated solid solution and age-hardened in controlled manner to allow precipitation of metastable phases in order to achieve superior properties in the final products.

A wide range of solution temperatures for Al-Si-Cu-Mg alloys have been reported. Conventionally, solution treatment temperatures are restricted within a narrow range to avoid undesirable incipient melting of copper rich phases which can deleteriously affect the mechanical properties. Solution treatment temperatures are highly dependent on copper and magnesium concentrations. For instance, solution temperature for Al-Si-Mg without copper is limited to 550°C. However, Al-Si-Cu-Mg with high copper content is restricted below 495°C [30]. As for Al-Si-Cu-Mg containing 0.5wt% of Mg, solution temperature of 500°C was recommended [30-32]. Although it is desirable the keep the solution temperature below the incipient melting temperature of Cu-rich phases, some studies demonstrated that high temperature solution treatment (above the incipient melting point) was beneficial to enhance the properties of the final products [10, 33, 34].

In this study, the onset of partial melting for Ecka Alumix 231 baseline system (Al-15Si-2.5Cu-0.5Mg), Alloy A (Al-15Si-4.5Cu-0.5Mg), Alloy B (Al-15Si-2.5Cu-0.9Ni-0.5Mg) and Alloy C (Al-15Si-4.5Cu-0.9Ni-0.5Mg) was determined using differential scanning calorimetry and was found to be 505°C, 496°C, 515°C and 505°C respectively as displayed in Figure 5.4. Thus, several solution treatment temperatures as displayed in Table 5.7 ranging from 490°C to 520°C were investigated. To determine the effects of solution heat treatment on the subsequent

precipitation, artificial ageing was conducted at constant ageing temperature of 120°C over a period of 48 hours.

All the Al-Si based alloys demonstrated better age-hardenability at solution treatment temperature of 510°C as summarized in Table 5.8. In other words, high temperature solution treatment was found to be beneficial for Ecka Alumix 231 baseline system, Alloy A and C since higher Vickers hardness value was attained as shown in Figure 5.5(a),(b) and (d). It has been reported that high temperature solution treatment allowed more alloying additions to dissolve into α-aluminum matrix [35]. Furthermore, high temperature solution heat treatment was also suggested to enhance the atomic transfer of alloying elements and accelerate diffusion of Cu-rich phases into α-aluminum matrix which consequently resulted in formation of more precipitates contributing to better age-hardenability. This can be evidenced from Figure 5.15 whereby significant increase in copper content within the aluminum matrix can be noted after solution heat treatment.

In the previous studies by Heard et al., solution treatment temperature of 520°C was recommended for Ecka Alumix 231 since it resulted in measurable increase in tensile strength after ageing. However, Figure 5.5(a) showed that solution temperature of 510°C induced better age-hardenability and further increase of solution temperature to 520°C decreased the Vickers hardness of the compacts greatly over time. The result came in good agreement with the findings as reported by Toda et al. It was demonstrated that increase of solution temperature for Al-Si-Cu alloy to 534°C which was 16°C higher than the ternary eutectic temperature can significantly increase the

strength of Al-Si-Cu alloy. However, further increase of the solution temperature to 551°C was not desirable attributable to the reduction of copper content within α-aluminum matrix coupled with formation of coarse, irregular-shaped Al-Si-Cu eutectic due to instantaneous melting [34]. Thus, although age-hardenability of the baseline system increased effectively with the increase of solution temperature up to 510°C, higher solution temperatures was not desirable owing to certain negative factors that developed with time at 510°C and 520°C.

From Table 5.8, it can be seen that Alloy A (Al-15Si-4.5Cu-0.5Mg) achieved highest Vickers hardness as compared to other alloys. It was worthy to note that increase of copper content to 4.5wt% shifted the onset of solution temperature for Alloy A to a lower temperature (496°C) as compared to the baseline system. This can be attributed to the melting of $Al_5Mg_8Cu_2Si_6$ fine eutectic [33]. Figure 5.5(b) showed that age-hardenability for Alloy A increased with the increase of solution temperature. Maximum Vickers hardness was noted at solution temperature of 510°C. At high solution heat treatment temperature, dissolution of Cu into α-aluminum matrix was largely increased as evidenced in Figure 5.17, contributing to higher precipitation of metastable phases during ageing which later led to significant increase in the subsequent hardening effect.

Unlike other alloys, high temperature solution treatment was not desirable for Alloy B (Al-15Si-2.5Cu-0.9Ni-0.5Mg). Solution temperature of 510°C at which no fusion of low melting copper-rich phases occurred was found to yield better age-hardenability during ageing. It is interesting to note that liquid formation was suppressed with the

addition of nickel as shown by DSC trace in Figure 5.4. Higher onset melting point of 515°C was noted for Alloy B. Similar onset melting point was reported for A390 alloy (Al-17Si-4Cu-0.5Mg) with the addition of 1wt% Ni addition [36]. The increase of onset melting is suggested due to less polynary eutectic phases segregating at the grain boundaries since appreciable copper dissolved into intermetallic Al_3Ni_2. This is consistent with the findings reported by Wang et al. whereby the solution heat temperature applied for the study increased with the decrease of copper content [21].

Alloy C with the combined 4wt% copper and 0.9wt% Ni (Al-15Si-4.5Cu-0.9Ni-0.5Mg), on the other hand, was found to have Vickers hardness value higher than Ecka Alumix 231 baseline system but lower value as compared to Alloy A. Due to preferential dissolution of copper into Al_3Ni_2, it was realized that copper content in α-aluminum was comparatively lower than other alloys without nickel addition in both as-sintered state and after solution treatment (Figure 5.17). $Al_3(Ni,Cu)_2$ remained intact during solution heat treatment as observed in Figure 5.15(c) and (d). This consequently caused less amount of free copper available to dissolve within α-aluminum during solution treatment and impeded subsequent precipitation hardening.

Apart from solution treatment temperature, solution time also played a significant role in influencing the precipitation hardening. Sufficient solutionizing time was required to allow maximum dissolution of soluble phase into α-aluminum. Solution time varied depending on the thickness of the materials. Since the thickness of the compacts had been kept constant throughout the study, it was determined in Section 5.5.3 that

solutionizing time of 1 hour was sufficient for necessary dissolution of the Cu and Mg rich phases into α-aluminum matrix. It is generally undesirable to solution heat treat compacts for long time due to the high cost and deterioration of mechanical properties caused by microstructural coarsening. It can be evidenced from Figure 5.18 (b) whereby silicon rich phases underwent extensive spheroidization and coarsening due to Ostwald ripening. Longer solutionizing time also did not contribute to complete dissolution of Al_2Cu phases. Furthermore, slight decrease in Vickers hardness was noted. Thus, solution heat treating time of 1 hour was consistently applied throughout the study.

5.9.4 Artificial Ageing Response for Different Al-Si based Alloys

The final stage of properties development for heat treatable aluminum alloys involved ageing treatment. In the present study, artificial ageing treatment was applied and involved precipitation at elevated temperature in the range of 120°C to 200°C. Decomposition of supersaturated solid solution was very complex, particularly for multicomponent alloys. Strengthening of heat-treatable alloys was due to the formation of nanometer sized particles which were homogenously distributed within the matrix. These particles acted as an excellent barrier to dislocation movement and thus improved resistance deformation, contributing to better mechanical properties [37].

The precipitation sequence varied depending on the respective alloys. For Al-Si-Mg-Cu-(Ni) alloys, the ageing response was rather complicated owing to

occurrence of several metastable phases which may include β' (Mg_2Si), θ' ($CuAl_2$), S' (Al_2MgCu) or Q' ($Al_5Mg_8Si_6Cu_2$) [12, 38]. It has been reported elsewhere that Cu: Mg ratio in solid solution played a decisive role on precipitation [11, 39]. Table 5.15 displayed a summary of Cu:Mg ratio for different alloys. The Ecka Alumix 231baseline system (Al-15Si-2.5Cu-0.5Mg) and Alloy B (Al-15Si-2.5Cu-0.9Ni-0.5Mg) with the Cu:Mg ratio close to 4 (at%) was anticipated to promote the formation of Al_2Cu (θ' and/or θ") and Al_2CuMg (S'). However, microstructural studies and XRD analysis did not detect the presence of Al_2CuMg. It was suggested that formation of S' phase was suppressed due to the presence of high silicon content which promoted the formation of $Al_5Mg_8Si_6Cu_2$ phase (Q') [40], which was substantiated by the XRD traces as displayed in Figure 5.23. Meanwhile, with the increase of the copper content which give way to high Cu:Mg ratio, Alloy A (Al-15Si-4.5Cu-0.5Mg) and C (Al-15Si-4.5Cu-0.9Ni-0.5Mg) was suggested to have preferential precipitation of Al_2Cu. This was consistent with the microstructural studies whereby plate-like precipitation of metastable Al_2Cu phase was observed. Therefore, the precipitation for all alloys used in the study was suggested to follow the sequence below:

$$SSS \rightarrow GP\ zones \rightarrow \theta'' \rightarrow \theta' \rightarrow \theta$$

Increase of the copper content was found to promote precipitation of Al_2Cu phase, as evidenced in Table 5.10, whereby Vickers hardness for Alloy A exceeded that of the Ecka Alumix 231 baseline system after heat treatment. Although similar plate-like structure Al_2Cu precipitates formed for both alloys, Alloy A was found to have higher distribution density of Al_2Cu precipitates formed within α-aluminum matrix and the precipitates were relatively smaller in size as observed in Figure 5.20(b). Thus, the

ageing response for Alloy A was significantly enhanced. It is worth noting that increase of copper content also shifted the ageing temperature required to achieve maximum hardness value to lower temperature as displayed in Figure 5.8. Since both Alloy A (Al-15Si-4.5Cu-0.5Mg) and C (Al-15Si-4.5Cu-0.9Ni-0.5Mg) had high copper content in solid solution, it was suggested that these alloys had higher driving force for precipitation to occur. Furthermore, as evidenced from DSC results displayed in Figure 5.8, the onset temperature for semicoherent θ' (Al_2Cu) formation for Alloy A and C shifted to slightly lower temperature than the Ecka Alumix 231 baseline system. Thus, when ageing temperature increased to 160ºC, it provided sufficient thermodynamical stimulus to induce the precipitation of high volume fraction of semicoherent θ' (Al_2Cu) phase. The decreased time to reach peak hardness with the increase in copper content, on the other hand, had been demonstrated for Al-Cu alloy [34]. This suggested a qualitative agreement with the results reported in this study. High diffusion rates due to the increase of ageing temperatures also contributed to shorter ageing time to reach peak ageing.

As discussed earlier in Section 5.9.3, nickel addition was detrimental since it reduces the amount of copper dissolved into α-aluminum matrix. The low Vickers hardness value for Alloy B (Al-15Si-2.5Cu-0.9Ni-0.5Mg) and C (Al-15Si-4.5Cu-0.9Ni-0.5Mg) was thus attributed to less precipitation of strengthening phases during ageing. The result was consistent with the data in Table 5.11, whereby the reaction enthalpy of the θ" and θ' decreased with the addition of nickel, which implied less amount of precipitates were formed. Additionally, precipitation of coherent θ" phases for both Alloy B and C was found to shift to higher temperatures and the volume fraction for θ' phase was significantly reduced as compared to the baseline system. It is generally

known that semi-coherent precipitates contributed more efficiently to hardening than coherent particles. Since there were fewer amounts of semi-coherent phases to be precipitated, Alloy B and C showed poor precipitation response.

5.10 References

[1] G. Kipouros, W. Caley, and D. Bishop, "On the Advantages of Using Powder Metallurgy in New Light Metal Alloy Design," *Metallurgical and Materials Transactions A,* vol. 37, pp. 3429-3436, 2006.

[2] N. A. Belov, D. G. Eskin, and N. N. Avxentieva, "Constituent Phase Diagrams of the Al-Cu-Fe-Mg-Ni-Si System And Their Application To the Analysis of Aluminium Piston Alloys," *Acta Materialia,* vol. 53, pp. 4709-4722, 2005.

[3] M. Zeren, "Effect of Copper And Silicon Content On Mechanical Properties in Al-Cu-Si-Mg Alloys," *Journal of Materials Processing Technology,* vol. 169, pp. 292-298, 2005.

[4] R. M. German, *Sintering Theory and Practice*. New York, N.Y.: John Wiley and Sons, 1996.

[5] W. F. Smith, *Structure and Properties of Engineering Alloys*. Montreal, Canada: McGraw-Hill Publishing Company, 1981.

[6] M. Lieblich, J. L. González-Carrasco, and G. Caruana, "Thermal Stability of An Al/Ni3Al Composite Processed by Powder Metallurgy," *Intermetallics,* vol. 5, pp. 515-524, 1997.

[7] Y. Yang, K. Yu, Y. Li, D. Zhao, and X. Liu, "Evolution of Nickel-Rich Phases in Al-Si-Cu-Ni-Mg Piston Alloys with Different Cu Additions," *Materials & Design,* vol. 33, pp. 220-225, 2012.

[8] C. W. Hennessey, W. F. Caley, G. J. Kipouros, and D. P. Bishop, "Development of Al-Si-Based P/M Alloys," *International Journal of Powder Metallurgy,* vol. 41, pp. 50-63, 2005.

[9] E. Sjölander and S. Seifeddine, "The Heat Treatment of Al-Si-Cu-Mg Casting Alloys," *Journal of Materials Processing Technology,* vol. 210, pp. 1249-1259, 2010.

[10] D. W. Heard, I. W. Donaldson, and D. P. Bishop, "Metallurgical Assessment of a Hypereutectic Aluminum-Silicon P/M Alloy," *Journal of Materials Processing Technology,* vol. 209, pp. 5902-5911, 2009.

[11] A. H. Committee, *Heat Treating* vol. 4. United States of America: ASM International, 1991.

[12] G. Wang, Q. Sun, L. Feng, L. Hui, and C. Jing, "Influence of Cu Content on Ageing Behavior of AlSiMgCu Cast Alloys," *Materials & Design,* vol. 28, pp. 1001-1005, 2007.

[13] R. M. Gomes, T. Sato, H. Tezuka, and A. Kamio, "Precipitation Behavior of P/M Hypereutectic Al-Si-Cu-Mg Alloys Containing Fe and Ni," *Materials Transactions,* vol. 39, pp. 357-364, 1998.
[14] I. Alfonso, C. Maldonado, G. Gonzalez, and A. Bedolla, "Effect of Mg Content And Solution Treatment on The Microstructure of Al-Si-Cu-Mg Alloys," *J. Mater. Sci. ,* vol. 41, pp. 1945-1952, 2006.
[15] E. A. Starke and T. H. Sanderes, Jr., *Aluminum Alloys- Physical and Mechanical Properties*. West Midlands: EMAS, 1986.
[16] J. A. Greenwood and J. H. Tripp, "The Elastic Contact of Rough Spheres," *Journal of Applied Mechanics,* vol. 89, pp. 153-159, 1967.
[17] J. Kerry, "Effect of Particle Shape on Unconfined Yield Strength," *Powder Technology,* vol. 194, pp. 246-251, 2009.
[18] S. J. L. Kang, "Sintering: Densification, Grain Growth & Microstructure," *Elsevier Butterworth-Heinemnn, Oxford, UK,* 2005.
[19] R. M. German, *Liquid Phase Sintering*. Troy, New York: Plenum Press, 1985.
[20] A. Prince, Effenberg in G., G. Petzow, and G. Effemberg, *A Comprehensive Compendium of Evaluated Constitutional Data and Phase Diagram* vol. 4. Basel, Switzerland: VHC Publishing, 1991.
[21] G. Wang, X. Bian, W. Wang, and J. Zhang, "Influence of Cu and minor elements on solution treatment of Al-Si-Cu-Mg cast alloys," *Materials Letters,* vol. 57, pp. 4083-4087, 2003.
[22] G.B. Schaffer, T.B. Sercombe, and R. N. Lumley, "Liquid Phase Sintering of Aluminium Alloys," *Materials Chemistry and Physics,* vol. 67, pp. 85-91, 2001.
[23] K. S. Dunnett, R. M. Mueller, and D. P. Bishop, "Development of Al-Ni-Mg-(Cu) Aluminum P/M Alloys," *Journal of Materials Processing Technology,* vol. 198, pp. 31-40, 2008.
[24] J. Zhou and J. Duszczyk, "Liquid Phase Sintering of an AA2014-Based Composite Prepared From an Elemental Powder Mixture," *Journal of Materials Science,* vol. 34, pp. 545-550, 1999.
[25] H. C. Neubing, J. Gradhl, and H. Danninger, *Advances in Powder Metallurgy and Particulate Materials*. Princeton, NJ: Metal Powder Industries Federation, 2002.
[26] D. P. Bishop, B. Hofman, and K. R. Couchman, *Advances in Powder Metallurgy and PArticulate Materials* vol. 1. Princeton, NJ: Metal Powder Industries Federation, 2000.
[27] Su.S.S. and I. T. Chang, "Effect of Processing Conditions on Hypereutectic Aluminum-Silicon P/M Alloys," 2010, pp. 49-57.
[28] R. M. German, P. Suri, and S. J. Park, "Review: Liquid Phase Sintering," *Journal of Materials Science,* vol. 44, pp. 1-39, 2009.
[29] R. W. Cooke, R. L. Hexemer, Jr, , I. W. Donaldson, and D. P. Bishop, "Dispersoid Strengthening of Al-Cu-Mg P/M Alloy Utilising Transition Metal Additions," *Powder Metallurgy,* vol. 54, pp. 1-9, 2011.
[30] P. Ouellet and F. H. Samuel, "Effect of Mg On The Ageing Behaviour of Al-Si-Cu 319 Type Aluminium Casting Alloys," *Journal of Materials Science,* vol. 34, pp. 4671-4697, 1999.
[31] P. Ouellet, F. H. Samuel, D. Gloria, and S. Valtierra, "Effect of Mg Content On the Dimensional Stability And Tensile Properties of Heat Treated Al-Si-Cu (319)

Type Alloys," *International Journal of Cast Metals Research,* vol. 10, pp. 67-78, 1997.
[32] F. H. Samuel, "Incipient Melting of Al5Mg8Si6Cu2 and Al2Cu Intermetallics In Unmodified And Strontium-Modified Al–Si–Cu–Mg (319) Alloys During Solution Heat Treatment," *Journal of Materials Science,* vol. 33, pp. 2283-2297, 1998.
[33] J. H. Sokolowski, M. B. Djurdjevic, C. A. Kierkus, and D. O. Northwood, "Improvement of 319 Aluminum Alloy Casting Durability by High Temperature Solution Treatment," *Journal of Materials Processing Technology,* vol. 109, pp. 174-180, 2001.
[34] H. Toda, T. Nishimura, K. Uesugi, Y. Suzuki, and M. Kobayashi, "Influence of High-Temperature Solution Treatments on Mechanical Properties of An Al-Si-Cu Aluminum Alloy," *Acta Materialia,* vol. 58, pp. 2014-2025, 2010.
[35] G. Timmermans, L. Froyen, and J. V. Humbeeck, "Solid ↔ Liquid Phase Transformations in Hypereutectic P/M Al-Si-Fe-X Alloys," *Journal of Materials Science,* vol. 35, pp. 3289-3299, 2000.
[36] P. Kapranos, D. H. Kirkwood, H. V. Atkinson, J. T. Rheinlander, J. J. Bentzen, P. T. Toft, C. P. Debel, G. Laslaz, L. Maenner, S. Blais, J. M. Rodriguez-Ibabe, L. Lasa, P. Giordano, G. Chiarmetta, and A. Giese, "Thixoforming of an Automotive Part in A390 Hypereutectic Al-Si Alloy," *Journal of Materials Processing Technology,* vol. 135, pp. 271-277, 2003.
[37] J. Zander and R. Sandström, "One Parameter Model for Strength Properties of Hardenable Aluminium Alloys," *Materials & Design,* vol. 29, pp. 1540-1548, 2008.
[38] W. Reif, S. Yu, J. Dutkiewicz, R. Ciach, and J. Król, "Pre-ageing of AlSiCuMg Alloys in Relation To Structure And Mechanical Properties," *Materials and Design,* vol. 18, pp. 253-256, 1997.
[39] L. F. Mondolfo, *Aluminum Alloys: Structure and Properties*. London: Butterworth & Co. Ltd, 1979.
[40] A. K. Gupta, M. C. Chaturvedi, and A. K. Jena, *Mater. Sci.Tecj.,* vol. 5, p. 52, 1989.

Chapter 6

Conclusions and Future Work

6.1 Conclusion

- Green density of the compact increased with increasing compaction pressure. At 400MPa, the green density of the Ecka Alumix 231(Al-15Si-2.5Cu-0.5Mg) achieved 2.27g/cm^3 or 85.30% of theoretical density. Above which little densification was observed. No significant improvement in relative densification with the addition of copper and/or nickel addition was observed as compared to that of commercial Ecka Alumix 231. However, slight increase in relative densification can be noted at lower compaction pressure for Alloy A (Al-15Si-4.5Cu-0.5Mg), B (Al-15Si-2.5Cu-0.9Ni-0.5Mg) and C (Al-15Si-3.5Cu-0.9Ni-0.5Mg) which was mainly attributed to better packing behavior.
- The efficacy of the sintering atmosphere for Al-Si-Cu-Mg increased in the order: nitrogen> vacuum> nitrogen with 3% hydrogen. Nitrogen atmosphere was the most efficacious sintering atmosphere due to the formation of AIN which later induced pore filling effect. Presence of hydrogen in the sintering atmosphere had detrimental effects in sintering due to the formation of MgH_2 which decomposed at higher temperature and lead to an increase in the pore pressure. Hence, pore swelling effect occurred and inhibited compact densification.

- Densification of Al-Si-Cu-Mg alloy systems depended largely on both sintering atmosphere and amount of liquid phase presented. The optimum condition for sintering of Ecka Alumix 231 is 560^{o}C or 15% liquid content under nitrogen atmosphere to attain compacts with higher sintered density, less porosity and better mechanical properties. Sintering time of 60 minutes is preferential for sufficient densification to carry out.
- Shrinkage counteracted the thermal expansion when the sintering of the compact started. Overall compact shrunk by 0.6% when sintered at 560^{o}C. The volume change can attribute to the presence of entrapped gas, diffusion reaction and wettability of the liquid.
- Ecka Alumix 231 consisted of master alloy with the composition of Al-28Si-5Cu-1Mg (wt%) mixed with elemental aluminum powder. Globulization of the Si and coarsening of Si particles occurred during the heating event. Upon reaching 547^{o}C, fine dispersion of Si particles was eliminated. The web-like Cu-rich region dissolved and form liquid phase which surrounded the grain boundaries to form the necklace-like structure. Phase identified included α- Al, Si, $CuAl_2$ phase (θ) and Q phase ($Cu_2Mg_8Si_6Al_5$.). Traces of $FeSiAl_5$ were observed at the grain boundaries due to the low solubility of Fe in the aluminum matrix.
- Addition of copper up to 4.5wt% in Alloys A and C enhanced the liquid phase formation leading to lower sintering temperature required. Higher sintered density was obtained for compacts with copper additions.
- Nickel addition was detrimental to sintering response and reduced the amount of liquid phase necessary for densification due to the formation of $Al_3(Ni, Cu)_2$

phase. Thus, Alloy B and C with 0.9wt% Ni additions experienced slight decrease in sintering response as compared to the baseline system.

- Nickel addition did not strengthen the base alloy through dispersoid mechanism since it formed coarse intermetallic $Al_3(Ni,Cu)_2$ phase along the grain boundaries with no obvious dispersoid strengthening features being observed in α-aluminum grains.
- The optimal solution treatment for all alloy systems was solution heat treatment at 510°C for 1 hour. Ecka Alumix showed an increase in age-hardenability with the increase of solution temperature up to 510°C. Subsequent increase of solution temperature to 520°C was detrimental since the Vickers hardness decreased with time. High solution heat treatment temperature was beneficial for baseline system (Ecka Alumix 231), Alloy A, C. Meanwhile, Alloy B favored solution treatment temperature below fusion of low eutectic melting point.
- It was suggested that Al_2Cu precipitates were the main strengthening phase for all alloy systems. Precipitation sequence for Al-Si-Cu-Mg-(Ni) was supersaturated solid solution (SSS)→ GP zones → θ”→ θ’→ θ.
- Increase of copper content had beneficial effects on heat treatment since it increased the Vickers hardness value, shifted the maximum hardness to lower ageing temperatures and time. Nickel addition, however, reduced the amount of copper content dissolved in the α-aluminum and reduced the precipitation of semicoherent θ’ phases during subsequent precipitation hardening.

6.2 Future Work

The final properties of the compacts had been determined to be influenced largely by the thermal processing conditions (i.e. sintering, solution treatment and precipitation hardening) and additions of different alloys. However, some aspects of this study still remain unclear. An outline of the proposed work is suggested as below:

- Introduction of elemental alloying addition to mixtures of master alloy powder in this study has generated large pores. Thus, it is necessary to control the size of the elemental alloy additions. It is also suggested that introduction of master alloys (i.e. Al-Cu, Al-Ni, Al-Si) into the powder mixtures and use of prealloyed powder with the designated composition can contribute to better densification and less porosity.
- Although sufficient sintering time is required for compact densification, concurrent microstructural coarsening also takes place. Thus, modification in the powder metallurgy process is proposed to carry out by heating the mixed powder until it reaches to the lowest melting temperature of the powder constituent prior to compaction. It is anticipated that with the formation of small amount of liquid phase coupled with the optimum compaction pressure, it might result in better pore closure and more interparticle bonding which will consequently reduce the amount of time required for sintering.
- Pore closure and high densification were achieved at the optimal sintering temperature and time. However, it remains unclear whether variation in the cooling rates has significant influence on the final properties. Furthermore,

it is also necessary to study the effect of cooling rates in the subsequent solution heat treatment

- Single step solution heat treatment was used in this study. Although it is desirable to maximize the dissolution of copper rich phases by applying high temperature, localized incipient melting can lead to deterioration in mechanical properties. It has previously been determined that two steps solution heat treatments can produce optimum combination of strength and ductility for 319 aluminum alloy [1, 2]. Hence, further studies can seek to improve the mechanical properties by applying multiple step solution heat treatments.
- Following solution heat treatment, quenching is carried out immediately in order to suppress precipitation. Although quenching was kept constant in this study, it is suggested that further studies can investigate variation in quenching rate and quenching medium to better enhance the properties of the final products.
- In order to obtain clearer understandings on the effects of alloying additions (i.e. Cu, Ni), it is suggested that a wider range of different weight percentage of alloying additions should be added to the baseline systems. The subsequent sintering, heat treatment response due to the variation in alloy composition can further be investigated. Statistical approach can be applied to design the experiment. Apart from incorporating Cu and Ni as the alloying additions, more studies should be extended to other alloying additions. For instance, zinc additions which can increase the strength and Fe additions which can increase the ductility [3].

- The high silicon content of the alloys used in this study is suggested to have considerable good wear resistance. It will be very useful to study the tribological behavior of Ecka Alumix 231 and the effects of alloying additions and heat treatment on the wear behavior of the alloys.

6.3 References

[1] J. H. Sokolowski, M. B. Djurdjevic, C. A. Kierkus, and D. O. Northwood, "Improvement of 319 Aluminum Alloy Casting Durability by High Temperature Solution Treatment," *Journal of Materials Processing Technology,* vol. 109, pp. 174-180, 2001.

[2] J. H. Sokolowski, X. C. Sun, G. Byczynski, D. O. Northwood, D. E. Penrod, R. Thomas, and A. Esseltine, "The Removal of Copper-Phase Segregation And The Subsequent Improvement in Mechanical Properties of Cast 319 Aluminium Alloys by a Two-Stage Solution Heat Treatment," *Journal of Materials Processing Technology,* vol. 53, pp. 385-392, 1995.

[3] A. H. Committee, *Properties and Selection: Nonferrous Alloys and Special Purpose Materials* vol. 2: ASM International, 1990.